UC San Diego
UC San Diego Electronic Theses and Dissertations

Title
Tribological Study of Contact Interfaces in Hard Disk Drives

Permalink
https://escholarship.org/uc/item/3tb2h83q

Author
Fu, Youyi

Publication Date
2016

Peer reviewed|Thesis/dissertation

UNIVERSITY OF CALIFORNIA, SAN DIEGO

Tribological Study of Contact Interfaces in Hard Disk Drives

A dissertation submitted in partial satisfaction of the requirements for the degree

Doctor of Philosophy

in

Engineering Sciences (Mechanical Engineering)

by

Youyi Fu

Committee in charge:

Professor Frank E. Talke, Chair
Professor Yuri Bazilevs
Professor Vitaliy Lomakin
Professor Vlado A. Lubarda
Professor Hidenori Murakami

2016

The dissertation of Youyi Fu is approved, and it is acceptable in quality and form for publication on microfilm and electronically:

_____

_____

_____

_____

_____

Chair

University of California, San Diego

2016

to my parents Wei Fu and Haihong Li, my brother Youyan Fu,

and my grandparents Chengjie Fu, Xi Zhao, Xuanwen Li and Yunhua Ye

TABLE OF CONTENTS

LIST OF FIGURES

LIST OF TABLES

ACKNOWLEDGEMENTS

First, I would like to express my sincere appreciation to my advisor Professor Frank E. Talke for his guidance, support, and kind help during my Ph.D. study. Without him, it would have been impossible for me to achieve the work that I show in this dissertation. In the past five years, Professor Talke led by example and continued to motivate me to try to become an outstanding researcher and engineer. He not only helped me build a strong technical foundation for my engineering career, but also helped me develop a critical attitude and passion towards research. I will forever be grateful for the opportunities he has laid out in front of me.

I would also like to thank Professor Vlado A. Lubarda. His insight in solid mechanics always enlightened me in all of my research projects. His eloquent explanations directed me into new ways of thinking about my work and how to advance it.

I am grateful to Dr. Andrey Ovcharenko, Dr. Min Yang, Dr. Jih-Ping Peng, Dr. Hao Zheng, and Dr. Ralf Brunner for being my mentors during my summer internships at Western Digital Corporation as well as when I was back at school in UCSD. The opportunity to spend such valuable time with them and to discuss my work with them was very helpful. I am also grateful to John Hogan and Ross Cuyler from NHK Corporation for their interest and support of my research.

I would like to thank my labmates Karcher Morris, Young Woo Seo, Benjamin Suen, Liane Matthes, Phuong Truong, Alex Phan, and Tan Trinh for their help during my Ph.D. study. I am grateful to have had such a diverse group of thinkers around me

making my days more enjoyable. I also wish to thank Iris Villanueva for her help with administrative matters, and Ray Descoteaux for his help with my experimental studies.

Last but certainly not least, I want to thank my family. I would like to thank my parents and grandparents for raising me and instilling in me the values that carry me through each day. Being 6,359 miles away from home is not ideal, but I felt like you were with me every day because of your constant encouragement and words of wisdom. I would also like to thank my twin brother Youyan Fu for growing up with me and always making the extra effort to make me happy. I would like to thank my aunt Haitao and my uncle Xiaohui for providing me with a great deal of help and guidance during my study at their alma mater UC San Diego.

Chapter 4, in part, is a reprint of the material as it appears in "The effect of diamond-like carbon overcoat on the tribological performance of the dimple/gimbal interface in hard disk drives," Y. Fu, V. A. Lubarda, and F. E. Talke, Journal of Tribology, vol. 138, no. 4, pp. 041901–1 – 041901–12, 2016. The dissertation author was the primary investigator and author of this paper.

Chapter 5, in part, is a reprint of the material as it appears in "The effects of parking time, temperature, and slider position on lubricant migration in hard disk drives," Y. Fu, R. Brunner, J. P. Peng, J. Apte, J. McFadyen, and F. E. Talke, IEEE Transactions on Magnetics, vol. 50, no. 11. pp. 1–4, 2014. The dissertation author was the primary investigator and author of this paper.

Chapter 6, in part, is a reprint of the material as it appears in "Modeling of thermal sensor response to disk asperities," Y. Fu, C. Zhang, A. Ovcharenko, M. Yang, and F. E. Talke, IEEE Transactions on Magnetics, vol. 52, no. 9, pp. 3301708–1–

3301708–8, 2016. The dissertation author was the primary investigator and author of this paper.

Chapter 7, in part, is a reprint of the material as it appears in "Wear between lift tab and load/unload ramp in hard disk drives," Y. Fu, M. Yang, J. P. Peng, and F. E. Talke, accepted by IEEE Transactions on Magnetics, 2016. The dissertation author was the primary investigator and author of this paper.

Chapter 7, in part, is a reprint of the material in "Simulation of lift tab ramp contact during load unload," Y. Fu, K. Morris, and F. E. Talke, currently under preparation for publication. The dissertation author was the primary investigator and author of this paper.

VITA

07/2010   Bachelor of Science in Mechanical Engineering, Beihang
                       University (BUAA), Beijing, China

09/2011-09/2016   Research and Teaching Assistant, Center for Memory and
                       Recording Research, Department of Mechanical and Aerospace
                       Engineering, University of California, San Diego, La Jolla, CA,
                       USA

06/2012-09/2012   Full-time summer intern, Western Digital, San Jose, CA, USA

03/2013   Master of Science in Mechanical Engineering, University of
                       California, San Diego, La Jolla, USA

06/2013-09/2013   Full-time summer intern, Western Digital, San Jose, CA, USA

06/2014-09/2014   Full-time summer intern, Western Digital, San Jose, CA, USA

12/2016   Doctor of Philosophy in Engineering Sciences (Mechanical
                       Engineering), University of California, San Diego, La Jolla, CA,
                       USA

PUBLICATIONS

Y. Fu, R. Brunner, J. P. Peng, J. Apte, J. McFadyen, and F. E. Talke, "The effects of parking time, temperature, and slider position on lubricant migration in hard disk drives," IEEE Transactions on Magnetics, vol. 50, no. 11. pp. 1–4, 2014.

Y. Fu, V. A. Lubarda, and F. E. Talke, "The effect of diamond-like carbon overcoat on the tribological performance of the dimple/gimbal interface in hard disk drives," Journal of Tribology, vol. 138, no. 4, pp. 041901–1 – 041901–12, 2016.

Y. Fu, C. Zhang, A. Ovcharenko, M. Yang, and F. E. Talke, "Modeling of thermal sensor response to disk asperities," IEEE Transactions on Magnetics, vol. 52, no. 9, pp. 3301708–1–3301708–8, 2016.

Y. Fu, M. Yang, J. P. Peng, and F. E. Talke, "Wear between lift tab and load/unload ramp in hard disk drives," accepted by IEEE Transactions on Magnetics, 2016

Y. Fu, K. Morris, and F. E. Talke, "Numerical simulation of contact between the suspension lift tab and the ramp during the load/unload process of hard disk drives," currently under preparation for publication.

ABSTRACT OF THE DISSERTATION

Tribological Study of Contact Interfaces in Hard Disk Drives

by

Youyi Fu

Doctor of Philosophy in Engineering Sciences (Mechanical Engineering)

University of California, San Diego, 2016

Professor Frank E. Talke, Chair

To achieve an areal density of 1 terabits per square inch (1.55 gigabits/mm^2) in hard disk drives, the size of magnetic grains in hard disks has been reduced to approximately 7 nm and the spacing between the magnetic head and the disk has been minimized to 1 to 2 nm. At a spacing on the order of 1 to 2 nm between the head and the disk, it is likely that contacts between the magnetic head and the disk occur during reading and writing, causing erasure of data or even failure of the head/disk interface. Wear particles can be generated as a consequence of contacts between slider and disk, and if particles enter the head/disk interface, catastrophic failure of the head/disk

interface can occur. To reduce the generation of wear particles and avoid failure of the head/disk interface, it is important to investigate how the tribological performance of all contact interfaces in hard disk drives can be improved.

In this dissertation, the tribological performance of the most important contact interfaces in a hard disk drive are investigated with a focus on the generation of wear particles and lubricant migration. First, fretting wear is investigated to study the effect of a diamond-like carbon (DLC) overcoat on wear of the dimple/gimbal interface. A numerical simulation model based on finite element analysis was developed to explain the experimental results. Then, lubricant migration on the air bearing surface and its effect on the head medium spacing (HMS) was investigated as a function of temperature, slider position, and "parking time" of the slider on the ramp. Thereafter, the thermal response of a thermal sensor during contact with asperities on the disk surface was analyzed. The effects of experimental and environmental conditions on the resistance change of the sensor were studied. Finally, experimental and numerical investigations were performed to analyze contact between the suspension lift tab and the ramp in hard disk drives. The voice coil motor current was used to characterize the change of the friction force and the generation of wear debris at the lift tab/ramp interface during load/unload testing. Numerical simulations were performed to analyze how to reduce contact stress between the lift-tab and the ramp.

The results of this dissertation will be helpful in improving the tribological performance of hard disk drives.

Chapter 1

Introduction

1.1 History of Hard Disk Drives

Computer technology has developed at a very fast rate in the past few decades. New hardware and software products are invented every day. Enormous amounts of digital data are generated at an increasing amount in the form of pictures, videos, music, phone message, medical records, purchase records, map information, etc. According to studies by IBM in 2012 [1], 2.5 billion gigabytes (GB) of data are created in the world every day. In order to store such a large quantity of data, hard disk drives are the storage devices of choice because of their high capacity and low cost in comparison to other storage devices, such as solid state drive.

Figure 1.1 shows the IBM 305 RAMAC (Random Access Memory Accounting System), the first hard disk drive in the world, created in 1956. While the storage capacity of the RAMAC was a mere 5 megabytes (MB), it occupied a room with an area of 9 m by 15 m [2]. With the rapid development of hard disk drive technology, the storage density of hard drives has increased by more than ten million times over the past sixty years. In 2015, Western Digital's HGST division announced a new product, the "Ultrastar He10". It has a storage capacity of 10 terabytes (TB) with an areal density of 816 gigabits/inch^2 (1.26 gigabits/mm^2).

1

Figure 1.1 The world's first hard disk drive, created by IBM (courtesy of [3])

In 2016, Seagate launched the "thinnest 2TB hard disk drive" in the world, with dimensions of 113.5 mm (length) by 76 mm (width) by 9.6 mm (height). This device weighs only 135 grams (g), while the RAMAC had a weight of over one ton [4]. Although engineers have achieved incredible improvement in the storage capacity of hard disk drives, there is still a heavy demand for drives with higher areal density and better reliability in order to store the huge amount of data created every day.

1.2 Mechanical Design of Hard Disk Drives

Figure 1.2 shows the typical design of a hard disk drive. Inside today's typical hard disk drive, several disks are mounted on the same spindle. The magnetic disks rotate at high speed when the hard disk drive is in operation. A suspension which carries the slider is fixed to the actuator arm. When the hard disk drive is not in operation, the slider is "parked" on the load/unload ramp. If the hard disk drive needs to read or write

data, a torque is generated by the voice coil motor to rotate the actuator arm with respect to the pivot, and load the slider onto the disk. This process is called "loading." If the hard disk drive shuts down, the slider on the suspension retracts from the disk back to the load/unload ramp. This process is called "unloading."
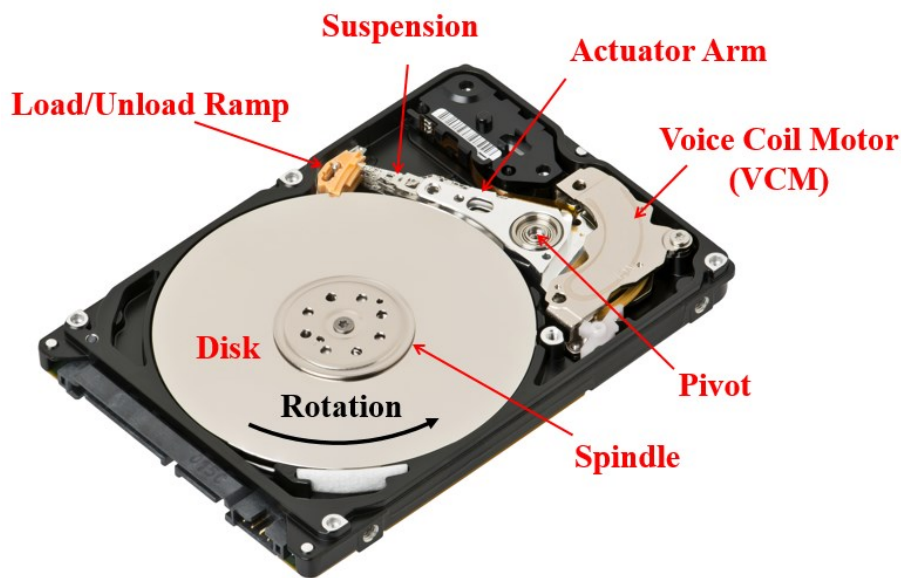
Figure 1.2 Typical mechanical design of hard disk drive (after [5])

Figure 1.3 shows a schematic of the head gimbal assembly (HGA). It consists of the suspension, the flexure, and the slider. The slider is attached to the suspension through the flexure. One surface of the slider is bonded to the flexure, and the flexure is welded to the suspension. Between the flexure and the suspension is the dimple/gimbal contact interface which allows the slider to perform pitch or roll motions while the slider is flying on the disk. The disk-facing surface of the slider is called the air bearing surface (ABS). As shown in Figure 1.4, the air bearing surface is etched to a particular pattern to generate the desired pressure distribution on the slider. This pressure distribution is used to support the slider over the disk and to keep a constant spacing between the slider

and the disk. The base plate of the suspension adheres to the actuator arm. The suspension is rotated by the actuator arm.
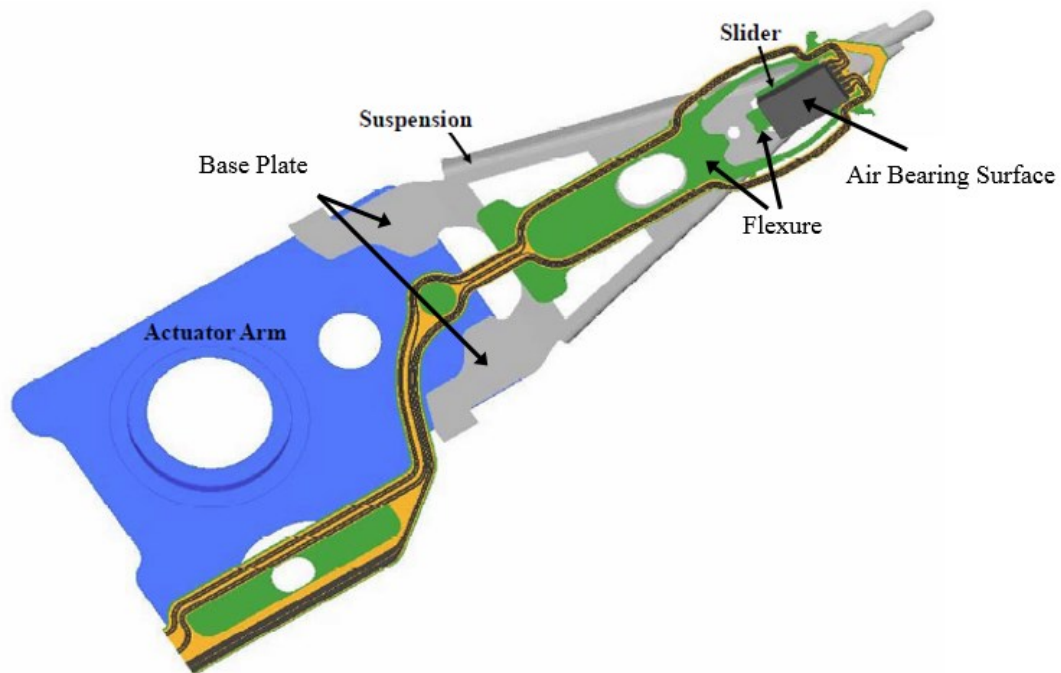
Figure 1.3 Schematic of head gimbal assembly (HGA) in hard disk drives (courtesy of [6])

Figure 1.4 Typical air bearing surface design used in current hard disk drives

1.3 Principle of Magnetic Recording

Since the invention of the first hard disk drive, a number of read and write techniques has been used to increase the areal density and the signal to noise ratio (SNR) of hard disk drives. However, the fundamental principle of magnetic recording in hard disk drives have remained the same. In this section, the process of writing and reading in a hard disk drive is discussed.

1.3.1 Principle of Writing

Information is processed in modern computers using binary numbers represented by a string of "0"s and "1"s. For this reason, data stored in hard disk drives are required to also be in binary format. On a magnetic disk, "0" and "1" are represented by the magnetization direction of magnetic bits. Figure 1.5 illustrates the writing process of a hard disk drive. Binary data from the computer is first processed by a pre-amplifier in the hard disk drive, and an electric current waveform is generated according to the binary data. The current waveform is then sent to the write element in the magnetic head and a magnetic field is created to change the magnetization direction of magnetic bits on the disk. After the writing process, information in the form of "0" and "1" is stored on the magnetic disk. This is represented by the "up" and "down" direction of magnetic bits for a perpendicular magnetic recording (PMR) disk. For a longitudinal magnetic recording (LMR) disk, "0"s and "1"s are represented by "left" and "right" going arrows of magnetic bits.
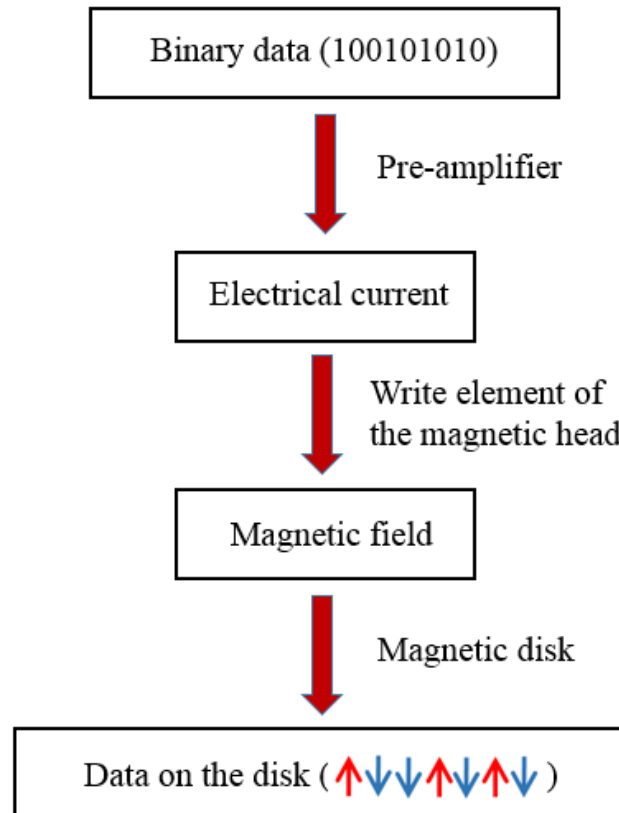
Figure 1.5 The write process of a hard disk drive

Figure 1.6 shows the schematic of a magnetic head writing data on a perpendicular magnetic recording disk. The write element of the magnetic head consists of a write pole, a coil, and a return pole. During writing, a current is applied to the coil on the write pole to generate an external magnetic field between the write pole and the return pole. When the magnetic head flies over the disk, the external magnetic field changes the magnetization direction of magnetic bits by altering the direction of the current. When the external field moves away, magnetic bits maintain their magnetization direction due to their crystalline anisotropy.
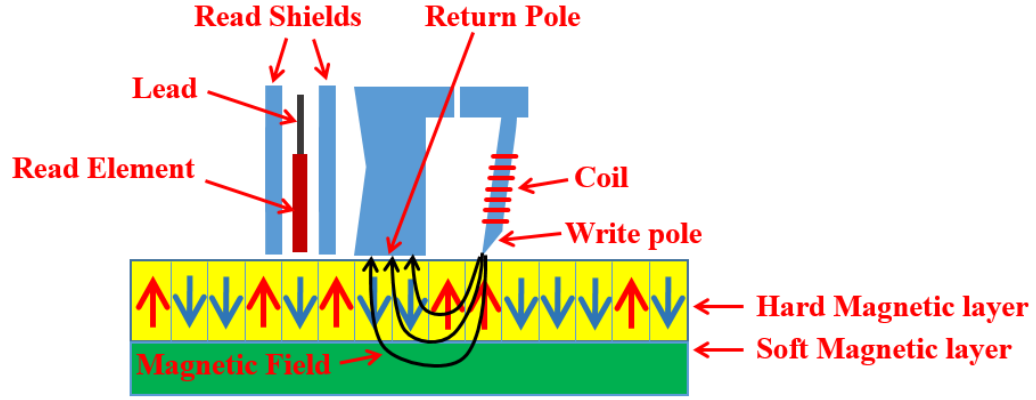
Figure 1.6 Schematic of magnetic head writing data on the disk (after [7])

1.3.2 Principle of Reading

The reading process of a hard disk drive which is shown in Figure 1.7 is essentially the reverse of the writing process that is shown in Figure 1.5. When the magnetic head flies over the disk, the magnetic field generated by the magnetic bits induces a voltage pulse in the read element according to Faraday's law of induction

$$V = -N\frac{d\phi}{dt} \tag{1.1}$$

where V is the induced voltage, N is the number of turns of the coil, and $\frac{d\phi}{dt}$ is the change of the magnetic flux. A preamplifier then amplifies the voltage and an AC/DC converter converts the analog signal to a digital signal.

In current hard disk drives, the physical mechanism of reading data from the disk is based on the magnetoresistive effect, which states that the resistance of a magnetoresistive material changes if an external magnetic field is applied. Figure 1.8 shows a magnetic head reading data from the disk. As the slider flies over the disk, the resistance of the read element changes due to the presence of the magnetic field generated by the magnetic bits on the disk. Since a constant current is applied across the

read element, the voltage in the read element changes. After amplification and AC/DC conversion, a high voltage amplitude represents a "1" and a low voltage amplitude represents a "0". In this way, magnetic information stored on the disk can be converted to the binary information and processed by the computer.
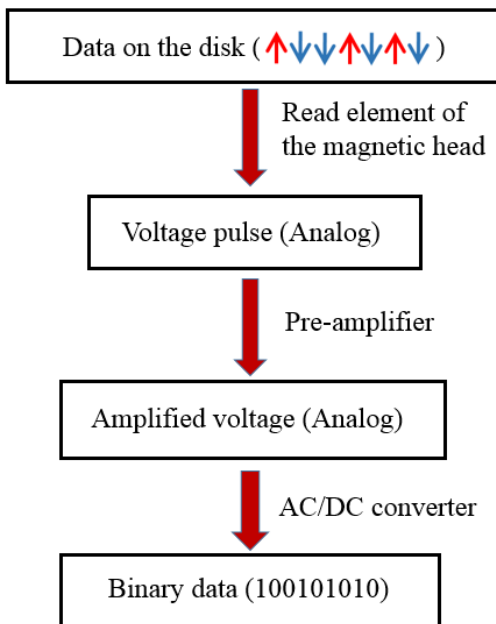
Figure 1.7 The reading process of a hard disk drive
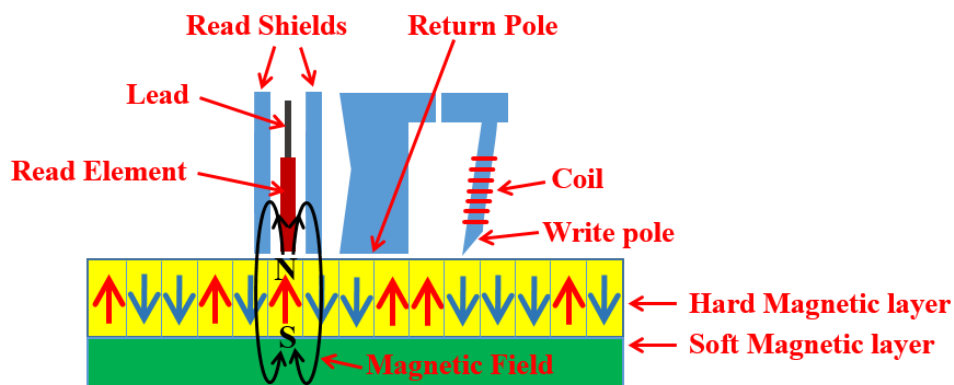
Figure 1.8 Schematic of magnetic head reading data on the disk (after [7])

1.4 Evolution of Hard Disk Drive Technology

1.4.1 Magnetic Media in Hard Disk Drives

Figure 1.9 shows the schematic of a recording media in a hard disk drive. Data is stored in the circumferential direction on a magnetic track. The areal density is a parameter that relates to the capacity of the disk, that is, how many magnetic bits are
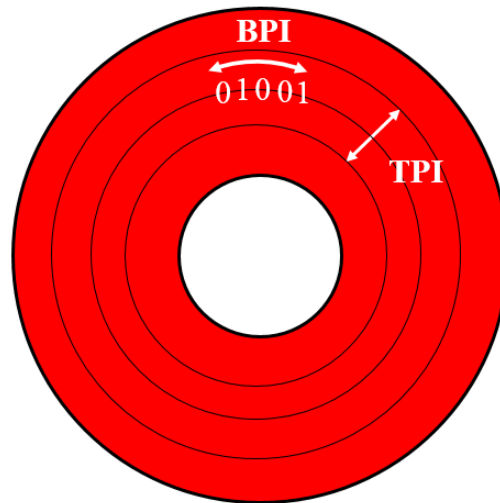
Figure 1.9 Schematic of magnetic tracks on a disk

stored on a square inch of disk. The areal density is defined as

$$Areal\ density = TPI * BPI \qquad (1.2)$$

where, the track density, TPI, measures the number of tracks per inch (25.4 mm) in the radial direction and the linear density, BPI, measures the number of bits per inch along a track.

Longitudinal Magnetic Recording (LMR)

Prior to 2005, all hard disk drives used longitudinal magnetic recording (LMR) technology. Figure 1.10 shows a schematic of longitudinal magnetic recording technology. The magnetization direction of magnetic bits on the longitudinal magnetic recording media is parallel to the disk surface (longitudinal). In order to increase the areal density of longitudinal magnetic recording media, the volume of magnetic grains needs to be reduced. However, if the volume becomes too small, the magnetic grains become thermally unstable and randomly flip their magnetization direction with a change in temperature. This phenomenon is referred to as the superparamagnetic effect [8]. To keep the data on a disk stable for more than ten years, the energy barrier of a magnetic grain E_b must satisfy the relationship [9]

$$E_b \approx \frac{\mu_0 H_c^{\ 2}}{4\sqrt{2}N_d} V_g > 40 k_B T \tag{1.3}$$

where μ_0 and H_c are the permeability and coercivity of the magnetic material, N_d is the
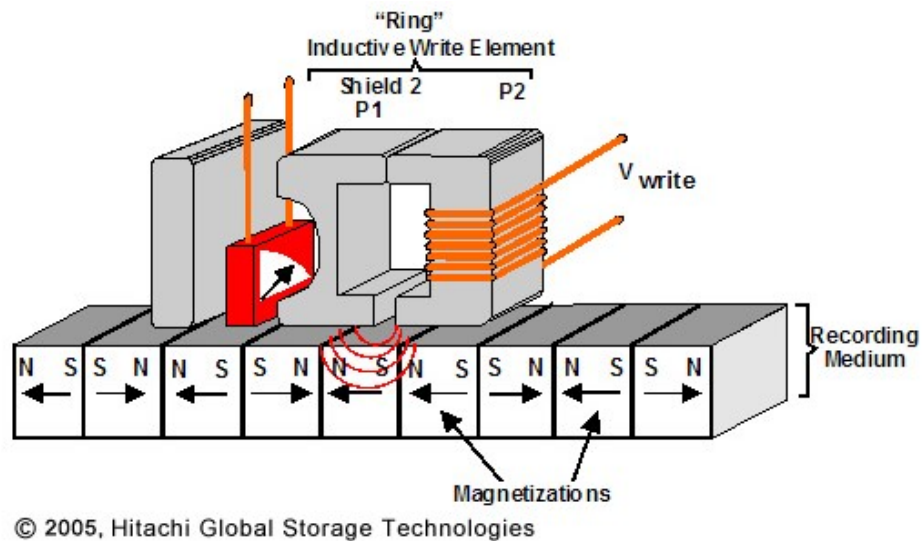
Figure 1.10 Schematic of longitudinal magnetic recording (courtesy of [10])

worst-case demagnetizing factor, V_g is the grain volume, k_B is the Boltzmann's constant, and T is the temperature. According to Equation 1.3, the minimum volume of a thermally stable magnetic grain within the media is about 600 nm^3. Therefore, the areal density of longitudinal magnetic recording media has an upper limit of approximately 100 to 200 Gb/inch^2 [11].

Perpendicular Magnetic Recording (PMR)

Perpendicular magnetic recording (PMR) technology is implemented in most disk drives that were manufactured after 2005 to increase the areal density of the media. As shown in Figure 1.11, magnetic bits on a perpendicular magnetic recording media are magnetized in the direction perpendicular to the disk. Since the area of a magnetic bit on perpendicular recording media is almost five times smaller than that of a magnetic bit on longitudinal recording media, the areal density of the perpendicular magnetic recording media can be up to five times greater than that of longitudinal magnetic recording media [12]. Because magnetic grains in perpendicular magnetic recording

© 2005, Hitachi Global Storage Technologies
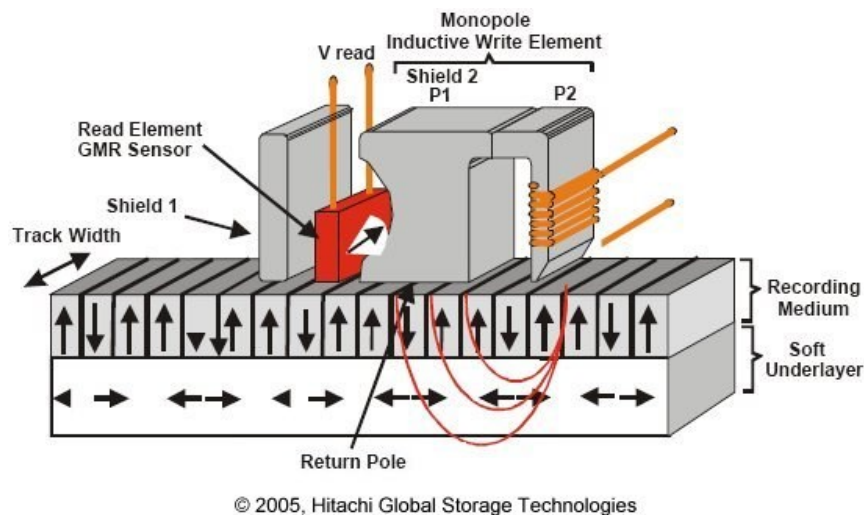
Figure 1.11 Schematic of perpendicular magnetic recording (courtesy of [10])

media have a smaller diameter than magnetic grains in longitudinal magnetic recording media, the perpendicular magnetic recording magnetic grains are more thermally stable than those in longitudinal magnetic recording media. During the writing process the soft under-layer in perpendicular magnetic recording media assists in producing a strong magnetic field that allows magnetic grains with high coercivity to be used in perpendicular magnetic recording media and increases the thermal stability. The upper limit of areal density for perpendicular magnetic recording media is predicted to be approximately 1 Tb/ inch^2 (1.55 gigabits/mm^2) [9].

Figure 1.12 shows a transmission electron microscopy (TEM) image of perpendicular magnetic recording media. The granular dots represent magnetic grains and each magnetic bit (blue or red areas) consists of several magnetic grains. According to the grain-counting argument [13], the signal to noise ratio of a magnetic recording media is proportional to the number of magnetic grains per magnetic bit

$$SNR_{media} \propto \frac{Wbt}{V_g} = \frac{bit\ volume}{grain\ volume} \tag{1.4}$$

where W, b, and t are the width, length, and thickness, respectively, of a magnetic bit. V_g denotes the volume of a single magnetic grain. To increase the areal density of perpendicular magnetic recording media, the volume of magnetic bits must be decreased, which causes the signal to noise ratio of perpendicular magnetic recording media to drop significantly [14].
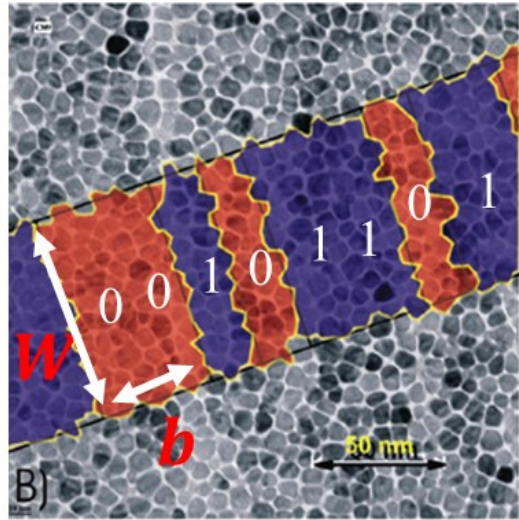
Figure 1.12 TEM image of magnetic bits within the PMR media (courtesy of [15])

Bit-Patterned Media (BPM)

Another type of magnetic media is bit-patterned media (BPM). Figure 1.13 shows a comparison between perpendicular magnetic recording media and bit-patterned media. As shown in Figure 1.13 (a), each magnetic bit in perpendicular magnetic recording media is formed by several magnetic grains. However, in Figure 1.13 (b), each magnetic bit in bit-patterned media is represented by an independent magnetic "island." Since the feature size of these "islands" is very small, bit-patterned media must be manufactured using nanolithography or self-assembly of nanoparticles [16]. Small feature sizes enable the bit-patterned media to achieve an areal density greater than 1 Tb/ inch^2 while maintaining a high signal to noise ratio. In addition, the separation of these islands is advantageous because it significantly reduces crosstalk between magnetic bits. Due to the high cost of mass production of bit-patterned media, bit-patterned media recording technology is not used in current hard disk drives.

(a) perpendicular magnetic recording media   (b) bit patterned media
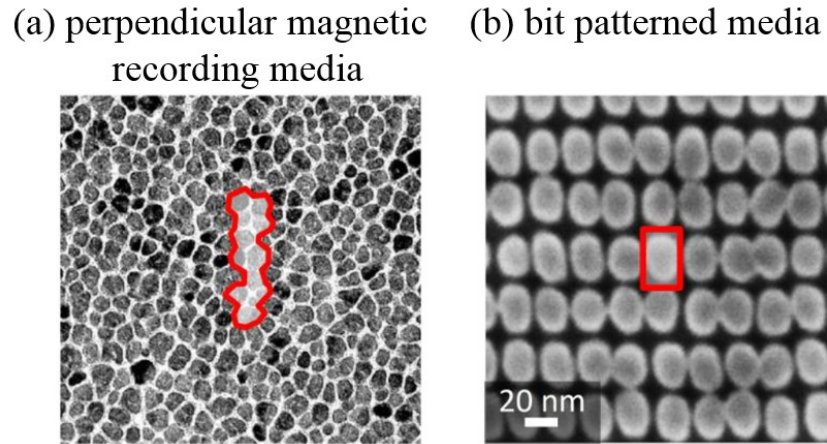
Figure 1.13 TEM image of magnetic bits within (a) perpendicular magnetic recording media and (b) bit-patterned media (courtesy of [14])

Shingled Magnetic Recording (SMR)

The latest improvement in magnetic recording technology is called shingled magnetic recording (SMR). Similar to perpendicular magnetic recording media and bit-patterned media, magnetic grains in the shingled magnetic recording media are perpendicular to the disk. Figure 1.14 compares the layout of magnetic tracks on a conventional perpendicular magnetic recording media and a shingled magnetic recording media. In conventional perpendicular magnetic recording media, a gap exists between magnetic tracks. However, in shingled magnetic recording media, magnetic tracks overlap with each other in order to increase the areal density of the disk. According to Seagate, the areal density of shingled magnetic recording media is 25% greater than that of conventional perpendicular magnetic recording media [17].

Although shingled magnetic recording technology significantly improves the areal density, shingled magnetic recording technology has some disadvantages. One of these is slow rewriting speed. With shingled magnetic recording media, if data on a
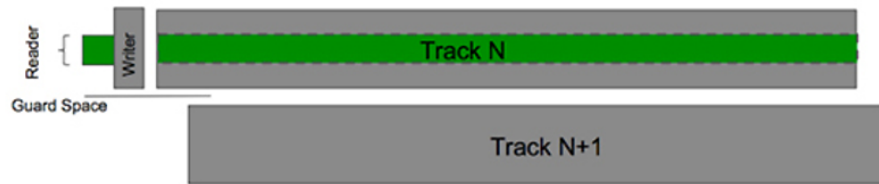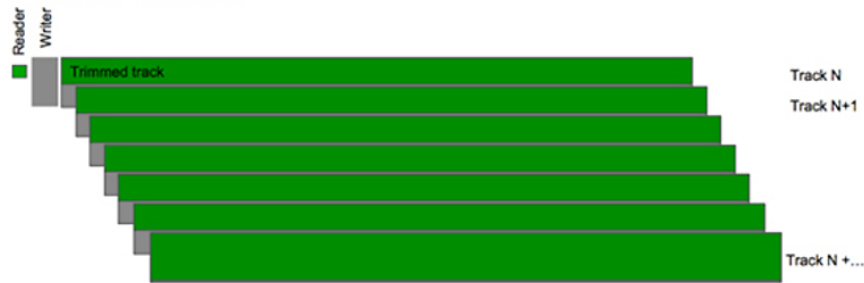
Figure 1.14 Comparison of magnetic tracks layout on conventional and SMR media (courtesy of [17])

particular track need to be rewritten, the data saved on the following tracks must also be rewritten. Since the write head is wider than the "trimmed" magnetic tracks, rewriting data on previous tracks causes erasure of data on subsequent tracks. In addition, improved servo control is required to make the magnetic head follow the narrower magnetic tracks with minimal errors. Another disadvantage of shingled magnetic recording technology is the inter-track interference (ITI) from neighboring tracks that can lead to low signal to noise ratio of the read-back signal. This is due to the fact that the track width of shingled magnetic recording media is equal to or smaller than the width of the read head. To increase the signal to noise ratio, two-dimensional magnetic recording (TDMR) technology has been proposed to read data from shingled magnetic recording media. With two-dimensional magnetic recording, a two dimensional read-back signal "image" is obtained by scanning several tracks simultaneously using

multiple read heads, or by scanning several tracks with multiple passes using one read head [18]. Researchers predicted that shingled magnetic recording combined with two-dimensional magnetic recording enables hard disk drive to achieve an areal density of 10 Tbit/inch^2 (15.5 gigabits/mm^2) [19], [20].

1.4.2 Magnetic Heads in Hard Disk Drives

Another important component of hard disk drives is the magnetic head that is used to read or write data. To increase the areal density and the read/write speed of hard disk drives, the sensitivity of magnetic heads has been dramatically improved and the size of the heads has been significantly reduced.

Ferrite Magnetic Heads

Before the 1990s, hard disk drives employed ferrite magnetic heads shown in Figure 1.15. As one can see, a ferrite magnetic head is a typical electromagnet that has a ferrite magnetic core wrapped with a copper coil. During writing, an electric current is applied to the coil and a magnetic field is generated to magnetize magnetic bits on the disk. The polarity of the magnetic field is changed when the direction of the current is reversed. During reading, a voltage is induced in the coil due to the magnetic field generated by the magnetic bits on the disk. The polarity of the voltage is determined by the polarity of the magnetic field. While ferrite magnetic heads are easily manufactured at low cost, they require a high electric current in order to write data onto magnetic disks with high coercivity. Another disadvantage of ferrite magnetic heads is the large size that limits their ability to fly on disks with small spacing.
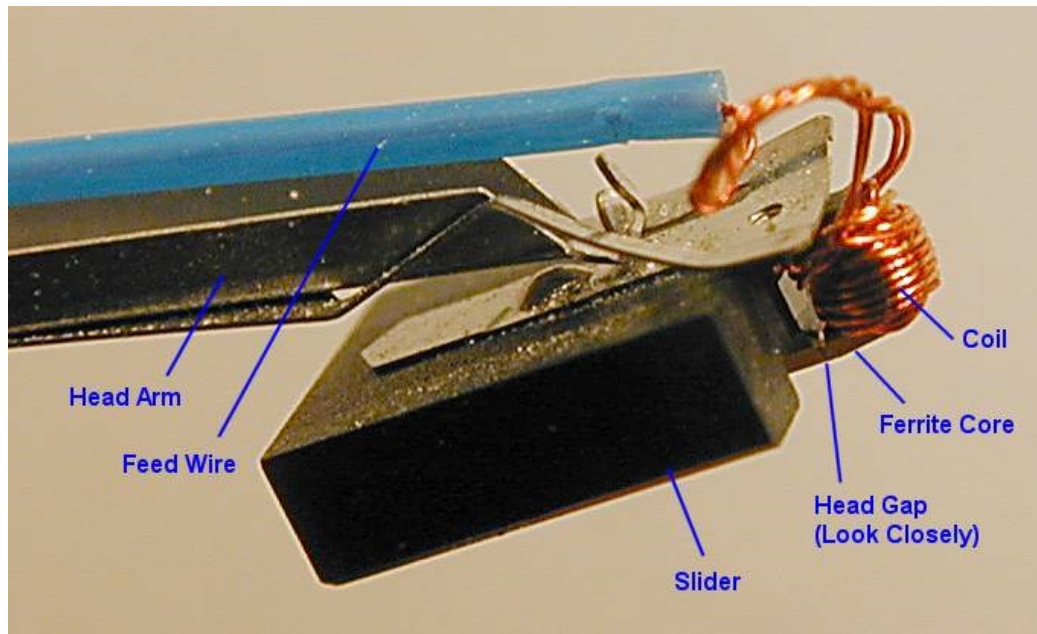
Figure 1.15 Ferrite magnetic head in Seagate ST-251 (courtesy of [21])

Metal-In-Gap Heads

During the 1990s, metal-in-gap (MIG) heads began to replace ferrite magnetic heads. While the design of the metal-in-gap head is similar to that of ferrite magnetic heads, the capability of ferrite heads has been improved by adding high permeability metallic alloy into the head such that the metal-in-gap heads have a greater resistance to magnetic saturation.

Thin Film Heads

To further increase the areal density in hard disk drives, thin film heads were developed. This type of magnetic head is manufactured using photolithography. The size of thin film heads is much smaller than that of ferrite and metal-in-gap heads, and the patterns of thin film heads can be precisely controlled during mass production. Since thin film heads are small and lightweight, their flying height is lower than that of ferrite

and metal-in-gap heads. Though the flying height is low, thin film heads are well protected from damage caused by head/disk contacts with addition of the surrounding hard alumina material (Al_2O_3). In addition, the core of thin film heads consists of an iron and nickel alloy, which allows thin film heads to generate a magnetic field four times stronger than ferrite and metal-in-gap heads during writing. Furthermore, thin film heads are much more sensitive than ferrite and metal-in-gap heads during reading.

Magnetoresistive Heads

Magnetoresistive materials exhibit the phenomenon that their resistance changes in response to an external magnetic field. Three types of magnetoresistive effects exist: the anisotropic magnetoresistive (AMR) effect, the giant magnetoresistive (GMR) effect, and the tunneling magnetoresistive (TMR) effect.

The anisotropic magnetoresistive effect was first discovered by Thomson in 1856 [22]. He found that an external magnetic field can change the resistance of a conductive wire. If the direction of current in a conductive wire is parallel to the direction of the external magnetic field, the conductive wire has maximum resistance. Conversely, if the direction of the current is vertical to the direction of the external magnetic field, the conductive wire has minimum resistance.

The giant magnetoresistive effect was observed by Fert [23] and Grünberg [24] in 1988. They were awarded the 2007 Nobel Prize in Physics "for the discovery of Giant Magnetoresistance" [25]. They found that, for a thin film structure of two ferromagnetic layers separated by a non-magnetic layer, the resistance of the thin film structure changes according to the magnetization direction of the two ferromagnetic layers. As shown in Figure 1.16. If magnetization of the two ferromagnetic layers is antiparallel,

the resistance of the thin film structure is at a maximum. However, if magnetization of the two ferromagnetic layers is in parallel, the resistance of the thin film structure is at a minimum.
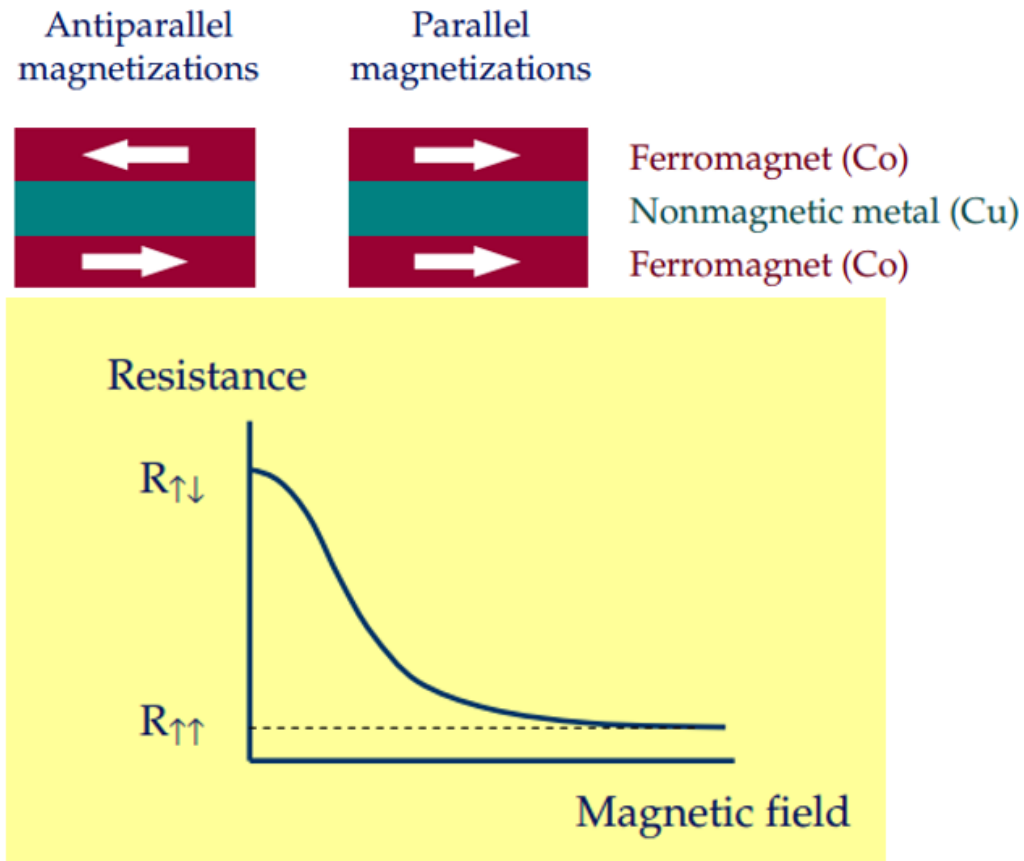
Figure 1.16 Change of material resistance due to the GMR effect (courtesy of [26])

Figure 1.17 shows the design of a typical giant magnetoresistive head. Unlike ferrite, metal-in-gap, and thin film heads, read and write elements inside giant magnetoresistive heads are separated. The write element is of the thin film type head, while the read element is a giant magnetoresistive head that utilizes the giant magnetoresistive effect to read data from the disk. As shown in Figure 1.17, the ferromagnetic NiFe free layer and the Co pinned layer are separated by a nonmagnetic

Cu spacer. The Co pinned layer has a fixed direction of magnetization. During reading, the magnetic orientation of the NiFe free layer is altered according to the orientation of the magnetic grains on the disk. If the magnetic orientation of the free layer is parallel to the magnetic orientation of the pinned layer, then the resistance of the giant

GMR Head Structure
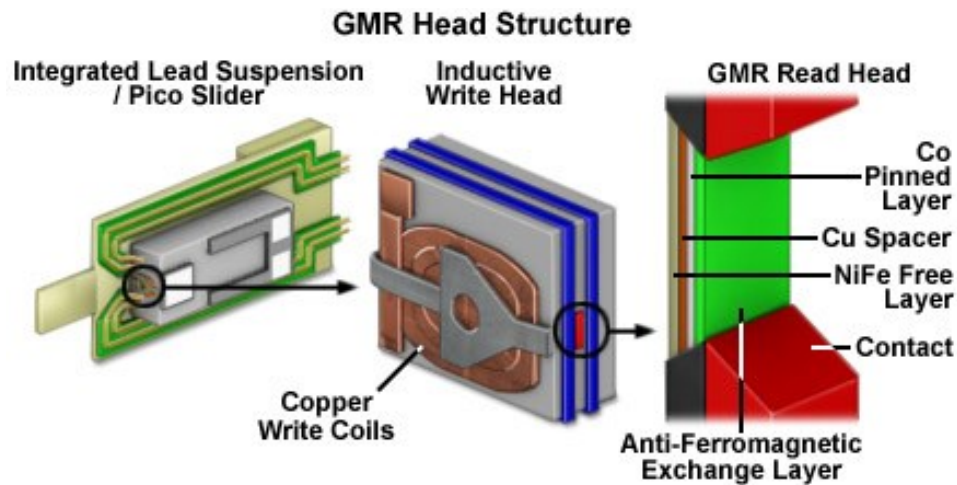
Figure 1.17 Design of a typical GMR head used in hard disk drives (courtesy of [27])

magnetoresistive head is minimal; conversely, if the magnetic orientation of the free layer is anti-parallel to the magnetic orientation of the pinned layer, then the resistance of the giant magnetoresistive head is maximal. Thus, the low and high resistance of the giant magnetoresistive read head can be used to represent "0" and "1" on the hard disk. The anti-ferromagnetic exchange layer of giant magnetoresistive read head prevents the pinned layer from being influenced by the external magnetic field. Since giant magnetoresistive read heads are far more sensitive than thin film heads and anisotropic magnetoresistive heads, they can read small magnetic bits which thin film heads or anisotropic magnetoresistive heads cannot read.

The tunneling magnetoresistive effect was first observed by Julliere [28] in 1975. It was found that for a thin film structure of two ferromagnetic layers separated by an

insulator, the resistance of the structure is determined by the magnetic direction of the two ferromagnetic layers. In current commercially available hard disk drives, tunneling magnetoresistive heads are utilized to increase the sensitivity of the read head. As shown in Figure 1.18, tunneling magnetoresistive read head has a design similar to the giant magnetoresistive read head. However, the two ferromagnetic layers (tunneling valve films) in the tunneling magnetoresistive head are separated by an insulator (tunneling barrier) instead of a non-magnetic layer. The thin film structure of the tunneling magnetoresistive read head is called magnetic tunnel junction (MTJ). If the thickness of
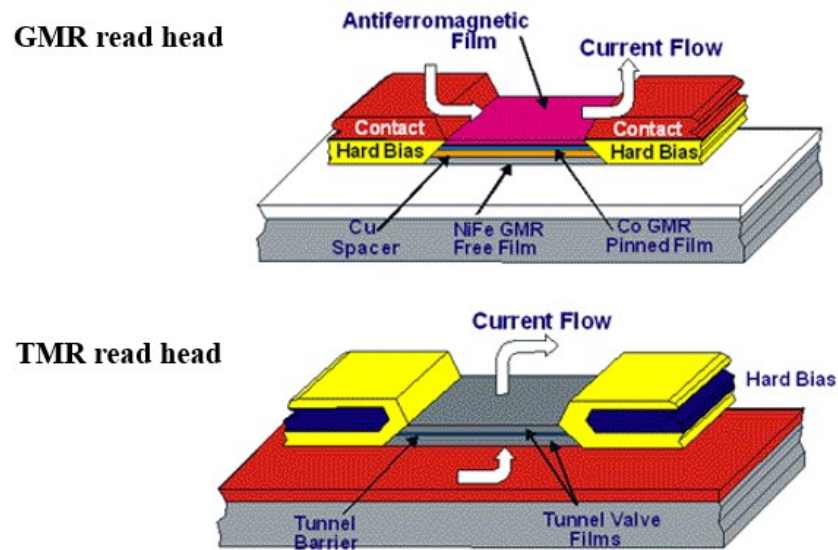
Figure 1.18 Schematic of a GMR read head, and a TMR read head in hard disk drives (courtesy of [29])

the insulator is on the order of several nanometers and the magnetic orientation of the two ferromagnetic layers is parallel, then the electrons can tunnel through the insulator, which means that the resistance of magnetic tunnel junction in the tunneling magnetoresistive head becomes very small; conversely, if the magnetic orientation of

the two ferromagnetic layers is anti-parallel, then the resistance of magnetic tunnel junction in the tunneling magnetoresistive head is very high.

The amplitude of the magnetoresistive effect can be evaluated by the MR ratio, which is expressed as

$$MR\ Ratio = \frac{R_{antiparallel} - R_{parallel}}{R_{parallel}} \tag{1.5}$$

where $R_{antiparallel}$ is the lowest resistance of the read head in the case when the magnetic orientation of the two ferromagnetic layers is antiparallel, and $R_{parallel}$ is the highest resistance of the read head in the case when the magnetic orientation of the two ferromagnetic layers is in parallel. It was reported by Kobayashi et al. [30] that the MR ratio of a tunneling magnetoresistive head is approximately 27% but that the MR ratio of a giant magnetoresistive head is only a few percentages. Therefore, tunneling magnetoresistive read heads have a higher sensitivity than giant magnetoresistive read heads.

1.4.3 Future Technology of Hard Disk Drives: Heat-Assisted Magnetic Recording (HAMR)

Small magnetic grains on the order of 6 nm are required to achieve an areal density greater than 1 Tb/inch^2 (1.55 gigabits/mm^2). As the size of magnetic grains decreases, the coercivity of the magnetic media needs to increase in order to keep the data thermally stable. However, if the coercivity is very large, it is difficult for magnetic heads to generate a magnetic field strong enough to write data on the disk. To overcome this difficulty, energy-assisted magnetic recording (EAMR) technology is currently

being developed. There are two types of energy-assisted magnetic recording technologies: heat-assisted magnetic recording (HAMR) and microwave-assisted magnetic recording (MAMR). Since heat-assisted magnetic recording is more promising than microwave-assisted magnetic recording [31], the following discussion is going to focus on heat-assisted magnetic recording. Figure 1.19 shows the relationship between coercivity of magnetic grains and temperature. The coercivity of any magnetic material begins to drop significantly if the material temperature is increased to a value close to its Curie temperature. At the Curie temperature, a magnetic material loses its magnetic properties. This unique property of magnetic materials enables one to write data on magnetic grains with high magnetic coercivity. In heat-assisted magnetic recording hard disk drives, a laser beam is directed at the disk surface and heats up the location where the data will be written. Once the temperature of the magnetic grains on
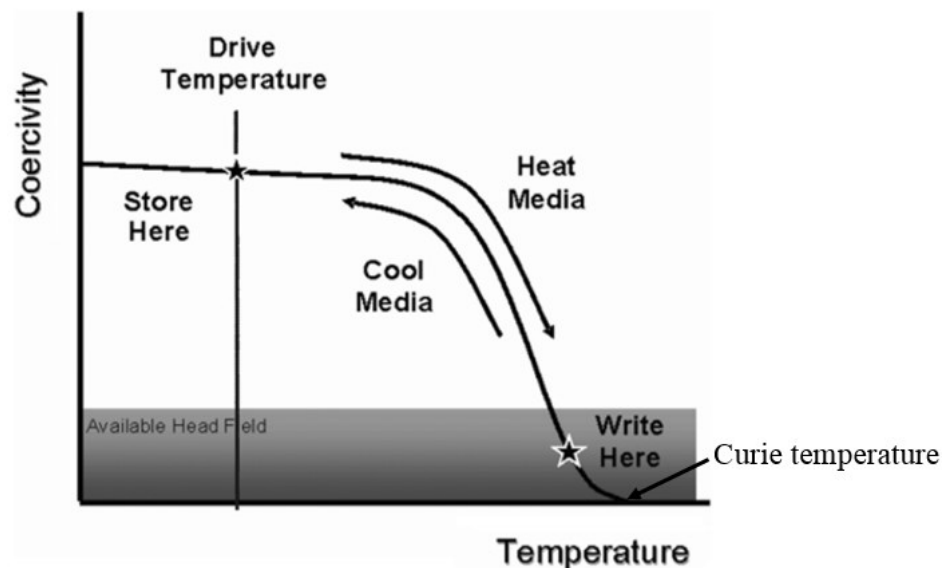
Figure 1.19 Coercivity of magnetic grains on the disk as a function of temperature (courtesy of [32])

the disk is greater than their Curie temperature, the coercivity of the magnetic grains is zero. If the laser is turned off, the heated material will cool down. During cooling down, the coercivity is initially very low and the write head starts to write data on the disk. After the information has been written, the media returns to its original temperature and the data is "frozen" on the disk.

Figure 1.20 shows a typical heat-assisted magnetic recording head design proposed by Challener et al. [33]. A laser is placed on the E block of the head stack assembly (HSA) and emits laser light at the grating. The waveguide acts as a planar solid immersion mirror to deliver the laser light to the near-field transducer. The near field transducer focuses the laser light on the location where the data will be written. The heating of adjacent magnetic bits is prevented by ensuring that the diameter of the laser spot is smaller than 50 nm, for media with an areal density of 1 Tbit/inch^2 (1.55 gigabits/mm^2) [34]. As shown in Figure 1.20, a heat sink beneath the magnetic layer accelerates the cooling process of the media. To achieve the same read/write speed as conventional hard disk drives, the cooling time of heat-assisted magnetic recording media should be shorter than 1 ns [35]. Due to many technical difficulties, there are no commercially available heat-assisted magnetic recording hard disk drives presently on the market. For example, it is a challenge to generate a small enough laser spot to avoid thermal erasure of neighboring tracks. Also, in order to obtain a high enough signal to noise ratio for the read-back signal, the spacing between the magnetic head and the disk needs to decrease below 1 nm, which is likely to cause severe head/disk contacts. In addition, it is difficult to manufacture high coercivity media with a well-controlled Curie temperature.
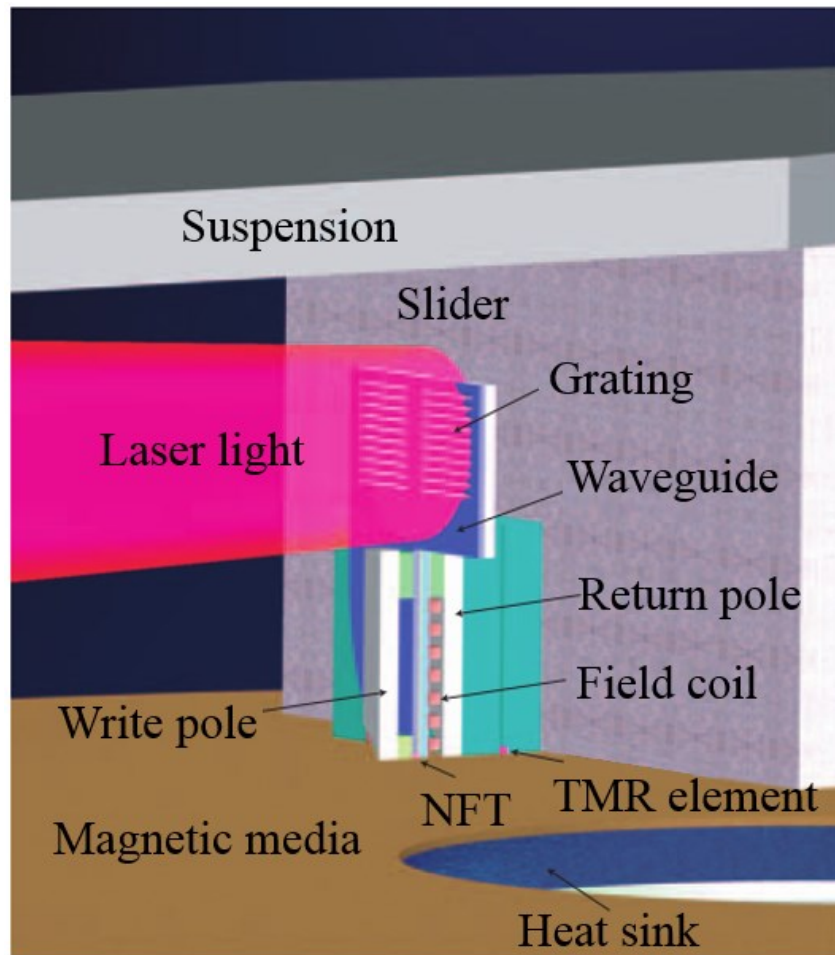
Figure 1.20 Schematic of heat-assisted magnetic recording magnetic head (courtesy of [33])

1.5 Organization of the Dissertation

This dissertation focuses on investigation of the tribological performance of contact interfaces in hard disk drives, which includes the head/disk interface, the dimple/gimbal interface, and the lift tab/ramp interface.

Chapter 1 provides a brief introduction to the history and design of hard disk drives. The principle of reading and writing processes of hard disk drives is explained

and a discussion is presented on the evolution of magnetic recording technologies for increasing areal density and enhancing the performance of hard disk drives.

Chapter 2 discusses the tribology of the head/disk interface in hard disk drives. Air bearing surface design, lubricant transfer between the head and the disk, and thermal flying height control (TFC) are explained. A discussion on the failure of hard disk drives caused by head/disk contacts concludes this chapter.

Chapter 3 reviews and compares different theoretical models for various types of wear and wear mechanisms. Experimental techniques for characterizing surface profiles and material compositions are presented, followed by an examination of various methods for reducing wear.

Chapter 4 investigates the effect of a carbon overcoat on the tribological performance of the dimple/gimbal interface in hard disk drives. Both experimental results and numerical simulation are presented in this chapter. Experimental studies were performed using a fretting wear tester and numerical simulation results were obtained by conducting finite element analysis calculations. In order to explain the phenomena observed in the experimental studies, numerical and experimental results were compared.

Chapter 5 investigates lubricant migration on the air bearing surface of the slider. A "drive-level" lubricant migration test was performed to study the effects of parking time, temperature, and slider position on lubricant migration in a hard disk drive.

Chapter 6 simulates the thermal response of a thermal asperity sensor to disk asperities using the finite element analysis method. The change in temperature of a thermal asperity sensor during contact with disk asperities was calculated and converted

to the resistance change of the sensor. The effects of bias voltage, friction coefficient, disk velocity, and contact interference on the thermal response of the sensor were investigated.

Chapter 7 examines the generation of wear debris at the lift tab/ramp interface during the load/unload process of hard disk drives. "Drive-level" load/unload tests were performed in a temperature controlled chamber to study the generation of wear debris by measuring the change of the voice coil motor current. A finite element analysis model was constructed to study how to reduce contact stress and the amount of wear debris generated at the lift tab/ramp interface.

Chapter 8 is the conclusion and summary of this dissertation.

Chapter 2

Tribology of the Head/Disk Interface

In order to reach an areal density of 1 Tb/inch^2 (1.55 Gb/mm^2), the spacing between the magnetic head and the magnetic disk must be decreased to the order of 1 to 2 nm. At a spacing of 1 to 2 nm [36], it is likely that head/disk contacts occur during reading and writing, causing damage of the magnetic head and erasure of data on the disk. This chapter discusses how to achieve small spacing between the slider and the disk while preventing head/disk contacts.

2.1 Air Bearing Surface and Reynolds Equation

Figure 2.1 shows a schematic of the head/disk interface in a typical hard disk drive. When the hard drive is in operation, the disk rotates at speeds between 5400 rpm and 15,000 rpm. An air bearing force is generated between the slider and the disk to support the slider on a thin air bearing and prevents it from coming into contact with the disk. Figure 2.2 shows a schematic of the slider during operations. The slider can perform pitch and roll when external forces and moments are applied. The equation of motion of the slider for the z direction and the pitch and roll motion directions are

$$\iint (p - p_{atm})dA - F_{vertical} = m\ddot{z} \qquad (2.1)$$

$$M_{pitch} + \iint (p - p_{atm})(x_{gimbal} - x)dA = J_{xz}\ddot{\theta} \qquad (2.2)$$

$$M_{roll} + \iint (p - p_{atm})(y_{gimbal} - y)dA = J_{yz}\ddot{\varphi} \qquad (2.3)$$
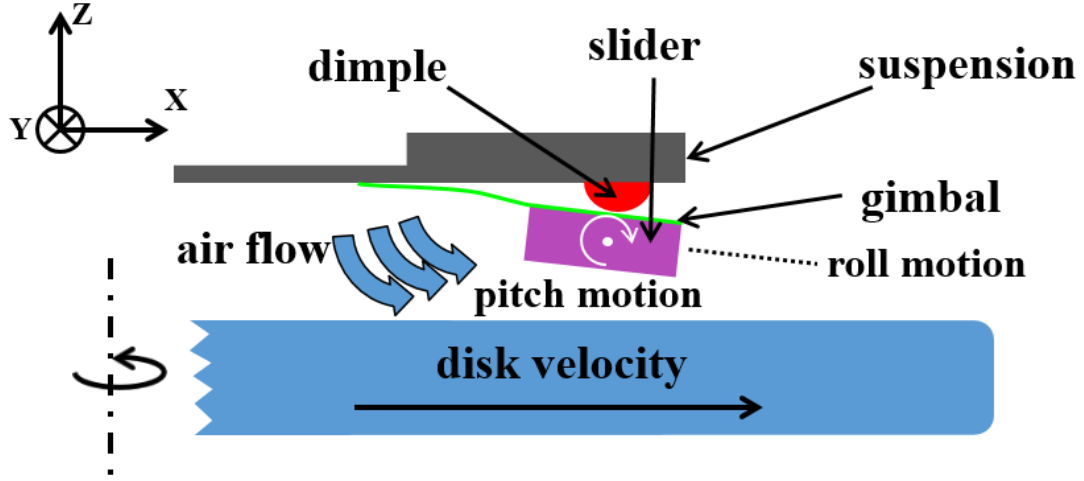
Figure 2.1 Schematic of head/disk interface

where $F_{vertical}$, M_{pitch}, and M_{roll} are force and moments applied by the suspension. The variable p represents the air bearing pressure. The atmospheric pressure applied on the upper surface of the slider is p_{atm}. The rotation axes of the slider in pitch and roll directions are at $x = x_{gimbal}$ and $y = y_{gimbal}$, respectively. The mass of the slider is assumed to be m. J_{xz} and J_{yz} are the moment of inertia of the slider for pitch and roll motions. Acceleration of the slider in the z direction and angular acceleration of the slider for the pitch and roll motions are denoted by $\ddot{z}$, $\ddot{\theta}$ and $\ddot{\varphi}$, respectively.
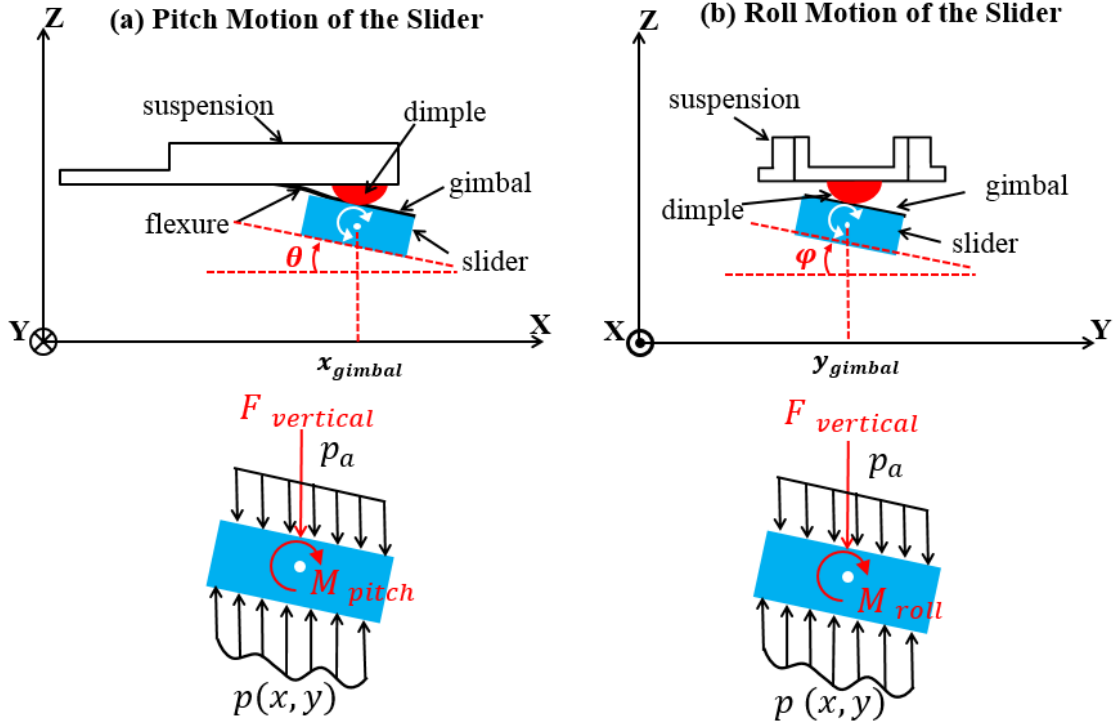
Figure 2.2 Pitch and roll motion of a slider

For continuum flow situations, the air bearing pressure generated can be calculated using the compressible Reynolds equation [37]

$$\frac{\partial}{\partial x}\left(ph^3\frac{\partial p}{\partial x}\right) + \frac{\partial}{\partial y}\left(ph^3\frac{\partial p}{\partial y}\right) = 6\mu U\frac{\partial ph}{\partial x} + 6\mu V\frac{\partial ph}{\partial y} + 12\mu\frac{\partial ph}{\partial t} \qquad (2.4)$$

where p is the pressure at point (x, y) of the air bearing surface and h is the distance between this point and the disk. U and V are disk velocities in x and y directions, and the dynamic viscosity of air is denoted by μ. Since the spacing between the slider and the disk in current hard disk drives is only several nanometers, the air flow is not a perfect continuum flow and the so-called "rarefaction effects" need to be considered [38]. The compressible Reynolds equation accounting for rarefaction effects is given by

$$\frac{\partial}{\partial x}\left(Qph^3\frac{\partial p}{\partial x}\right) + \frac{\partial}{\partial y}\left(Qph^3\frac{\partial p}{\partial y}\right) = 6\mu U\frac{\partial ph}{\partial x} + 6\mu V\frac{\partial ph}{\partial y} + 12\mu\frac{\partial ph}{\partial t} \quad (2.5)$$

where Q is the non-dimensional flow rate which is a function of the Knudsen number

of air. The relationship between the flow rate Q and the inverse Knudsen number D was

derived by Fukui and Kaneko [39] as

$$Q = \begin{cases} -2.22919D + 2.10673 + \dfrac{0.01653}{D} - \dfrac{0.0000694}{D^2} & (0.01 \leq D \leq 0. \\[2mm] 0.13852D + 1.25087 + \dfrac{0.15653}{D} - \dfrac{0.00969}{D^2} & (0.15 \leq D \leq 5) \quad (2.6) \\[2mm] \dfrac{D}{6} + 1.0162 + \dfrac{1.0653}{D} - \dfrac{2.1354}{D^2} & (D \geq 5) \end{cases}$$

The Reynolds equation shown in Equation 2.5 is a non-linear partial differential

equation. The pressure distribution on the air bearing surface of a slider can be obtained

by solving the Reynolds equation numerically using finite element methods [40], finite

difference methods [41], or finite volume methods [42]. Figure 2.3 shows a finite

element mesh of a typical air bearing surface design and its pressure distribution

obtained using the CMRR Air Bearing Simulator [40]. This software program was

developed over a number of years by students and postdocs in Professor Talke's

research group [40], [43]–[45]. In Figure 2.3, the rotation speed of the disk is 6400 rpm

and the minimum flying height of the slider is 9 nm. To ensure that the magnetic head

writes data with a high efficiency and reads data with a high signal to noise ratio, the

slider is designed to fly closer to the disk at the trailing edge than at the leading edge.

Thus, as shown in Figure 2.3 (b), the pressure at the trailing edge is much higher than

the pressure at other regions on the air bearing surface.
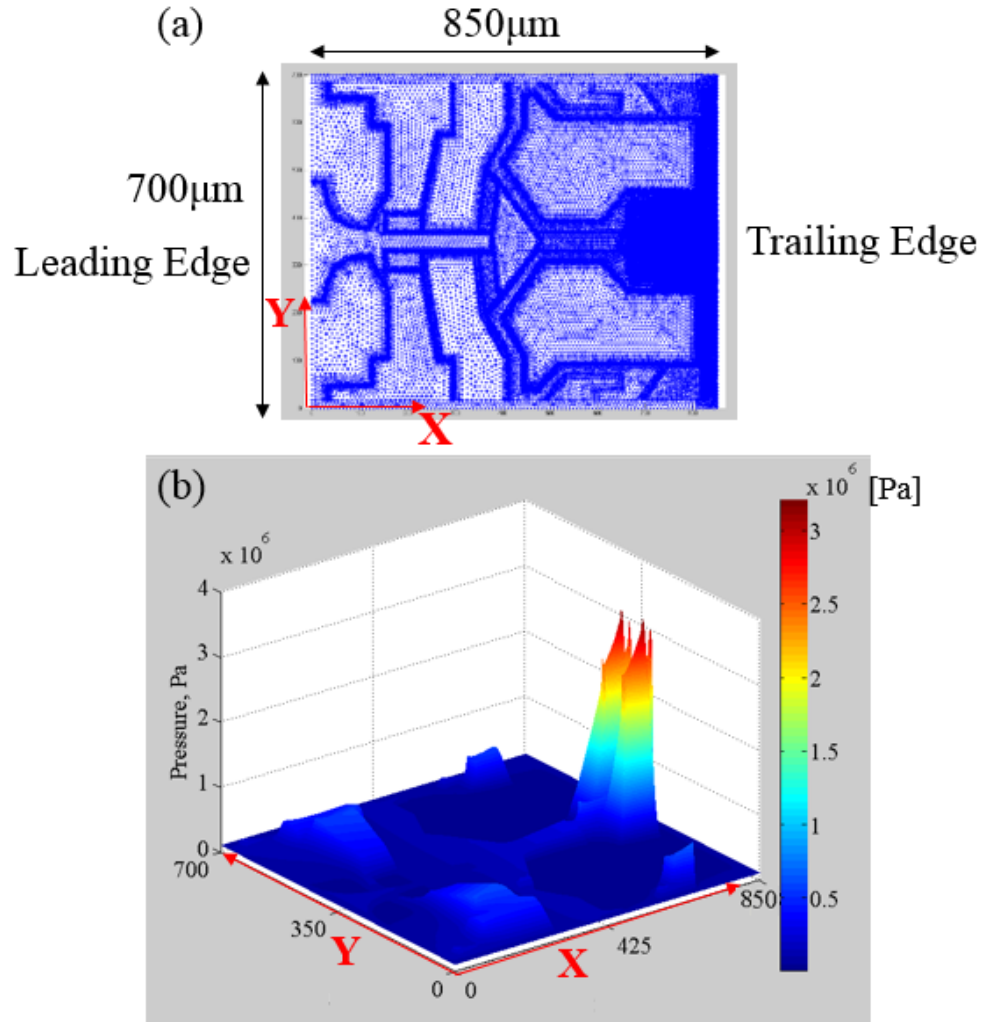
Figure 2.3 (a) Finite element mesh of a typical air bearing surface and (b) pressure distribution on air bearing surface obtained using the CMRR Air Bearing Simulator

2.2 Thermal Flying Height Control

In current hard disk drives, the flying height is on the order of 1 to 2 nm. This is achieved by the so-called thermal flying height control (TFC) technology [46]–[48], which keep the spacing between the slider and the disk constant by controlling the power applied to the heater inside the slider. Figure 2.4 shows a cross sectional image of a TFC slider. In addition to read/write elements and shields, a heater is embedded into the slider.

When an electric current is applied to the heater, the heat generated causes a thermal protrusion on the air bearing surface, which "lowers" the flying height of the slider. Figure 2.5 shows the shape of a thermal flying height control slider before and after the application of heater power. We observe that the read/write element is closer to the disk when the heater power is on. This clearly enhances the performance of the read/write element. As an extension of the single heater thermal flying height control slider, a slider with two heaters shown in Figure 2.6 was proposed by Zheng et al. [47]. This thermal flying height control slider design was shown to further reduce the flying height of the slider [47].
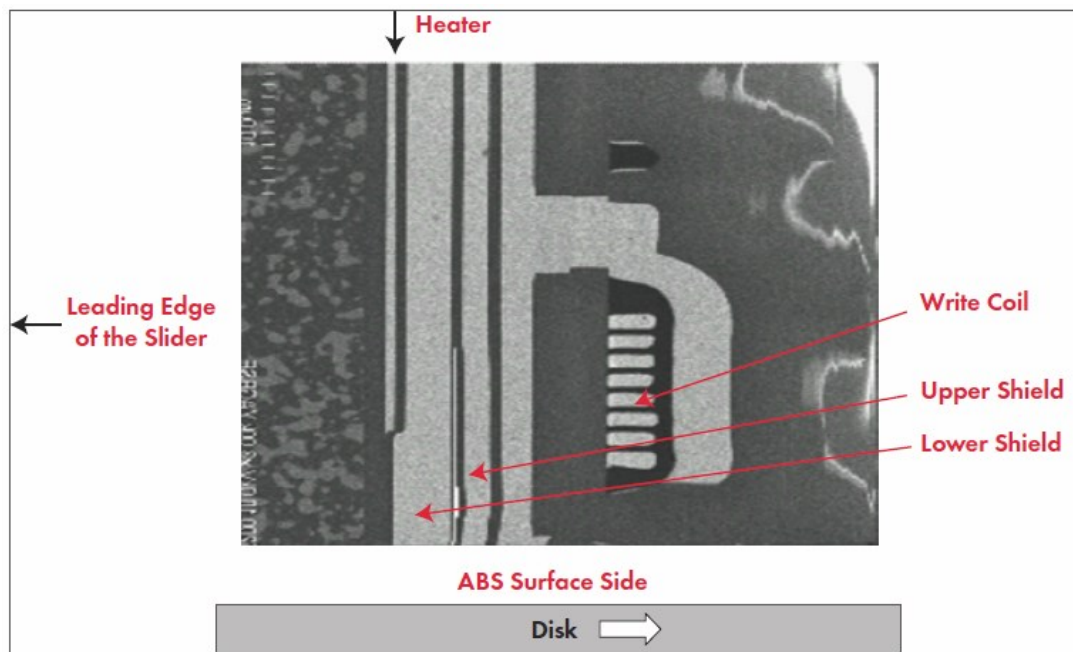
Figure 2.4 Cross-section view of a TFC slider (courtesy of [47])

(a) Slider without thermal protrusion
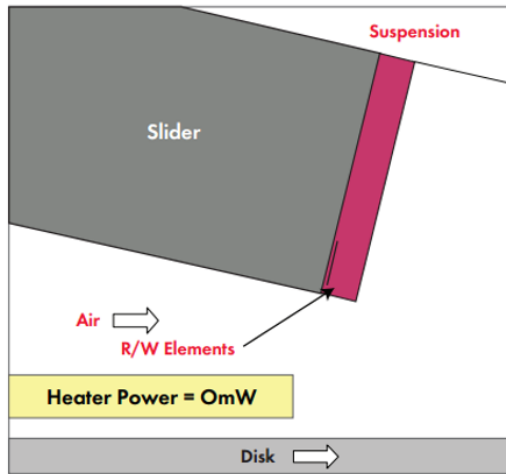
(b) Slider with thermal protrusion
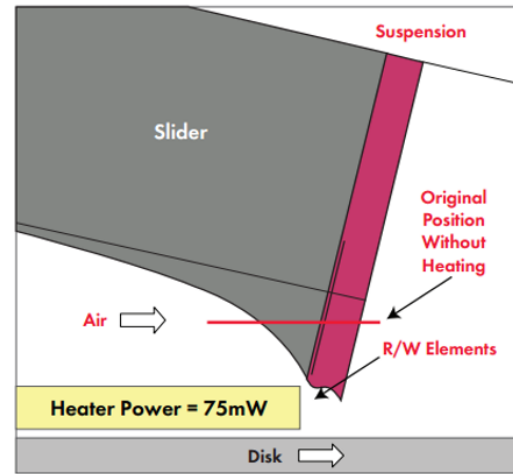
Figure 2.5 Shape of a TFC slider (a) with and (b) without heater power applied (courtesy of [47])
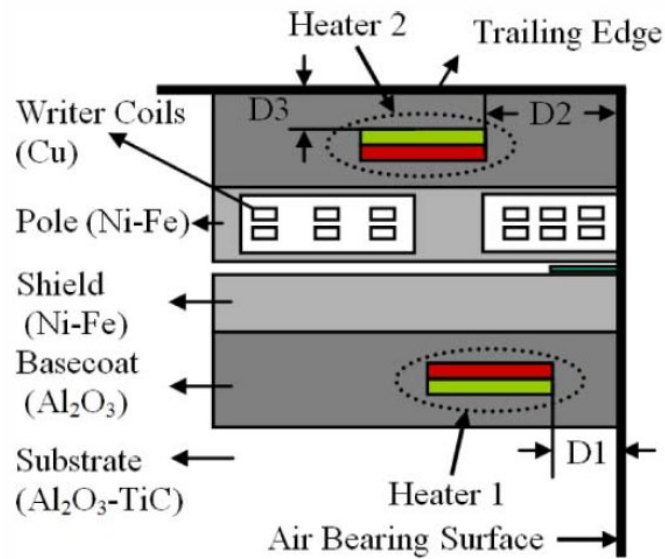
Figure 2.6 TFC slider with two heaters (courtesy of [49])

In addition to reducing the spacing between the slider and the disk, thermal flying height control technology can also be used to minimize the flying height variation of a slider by actively controlling the electrical power applied to the heater. For example, Boettcher et al. [50] used a feedforward control algorithm to adjust the power applied

to the heater. They reported a reduction in repeatable flying height variations of a thermal flying height control by about 66.7%.

2.3 Lubricant Transfer at the Head/Disk Interface

In present day disk drives, a diamond-like carbon film with a thickness of about 3 nm is deposited onto the disk [46]. Since the DLC overcoat has a high hardness [51]–[53], it can prevent damage of the magnetic layer during head/disk contact. DLC is an inert material which can also prevent corrosion of the magnetic media. To reduce the friction force between the slider and the disk, as well as to provide further protection of the magnetic media during contact, a lubricant layer with a thickness of 1 to 2 nm is applied on top of the carbon overcoat [54]. Perfluoropolyether (PFPE) is widely used as disk lubricant because of its excellent durability, chemical stability, low surface
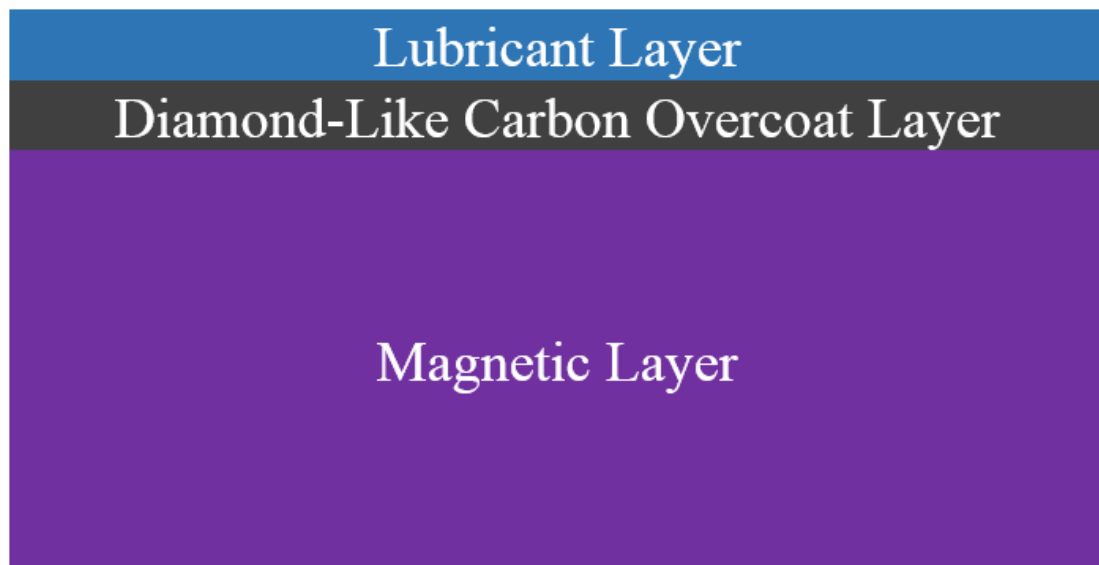
Figure 2.7 Layout of typical magnetic recording media

tension, low vapor pressure, and strong bonding strength to the DLC layer [55]. Two types of PFPE lubricant are commonly used in hard disk drives: Z-Dol and Z-Tetraol. The chemical structure of Z-Dol and Z-tetraol lubricant is shown in Figure 2.8. We observe that Z-Dol and Z-tetraol have a similar chemical structure but different end group R, which determines the bonding strength of the lubricant to the carbon overcoat layer. For both Z-Dol and Z-tetraol, the backbone is constructed with perfluoromethylene-oxide ($[-CF_2-CF_2-O-]_m$) and perfluoroethylene-oxide ($[-CF_2-O-]_n$). The molecular weight of PFPE lubricant can be adjusted by changing the number of the perfluoromethylene-oxide end groups and the number of the perfluoroethylene-oxide end groups.

$$R- O-[-CF_2-CF_2-O-]_m-[- CF_2-O-]_n-R$$

For Z-Dol: $R = -CF_2-CH_2-OH$

For Z-Tetraol: $R = -CF_2-CH_2-O-CH_2-CH(OH)-CH_2-OH$
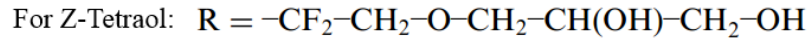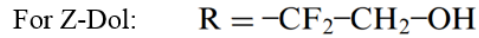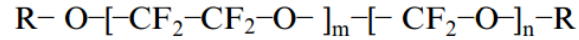
Figure 2.8 Chemical structure of PFPE lubricant: Z-Dol and Z-Tetraol

In regards to PFPE lubricants on magnetic disks, mobility of the lubricant is crucial for achieving desired tribological performance of the head/disk interface. It was reported in [56] that PFPE lubricants with a small molecular weight have high mobility. The mobility of a lubricant is also characterized by the bonding ratio, which can be obtained by dividing the number of lubricant molecules bonded to the DLC overcoat by the total number of lubricant molecules on the disk [56]. Lubricants with a low bonding ratio exhibit better mobility than lubricants with high bonding ratio. If a slider makes contact with a disk, mobile PFPE lubricant can replenishe the area where lubricant is

depleted. However, if the mobility of a lubricant is too high, the shear stress applied by the air flow can move the lubricant off the disk. For PFPE lubricant, the bonding ratio is typically 60% to 80% [57].

At the head/disk interface, lubricant transfer from the disk to the slider is always observed. This transfer is undesirable because it may cause stiction between the disk and the slider, which can lead to the unstable flying of the slider and to poor read/write performance of the magnetic head [58]–[60]. It is clear that lubricant transfer occurs if the slider contacts the disk directly. However, lubricant transfer can occur even without direct contact between the slider and the disk. This type of lubricant transfer is a result of the evaporation/condensation processes of low weight lubricant molecules [61], [62].

Lubricant transfer a complicated process, which is affected by many factors including lubricant type, lubricant thickness, air bearing surface design, disk velocity, slider-disk spacing, and mobility of the lubricant [63], [64]. During lubricant transfer, lubricant "moguls" may be formed on the disk due to the redistribution of lubricant. These "moguls" are defined as the accumulation of lubricant with a height of about 2 to 10 nm [65]. They can cause catastrophic contact between the slider and the disk and damage the magnetic head.

2.4 Failure of Hard Disk Drives Due to Head/Disk Contacts

In hard disk drives, when a slider contacts a disk rotating at high speed, frictional heat is generated, which significantly increases the local disk temperature during a

contact (flash temperature). If the disk temperature is higher than the Curie temperature, magnetic data on the disk will be either partially erased or entirely deleted [66]. Moreover, it was found that plastic deformation of the magnetic layer may also lead to magnetic erasure, especially for perpendicular magnetic recording media [67], [68]. When plastic deformation occurs, magnetic grains perpendicular to the disk surface may become tilted by the high contact stress. As a consequence, magnetic information can be erased from the media if the coercivity of the magnetic material decreases [69].

Furthermore, head/disk contacts could also cause severe damage to the magnetic head, especially if asperities are present on the disk. Figure 2.9 shows an scanning electron microscope image of the portion of a slider surface where the magnetic head is located. We observe several scratches on the slider surface due to contact between the slider and the asperity on the disk. Using numerical simulation, it was found by Song et al. [70] that contact between a slider and a disk asperity can lead to plastic deformation of the slider and to damage of the magnetic head.
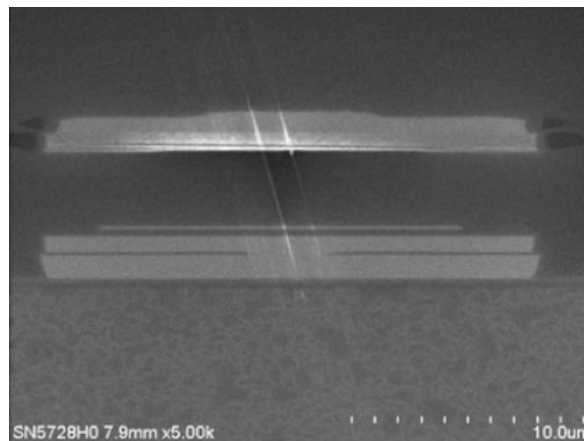
Figure 2.9 Scratches on a slider surface due to head/disk contacts (courtesy of [70])

Asperities on the disk come from several sources. For example, the polishing slurry used in the manufacturing of the disk surfaces contains abrasive material such as alumina. After the polishing process, some alumina may stay on the disk surface and form undesired asperities. Another source of asperities on the disk is wear particles generated at contact interfaces in hard disk drives such as the dimple/gimbal interface and the lift tab/ramp interface. Therefore, it is important to understand the mechanism of wear particle generation at these contact interfaces and to investigate how to reduce the number of wear particles generated in a disk drive.

Chapter 3

Friction and Wear at Contact

Interfaces

In order to minimize the generation of wear particles at an interface, knowledge of friction and wear is necessary. In this chapter, the origin of friction and wear will be discussed, including a review of various contact models and analytical instrumentation necessary for the analysis of contact and wear of surfaces.

3.1 Friction

Friction is defined as the resistance to relative motion of bodies in contact [71]. In 1699, Amontons developed the first mathematical equation to define the friction force. He proposed that the friction force between two bodies in sliding contact is proportional to the normal force N between the two contact bodies and a constant μ

$$F_{Friction} = \mu \cdot N \tag{3.1}$$

The constant μ is defined as the coefficient of friction. In Amontons' law, it is assumed that the friction force is independent of the apparent contact area between the two sliding bodies, and that the coefficient of friction is not a function of sliding speed.

To further understand friction, one needs to look at the contact interface at the microscopic level. Figure 3.1 shows both macroscopic and microscopic views of a contact interface. As illustrated in Figure 3.1 (a), the contact area observed from the

macroscopic view is called the "apparent contact area". The contact area observed from the microscopic view illustrated in Figure 3.1 (b) is called the "real contact area". As one can see from the microscopic view, some asperities are touching, while others are not. Therefore, the actual contact area is always smaller than the apparent contact area. The theory of friction which is based on microscopic observation is referred to as "welding-shearing-ploughing" theory. According to Bowden and Tabor [72], the friction force is generated by the deformation and adhesion of surface asperities, i.e.,

$$F_{Friction} = F_{deformation} + F_{adhesion} \tag{3.2}$$
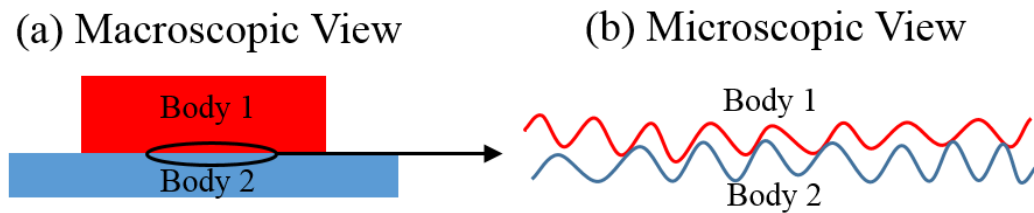
Figure 3.1 Macroscopic and microscopic views of a contact interface

As shown in Figure 3.1 (b), asperities on contacting surfaces interlock with each other. If relative motion occurs, asperities undergo either elastic or plastic deformation. Since the deformation of asperities requires external energy, deformation of asperities is one of the contributors to friction force. If the hardness of two contact bodies is significantly different, hard asperities can penetrate into soft asperities and plough the soft material during relative motion. This will increase the friction force and generate wear particles at the contact interface. To diminish the friction force caused by the deformation of asperities, one can reduce the roughness of contact surfaces, use materials of similar hardness, or apply lubricant to the contact interface [71].

In addition to deformation of asperities, adhesion also contributes to the friction force between contact surfaces. Adhesion between asperities occurs due to electrostatic force or van der Waals force when the two surfaces are in close proximity. Adhesive forces between asperities cause "cold welding" of asperities. As the contact surfaces undergo relative motion, adhesive bonding resists the movement and a shear force is required to break the bond. Thus, the friction force caused by adhesion can be expressed as a function of shear strength between the contact surfaces

$$F_{adhesion} = A_r \tau \tag{3.3}$$

where A_r is the real contact area and τ is the average shear stress of asperities that are in contact. A common method to reduce friction force due to adhesion is to apply a lubricant on the contact interface. The friction force can also be influenced by chemical composition, atomic structure, and the temperature of contacting materials [73].

3.2 Wear

Wear is defined as "the removal of material from solid surfaces as a result of mechanical action or chemical reaction" [74]. It can be classified into several types: adhesive wear, abrasive wear, fretting wear, fatigue wear, corrosive wear. In many wear situations, several types of wear occur simultaneously. Archard's equation is most commonly used to quantify adhesive wear behavior and is expressed as [75]

$$W = \frac{KNL}{H} \tag{3.4}$$

In Equation 3.4, W denotes the volume of wear generated on the softer surface. H is hardness, N is the normal force, and L is the sliding distance. K is a dimensionless

constant, the so-called wear coefficient. This coefficient is significantly different for different types of wear [76].

Adhesive Wear

Adhesive wear is the wear generated by adhesive forces when two surfaces slide relative to reach other. When two surfaces come into contact, adhesive forces bond the two surfaces together. If the bond is broken during relative motion, material on the surface with low cohesive energy is removed and adheres to the other surface due to adhesion. Therefore, in addition to the generation of wear particles, material transfer is also observed when adhesive wear occurs [77].
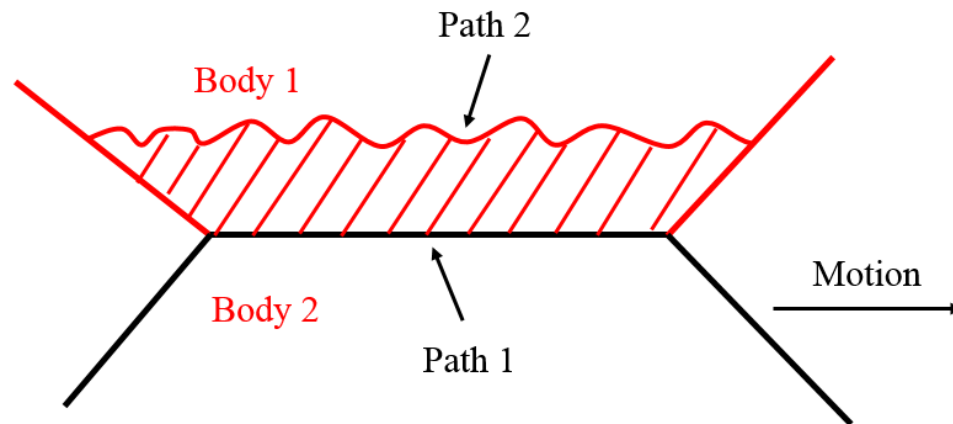
Figure 3.2 Generation of adhesive wear at contact interface (after [74])

Figure 3.2 shows the generation of adhesive wear when two bodies are in relative motion. It is assumed that an adhesive bond exists between body1 and body 2 along path 1. If the force required to break the adhesive bond is greater than the force required to break the cohesive bond in body 1, shear along path 2 can generate a small adhering wear particle on body 1 (dashed area). This particle is transferred to body 2 due to adhesion. It was reported by Greenwood and Tabor [78] that material transfer is more

likely to occur if the plane of the adhesive bond (path 1) is not parallel to the direction of motion. Since adhesive forces exist not only between rough surfaces but also exist between smooth surfaces, adhesive wear can occur even if the two contact bodies are very smooth [74].

Abrasive Wear

Abrasive wear can be observed when two surfaces with significantly different hardness move relative to each other. As shown in Figure 3.3, two types of abrasive wear can be observed: two-body abrasive wear and three-body abrasive wear. For two-body abrasive wear, embedded hard particles or asperities on the hard surface penetrate the softer surface. During relative motion, hard particles or hard asperities create grooves and scratches on the soft surface in the sliding direction and cause the removal of material from the soft surface [79]. For three-body abrasive wear, hard particles are trapped between two surfaces and slide or roll between them. It was found that the wear rate of materials under two-body abrasion is usually greater than the wear rate of
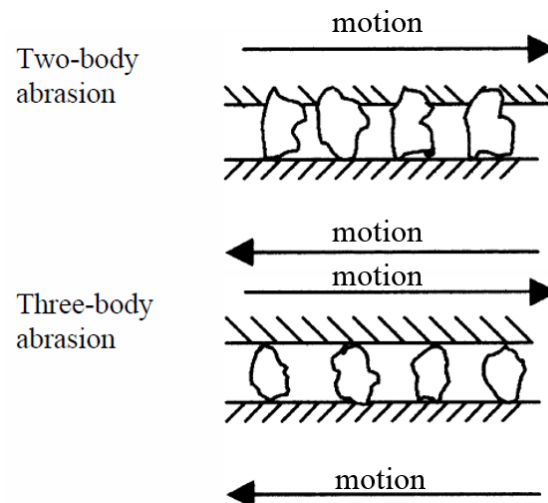
Figure 3.3 Comparison between two-body abrasion and three-body abrasion (courtesy of [80])

materials under three-body abrasion [81]–[83]. Since wear debris or wear particles generated during abrasion can be trapped between contact surfaces, abrasion can transition from two-body to three-body abrasion [84].
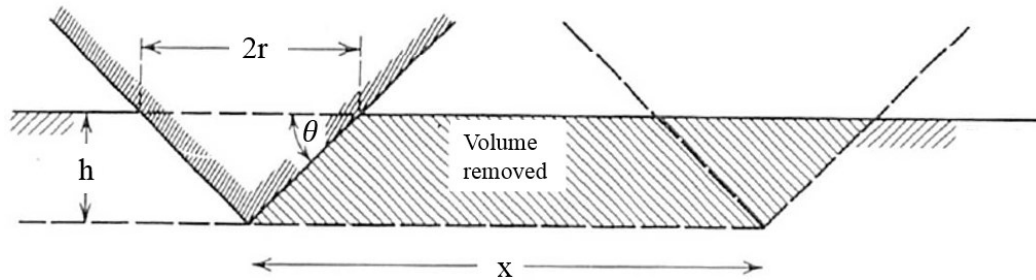
Figure 3.4 Removal of material due to abrasive wear (courtesy of [74])

Figure 3.4 schematically shows the generation of abrasive wear on a surface. It is assumed that the hard surface is rough and has conically shaped asperities on it. The soft surface is assumed to be flat. The contact radius between the asperity and the flat surface is r and the penetration depth is h. The angle between the outer edge of the asperity and the flat surface is θ. If the asperity moves by a distance of x, the volume removed from the flat surface is given by [74]

$$V = \frac{P \cdot x \cdot tan\theta}{\pi H} \tag{3.5}$$

where P is the normal load and H is the hardness of the soft surface.

Fatigue Wear

Fatigue wear occurs during repeated rolling or sliding when a cyclic load is applied to contacting surfaces. In fatigue processes, the yield strength of materials decreases with an increase in the number of load cycles. This relationship can be demonstrated by the S-N curve as shown in Figure 3.5, where S is the yield strength and N is the number of cycles [85]. Severe plastic deformation is observed in fatigue wear,

especially in cases with large number of cycles. Usually, both cracks and wear are observed in materials which undergo fatigue wear.
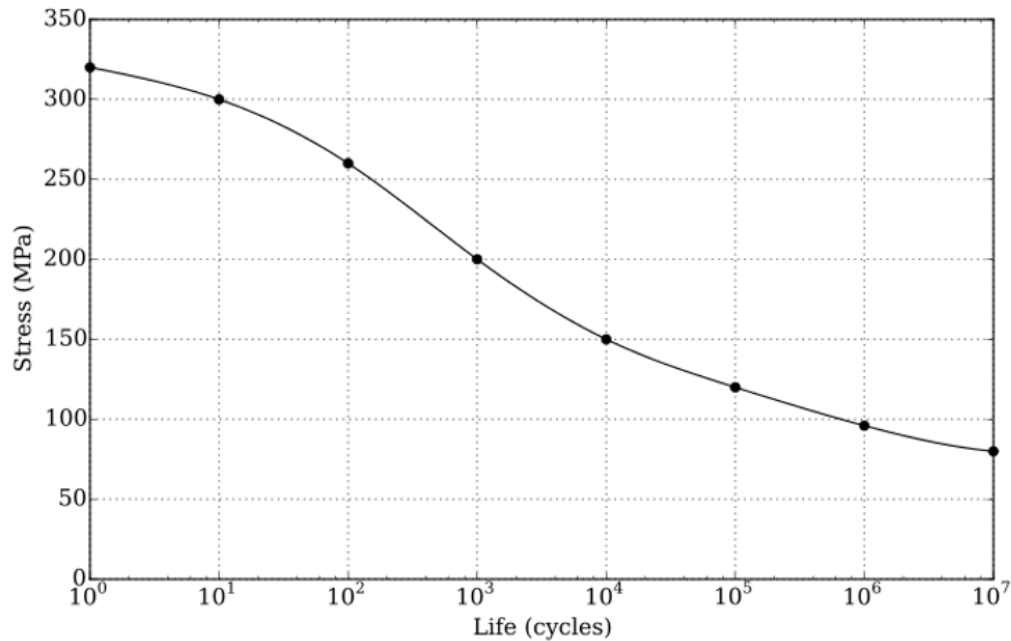
Figure 3.5 S-N curve of an aluminum material (courtesy of [86])

Fretting Wear

Fretting wear is defined as the damage of tribo-surfaces caused by small-amplitude oscillatory relative displacements on the order of micrometers to millimeters [87]. The relative motion is either sliding, rolling, or a combination of both. In fretting wear, crack formation in the material is often observed. In addition, oxidization can occur during fretting wear due to high temperature caused by frictional heating at the contact region [88].

Corrosive Wear

Corrosive wear is the deterioration of materials due to chemical or electrochemical reactions involving the contact materials, the lubricant, and the

environment [89]. Corrosion occurs in the absence of mechanical actions and its severity is significantly influenced by environmental conditions such as temperature, humidity, and the amount of oxygen present. Corrosive wear occurs if corrosive surfaces move relative to each other.

3.3 Lubrication

Lubrication is the technique for reducing the friction force between two surfaces and minimizing the amount of wear generated at the contact interface. Based on the relationship between the friction coefficient μ, lubricant viscosity η, relative sliding velocity v, and normal load P, lubrication can be divided into three regimes: boundary lubrication regime, mixed lubrication regime, and hydrodynamic lubrication regime. Figure 3.6 shows the Stribeck diagram. It shows the friction coefficient μ versus the number $\frac{\eta v}{P}$. As $\frac{\eta v}{P}$ increases, the friction coefficient first decreases, then increases.
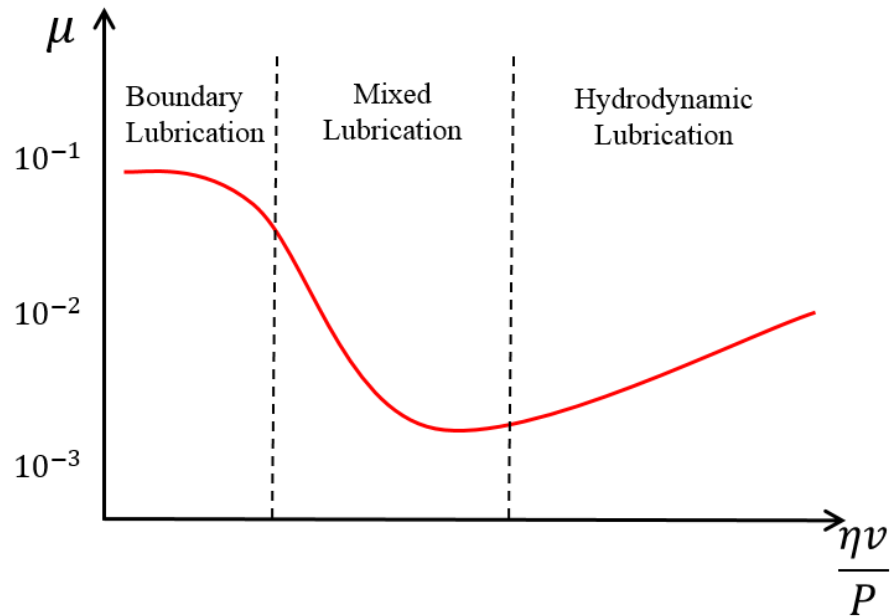
Figure 3.6 Stribeck diagram

When lubricant is applied to contact interfaces, the friction force can be expressed as

$$F = A[\alpha\tau_{solid} + (1 - \alpha)\tau_{liquid}] \tag{3.6}$$

where A is the apparent contact area, and α is the fraction of solid-solid contact between asperities. The shear strength between unlubricated asperities and the shear strength of the lubricant are denoted by τ_{solid} and τ_{liquid}, respectively.
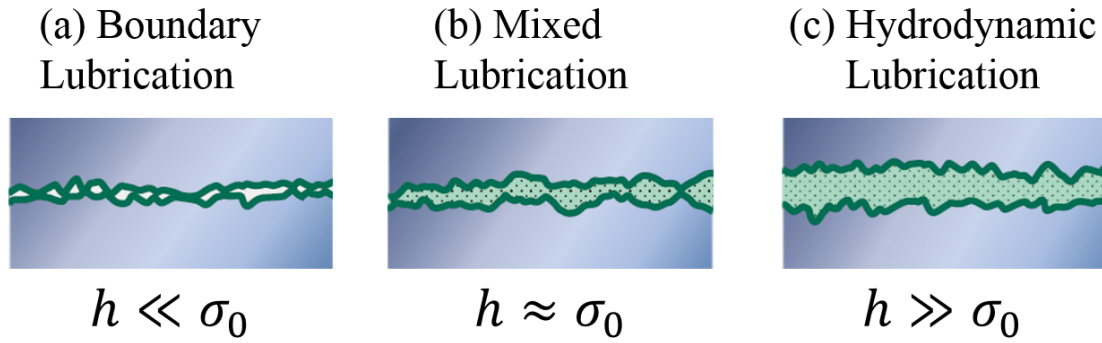
Figure 3.7 Schematic of three different lubrication regimes (courtesy of [90])

As shown in Figure 3.7, the type of lubrication condition present can also be determined by the relationship between lubricant film thickness h and root mean squared (RMS) surface roughness σ_0 of contact surfaces. In boundary lubrication, the lubricant film thickness is smaller than the root mean squared surface roughness σ_0. If α in Equation 3.6 is close to 1, the friction force between the surfaces is dominated by the shear strength between asperities. In the mixed lubrication regime, the lubricant film thickness and surface roughness are on the same order. However, in the hydrodynamic lubrication regime, the lubricant film thickness is much greater than the surface roughness. Therefore, the friction force between contact surfaces is dominated by the shear strength caused by lubricant viscosity [90].

3.4 Contact Models

To investigate friction and wear at contact interfaces, a knowledge of the contact area and contact pressure are necessary. In this section, various types of contact models used to describe contact between two surfaces will be discussed. These models will be used for interpreting the experimental and numerical simulation results shown in chapters 4, 6 and 7. We first present contact theories for two asperities (Hertzian model, Johnson-Kendal-Roberts model, Derjaguin-Muller-Toporov model, and Chang-Etsion-Bogy model), followed by the Greenwood-Williamson model for contact of two rough surfaces.

3.4.1 Elastic Contact of Two Spheres (Hertzian Contact Model)

Contact between two bodies is the sum of contacts between individual asperities on both surfaces. Contact between two asperities can be modeled as contact between two spheres. In 1881, Hertz [91] developed a model for elastic contact between two spheres. He assumed that the bodies in contact deform in the elastic regime and that the contact area is much smaller than the dimension of the two spheres. In his model, friction between the two spheres is ignored. Figure 3.8 shows the deformation of two spheres in contact with a normal load P. The dashed black lines show the shape of the spheres before deformation and the solid black lines depict the shape of the spheres after deformation. The displacement of point 1 in body 1 and point 2 in body 2 after deformation are denoted by δ_1 and δ_2, respectively. Based on Figure 3.8, the contact
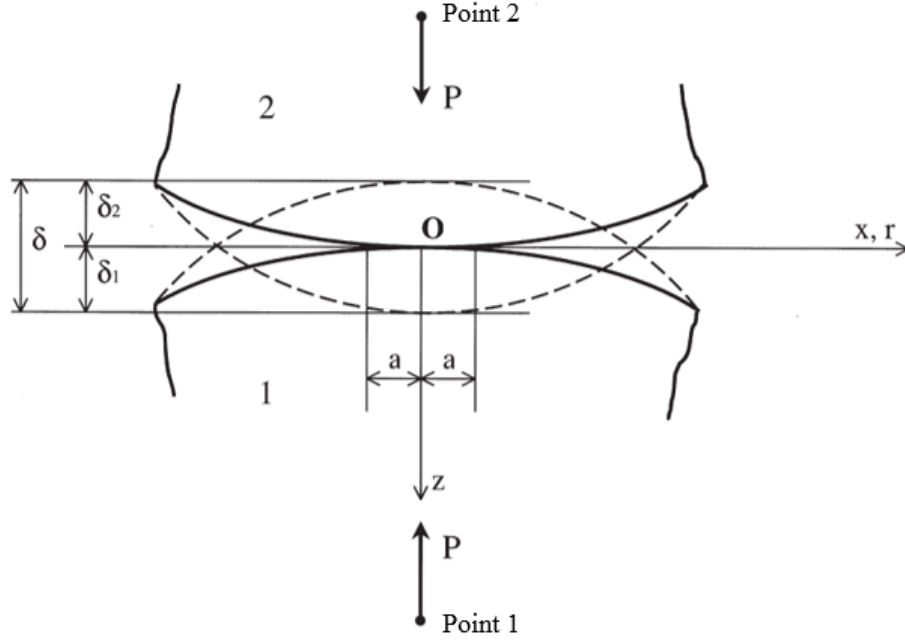
Figure 3.8 Contact between two elastic spheres in the Hertzian contact model (courtesy of [92])

interference δ between body 1 and body 2 is equal to the sum of δ_1 and δ_2. The contact

area has a circular shape with radius a. The radii of the spheres, the elastic moduli, and

the Poison's ratio for body 1 and body 2 are R_1, R_2, E_1, E_2, v_1, and v_2, respectively.

According to the Hertzian contact theory, the radius of the contact area is given by

$$a = \left(\frac{3PR^*}{4E^*}\right)^{1/3} \tag{3.7}$$

In Equation 3.7, the effective radius R^* and the effective elastic modulus E^* are defined

as

$$\frac{1}{R^*} = \frac{1}{R_1} + \frac{1}{R_2} \tag{3.8}$$

$$\frac{1}{E^*} = \frac{1-v_1{}^2}{E_1} + \frac{1-v_2{}^2}{E_2} \tag{3.9}$$

The contact interference between the two spheres is expressed as

$$\delta = \left(\frac{9P^2}{16R^*E^{*2}}\right)^{1/3} \tag{3.10}$$

The pressure distribution in the contact area is given by

$$p(r) = p_{max}\left(1 - \frac{r^2}{a^2}\right)^{1/2} \tag{3.11}$$

where the maximum contact pressure p_{max} is

$$p_{max} = \left(\frac{6PE^{*2}}{\pi^3 R^{*2}}\right)^{1/3} \tag{3.12}$$

3.4.2 Elastic Contact of Two Spheres with Adhesion in the Contact Area (Johnson-Kendal-Roberts (JKR) Contact Model)

In the Hertzian contact model, adhesion between the contacting bodies is not included. However, adhesive forces can have a significant effect on the contact behavior of asperities, especially when the normal load is small. In 1971, Johnson, Kendall, and Roberts [93] developed a contact model (JKR model) which includes adhesive forces. As shown in Figure 3.9, a_0 is the contact radius due to the applied normal load P_0. When the adhesive force F_s is included, the radius of the contact area increases and becomes a_1. The total normal load P_1 is equal to the sum of P_0 and F_s . In the JKR model, it is assumed that the adhesive force is present only inside the contact area ($r < a_1$). In addition, it is assumed that equilibrium between the two bodies in contact is reached when
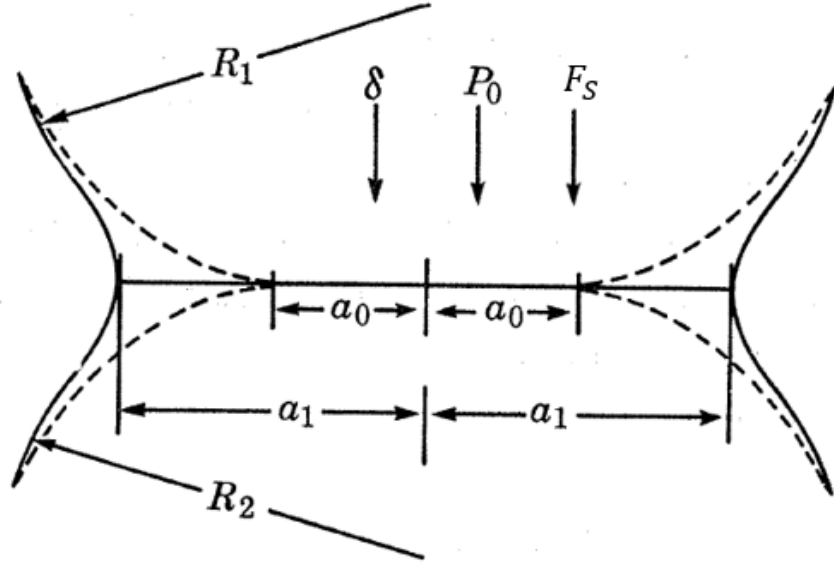
Figure 3.9 Contact between two elastic spheres in the JKR contact model (courtesy of [93])

$$\frac{dU_T}{da_1} = 0 \tag{3.13}$$

or

$$\frac{dU_T}{dP_1} = 0 \tag{3.14}$$

where U_T is the total energy of the contact bodies, defined as the sum of the elastic energy U_E, the mechanical energy caused by the external load U_M, and the surface energy between the contact surfaces U_S, i.e.,

$$U_T = U_E + U_M + U_S \tag{3.15}$$

$$U_E = \frac{1}{K_1^{2/3} R^{*1/3}} \left(\frac{1}{15} P_1^{5/3} + \frac{1}{3} P_0^2 P_1^{-1/3} \right) \tag{3.16}$$

$$U_M = \frac{-P_0}{K_1^{2/3} R^{*1/3}} \left(\frac{1}{3} P_1^{2/3} + \frac{2}{3} P_0^2 P_1^{-1/3} \right) \tag{3.17}$$

$$U_S = -\gamma \pi (R^* P_1 / K_1)^{2/3} \tag{3.18}$$

where

$$K_1 = \frac{4E^*}{3} \tag{3.19}$$

$$R^* = \frac{R_1 R_2}{R_1 + R_2} \tag{3.20}$$

In Equation 3.18, γ is the energy of adhesion between the two surfaces. Taking the derivative of Equation 3.15 with respect to a_1, one can express the total contact force P_1 as

$$P_1 = P_0 + 3\gamma \pi R^* + [6\gamma \pi R^* P_0 + (3\gamma \pi R^*)^2]^{1/2} \tag{3.21}$$

The second and third terms in Equation 3.21 account for the adhesive force. In the JKR model, the radius of the contact area is given by

$$a_1 = \left\{ \frac{R^*}{K_1} \left\{ P_0 + 3\gamma \pi R^* + [6\gamma \pi R^* P_0 + (3\gamma \pi R^*)^2]^{1/2} \right\} \right\}^{1/3} \tag{3.22}$$

and the contact interference can be expressed as

$$\delta = \frac{2P_1}{3K_1 a_1} \tag{3.23}$$

The pressure distribution is given by

$$p(r) = p_{max} \left(1 - \frac{r^2}{a^2} \right)^{\frac{1}{2}} + p_{max}' \left(1 - \frac{r^2}{a^2} \right)^{\frac{-1}{2}} \tag{3.24}$$

where

$$p_{max} = \frac{2a_1 E^*}{\pi R^*} \tag{3.25}$$

$$p_{max}' = -\left(\frac{4\gamma E^*}{\pi a_1}\right)^{1/2} \tag{3.26}$$

Since the adhesive force increases the contact force between contact bodies in the JKR model, the contact area, the contact interference, and the maximum contact pressure obtained from the JKR model are all greater than those obtained from the Hertzian contact model.

3.4.3 Elastic Contact of Two Spheres with Adhesion outside the Contact Area (Derjaguin-Muller-Toporov (DMT) Contact Model)

In 1974, Derjaguin, Muller, and Toporov [94] proposed another contact model (DMT model). Similar to the JKR model, this model takes into account adhesive forces outside the contact zone, while neglecting adhesive forces in the contact zone. Figure 3.10 compares the DMT and JKR models [95]. The DMT model assumes that contact inside the contact area is governed by the Hertzian contact model. The adhesive force, also known as van der Waals force, is exerted only on the region outside the contact area. Therefore, the equations for contact interference and pressure distribution inside the contact area of the DMT model are the same as those of the Hertzian contact model. In contrast, the JKR model assumes that adhesive force exists only inside the contact region. Another difference between the DMT model and the JKR model is the stress distribution inside the contact region. In the DMT model, stress inside the contact region is purely compressive. However, in the JKR model, stress inside the contact region is
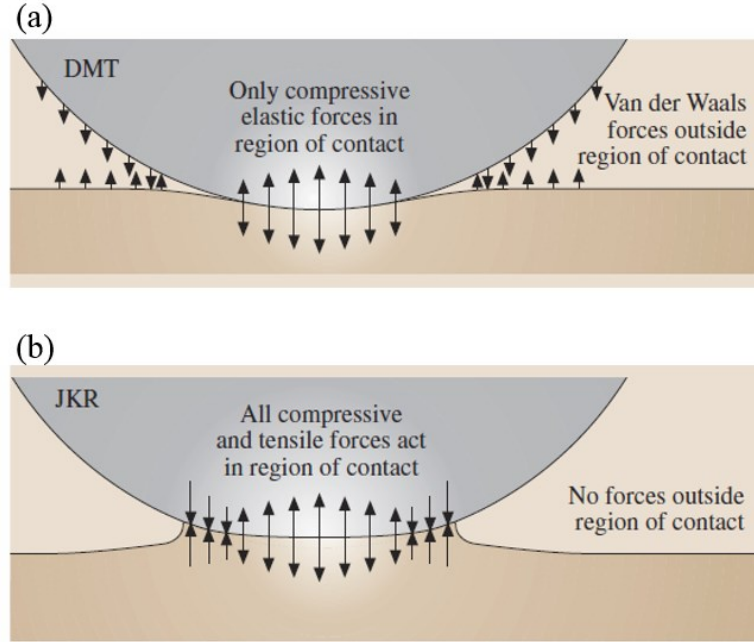
Figure 3.10 Comparison between (a) the DMT model and (b) the JKR model (courtesy of [95])

compressive at the center and tensile at the outer edges. At the border between the contact and the non-contact area, contact stress predicted by the JKR model goes to infinite. In the DMT model, the contact radius of the two spheres is given by

$$a = \left[\frac{3R^*}{4E^*} (P_0 + 4\gamma\pi R) \right]^{1/3} \tag{3.27}$$

The DMT and the JKR models were derived with different assumptions. To determine which of the two models should be used in a particular situation, one can use the Tabor coefficient [96] defined as

$$\lambda = \left[\frac{(\Delta\gamma)^2 R^*}{E^{*2} Z_0{}^3} \right] \tag{3.28}$$

where $\Delta\gamma$ is the work done by the adhesive force. Z_0 is the distance between the two contact bodies when the adhesive force changes from repulsive to attractive. For contact

between two spheres with a small radius of curvature and large effective elastic modulus ($\lambda \ll 1$), the DMT contact model is more accurate [97]. However, for contact between two spheres with large radius of curvature and small effective elastic modulus ($\lambda \gg 5$), the JKR contact model is more appropriate [97].

3.4.4 Elastic-Plastic Contact Model (Chang-Etsion-Bogy (CEB) Contact Model)

In addition to elastic deformation, plastic deformation can also occur when two surfaces come in contact. The plasticity index Ψ derived by Greenwood and Williamson [98] is usually used to determine whether the deformation of asperities is elastic or plastic. It is defined as [98]

$$\Psi = \frac{E^*}{H} \sqrt{\frac{\sigma_0}{R^*}} \tag{3.29}$$

where H is the hardness of the softer material and σ_0 is the RMS surface roughness. If Ψ is greater than 1.0, asperities undergo plastic deformation and if Ψ is smaller than 0.6, asperities experience elastic deformation.

The contact models discussed in the previous sections are insufficient to describe the contact behavior of surfaces involving plastic deformation. To account for both elastic and plastic deformations, an elastic-plastic contact model is needed. In 1987, Chang, Etsion, and Bogy [99] developed an elastic-plastic model (CEB model) to describe contact between a flat surface and a sphere, based on the assumption of conservation of volume. Figure 3.11 shows a schematic of the CEB contact model in which it is assumed that plastic deformation of a sphere occurs if the contact interference
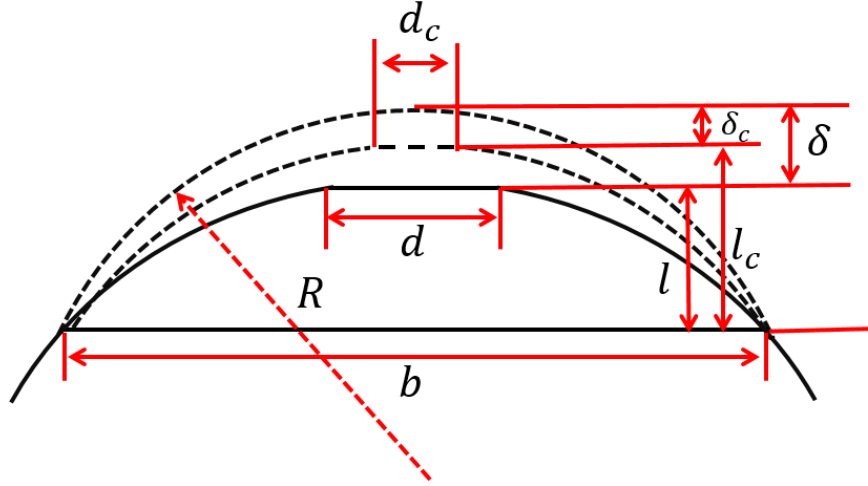
Figure 3.11 The CEB contact model (after [99])

δ is greater than the critical contact interference δ_c. The critical contact interface is defined as

$$\delta_c = \left(\frac{\pi K^* H}{2E^*}\right)^2 R \tag{3.30}$$

In Equation 3.30, R is the radius of the sphere and the hardness coefficient K^* is defined as [100]

$$K^* = 0.454 + 0.41\upsilon \tag{3.31}$$

where υ is the Poisson's ratio of the sphere. The critical contact diameter when plastic deformation occurs is assumed to be d_c. The control volume of the sphere is the region described by the height l_c and the width b shown in Figure 3.11. The height l_c and the width b are given by

$$l_c = K_1\delta \tag{3.32}$$

$$b = 2[2R(l_c + \delta_c)]^{1/2} \tag{3.33}$$

where K_1 is a constant. The control volume can be calculated using

$$V = \frac{\pi l_c}{6}(\frac{3}{4}d_c{}^2 + \frac{3}{4}b^2 + l_c{}^2) \qquad (3.34)$$

Since the CEB model assumes that the control volume remains constant as the sphere undergoes plastic deformation, the diameter of the contact area d can be expressed as

$$d = \sqrt{R\delta(2 - \frac{\delta_c}{\delta})} \qquad (3.35)$$

In the contact area, the pressure distribution is assumed to be uniform, with a magnitude of K^*H. Therefore, the contact force P can be calculated as

$$P = \pi R\delta(2 - \frac{\delta_c}{\delta})K^*H \qquad (3.36)$$

3.4.5 Greenwood-Williamson Multiple Asperities Contact Model

The contact models discussed in the previous sections are used for calculating the contact area and normal load between a single pair of asperities. In 1966, Greenwood and Williamson [98] developed a contact model to describe contact between two rough surfaces. In their model, contact between two rough surfaces is treated as contact between a perfectly smooth surface and a rough surface as shown in Figure 3.12. It is assumed that all asperities have the same radius β and the asperity height follows a Gaussian distribution $\phi(z)$. The height of asperities on the rough surface with respect to the reference plane is denoted by z. Assuming the distance between the smooth and rough surfaces is d, one finds that the probability of asperities contacting the smooth surface is given by

$$probability\ (z > d) = \int_d^\infty \phi(z)\, dz \tag{3.37}$$

If the total number of asperities on the rough surface is m, the expected number of asperities in contact will be

$$n = m \int_d^\infty \phi(z)\, dz \tag{3.38}$$
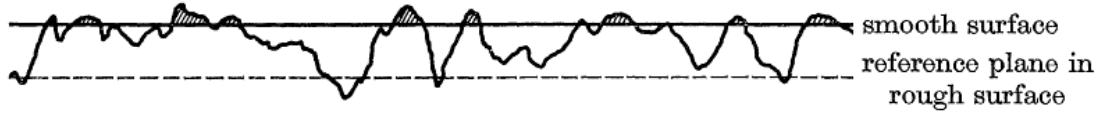
Figure 3.12 Contact between a flat surface and a rough surface (courtesy of [98])

The mean contact area of all asperities can then be expressed as

$$A_{mean} = \int_d^\infty \pi\beta(z - d)\phi(z)\, dz \tag{3.39}$$

and the total contact area between the two surfaces is given by

$$A = \pi n \beta \int_d^\infty (z - d)\phi(z)\, dz \tag{3.40}$$

The total contact load P will be

$$P = \frac{4}{3} n E^* \beta^{1/2} \int_d^\infty (z - d)^{3/2} \phi(z)\, dz \tag{3.41}$$

3.5 Experimental Techniques for Characterizing Surface Topography

In addition to calculating contact stress and contact area, examining surface topography is another important approach to investigate the wear mechanism at contact interfaces. In this section, two often used experimental techniques for characterizing surface topography are introduced. Both of these techniques, scanning electron microscopy and atomic force microscopy, are used in the experimental studies conducted in this dissertation.

3.5.1 Scanning Electron Microscopy

Scanning electron microscopy is one of the most popular techniques used to inspect surface topography on a microscopic scale with a resolution that can be as high as 1 nm. Figure 3.13 shows the design of a typical scanning electron microscope (SEM). An electron gun creates an electron beam, typically with a spot size smaller than 5 nm in radius, and shoots it at the sample surface. The condenser lens in the scanning electron microscope is used to condense electrons into a beam and focuses the beam on the sample surface. Unlike typical microscope lenses, scanning electron microscope lenses are not made of glass. Instead, they are electromagnetic lenses made of solenoidal coils. By changing the current applied to the coil, the magnitude of the Lorentz force applied to incident electrons is altered so that the focal length of the electromagnetic lenses is changed. Since the electron beam only focuses on a tiny spot, a raster scan is used to obtain a 2D image of the sample. To perform a raster scan, four plates are implemented

inside the objective lens, which surround the incident electrons. By changing the potentials between these plates, the direction of incident electrons can be adjusted so that the electron beam can scan the whole sample surface.
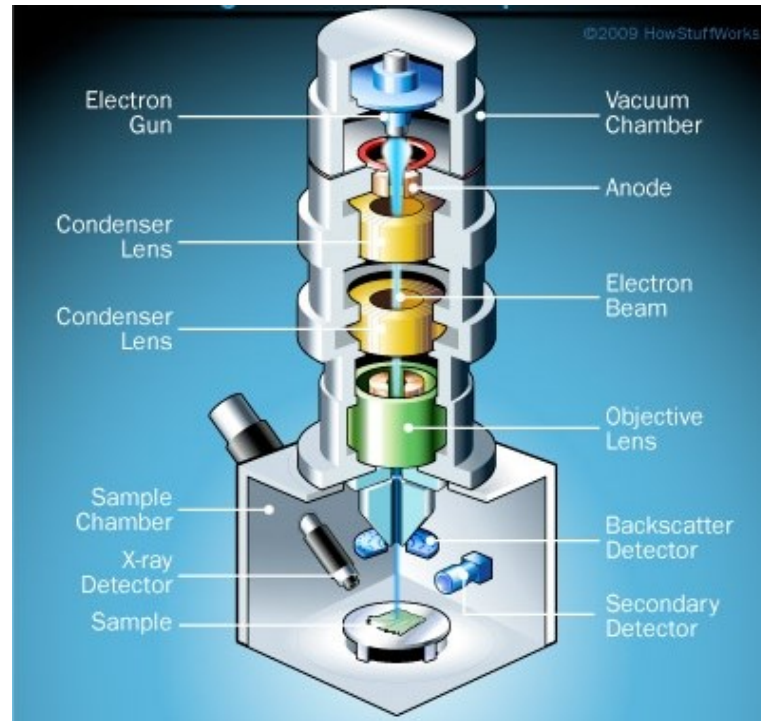
Figure 3.13 Schematic of scanning electron microscope (courtesy of [101])

As shown in Figure 3.14, due to collisions between incident electrons and the specimen, different types of electrons are reflected from the sample and detected by the detector inside the sample chamber. The electrons most commonly used for imaging are secondary electrons (SE) and backscattered electrons (BSE). Secondary electrons are generated by collisions between incident electrons and electrons of atoms at the surface of the sample material. Backscattered electrons are produced by the interaction between incident electrons and the nucleus of atoms below the sample surface. Based on the number of electrons, either secondary electrons or backscattered electrons detected
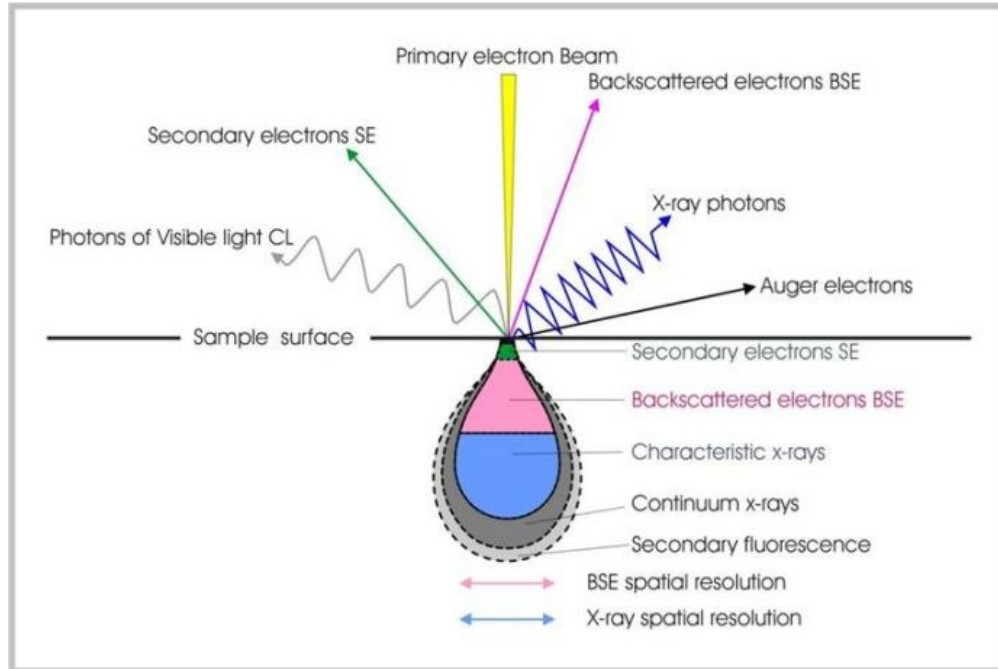
Figure 3.14 Electrons generated from a sample when an electron beam interacts with a sample surface (courtesy of [102]).

inside the chamber, the brightness of the sample is calculated. For example, if incident electrons are directed at a recessed area on the sample, the number of secondary electrons detected by the detector is small and a dark area will appear on the screen. However, if incident electrons are directed at a protruded area on the sample, a large number of secondary electrons will be detected and a bright area will appear on the screen. Since scanning electron microscope creates images according to brightness information, the scanning electron microscope images generated are all black and white.

3.5.2 Atomic Force Microscopy

Atomic force microscopy is another method used to characterize the roughness of a surface. It has a higher resolution than a scanning electron microscope. The vertical

resolution of atomic force microscope can be as high as 0.1 nm [103]. In an atomic force microscope, a cantilever beam with a very sharp tip makes contact with the sample or hovers above it at a small distance. Based on the amplitude of the beam deflection or the amplitude of the beam vibration, surface profile of a sample is obtained. In an atomic force microscope, two different modes can be used to measure the surface profile of a sample: the so-called contact mode and the tapping mode. Figure 3.15 shows the schematic of an atomic force microscope and its two modes. In both modes, a laser is directed at the cantilever beam and the reflected light is detected by a segmented photodiode. In the contact mode, the tip of the cantilever beam is in contact with the sample. As the tip moves across the surface of the sample, the cantilever beam deflects by different magnitudes at locations with varying heights. The deflection of the cantilever beam causes the laser light to be reflected back to different locations on the photodiode. Based on the magnitude of deflection, a feedback control algorithm is implemented to adjust the z-direction position of the beam so that the laser spot on the photodiode is directed at the reference position again. The adjustment of the z-direction position of the cantilever beam is achieved by applying different voltages to the piezoelectric actuator, which is connected to the cantilever beam holder. The voltage applied to the piezoelectric actuator can be correlated with the change in the z-direction position of the cantilever beam, which can be used to plot the surface profile of a sample.
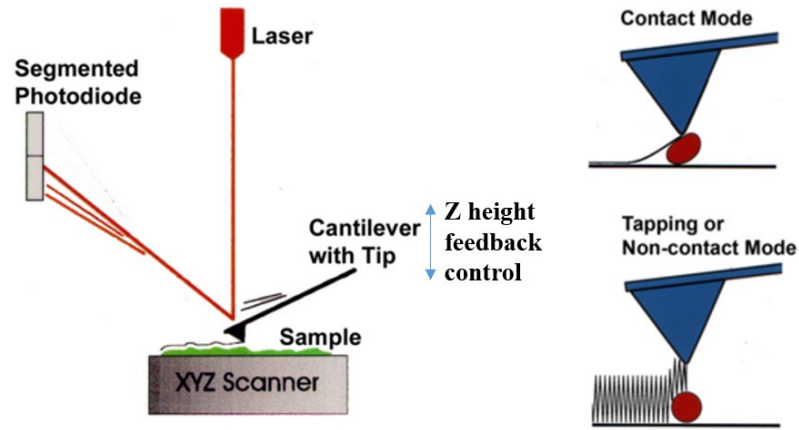
Figure 3.15 Schematic of an atomic force microscope (courtesy of [104])

Since the tip of the atomic force microscope touches the sample, it becomes blunt after usage, which leads to decreased image resolution. Also, in the case of live biological samples, an atomic force microscope may destroy the sample when operating in contact mode. In addition, material properties may be changed in some samples due to contact, which can lead to inaccurate results. To overcome these limitations, the tapping mode can be utilized. In the tapping mode, the tip of the cantilever beam is in close proximity to the sample, but has only intermittent contact with the sample surface. A piezoelectric element inside the cantilever holder oscillates the cantilever beam at a constant frequency and amplitude. While the tip is scanning the surface, the van der Waals force, dipole-dipole interactions, and electrostatic forces between the tip and the sample change due to the variation of the surface profile. Consequently, the oscillatory amplitude of the beam is altered. To change the oscillatory amplitude to the original value, the servo of the atomic force microscope adjusts the z-direction position of the cantilever beam. Then, the surface profile of the sample is obtained based on the change in the z-direction position of the cantilever.

3.6 Experimental Techniques for Characterizing Material Composition

To better understanding the wear mechanism between materials, one need to identify the chemical composition of wear debris and know how the chemical structure of contact material changes during wear process. In this section, three different experimental techniques for characterizing material composition are introduced. These three techniques are used in the experimental studies of chapters 4, 5, 6, and 7.

3.6.1 Energy Dispersive X-Ray Spectroscopy

Energy dispersive X-ray spectroscopy is a technique that allows the measurement of the chemical composition of a material. As shown in Figure 3.16, electrons from atoms in the sample material are emitted as secondary electrons when the incident electron beam is directed at the material. Once electrons are emitted, electrons at outer electron shells will jump to the inner electron shells. During this process, an X-ray signal is emitted by the sample. According to the energy or wavelength of the emitted X-ray signal, the chemical composition of the sample can be determined.
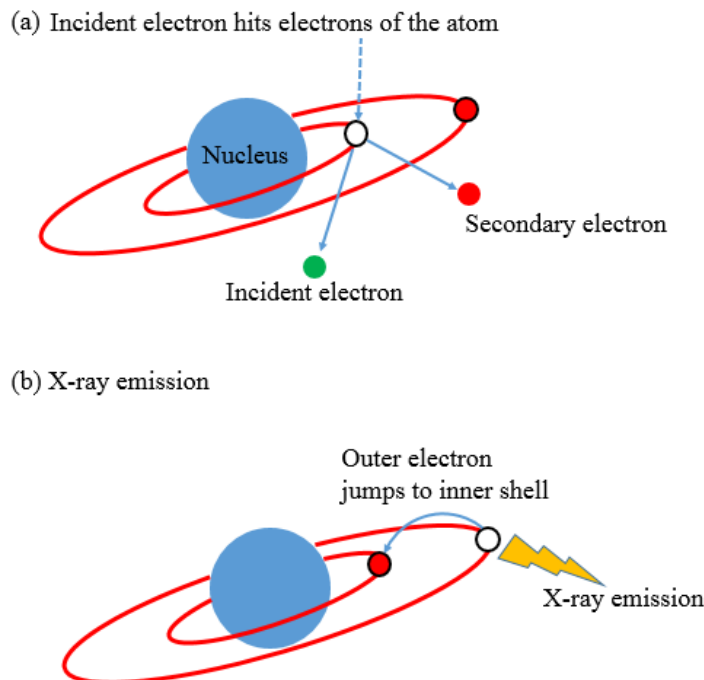
Figure 3.16 Emission of X-ray due to interaction between incident electron and sample material (after [105])

3.6.2 Electron Energy Loss Spectroscopy

Electron energy loss spectroscopy is another experimental technique used to characterize the chemical composition of a material. It is more sensitive than energy dispersive X-ray spectroscopy when measuring atoms with low atomic numbers. However, electron energy loss spectroscope is more complicated and difficult to use than energy dispersive X-ray spectroscope. Electron energy loss spectroscope determines the structure of a material according to the energy loss of inelastically scattered electrons, which are generated when incident electrons interact with the atoms of the specimen [106]. Figure 3.17 shows a schematic of an electron energy loss spectroscope (EELS), which consists of two components: the electron monochromator and the analyzer. The monochromator generates electrons and shoots them at the

specimen with energy ranging from 0.1 to 10 KeV. The electron spectrometer in the analyzer measures the energy loss of inelastically scattered electrons. Since the energy loss can be used to calculate the characteristic absorption frequency of different atoms, the composition of the specimen can be obtained [106].
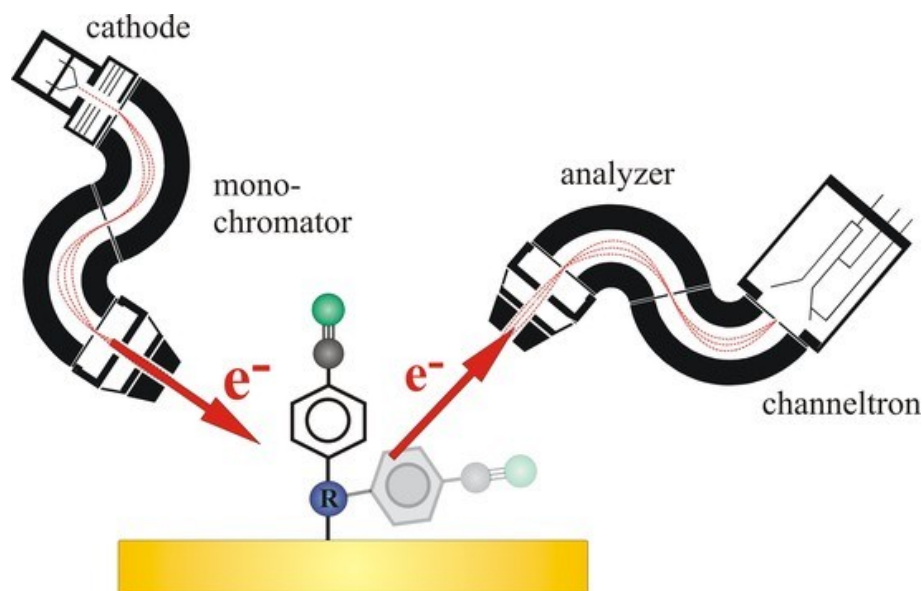
Figure 3.17 Principle of electron energy loss spectroscopy (courtesy of [107])

3.6.3 Time-of-Flight Secondary Ion Mass Spectrometry (ToF-SIMS)

To measure the chemical composition of thin films such as the lubricant on the slider or the disk surface, time of flight secondary ion mass spectrometry (ToF-SIMS), as shown in Figure 3.18 can be used. The detected depth of ToF-SIMS is only about 1 nm. The primary ion beam (Bi^+, Cs^+, C_{60}^+) generated by an ion gun is focused on the sample material. When primary ions hit the sample, secondary ions are ejected from the sample surface. The kinetic energy E_K of an ejected ion is given by

$$E_K = \frac{1}{2}mv^2 \tag{3.42}$$

where m is the mass and v is the velocity of the ion. According to Equation 3.42, one can know that ions with heavier weight have lower velocity and longer time of flight to the detector. Since the traveling distance of these ions is known and the time of flight can be measured, one can calculate the mass of the ion to determine the element composition of a sample material.
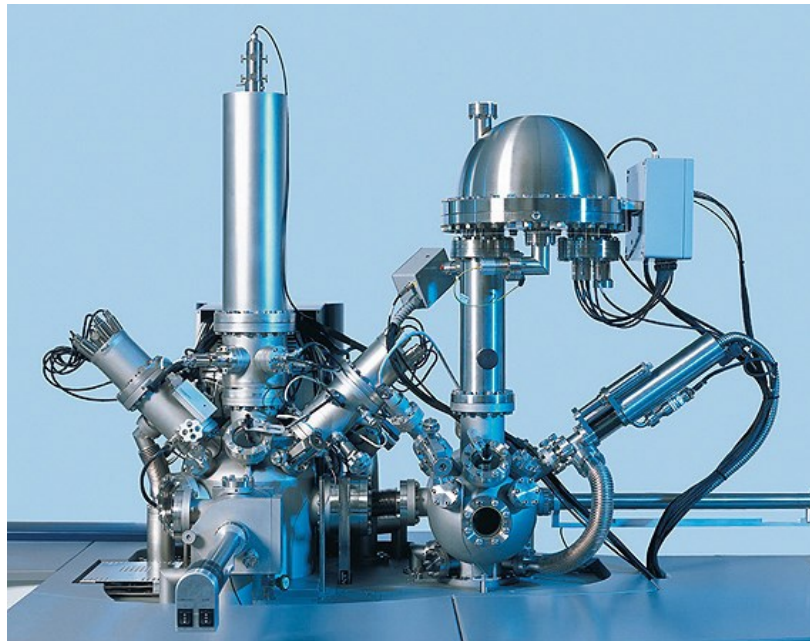
Figure 3.18 Experimental setup of Time-of-Flight Secondary Ion Mass Spectrometry (courtesy of [108])

Chapter 4

The Effect of Diamond-Like Carbon Overcoat on the Tribological Performance of the Dimple/Gimbal Interface

4.1 Introduction

Wear debris is detrimental for the reliability of the head/disk interface in hard disk drives since it can cause severe contact between the slider and the disk. In this chapter, fretting wear at the dimple/gimbal interface of a hard disk drive suspension was investigated for stainless steel dimples in contact with stainless steel gimbals coated with diamond-like carbon (DLC) of different thickness and different elastic modulus. Scanning electron microscopy was used to evaluate the size and characteristics of the wear scar of both the dimple and the gimbal. Numerical simulations were performed to calculate the maximum principal stress in the dimple and the gimbal with the goal of correlating wear and the maximum principal stress. The mechanism of wear and fatigue

crack formation is explained by comparing the simulation results with the experimental results.

As introduced in Chapter 3, fretting wear is defined as damage of tribo-surfaces caused by small-amplitude oscillatory relative displacements [87]. A typical example of fretting wear occurs in the dimple/gimbal interface of a hard disk drive suspension. As shown in Figure 4.1 (a) and (b), a spherical protrusion on the suspension, called the "dimple", is in contact with a flat part of the flexure spring, the so-called "gimbal". The contact point between the dimple and the gimbal allows roll and pitch motion of the slider in response to applied external forces. Roll and pitch motion of the slider during track seeking and track following causes small-amplitude oscillatory relative displacements between the dimple and the gimbal, leading to fretting wear and the formation of wear particles. The presence of wear particles in a hard disk drive is undesirable because it can lead to failure of the head disk interface.
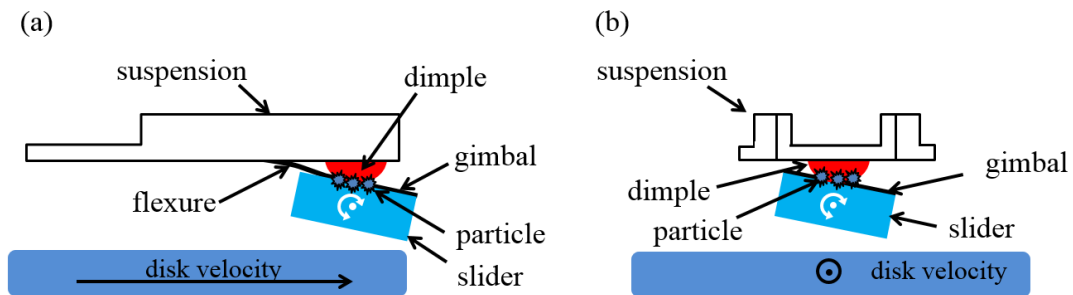
Figure 4.1 Schematic of the head/disk interface: (a) pitch motion and (b) roll motion of slider.

In the last decade, several studies of fretting wear at the dimple/gimbal interface of a hard disk drive suspension have been performed. Raeymaekers et al. [109] investigated the relationship between normal load and wear particle generation. In

addition, they studied the effect of surface roughness of the gimbal on the tribological performance of the dimple/gimbal interface. In another study, Raeymaekers et al. [110] studied the tribological degradation of nickel-coated and gold-coated gimbals against stainless steel dimples and observed a substantial reduction in friction and wear with an increase of the overcoat thickness. Yoon et al. [111] observed a similar result for wear of a stainless steel dimple in contact with a gold-coated gimbal. Li et al. [112] analyzed the change of the plasticity index of non-polished and laser-polished dimples during fretting wear. In a related study, Li et al. [113] created a finite element model of the interface and showed that high normal load is advantageous for reducing relative motion between the dimple and the gimbal, and for reducing fretting wear at the dimple/gimbal interface.

Although investigations in [109]–[113] have shown in detail the mechanism of wear at the dimple/gimbal interface, none of the above studies has dealt with the effect of a diamond-like carbon (DLC) overcoat on fretting wear. It is well known that a DLC overcoat has a low friction coefficient and can reduce wear at contact surfaces dramatically [114]–[116]. Consequently, in this study, fretting wear of a stainless steel dimple was investigated in contact with a stainless steel gimbal coated with a thin layer of DLC. The coefficient of friction was measured using a load cell and the wear scar was evaluated using scanning electron microscopy (SEM). The present study is an extension of the experimental work reported in [110]–[112] on fretting wear at the dimple/gimbal interface for the case of a thin carbon overcoat, although the nickel-coated and the gold-coated gimbals in [110] and [111] were tested at different experimental conditions (number of cycles, frequency, and normal load). Both

experimental and numerical studies were performed to investigate the effect of the thickness and the elastic modulus of the DLC overcoat on the tribological performance of the dimple/gimbal interface in hard disk drives.

4.2 Material and Methods

Fretting wear generated at the dimple/gimbal interface is caused by pitch and roll motion of the slider. In our work, we modeled the motion between the dimple and the gimbal along a fixed direction, so that the measured friction coefficient corresponds to this relative motion and the corresponding changes of the contact surfaces. As shown in Figure 4.2, a hard disk drive suspension was attached to the suspension mount using a single screw. The vertical position of the suspension was adjusted using a dial gauge to apply a normal load of 20 mN, in agreement with the typical pre-load of the dimple/gimbal interface in a hard disk drive. The gimbal was mounted on a stage attached to a piezoelectric actuator. A triangular voltage input signal was applied to the
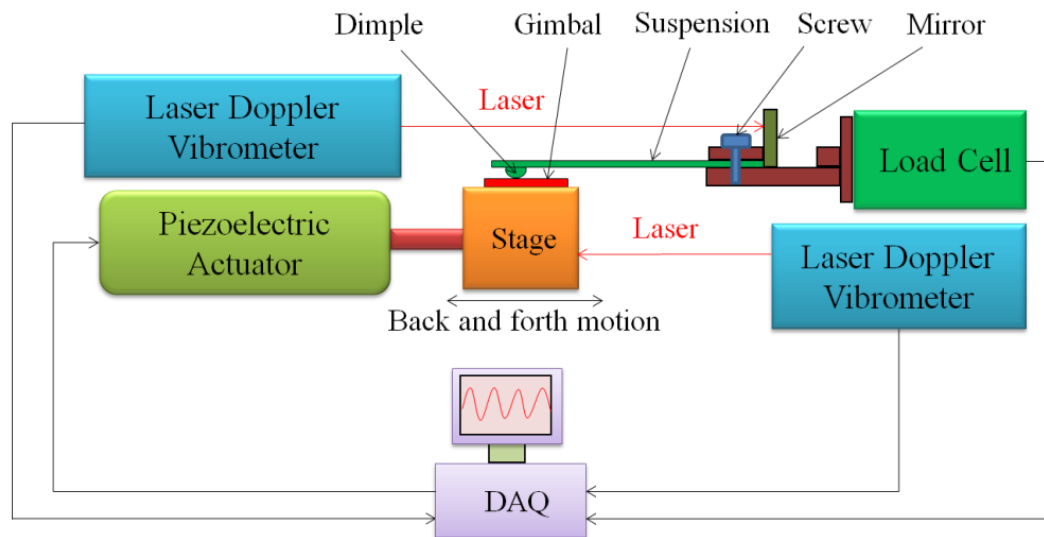
Figure 4.2 Schematic of fretting wear tester

piezoelectric actuator, resulting in horizontal movement of the gimbal relative to the dimple. The displacement amplitude $2D_d$ was approximately 10 μm. A load cell attached to the suspension mounting block was used to measure the friction force, while two independent Laser Doppler Vibrometers (LDVs) were used to measure the horizontal displacement of the gimbal and the suspension. The difference between the two LDV measurements gives the relative displacement between the dimple and the gimbal. For each dimple/gimbal interface, a fretting wear test was performed with a total number of 3.45×10^6 cycles at a frequency of 20 Hz. The duration for each test was 48 hours. The data were collected in real time using a data acquisition (DAQ) board and LabVIEW, a commercially available software.

$2D_d$ displacement amplitude
$2D_s$ sliding amplitude
S_c elastic slope
Q friction force
D_{rel} relative displacement
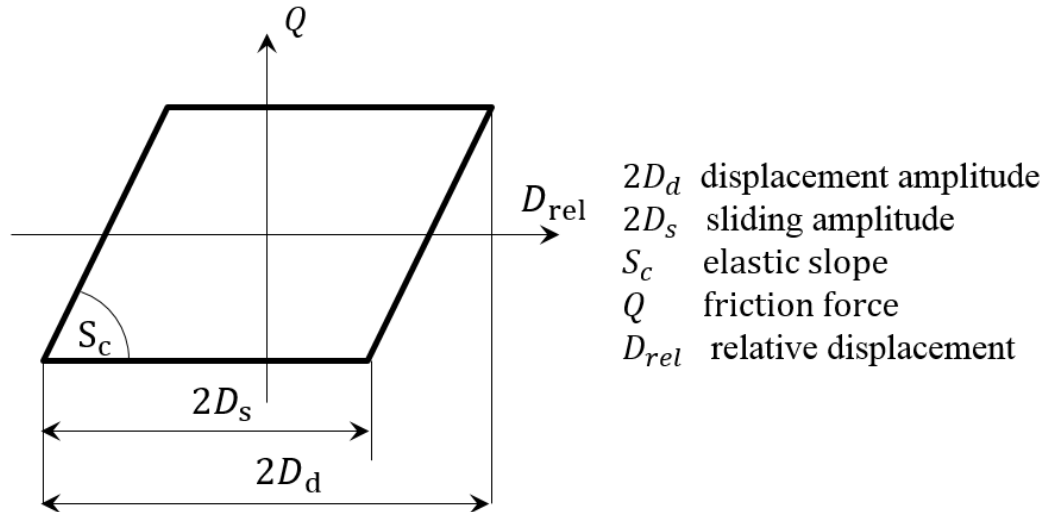
Figure 4.3 Typical friction hysteresis loop

An idealized friction versus displacement curve, also known as the "friction hysteresis loop" [111], is shown in Figure 4.3. The dissipated energy E_μ for each cycle is determined by numerical integration of the area enclosed by this loop. The average

coefficient of friction μ can be calculated from the dissipated energy E_μ, the displacement amplitude $2D_d$ and the normal load N according to [117]

$$\mu = \frac{E_\mu}{2 \cdot 2D_d \cdot N}$$
(4.1)

Table 4.1 Dimple/gimbal material combinations tested

	A	B	C	D	E
Dimple	304 Stainless Steel	304 Stainless Steel	304 Stainless Steel	304 Stainless Steel	304 Stainless Steel
Gimbal	304 Stainless Steel coated with 15 nm DLC (ta-C)	304 Stainless Steel coated with 70 nm DLC (ta-C:H)	304 Stainless Steel coated with 250 nm DLC (ta-C:H)	304 Stainless Steel coated with 690 nm DLC (ta-C:H)	304 Stainless Steel without DLC

A schematic of the dimple/gimbal interface is shown in Figure 4.4. Five different dimple/gimbal combinations were used (Table 4.1). Dimples were made from stainless steel (304 SST). The dimples are spherical protuberances with a radius of 200 μm. DLC overcoats, ranging in thickness from 15 nm to 690 nm, were deposited on stainless steel substrate (304 SST) of 40 μm thickness. The carbon overcoat was produced using filtered cathodic vacuum arc (FCVA). The 15 nm DLC overcoat consists of tetrahedral amorphous carbon (ta-C). The other three DLC overcoats are hydrogenated tetrahedral

amorphous carbon (ta-C:H). The average surface roughness of the four DLC coated gimbals is close to 200 nm. Uncoated gimbals were used as control group for this study.
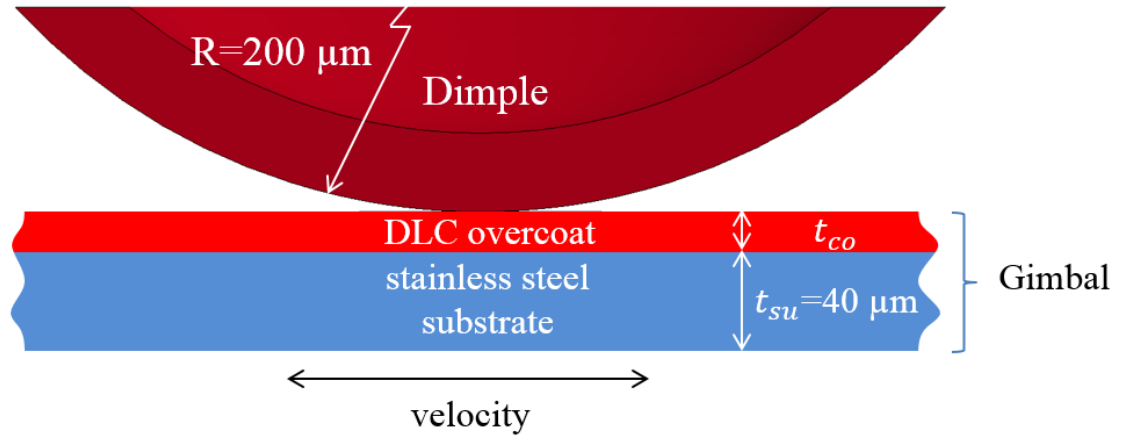
Figure 4.4 Schematic of dimple/gimbal interface coated with a thin layer of DLC. The radius of the spherical dimple is 200 µm. The thickness of the stainless steel substrate of the gimbal t_{su} is 40 µm. The thickness of the DLC overcoat t_{co} is 15 nm, 70 nm, 250 nm, and 690 nm, respectively.

4.3 Experimental Results and Discussion

4.3.1 Coefficient of Friction

Figure 4.5 shows the coefficient of friction as a function of the number of fretting wear cycles for different dimple/gimbal material combinations. Each curve is the average of three tests obtained for the same conditions. As seen from Figure 4.5, the friction coefficient for all material combinations increases slightly with the number of fretting wear cycles. The lowest friction coefficient was found for a carbon overcoat thickness of 690 nm (Figure 4.5 (d)), while the highest coefficient of friction occurred for a carbon overcoat thickness of 250 nm (Figure 4.5 (c)). The coefficient of friction for the 690 nm DLC overcoat showed fewer fluctuations than any of the other material
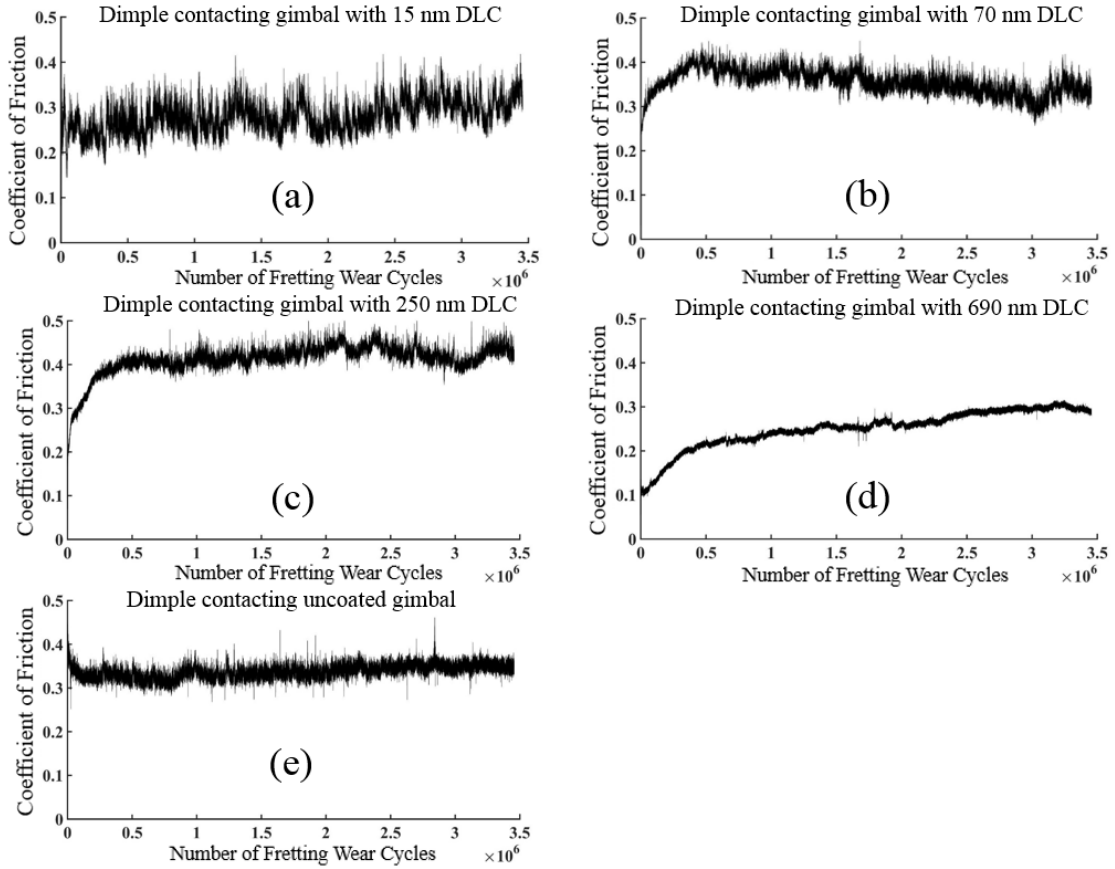
Figure 4.5 Coefficient of friction versus number of fretting wear cycles for (a) 15 nm DLC coated gimbal, (b) 70 nm DLC coated gimbal, (c) 250 nm DLC coated gimbal, (d) 690 nm DLC coated gimbal, and (e) uncoated gimbal.

combinations, most likely related to the fact that fewer wear particles were generated in the case of the 690 nm thick DLC overcoat. The mean friction coefficient for 3.45×10^6 fretting wear cycles is shown in Figure 4.6. We observe that the mean friction coefficient for the 15 nm DLC overcoat is about 0.28. The friction coefficient increases to 0.41 for the 250 nm DLC overcoat, and decreases to approximately 0.25 for an overcoat thickness of 690 nm. The mean friction coefficient for an uncoated gimbal is 0.33. The increase of the friction coefficient with the number of cycles is most likely related to the change of the surface roughness and the generation of wear particles

during the test. The smaller friction coefficient observed for the 690 nm DLC overcoat appears to be related to the formation of a transfer layer [118] on the gimbal. This point will be further discussed later in the paper.
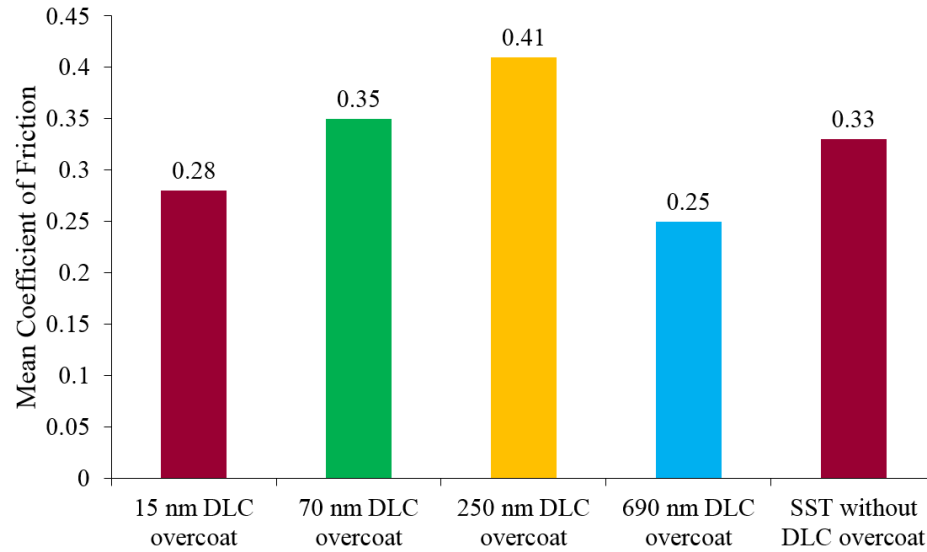
Figure 4.6   Mean coefficient of friction for different dimple/gimbal combinations

4.3.2 Wear Scar on Dimple

Figure 4.7 shows SEM images of wear scars on stainless steel dimples after 3.45×10^6 fretting wear cycles against gimbals coated with a DLC overcoat of 15 nm, 70 nm, 250 nm, and 690 nm thickness, and a gimbal without a DLC overcoat. The top row in Figure 4.7 corresponds to 1500x magnification, while the bottom row is for 6000x magnification. We observe that the wear scar on the dimple in Figure 4.7 (d) is much smaller than the wear scar on the other dimples (Figure 4.7 (a), (b), (c) and (e)). Comparing the wear scar in Figure 4.7 (d) with the wear scar in Figure 4.7 (a), (b), (c), and (e), we observe that fewer wear particles are present in Figure 4.7 (d) than in Figure 4.7 (a), (b), (c) or (e). In addition, the size of the wear particles in Figure 4.7 (d) is

(a) Dimple against gimbal with 15 nm DLC (b) Dimple against gimbal with 70 nm DLC (c) Dimple against gimbal with 250 nm DLC (d) Dimple against gimbal with 690 nm DLC (e) Dimple against uncoated gimbal
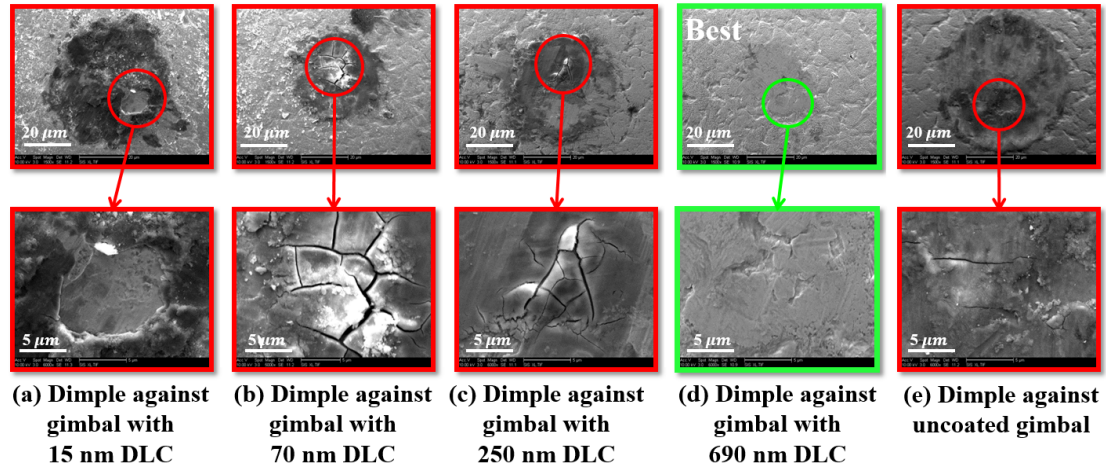
Figure 4.7 SEM images of typical wear scars on stainless steel dimples after 3.45×10^6 fretting wear cycles against (a) 15 nm DLC coated gimbal, (b) 70 nm DLC coated gimbal, (c) 250 nm DLC coated gimbal, (d) 690 nm DLC coated gimbal, and (e) uncoated gimbal.

smaller than the size of the wear particles in the other cases. Energy dispersive x-ray (EDX) analysis shows that these wear particles have the same chemical composition as the dimple, suggesting that the wear particles come from the dimple. In addition, we observe that the wear scar in Figure 4.7 (d) does not show any distinct black regions as can be seen on other samples. From EDX analysis, we observe that the percentage of oxygen in the black regions of the dimple increased from 6% to 25% after the fretting wear test, which implies that the dimple material is oxidized during the fretting wear test. The absence of dark regions in Figure 4.7 (d) suggests that the wear scar has not oxidized. From the SEM images at 6000x magnification shown in Figure 4.7, we observe the appearance of micro-cracks in Figure 4.7 (a), (b), (c) and (e). Micro-cracks were absent on dimples tested against gimbals with a 690 nm DLC overcoat (Figure 4.7 (d)).

4.3.3 Wear Scar on Gimbal

Figure 4.8 shows SEM images of wear scars of different gimbals after 3.45×10^6 fretting wear cycles. The high magnification SEM images in Figure 4.8 shows the region at the center of the gimbal wear scars. We observe the presence of micro-cracks in the wear scars of gimbal A, B, C, and E (Figure 4.8 (a), (b), (c), and (e)), but none in the wear scar of gimbal D (Figure 4.8 (d)). The uncoated gimbal has the largest cracks (Figure 4.8 (e)). The gimbal coated with 15 nm DLC (Figure 4.8 (a)) showed the smallest cracks. Gimbals coated with 70 nm DLC (Figure 4.8 (b)) and 250 nm DLC (Figure 4.8 (c)) showed cracks of similar size. From Figure 4.8 (d) we observe that a thin layer has formed in the contact area of the gimbal with a 690 nm thick DLC overcoat. This thin layer is likely to be a transfer layer [118]. EDX analysis was performed on the transfer layer. The results showed that the transfer layer is primarily carbon, which suggests that it is generated from the DLC overcoat. As reported in [118], a transfer

| (a) Gimbal with 15 nm DLC | (b) Gimbal with 70 nm DLC | (c) Gimbal with 250 nm DLC | (d) Gimbal with 690 nm DLC | (e) Uncoated gimbal |
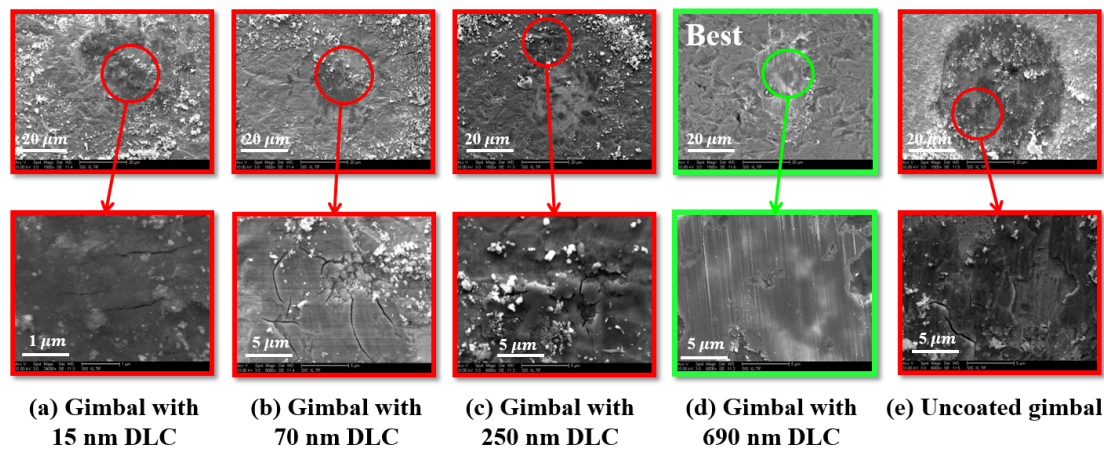
Figure 4.8 SEM images of typical gimbal wear scars on (a) 15 nm DLC coated gimbal, (b) 70 nm DLC coated gimbal, (c) 250 nm DLC coated gimbal, (d) 690 nm DLC coated gimbal, and (e) uncoated gimbal, after 3.45×10^6 fretting wear cycles.

layer can be formed by the graphitization of the DLC overcoat and the distortion of the DLC structure. Among the four DLC overcoats tested in this study, the 690 nm thick DLC layer has the lowest sp^3 bonding ratio of 67% as measured by electron energy loss spectroscopy (EELS). Thus, it is most likely that the 690 nm thick DLC layer is graphitized. The transfer layer formed on the 690 nm thick DLC overcoat can act as a solid lubricant and reduce the friction coefficient at the contact interface [119]. Therefore, the formation of the transfer layer could explain why the coefficient of friction of the 690 nm DLC coated gimbal was low and why the surface damage was less than that observed on other gimbals (Figure 4.8 (a), (b), (c), and (e)). Based on the absence of cracks and the reduced number of wear particles in Figure 4.7 (d) and Figure 4.8 (d), we conclude that gimbals coated with a 690 nm DLC film have the best protection against fretting wear.

We infer from Figure 4.7 (e) and Figure 4.8 (e) that the contact areas of both the stainless steel dimple and the stainless steel gimbal are oxidized during the fretting wear test. For other cases in which the gimbal is coated with DLC, only the contact area of the dimple is oxidized. Thus, the DLC overcoat prevents the gimbal from being oxidized, which may explain why the DLC overcoat improves the tribological performance of the dimple/gimbal interface.

4.3.4 Wear Mechanism

As observed from Figure 4.7, shallow fatigue-type surface cracks of different lengths are present on the dimple surface after a fretting wear test. The formation of these cracks is related to the change of stress from tensile to compressive during each

fretting cycle and appears to be a function of the mechanical properties, the thickness of the DLC overcoat, the bonding strength between the DLC overcoat and the substrate, and the number of fretting wear cycles. To understand the formation of cracks and the wear characteristics of the dimple/gimbal interface, we focus in the remainder of this chapter on the effect of mechanical properties of the dimple and the gimbal, and the effect of the thickness of the DLC overcoat.

The first step in the understanding of crack formation and wear is to determine the mechanical properties of the carbon overcoat such as its elastic modulus and hardness. In general, nano-indentation techniques are used to determine such properties of thin coatings [120]. However, in the case of a very thin overcoat on the order of 10 nm, nano-indentation measurements are strongly influenced by the underlying substrate [121]. To avoid this effect, it is common to characterize a very thin carbon overcoat using electron energy loss spectroscopy (EELS) [122]. In EELS measurement, the sp^3 bonding fraction of the carbon overcoat is determined. According to Xu et al. [123], the elastic modulus E and the indentation hardness H of a DLC overcoat are nearly proportional to the sp^3 fraction of the DLC overcoat. Therefore, we assume that the elastic modulus E and the indentation hardness H of a DLC overcoat can be calculated using the expressions

$$E = ar - b \qquad (4.2)$$

$$H = cr - d \qquad (4.3)$$

where r is the sp^3 fraction of the DLC overcoat obtained from EELS measurement. The coefficients a (1600 GPa), b (1010 GPa), c (256 GPa), and d (173 GPa) are values

obtained by performing a linear fit for the data reported by Xu et al. [123]. Figure 4.9

shows the sp^3 fractions, the elastic modulus and the hardness of the four DLC overcoats

used in this study. As shown in Figure 4.9 (a), the sp^3 fraction of the 15 nm, 70 nm, 250

nm, and 690 nm DLC overcoats is 90%, 70%, 70%, and 67%, respectively. Using the

sp^3 measurement, we obtain values for the elastic modulus of the 15 nm, 70 nm, 250

nm, and 690 nm DLC overcoats to be 430 GPa, 110 GPa, 110 GPa, and 62 GPa,

respectively, as shown in Figure 4.9 (b). The elastic modulus of the 690 nm DLC

overcoat (62 GPa) is close to 70 GPa as measured using nano-indentation. As shown in

Figure 4.9 (c), the hardness of the 15 nm, 70 nm, and 250 nm DLC overcoats is 57.4

GPa, 6.2 GPa and 6.2 GPa, respectively, obtained by applying Equation 4.3. Nano-

indentation shows that the hardness of the 690 nm DLC overcoat is 6.0 GPa. The dotted

lines in Figure 4.9 (b) and (c) indicate the elastic modulus (200 GPa) and the hardness

(5.0 GPa) of the stainless steel dimple.

Xie et al. [124] and others [125], [126] have shown that for a soft surface sliding

against a hard surface, wear occurs mainly on the softer surface. As shown in Figure 4.9

(c), for case A (15 nm DLC overcoat), the hardness of the dimple material (5.0 GPa) is

much smaller than that of the hardness of the DLC overcoat (57.4 GPa). Therefore, wear

and material removal should be observed predominately on the softer dimple surface

(Figure 4.7 (a)). Since the DLC overcoat on the gimbal is harder than the dimple

material, wear and crack formation on the gimbal (Figure 4.8 (a)) is expected to be less

pronounced than on the dimple (Figure 4.7 (a)). For cases B and C, the hardness of the

DLC overcoat is close to the hardness of the dimple. During the fretting wear test, the
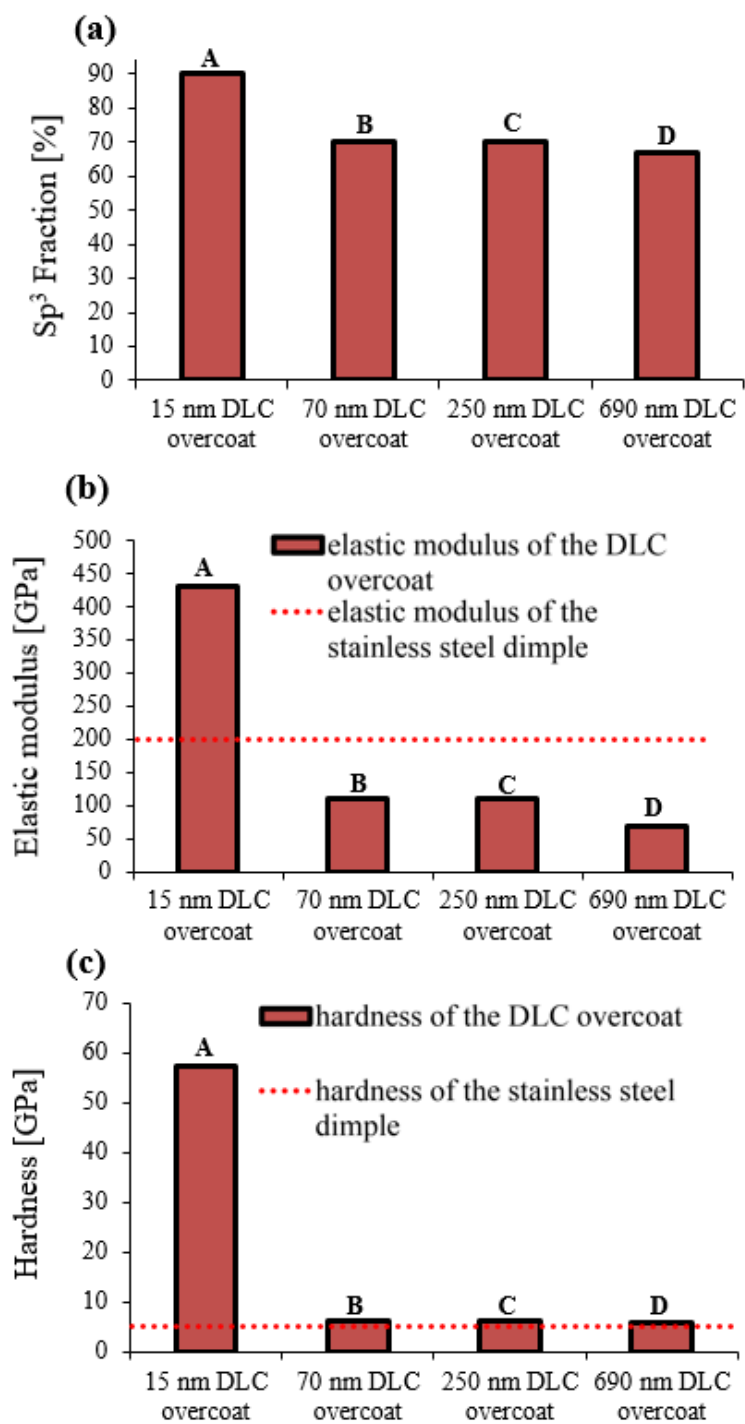
Figure 4.9 (a) sp^3 fraction, (b) elastic modulus, and (c) hardness of 15 nm, 70 nm, 250 nm, and 690 nm DLC overcoats.

same region of the dimple keeps contacting the gimbal throughout the test, while the contact region of the gimbal changes with the back and forth motion of the gimbal. Therefore, large cracks are present on the dimple material (Figure 4.7 (b), (c)) but smaller cracks are observed on the gimbal material (Figure 4.8 (b), (c)). For case D (690 nm DLC overcoat), we did not observe any cracks on either the dimple (Figure 4.7 (d)) or the gimbal surface (Figure 4.8 (d)). This result is most likely a consequence of the formation of the transfer layer.

Comparing the gimbal coated with DLC (Figure 4.8 (a), (b), (c), and (d)) and the uncoated gimbal (Figure 4.8 (e)), we observe that cracks on the gimbals coated with DLC (Figure 4.8 (a), (b), (c), and (d)) are smaller than cracks formed on the uncoated gimbal (Figure 4.8 (e)). This suggests that the tribological performance of the gimbal is improved by the DLC overcoat. However, the increased elastic modulus of the DLC overcoat causes higher contact stresses, leading to an increase in the wear of the dimple. Furthermore, only small cracks on the order of 1 μm were observed on the gimbal coated with 15 nm DLC (Figure 4.8 (a)), while large cracks on the order of 10 μm were formed on the mating dimple (Figure 4.7 (a)).

4.4 Numerical Simulation Results and Discussion

4.4.1 Finite Element Model

From the fretting wear test results, we have observed that DLC overcoats on a gimbal affect the number of wear particles and the formation of fatigue cracks on the

dimple and the gimbal. To understand the effect of material properties and the thickness of the DLC overcoat on the wear characteristics and crack formation at the dimple/gimbal interface, we turn next to the calculation of the contact stress between the dimple and the gimbal. Since the generation of wear particles and the formation of fatigue cracks are related to the maximum principal tensile stress [127], we will use principal stress as metric for analyzing the simulation results.

Contact between the dimple and the gimbal is a contact problem of a hemi-sphere sliding back and forth against a flat surface coated with a thin layer of material as shown in Figure 4.4. In addition to the normal load, a frictional force with alternating sign is present at the interface in a fretting wear situation. To calculate the contact stress, a model involving both the normal and tangential force is needed. The classical Hertzian contact model [92] is not applicable since it includes only a normal load. The reciprocal motion between the dimple and the gimbal causes friction at the contact interface, and the direction of the friction force changes with each cycle. Hamilton [128] developed a set of equations for calculating the contact stresses between two bodies in the presence of normal and tangential load. However, his model applies only to the case of homogeneous materials, which is not the case for the gimbal coated with a thin DLC overcoat as shown in Figure 4.4. Ling et al. [129] studied the problem of a layered elastic half-space under a moving load, but in their model the friction force was not included. Since no easy-to-use closed form equations exist for the case of a hemi-sphere sliding on a half-space coated with a thin layer, finite element analysis was used to calculate the contact stress between the dimple and a gimbal coated with a thin DLC overcoat.

Figure 4.10 (a) shows a 3-D finite element model for a dimple sliding against a stainless steel gimbal coated with a thin DLC overcoat. The blow-up of the contact region is shown in Figure 4.10 (b). In the calculations, the DLC overcoat thickness t_{co} was chosen to be 15 nm, 70 nm, 250 nm, and 690 nm, respectively. These values are the same as the thickness of the DLC overcoat used in our fretting wear tests. The thickness of the stainless steel substrate of the gimbal t_{su} is 40 μm. The radius of the stainless steel dimple R is 200 μm. A combination of 8 node brick elements and 6 nodes
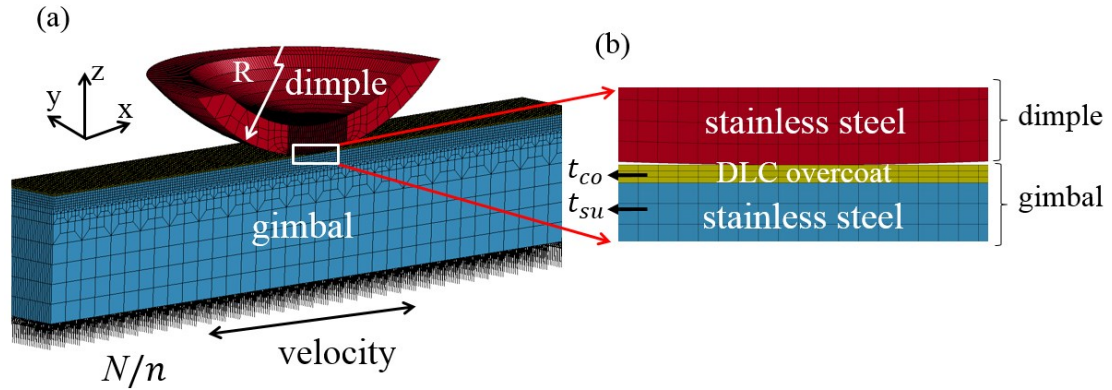
Figure 4.10 Finite element model for contact between dimple and gimbal

pentahedron elements was used to model the dimple. The gimbal substrate and the DLC overcoat were modeled using 8 node brick elements. Because the tangential motion of the gimbal is in the horizontal direction (x direction), the model is symmetric with respect to the x-z plane. Thus, only half of the dimple and the gimbal are modeled. Nodes at the top of the dimple are fixed in all six degrees of freedom. Nodes on the x-z plane are restrained from motion in the y direction. A displacement of 10 μm along the x direction is applied to the gimbal. Both the normal and the tangential load are considered. A distributed normal load N/n is applied to each node at the bottom of the gimbal in

the positive z direction, with the number of nodes n on the bottom of the gimbal being equal to 416. The normal load N is 10 mN, corresponding to half the normal load applied in the fretting wear test since our model simulates only half of the dimple and half of the gimbal. In the finite element model, the tangential force Q is the friction force between the dimple and the gimbal, given by

$$Q = \mu \cdot N \tag{4.4}$$

where μ is the friction coefficient between the dimple and the gimbal. The dimple and gimbal materials are assumed to be elastic. The elastic modulus of the DLC overcoat and the friction coefficient used in the simulation were obtained from electron energy loss spectroscopy (EELS) measurements and fretting wear tests, respectively. The numerical calculations were performed using the explicit solver of the commercially available finite element analysis software LS-DYNA [130].

4.4.2 Stress Distribution in the Dimple

Figure 4.11 shows the distribution of the maximum principal stress around the contact area of the dimple, for the gimbal coated with 690 nm DLC, sliding in the positive x direction (Figure 4.11 (a)) and the negative x direction (Figure 4.11 (b)). Since reciprocating sliding contact between the dimple and the gimbal is a quasi-static contact problem [131], the stress distribution in the dimple and the gimbal does not change with time over the contact region, assuming the friction remains constant throughout a fretting wear cycle. Thus, the stress distributions shown in this study correspond to arbitrary sliding positions between 0 and 10 μm. We observe from Figure 4.11 that the largest maximum principal tensile stress of about 80 MPa occurs in the dimple at the
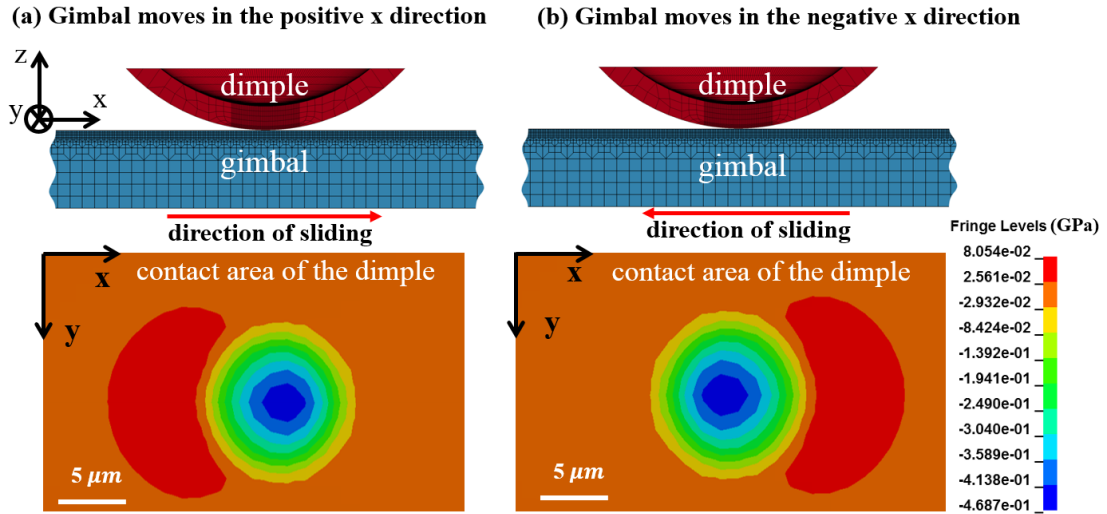
Figure 4.11 Distribution of the maximum principal stress near the contact area of a dimple if the gimbal is coated with 690 nm DLC and slides in (a) the positive x direction, and (b) the negative x direction.

trailing edge of the contact zone. If the sliding direction of the gimbal is reversed, the location of the largest maximum principal tensile stress changes to the leading edge of the contact zone. At this position, the maximum principal tensile stress varies for each pass between 0 and 80 MPa as the gimbal moves back and forth. Micro-cracks generated by this type of cyclic stresses are called "fretting fatigue cracks" [132].

Cracks due to fretting fatigue are likely to start at pre-existing material flaws such as inclusions and voids, or they are created as the result of dislocation movements [133]. Since the typical fatigue crack length on the dimples in our experiments is on the order of 10 to 20 μm, we refer to these cracks as "short fatigue cracks" [134]. In fracture mechanics, the stress intensity factor is commonly used to characterize the stress field ahead of a crack tip [135]. It was shown in [136] that a short fatigue crack can propagate even if the stress intensity factor at the tip of the crack is far below the threshold value of the stress intensity factor for long fatigue cracks. Although the propagation criteria

developed by Paris et al. [137] for long fatigue cracks may not strictly apply in our case, it is useful to calculate the range of cyclic stress $\Delta\sigma$ and then use this value in trying to explain the different crack patterns observed in the experiments, under the assumption that the propagation of short fatigue crack is proportional to $\Delta\sigma$ [138]. Since the smallest maximum principal tensile stress at the edge of the contact area of the dimple is zero during each cycle, the range of cyclic stress $\Delta\sigma$ at the edge of the contact area of the dimple is equal to the largest maximum principal tensile stress σ_{max}. We will use this value to interpret our simulation results.
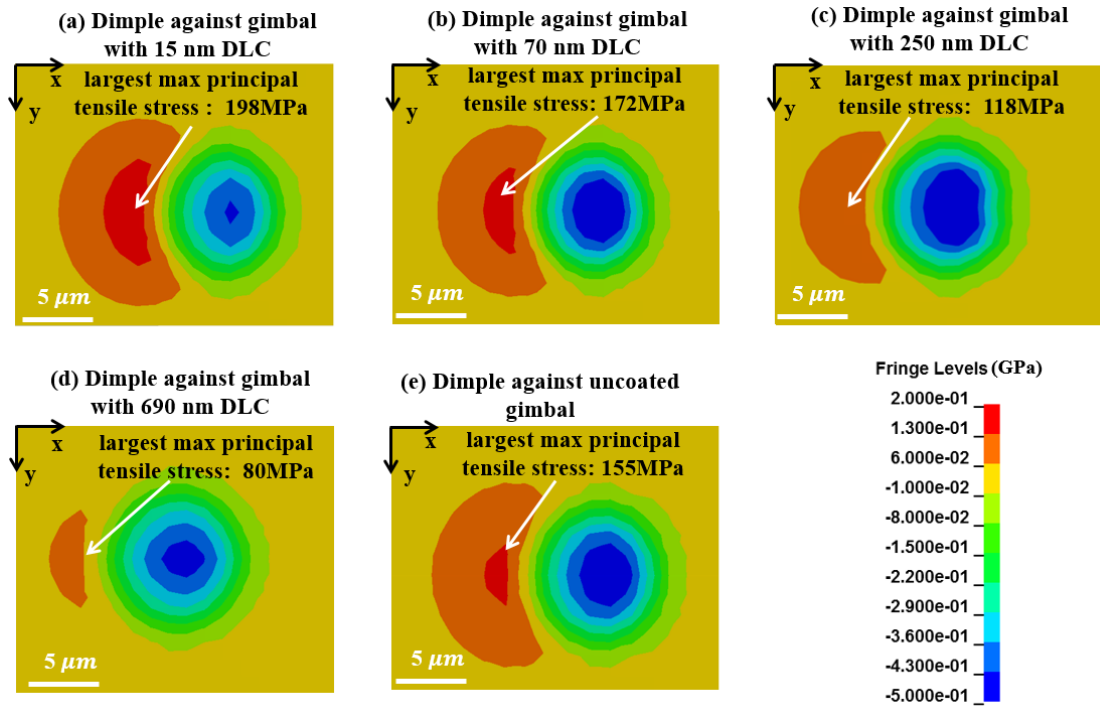
Figure 4.12 Distribution of the maximum principal stress near the contact area of a dimple contacting (a) a 15 nm DLC coated gimbal, (b) a 70 nm DLC coated gimbal, (c) a 250 nm DLC coated gimbal, (d) a 690 nm DLC coated gimbal, and (e) an uncoated gimbal for the case that the gimbal moves in the positive x direction.

Figure 4.12 shows the distribution of the maximum principal stress around the contact area of a dimple as the carbon coated gimbal moves in the positive *x* direction.

Simulation results are shown for a dimple contacting a gimbal with a DLC overcoat thickness of 15 nm (Figure 4.12 (a)), 70 nm (Figure 4.12 (b)), 250 nm (Figure 4.12 (c)), and 690 nm (Figure 4.12 (d)). In addition, the case without overcoat is shown in Figure 4.12 (e). For the dimple contacting an uncoated gimbal, the largest maximum principal tensile stress is 155 MPa (Figure 4.12 (e)). This value is close to the largest maximum principal tensile stress of 172 MPa for the case of 70 nm DLC overcoat (Figure 4.12 (b)). Cracks are observed in both contact areas (Figure 4.7 (b) and (e)). The dimple contacting a gimbal coated with 250 nm DLC shows the largest maximum principal tensile stress of 118 MPa (Figure 4.12 (c)), which is smaller than in the previous two cases. Therefore, crack formation should be less severe than in the other two cases. We observe from Figure 4.7 (c) that this is indeed the case, i.e., cracks are not as large as in the previous two cases (Figure 4.7 (b) and (e)). The largest maximum principal tensile stress of 80 MPa is observed for the case of 690 nm DLC (Figure 4.12 (d)). In this case, cracks are absent from the contact surface (Figure 4.7 (d)). For the dimple contacting a gimbal with 15 nm DLC, the largest maximum principal tensile stress is 198 MPa (Figure 4.12 (a)). This stress caused delamination as shown in Figure 4.7 (a). Comparing the SEM images in Figure 4.7 and the largest maximum principal tensile stress in Figure 4.12, we observe that cracks are larger for dimples with higher maximum principal tensile stress. This suggests that the maximum principal tensile stress is indeed a good indicator in explaining the wear results. The different amount of wear and the different length of cracks observed appear to be related to the different level of maximum principal tensile stress in the dimples. The effect of a different value of the maximum

principal tensile stress is magnified after a large number of fretting wear cycles, leading to a significant difference in the length of the cracks on the dimple.

Figure 4.12 shows furthermore that the largest maximum principal tensile stress occurs at the edge of the contact zone. This suggests that the micro-cracks observed in the fretting wear tests initiated at the edge of the contact zone. This has been observed in [139], [140]. As can be inferred from Figure 4.7 (b) and Figure 4.7 (c), several cracks can form and propagate in the region near the contact zone. During the propagation of these cracks, merging or "coalescing" of individual cracks may occur, which eventually leads to large scale delamination as shown in Figure 4.7 (a). The effect of merging of fatigue cracks was observed and discussed in an experimental study of fretting fatigue by Dubourg [141].

From the numerical results, one can also obtain the von Mises stress around the contact area of the dimple. As shown in Figure 4.13, the dimple contacting a gimbal coated with 15 nm DLC (Figure 4.13 (a)) shows the highest von Mises stress, and the dimple contacting a gimbal coated with 690 nm DLC (Figure 4.13 (d)) shows the lowest von Mises stress. Dimples in the other three cases (Figure 4.13 (b), (c), and (e)) show intermediate levels of the von Mises stress. This trend is in accordance with the trend observed for the values of the maximum principal tensile stress.
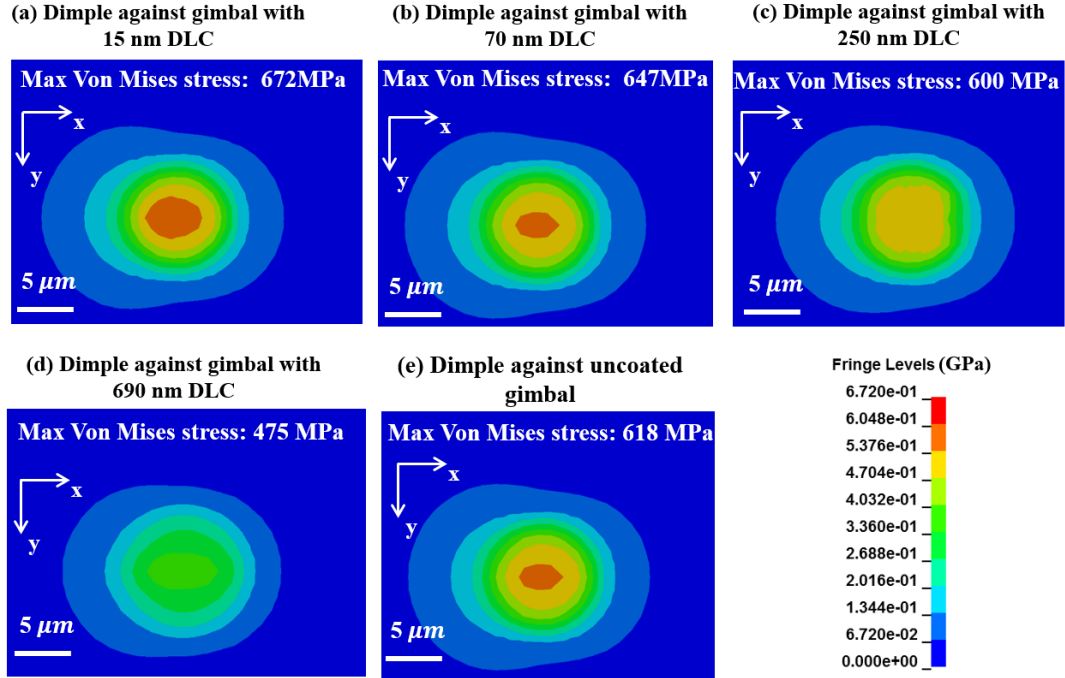
Figure 4.13 Distribution of the von Mises stress near the contact area of a dimple contacting (a) a 15 nm DLC coated gimbal, (b) a 70 nm DLC coated gimbal, (c) a 250 nm DLC coated gimbal, (d) a 690 nm DLC coated gimbal, and (e) an uncoated gimbal for the case that the gimbal moves in the positive x direction.

Figure 4.14 shows the von Mises stress around the contact area for the case that 690 nm DLC coated gimbal moves in the positive x direction (Figure 4.14 (a)) and the negative x direction (Figure 4.14 (b)). We observe that the location where the maximum von Mises stress occurs is at the center of the contact area for both cases. This location does not change with the direction of motion of the gimbal. In addition, we observe that the von Mises stress at the edge of the contact zone is independent of the direction of motion. Comparing the simulation results of the von Mises stress (Figure 4.14) with the maximum principal stress results (Figure 4.11), we find that the maximum principal stress is more suitable for studying crack formation in fretting wear because it changes with each cycle, causing fatigue cracks due to the alternating stress. For other wear

situations, however, it is conceivable that the von Mises stress may be an equally good or better wear predictor, especially for ductile materials undergoing plastic deformation [37], [142], [143].

(a) Gimbal moves in the positive x direction   **(b) Gimbal moves in the negative x direction**
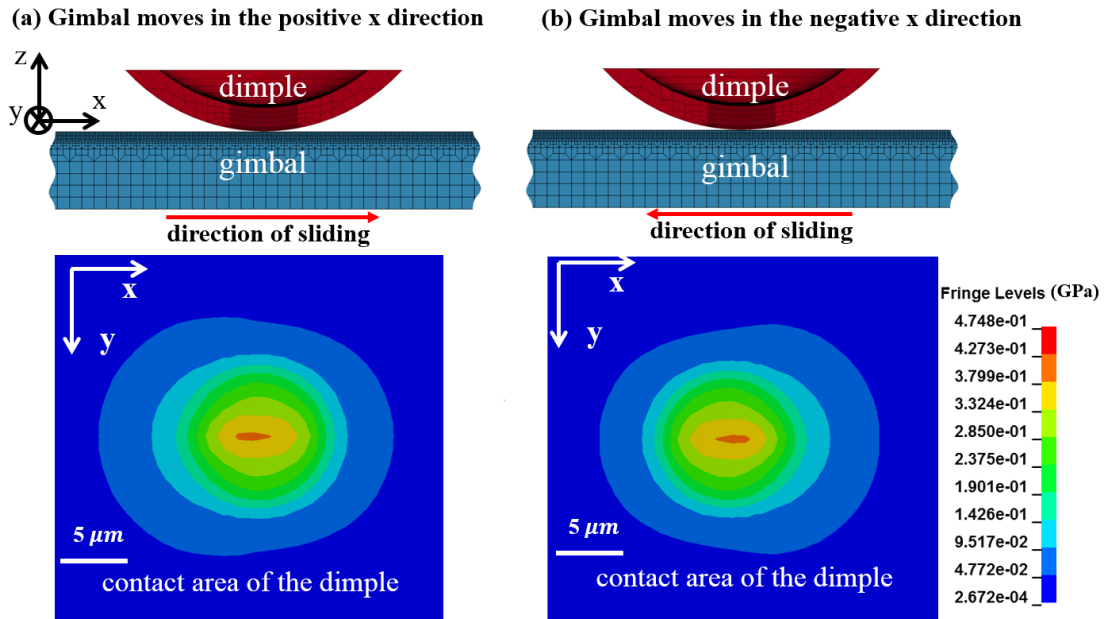
Figure 4.14 Distribution of the von Mises stress near the contact area of the dimple if the gimbal is coated with 690 nm DLC and slides in (a) the positive *x* direction, and (b) the negative *x* direction.

4.4.3 Stress Distribution in the Gimbal

Figure 4.15 shows the distribution of the maximum principal stress around the contact area of a gimbal coated with 690 nm DLC, sliding in the positive (Figure 4.15 (a)) and negative *x* direction (Figure 4.15 (b)). Similar to the dimple, the location where the largest maximum principal tensile stress occurs changes if the direction of motion of the gimbal reverses. Cyclic stresses are applied to the edge of the contact zone as the gimbal moves back and forth. Hence, micro-cracks generated at the gimbal surface could be categorized as "fretting fatigue cracks".
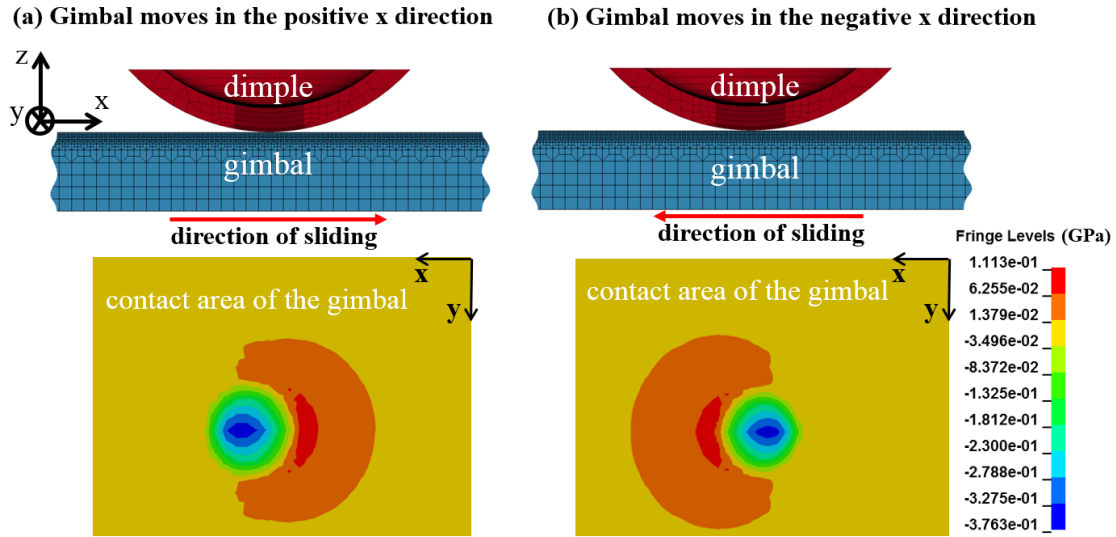
Figure 4.15 Distribution of the maximum principal stress near the contact area of the gimbal if the gimbal is coated with 690 nm DLC and slides in (a) the positive *x* direction, and in (b) the negative *x* direction.

Figure 4.16 shows numerical results for the maximum principal stress around the contact area of a gimbal with a carbon overcoat thickness of 0, 15 nm, 70 nm, 250 nm, and 690 nm, respectively, moving in the positive *x* direction. We observe that the uncoated gimbal has a maximum principal tensile stress of 178 MPa (Figure 4.16 (e)). A large amount of wear debris and large cracks were produced on the wear scar (Figure 4.8 (e)). The gimbal coated with 15 nm DLC shows the largest maximum principal tensile stress of 729 MPa (Figure 4.16 (a)). However, wear and crack formation on this wear scar (Figure 4.8 (a)) are less pronounced than on the uncoated gimbals (Figure 4.8 (e)). This is related to the higher hardness of the 15 nm DLC overcoat. The largest maximum principal tensile stress for gimbals coated with 70 nm (Figure 4.16 (b)) and 250 nm DLC (Figure 4.16 (c)) is 256 MPa and 278 MPa, respectively. These values are much smaller than the largest maximum principal tensile stress value for the gimbal coated with 15 nm DLC (Figure 4.16 (a)). However, a large amount of wear particles
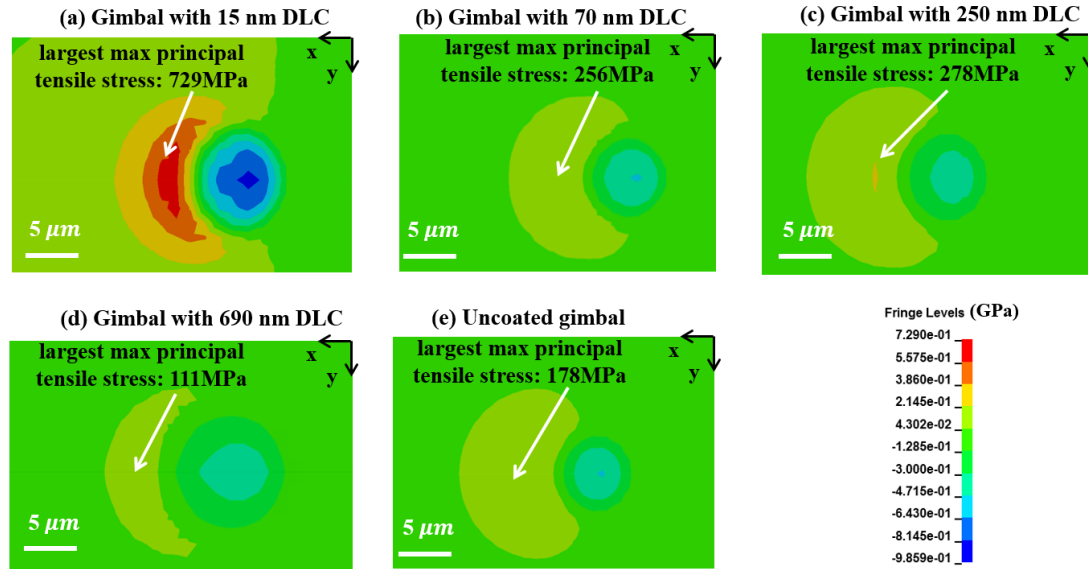
Figure 4.16 Distribution of the maximum principal stress near the contact area of (a) a 15 nm DLC coated gimbal, (b) a 70 nm DLC coated gimbal, (c) a 250 nm DLC coated gimbal, (d) a 690 nm DLC coated gimbal, and (e) an uncoated gimbal sliding in the positive *x* direction.

and long cracks were observed for these cases (Figure 4.8 (b) and (c)), most likely related to lower hardness of the DLC overcoat. For a gimbal coated with 690 nm DLC, surface damage was small (Figure 4.8 (d)). This case is characterized by a low value of the largest maximum principal tensile stress of 111 MPa (Figure 4.16 (d)). Comparing the simulation results (Figure 4.16) with the experimental results (Figure 4.8), one can conclude that high maximum principal tensile stress in the gimbal does not seem to cause an increase in the amount of wear or an increase in the length of cracks formed. For gimbals with DLC overcoat, the amount of wear and the size of cracks generated during a fretting wear test are likely affected by the hardness of the DLC.

4.4.4 Effect of the Elastic Modulus of Diamond-Like Carbon Overcoat

Since the experimental results show that wear and cracks are predominantly generated on the dimple, numerical simulations were performed to investigate the effect of the elastic modulus of the DLC overcoat on the maximum principal stress in the dimple as a function of the DLC overcoat thickness (70 nm and 690 nm). For this calculation, we assumed a constant coefficient of friction of 0.28 between the dimple and the gimbal in both cases. The elastic modulus of the DLC overcoat was taken to vary from 70 GPa to 400 GPa. In Figure 4.17, we plot the largest maximum principal tensile stress as a function of the elastic modulus of the DLC overcoat for a "thin" (70 nm) and a "thick" (690 nm) overcoat. The 690 nm DLC overcoat with a low elastic
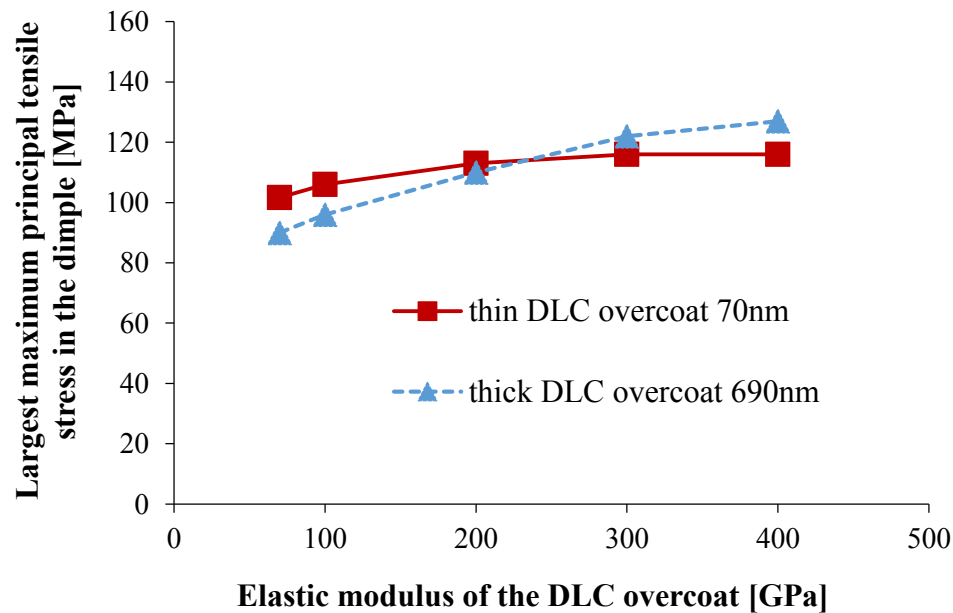
Figure 4.17 The largest maximum principal tensile stress in a dimple contacting a gimbal coated with 70 nm and 690 nm DLC of different elastic moduli, assuming the friction coefficient is constant.

modulus of 70 GPa shows the smallest maximum principal tensile stress. This is attributed to the low elastic modulus, and, therefore, the low effective elastic modulus of the gimbal, leading to a larger contact area and a lower contact stress than in the other cases with higher elastic modulus. In addition, the largest maximum principal tensile stress in the dimple increases as the elastic modulus of the DLC overcoat increases. This suggests that for both 70 nm and 690 nm DLC overcoats on the gimbal, an increase in the elastic modulus of the DLC overcoat leads to a larger contact stress, which may cause a larger amount of wear and longer cracks on the dimple during fretting wear. We also observe from Figure 4.17 that the increase of the largest maximum principal tensile stress in a dimple contacting a 690 nm DLC overcoat is greater than the increase of the largest maximum principal tensile stress in a dimple contacting a 70 nm DLC overcoat. This situation can be qualitatively explained by the Hertzian contact theory [92]. The maximum contact pressure p_0 for the contact between a sphere and a flat half-space is given by

$$p_0 = \frac{1}{\pi} \left(\frac{6NE_*^2}{R^2} \right)^{1/3} \tag{4.4}$$

Here, N is the applied normal force, R is the radius of the sphere, and E_* is the "combined-effective" elastic modulus of the dimple and the gimbal defined by

$$\frac{1}{E_*} = \frac{1 - v_1^2}{E_1} + \frac{1 - v_2^2}{E_2} \tag{4.5}$$

where E_1, E_2 are the elastic moduli, and v_1 and v_2 are the Poisson's ratios of the sphere and the half-space, respectively. We assume that v_1 and v_2 are both equal to 0.3. For

the contact between the dimple and the gimbal, E_1 is the elastic modulus of the dimple, and E_2 is the effective modulus of the gimbal coated with DLC. For both the 70 nm and the 690 nm DLC overcoats, the increased elastic modulus of the overcoat increases the effective modulus of the gimbal E_2 in Equation 4.6 and thus E_* in Equations 4.5 and 4.6. Since the DLC overcoat of 690 nm thickness has a greater influence on the effective elastic modulus of the gimbal than the thinner 70 nm DLC overcoat, E_2 and E_* of the gimbal coated with 690 nm DLC increase more as the elastic modulus of the DLC overcoat increases. Therefore, the contact pressure and the largest maximum principal tensile stress for a dimple contacting a 690 nm DLC overcoat increases more than for a dimple contacting a 70 nm DLC overcoat.

The results also show that the rate of increase in the largest maximum principal tensile stress in the dimple decreases as the elastic modulus of the DLC overcoat increases. As shown in Figure 4.17, the largest maximum principal tensile stress does not increase significantly for either the 70 nm or the 690 nm overcoat, if the elastic modulus of the DLC overcoat increases from 300 GPa to 400 GPa. This suggests that a further increase of the elastic modulus of the DLC overcoat does not lead to a larger amount of wear or longer cracks on the dimple.

4.4.5 Effect of the Thickness of Diamond-Like Carbon Overcoat

In Figure 4.18, we plot the largest maximum principal tensile stress as a function of the thickness of the DLC overcoat for a "compliant" (100 GPa) and a "stiff" (400
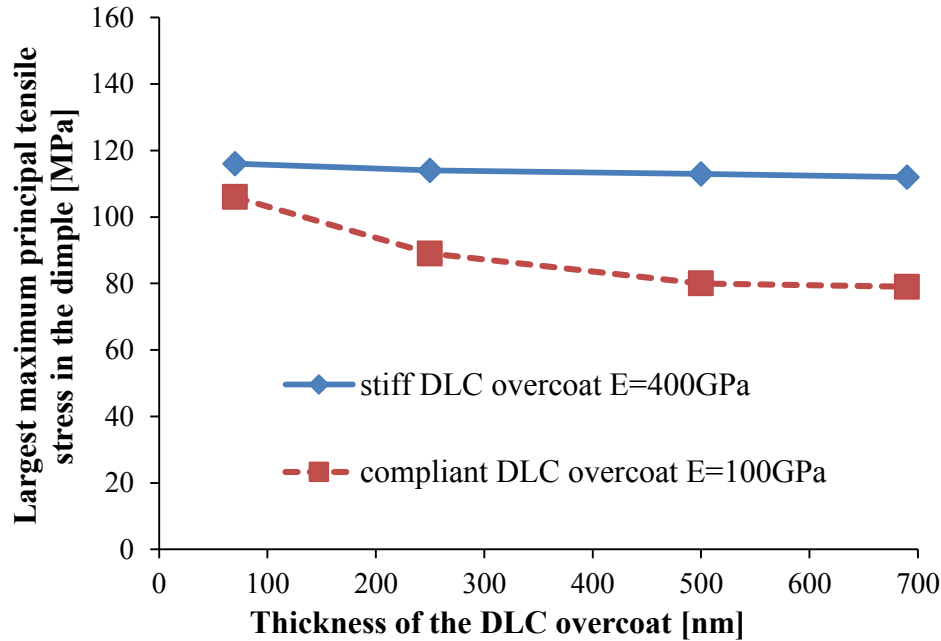
Figure 4.18 The largest maximum principal tensile stress in a dimple contacting a gimbal coated with stiff and compliant DLC overcoat of different thickness, assuming the friction coefficient is constant.

GPa) overcoat. For both cases, a constant coefficient of friction of 0.28 between the dimple and the gimbal was assumed. As seen from Figure 4.18, the largest maximum principal tensile stress in the dimple contacting the DLC overcoat with elastic modulus of 400 GPa is almost constant. This can be explained by Equations 4.5 and 4.6. For the dimple contacting a DLC overcoat with an elastic modulus of 400 GPa, the increase in the thickness of the stiff DLC overcoat increases the effective elastic modulus of the gimbal E_2 in Equation 4.6. However, the first term in Equation 4.6 with the smaller elastic modulus E_1 of the dimple material dominates Equation 4.6. Therefore, the influence of the thickness of the 400 GPa DLC overcoat on E_* in Equations 4.5 and 4.6 is small, and the maximum contact stress in Equation 4.5 does not change significantly.

For the gimbal coated with a DLC layer having an elastic modulus of 100 GPa, the effective elastic modulus of the gimbal E_2 decreases, although the thickness of the coating increases. This leads to a smaller E_* and a smaller contact pressure according to Equations 4.5 and 4.6. Consequently, the largest maximum principal tensile stress in the dimple decreases from 106 MPa to 80 MPa, while the thickness of the DLC overcoat increases from 70 nm to 690 nm. This suggests that less wear and shorter cracks occur if the thickness of the "compliant" DLC overcoat increases, assuming the friction coefficient is constant.

4.5 Conclusion

In this study, both experimental and numerical studies were performed to investigate the effect of a DLC overcoat on the tribological performance of the dimple/gimbal interface in hard disk drives. From the experimental results, we have found that: (1) Stainless steel dimples in contact with a 690 nm thick carbon coated gimbal show the lowest friction coefficient and the smallest amount of wear debris compared to dimples in contact with gimbals having thinner carbon overcoats (15 nm, 70 nm, and 250 nm). (2) For stainless steel dimples contacting gimbals coated with DLC, wear particles at the dimple/gimbal interface are generated mostly on the dimple. (3) DLC overcoats on the gimbal can improve the tribological performance of the gimbal, but may increase wear and cracks on the dimple.

From the simulation results, we observe that: (1) The maximum principal tensile stress is a good measure for analyzing fretting wear results. The amount of wear and the size of cracks observed experimentally are related to the maximum principal tensile

stress in the dimple. (2) The dimple contacting a gimbal coated with a "stiff" DLC overcoat exhibits large maximum principal tensile stress, which leads to the generation of wear particles and large cracks on the dimple. (3) "Stiff" DLC overcoats cause large maximum principal tensile stress in the gimbal, but do not lead to an increase in wear and the size of cracks on the gimbal because of the high hardness of the DLC overcoats. (4) With respect to the effect of thickness of the DLC overcoat, if the DLC overcoat is "stiffer" than the substrate, the thickness of the DLC overcoat does not have a significant influence on the level of stress in the dimple. On the other hand, if the DLC overcoat is more "compliant" than the substrate, an increase in the thickness of the DLC overcoat reduces the level of stress in the dimple.

To achieve the best tribological performance of the dimple/gimbal interface, the elastic modulus and the thickness of the carbon overcoat on the gimbal need to be optimized simultaneously. Based on the experimental and simulation results of this study, we conclude that a "compliant" and "thick" carbon overcoat on the gimbal is best for the tribological performance of the dimple/gimbal interface. A "compliant" and "thick" carbon overcoat causes low contact stress at the dimple/gimbal interface and can significantly reduce the generation of wear particles and the formation of cracks on both the dimple and the gimbal. To deposit a thick DLC overcoat with good tribological properties on the gimbal, it is crucial that the DLC layer has a uniform thickness and a uniform sp^3 bonding ratio. In addition, it is desirable that low residual stress is present in the DLC layer in order to prevent delamination [144].

The normal load between the sphere and the coated half-space in our study was kept constant at 20 mN and the material deformation in our simulation was in the elastic

range. In other industrial applications, the normal load can be much higher. This may lead to elastic-plastic deformation of the coating and the substrate [145]. The coating thickness investigated in our study was in the range from 15 nm to 690 nm and the elastic modulus of the substrate was kept constant at 200 GPa. In other contact problems, the coating can be much thicker and the elastic modulus of the substrate can vary in the range of several hundred GPa. The different range of the coating thickness and the elastic modulus of the substrate lead to different substrate effects on the contact stresses. Therefore, it is difficult to predict *a priori* what will happen for different values of load, thickness and elastic modulus of the overcoat. To find the optimized elastic modulus and overcoat thickness for other cases, finite element calculations may need to be performed for each particular situation.

4.6 Acknowledgement

Chapter 5

Lubricant Migration on the Air Bearing Surface of the Slider

5.1 Introduction

A thin layer of lubricant on the order of 1 to 2 nm in thickness is applied to the surface of a hard disk to protect the head/disk interface from wear during slider/disk contacts. At very close slider disk spacing, lubricant transfer from the disk to the slider occurs [146], [147], changing the flying characteristic of the head disk interface. During flying, lubricant transferred from the disk to the slider can accumulate in the cavities of the air bearing surface and at the trailing edge of the slider. If a slider is "parked" on the ramp, after lubricant has been picked up from the disk surface, redistribution of the accumulated lubricant is likely to occur since during parking the shear forces responsible for lubricant pick-up are absent. Depending on the length of parking of the slider, accumulated lubricant is likely to migrate over the air bearing surface resulting in the formation of a thin lubricant layer on the slider. If a slider with an adhering lubricant film on the air bearing surface is flown on the disk after parking, a change in head medium spacing (ΔHMS) will be observed due to the presence of the adhering lubricant film. In this chapter, we describe the formation and removal of a lubricant film on an air bearing surface as "lubricant migration".

To investigate lubricant migration on a slider, Marchon et al. [148] investigated the effect of a thin lubricant layer on the recording performance of a magnetic head using a spin stand. In their study, Marchon et al. observed that lubricant migration during parking of the slider degrades the read/write performance of a magnetic head in subsequent read/write operations. They proposed that the degradation of the read/write performance was caused by the increase in spacing due to the formation of a thin lubricant film on the air bearing surface. In a later study, Mate et al. [149] applied a lubricant droplet on the slider surface prior to flying the slider on the disk, and studied the change in head medium spacing due to the formation of a thin lubricant film on the slider.

In this chapter, drive-level lubricant migration tests were carried out to study the effects of "parking time", temperature, and slider position on lubricant migration in a hard disk drive. The change in head medium spacing (HMS) after parking the slider on the load/unload ramp was determined from read-back signal measurements using the Wallace equation [150]. Time-of-flight secondary ion mass spectrometry was used to correlate the change in head medium spacing with the amount of lubricant migrated to the air bearing surface during parking. The change in head medium spacing as a function of parking time, temperature and slider position is determined.

5.2 Experimental Procedure

Figure 5.1 shows a schematic of the experimental procedure used for lubricant migration test and the schematic of lubricant motion on the air bearing surface during test. As shown in Figure 5.1 (a), the slider was first loaded onto the disk and swept back
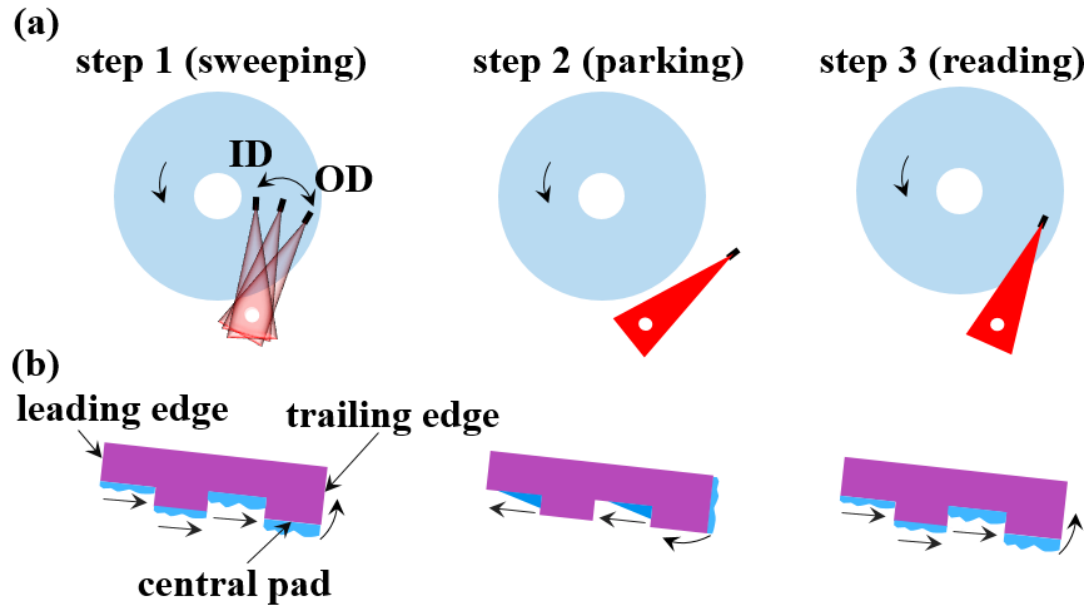
Figure 5.1 (a) Experimental procedure for measuring the change in head medium separation (b) schematic of lubricant motion on the air bearing surface during operation and parking of the slider

and forth between inner diameter (ID) and outer diameter (OD) for 30 minutes (step 1).

During "sweeping" of the slider in step 1, the flying height is on the order of 11 to 12

nm with the thermal flying height control heater off. Then, the slider was unloaded from

the disk and "parked" on the ramp for a period of time (step 2). Thereafter, the slider

was re-loaded onto the disk, and read-back measurements were performed as a function

of time (step 3). In this step, the flying height is around 2 nm with the thermal flying

height control heater on. The read-back signal was analyzed to determine the change in

head medium spacing according to the Wallace equation [150]. As shown in Figure 5.1

(b), during sweeping of the slider (step 1), lubricant is picked up and moved to the

trailing edge and the cavities of the air bearing surface by shear forces between slider

and disk. During parking (step 2), lubricant migrates from the trailing edge and the

cavities to the air bearing surface of the slider due to diffusion [148]. If the lubricant

film on the slider adheres strongly to the air bearing surface, an increases in head medium spacing occurs as the slider is flown again on the disk (step 3). Over time, the thin lubricant film on the air bearing surface is reduced in thickness due to shear forces in the air bearing. As a consequence, the flying height of the slider is reduced and the slider eventually reaches its steady state flying height again.

A typical experimental result for the change in head medium spacing for step 3, i.e., for flying after parking, is shown in Figure 5.2. This result is normalized by the maximum change in head medium separation at the end of the measurement. The flying height of the slider in the presence of an adhering lubricant film is defined as the reference head medium spacing at t=0. The flying height of the slider decreases as a function of time due to the removal of the lubricant film. The experimental data can be approximated by
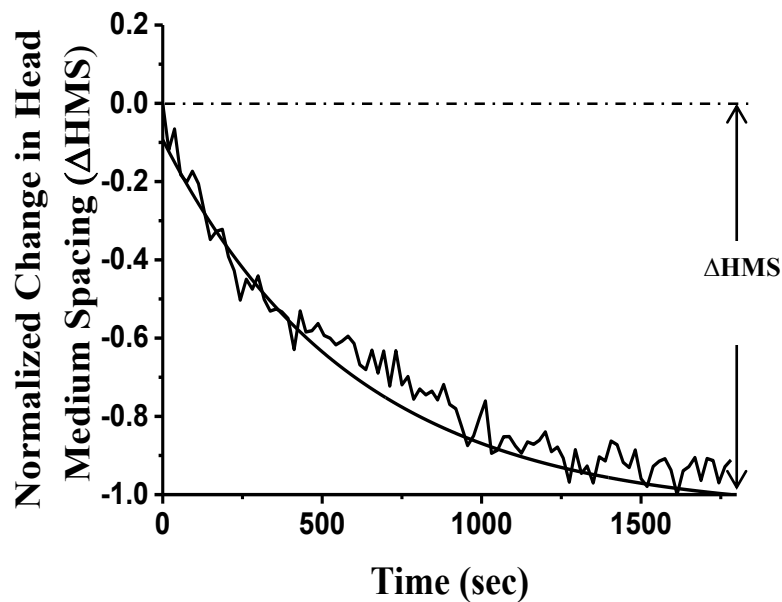
Figure 5.2 Typical change in head medium spacing as a function of time

$$\Delta HMS = ae^{-bt} + c \qquad\qquad (5.1)$$

where b is the time constant characterizing the lubricant removal rate from the air bearing surface. The change observed in the head medium spacing due to lubricant migration is less than 1 nm, which is on the same order as that reported by Marchon [148] and Mate [149]. In our study, the time for the slider to reach steady state head medium spacing after parking was about 10 to 30 minutes depending on the experiment conditions. This time is on the same order of magnitude as the time reported by Marchon [148] (25 minutes) and Mate [149] (10 minutes). Since Marchon and Mate et al. [148], [149] used different air bearing contours and different lubricants in their experiments, some differences between their results and the present study are to be expected.

To investigate the effect of parking time, temperature and slider position on lubricant migration, three groups of experiments were performed. Each group of experiments was repeated using three drives with eight heads each. All drives were manufactured in the same way using the same air bearing surface design and the same media type and perfluoropolyether (PFPE) lubricant. All drives were evaluated at 7200 rpm rotational speed. In each test, the average change of the head medium spacing for 24 heads is shown. Parking time is defined as the length of time a slider is parked on the ramp in step 2 of the test. Slider position indicates the radial position of the slider on the disk at which the change in head medium spacing is measured in step 3 of the test. The effect of temperature is measured by conducting the parking and read-back tests in a temperature controlled environment.

Time-of-flight secondary ion mass spectrometry (ToF-SIMS) was used to characterize the amount of lubricant on the air bearing surface of the slider after

lubricant migration. Samples were analyzed on a commercially available ToF-SIMS instrument (Trift 5 nanoToF, Physical Electronics) with a Bi_1^+ primary ion in "bunched mode" with a pulse width of 2 ns. The raster size was 640 μm. Each measurement was performed for 5 minutes so that each sample received the same primary ion dose.

5.3 Experimental Results

5.3.1 Correlation between Change in Head Medium Spacing and Lubricant Migration

The change in head medium spacing is an indication of the thickness change of the lubricant layer on the air bearing surface due to lubricant migration. ToF-SIMS measurements were used to evaluate the amount of lubricant on the air bearing surface as a function of the change in head medium spacing. Figure 5.3 (a), (b), and (c) show secondary ion images of lubricant fragments CF^+ and $C_2F_5^+$ present on the air bearing surface for three sliders exhibiting different values of head medium spacing change after lubricant migration. We observe that the largest amount of lubricant is present on the air bearing surface with the largest spacing change of 1.23 nm (Head 3). The smallest amount of lubricant is observed on the slider with the smallest spacing change of 0.46 nm (Head 1). For comparison, Figure 5.3 (d) shows a scanning electron microscope (SEM) image of the air bearing surface for the type of sliders used in this study. The field of view of the SEM image is the same as the raster size of the ToF-SIMS image.

(a) Trailing edge	(b) Trailing edge	(c) Trailing edge	(d) Trailing edge
Head 1 $\Delta HMS=0.5$ nm	Head 2 $\Delta HMS=0.8$ nm	Head 3 $\Delta HMS=1.2$ nm	Air Bearing Surface
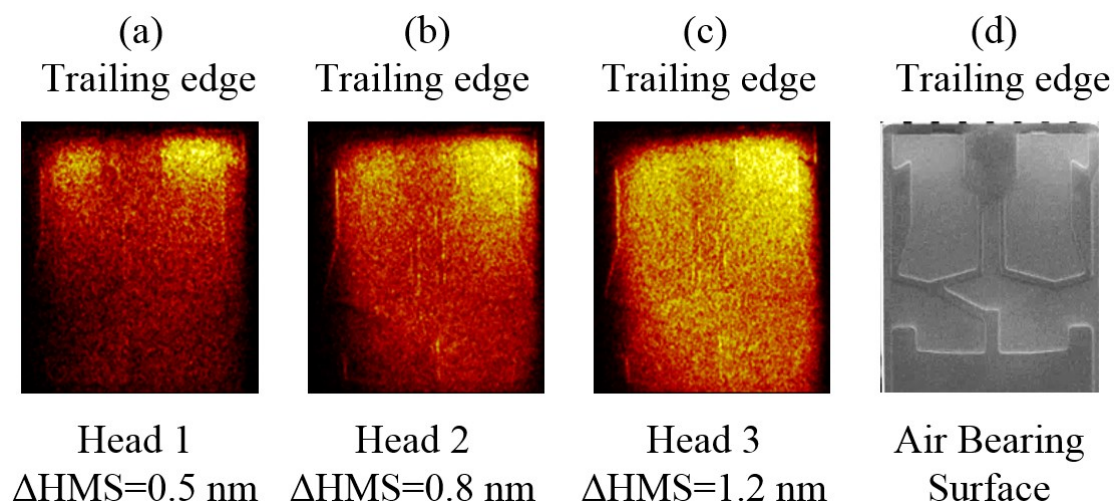
Figure 5.3 (a) (b) (c): ToF-SIMS images of lubricant fragments CF^+ and $C_2F_5^+$ on the air bearing surface of three sliders with different changes in head medium spacing after lubricant migration (d): SEM image of a clean air bearing surface.

The signal intensity of Al^+ represents the slider background since the slider material consists of alumina-titanium carbide. CF^+ and $C_2F_5^+$ are high-intensity secondary ions emitted from the fluorinated lubricant. The signal intensity ratio of $(CF^++C_2F_5^+)/Al^+$ can be used to characterize the amount of lubricant on the slider normalized by the background signal. As shown in Figure 5.4, the signal intensity ratio of $(CF^++C_2F_5^+)/Al^+$ correlates directly with the measured change in head medium spacing of the slider. Thus, it is apparent that the change in head medium spacing can be used to quantify the amount of lubricant migration.
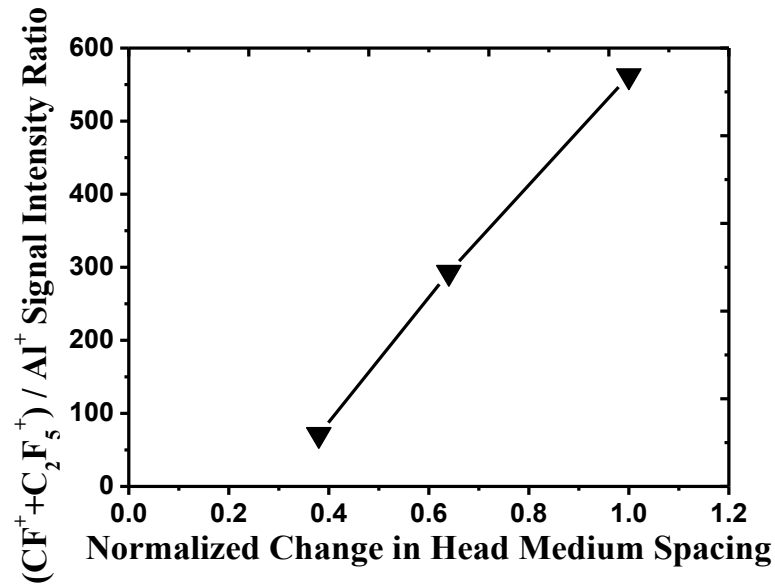
Figure 5.4 $(CF^++C_2F_5^+)/Al^+$ signal intensity ratio as a function of the change in head medium spacing

5.3.2 Effect of Parking Time

Head medium spacing measurements were performed as a function of parking time at the outer diameter of the disk at an ambient temperature of 25 °C. Figure 5.5 shows the change in head medium spacing and the lubricant removal rate as a function of parking time of the slider on the ramp. The change in head medium spacing is normalized by the maximum value of spacing change observed after a parking time of 5 hours. The removal rate is normalized by the maximum removal rate observed after a parking time of 10 minutes. We observe that the change in head medium spacing increases with an increase in parking time. This indicates that an increase in parking time allows more lubricant to migrate to the air bearing surface, causing an increase in the thickness of the lubricant layer on the slider during parking on the ramp. Clearly, a

larger change in head medium spacing occurs if the parking time is increased before the slider is re-loaded onto the disk.
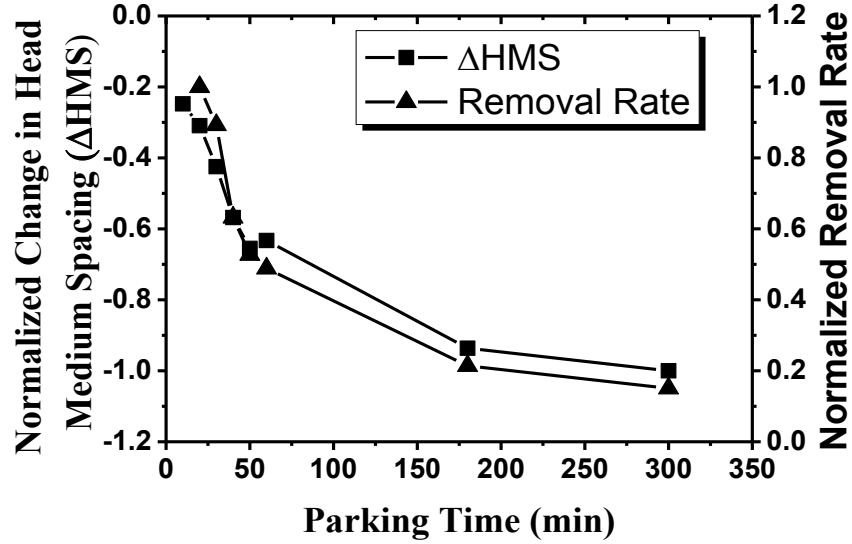
Figure 5.5 Change in head medium spacing (ΔHMS) and lubricant removal rate as a function of parking time

From Figure 5.5, we also observe that the slope of the change in the head medium spacing curve decreases from an initially high value to a low value with an increase in parking time to 5 hours. This phenomenon can be explained by considering the change of the gradient of lubricant thickness. Diffusive flow q from the trailing edge and the cavities to the air bearing surface is driven by the gradient of lubricant thickness h, i.e.,

$$q = -D \frac{\partial h}{\partial x} \tag{5.2}$$

where q is the diffusive flow, D is the diffusion coefficient, and $\frac{\partial h}{\partial x}$ is the gradient of the lubricant thickness. At the beginning of parking, the thickness gradient of lubricant at the trailing edge and in the cavities is high. Since lubricant migrates to the air bearing

surface of the slider during parking, the gradient of lubricant thickness gets smaller. Therefore, the rate of lubricant migration to the air bearing surface decreases.

Since a larger amount of lubricant migrates to the air bearing surface with an increase in parking time, it should take a longer time for lubricant to be moved to the trailing edge and the cavities in step 3. Therefore, the lubricant removal rate decreases with an increase in parking time as shown in Figure 5.5.

5.3.3 Effect of Temperature

Figure 5.6 shows the normalized change in head medium spacing and the lubricant removal rate after parking the slider for 5 hours at temperature of 0 °C, 10 °C, 25 °C, 50 °C, 60 °C, and 75 °C, respectively. The measurements were performed with the slider flying on the outer diameter of the disk. The change in head medium spacing at different temperatures is normalized by the maximum spacing change observed at 50 °C. The removal rate is normalized by the maximum removal rate observed at 75 °C.
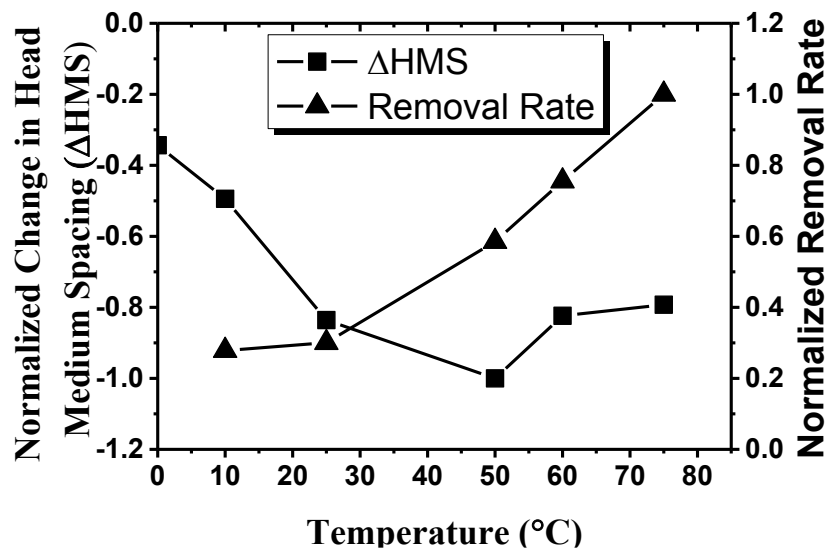
Figure 5.6 Change in head medium spacing (ΔHMS) and lubricant removal rate as a function of temperature

We observe that the change in head medium spacing increases initially with temperature, reaching a maximum at about 50 °C. For temperatures above 50 °C, the change in head medium spacing is smaller than that at 50 °C. From Figure 5.6 we also observe that the normalized lubricant removal rate increases monotonically with temperature.

For temperature from 0 °C to 50 °C, the observed behavior can be related to the change of lubricant diffusivity given by

$$D = \frac{kT}{6\pi r\eta} \tag{5.3}$$

where D is the diffusion coefficient, T is temperature, η is viscosity, r is the radius of lubricant molecule and k is the Boltzmann's constant. The viscosity of the PFPE lubricant decreases with an increase in temperature [151]. Therefore, if the temperature increases from 0 °C to 50 °C, the effect of increased temperature and decreased viscosity increases the diffusion coefficient of the lubricant. This causes a larger amount of lubricant in the cavities and at the trailing edge of the slider to migrate to the air bearing surface to form a thicker lubricant layer on the air bearing surface during parking of the slider. When the slider is re-loaded onto the disk, a larger change in head medium spacing is observed.

For temperatures above 50 °C, the change in head medium spacing smaller than at 50 °C could be explained by a change in lubricant bonding ratio with temperature. Zhao [152]and Kawaguchi [153] reported that at high temperature the bonding ratio of lubricant on diamond-like carbon surfaces increases. As a result, more lubricant is bonded to both the carbon-coated disk and the carbon-coated slider at 60 °C and 70 °C in comparison to 50 °C. Therefore, less lubricant is transferred from the disk to the slider.

Furthermore, because of the higher bonding ratio of the lubricant at higher temperature, less lubricant is moved along the air bearing surface by shear forces.

5.3.4 Effect of Slider Position

To study the lubricant migration as a function of the position of the slider on the disk, we have measured the change in head medium spacing at the outer diameter (OD), the middle diameter (MD), and the inner diameter (ID) of the disk, respectively. The measurements were performed at ambient temperature of 25 °C after parking the slider for 5 hours. Figure 5.7 shows the change in head medium spacing and the lubricant removal rate as a function of the slider position on the disk. The change in head medium spacing is normalized by the spacing change of the slider flies at the OD. The lubricant removal rate is normalized by the removal rate of the slider at the ID. We observe that the change in head medium spacing is not affected by the radial position of the slider on the disk. However, the lubricant removal rate is seen to be a strong function of the radial
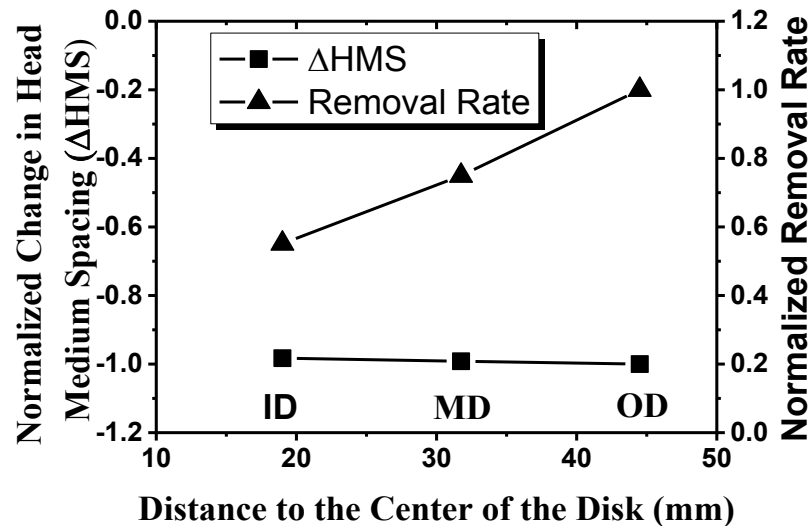
Figure 5.7 Change in head medium spacing (ΔHMS) and lubricant removal rate as a function of radial position of the slider on the disk

position of the slider on the disk, increasing with an increase in radius. Since the angular velocity of the disk is constant, the linear velocity at the outer diameter is higher than at the inner diameter. Shear forces applied to the lubricant are a function of velocity between slider and disk for a constant flying height. Therefore, when the slider flies at the outer disk position, shear forces applied to the lubricant are higher than those at the inner diameter, resulting in accelerated lubricant motion from the air bearing surface to the trailing edge and the cavities of the slider.

5.4 Conclusion

From this study, the following conclusions can be made: (1) The signal intensity ratio of $(CF^++C_2F_5^+)$ to Al^+ obtained from ToF-SIMS can be used to quantify the amount of lubricant migration. (2) An increase in parking time was found to cause an increase in lubricant migration and a decrease in the removal rate. (3) Temperature was found to affect the amount of lubricant migration and the lubricant removal rate. The largest change in head medium spacing occurred at a temperature of 50 °C. (4) The lubricant removal rate changes with the position of the slider on the disk. The change in head medium spacing is not a function of the position of the slider on the disk.

5.5 Acknowledgement

on Magnetics, vol. 50, no. 11. pp. 1–4, 2014. The dissertation author was the primary investigator and author of this paper.

Chapter 6

Thermal Response of a Thermal Asperity Sensor to Disk Asperities

6.1 Introduction

Disk asperities which make contact with a flying magnetic head in hard disk drives are generally called "thermal asperities" [154]–[157]. Contact between a disk asperity and a magnetic head can cause elastic-plastic deformation and high temperatures at the head/disk interface [70], [158]–[160]. To prevent failure of the head/disk interface, it is necessary to detect the location of thermal asperities on a magnetic disk and avoid interactions between thermal asperities and the read and write elements. In recent years, thermal asperity sensors have been developed in hard disk drives to detect thermal asperities on the disk surface [161]. During contact between disk asperities and the sensor, heat transfer occurs, changing the temperature and, consequently, the resistance, of the sensor. Thus, a change in the output signal of the sensor indicates that contact between the magnetic head and the thermal asperity has occurred.

Many studies have been performed in the past to investigate the response of a thermal sensor to thermal asperities. Shimizu et al. [162] conducted an experiment and showed that a thermal sensor embedded in a slider can detect nano-scale disk defects if

the flying height is less than 2 nm. Li et al. [163] performed numerical investigations and found that a typical sensor has maximum resistance change if the width of the sensor is about 1 μm. Lee et al. [164] conducted a parametric study to investigate the effect of asperity dimensions and contact conditions on flash temperature at the contact interface. Mate et al. [165] investigated the temperature change of a typical thermal sensor during contact with disk asperities. They found that an increase in contact interference increases the sensor temperature initially, followed by a decreases due to "contact cooling". In addition, Zhang et al. [166], [167] studied the thermal response of a thermal sensor during contact with asperities of different material properties and different contact conditions.

In this chapter, a finite element model, similar to that of Zhang [167], is used to calculate the temperature and resistance change of a thermal asperity sensor during contact with a disk asperity. In particular, we focus on understanding the effects of bias voltage, friction coefficient, contact interference, disk velocity, and asperity material properties on the response of the sensor.

6.2 Finite Element Model

In Figure 6.1, a schematic of the 3-D finite element model used in this study is shown, consisting of the disk, the slider, the thermal asperity, and the thermal sensor. Figure 6.1 (a) shows the head/disk interface, and Figure 6.1 (b) shows a blow-up of the thermal sensor and the thermal asperity. The thermal sensor, with dimensions of 0.5 μm×0.06 μm×0.16 μm, is embedded in the trailing edge region of the slider. A thermal asperity with a diameter of 0.36 μm and a height of 10 nm is assumed to be present on
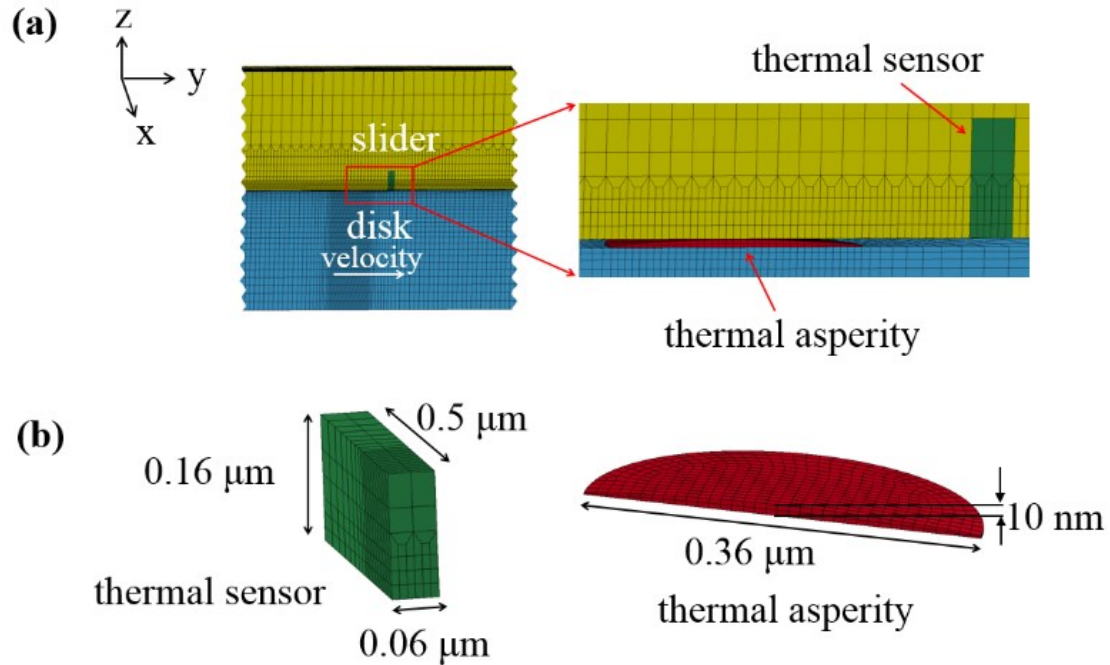
Figure 6.1 (a) Finite element model for simulating contact between a thermal sensor and a thermal asperity; (b) Dimensions of the thermal sensor and the thermal asperity used in the model.

the disk. The thermal asperity moves with the disk in the y-direction with a linear velocity v. The maximum contact interference δ between the asperity and the disk is chosen to be 8 nm, representing the flying height at the thermal sensor location of 2 nm. The model is symmetric with respect to the y-z plane. Thus, only one half of the slider and disk is considered. Nodes on the plane of symmetry are constrained from moving in the x-direction. Nodes on the top surface of the slider are fixed in all six degrees of freedom. Nodes at the bottom surface of the disk can translate only in the y-direction. The material properties of the slider, the disk, the thermal asperity sensor, and the thermal asperity are assumed to be elastic-plastic with 2% strain hardening [158]. A summary of the properties is given in Table 6.1. Alumina asperities originating from the polishing slurry have an elastic modulus of 400 GPa. The alumina region on the slider

is sputtered alumina with an elastic modulus of 120 GPa. To simplify the model, "air cooling", material removal, and adhesive forces were not included in the simulation. The finite element model was solved using the explicit solver of the commercially available finite element analysis software LS-DYNA [130].

Table 6.1 Material properties

Title	Thermal sensor (NiFe)	Asperity $(Al_2O_3^{\#1})$	Disk (NiP)	Slider $(Al_2O_3^{\#2})$
Young's modulus [GPa]	205	400	114	120
Yield strength [MPa]	170	640	300	300
Poisson ratio	0.22	0.23	0.31	0.25
Thermal expansion coefficient $[10^{-6}m \cdot K^{-1}]$	12	5.5	13.3	7.1
Specific heat $[J \cdot kg^{-1} \cdot K^{-1}]$	440	780	440	780
Thermal conductivity $[W \cdot m^{-1} \cdot K^{-1}]$	35	1	4.4	1

6.3 Simulation Results

6.3.1 Effect of Bias Voltage of Thermal Sensor

To detect thermal asperities, the bias voltage applied to the sensor is kept constant, and the current through the sensor is measured to determine the resistance change of the sensor due to the temperature change. In the finite element calculation, the temperature change of the sensor is obtained rather than the resistance change. In order to compare experimental results for the resistance change of the sensor with our

simulation results, it is necessary to convert the predicted temperature change of the sensor to resistance values.

For the finite element model under investigation, the initial temperature of the disk and the thermal asperity was chosen to be 300 K and the operational temperature of the sensor was assumed to be in the range from 400 K to 550 K corresponding to the bias voltage that the thermal sensor can sustain without breakdown (250 mV to 500 mV). The operational temperature is defined as the initial temperature of the sensor before asperity contact occurs. The initial temperature of the sensor is assumed to be uniform. From a coupled electrical and thermal finite element analysis, we determined that the steady state average sensor temperature T [K] increases linearly with the bias voltage U [mV] applied to the sensor according to

$$T = a_1 U + a_2 \qquad (6.1)$$

where the average temperature of the sensor T is defined as the average of the temperature at all nodes of the sensor. The coefficient a_1 is 0.678 K/mV and the coefficient a_2 is 229 K. According to Equation 6.1, the operational temperatures of 400 K, 450 K, 500 K and 550 K correspond to a bias voltage of 252 mV, 326 mV, 400 mV, and 473 mV, respectively.

To obtain the relationship between the resistance and the temperature of the sensor, we used a multimeter to measure the resistance of three NiFe sensors as a function of temperature in a temperature chamber prior to the finite element simulation. During this measurement, no bias voltage was applied to the sensor. The measurement results are shown in Figure 6.2. Using curve fitting, we determined that the resistance of the sensor R [Ω] is proportional to the average temperature of the sensor T [K], i.e.,

$$R = b_1T + b_2 \qquad (6.2)$$

where the coefficients b_1 and b_2 are 0.177 Ω/K and 22 Ω, respectively.
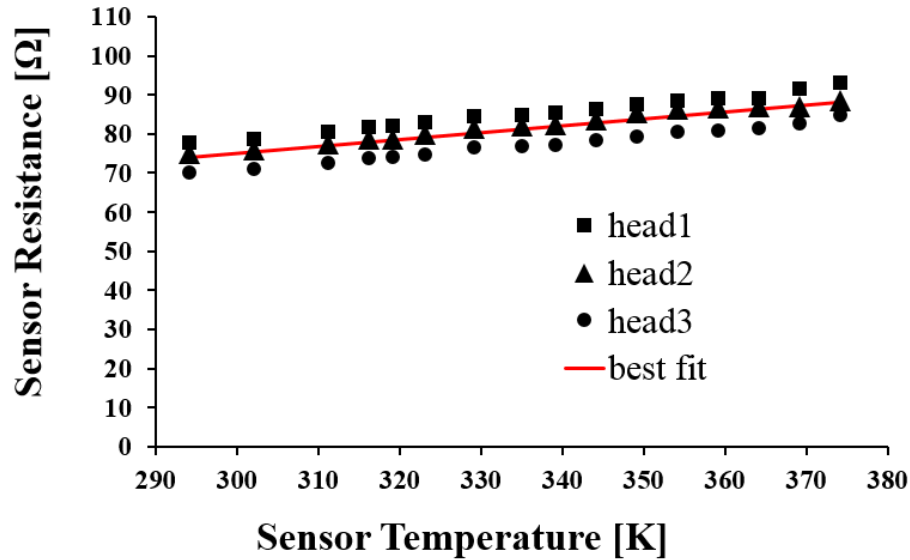
Figure 6.2 Resistance of the thermal asperity sensor as a function of the sensor temperature

Figure 6.3 shows simulation results for the temperature and the resistance of the thermal asperity sensor under investigation as a function of time during contact with an Al_2O_3 thermal asperity for bias voltages of 252 mV, 326 mV, 400 mV, and 473 mV, respectively. The friction coefficient is assumed to be 0.2. The first column in Figure 6.3 shows the temperature change of the sensor obtained from the simulation and the second column shows the resistance change of the sensor converted from the temperature results according to Equation 6.2. Since the temperature and resistance of the sensor have a linear relationship, the shape of the temperature curve and the resistance curve is the same. In the following sections of this chapter, we will only use the resistance results to discuss the response of the sensor to disk asperities. As can be seen from Figure 6.3 (a), the resistance of the sensor increases quickly from its steady
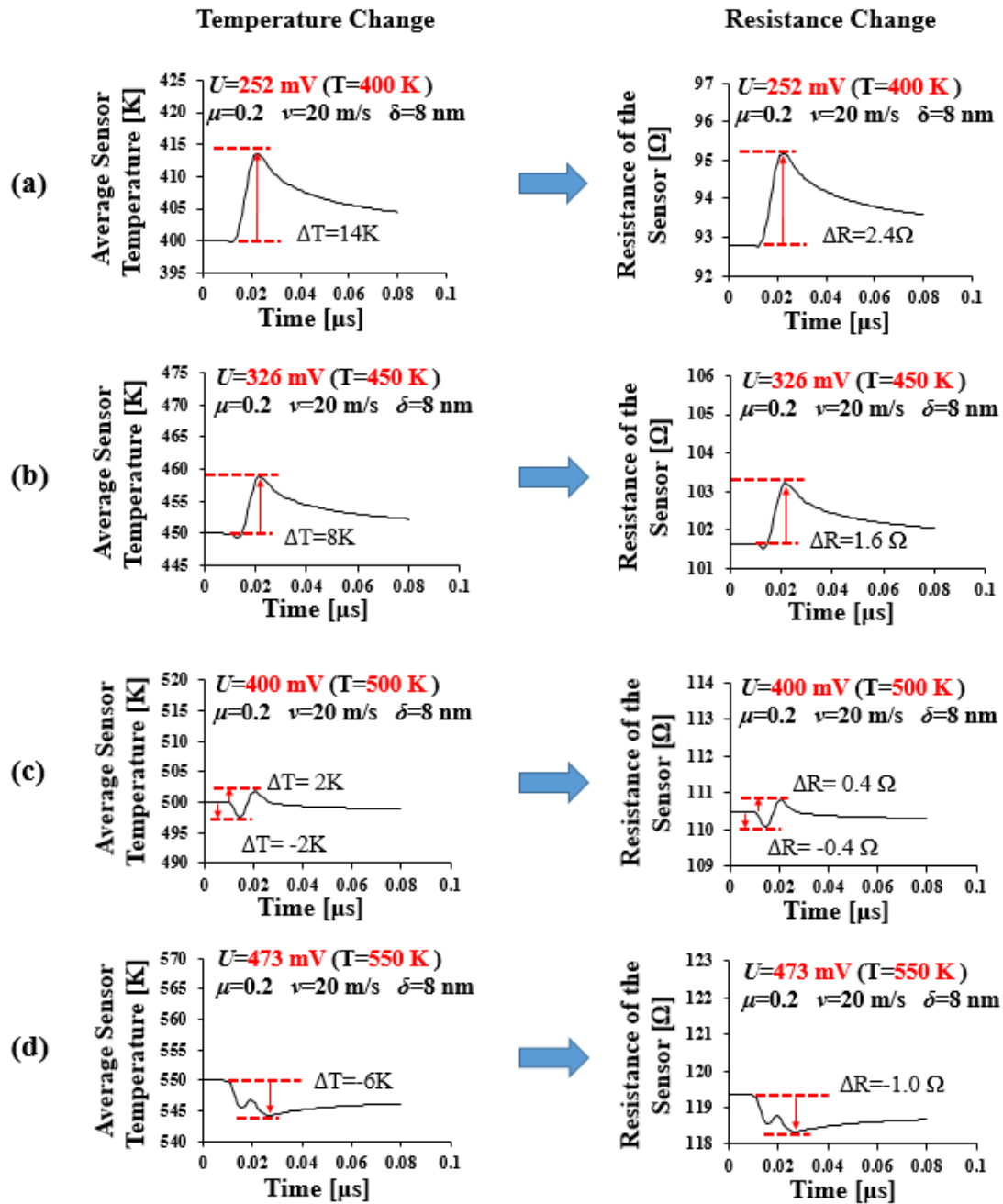
Figure 6.3 Average sensor temperature and resistance of a thermal asperity sensor at a bias voltage of (a) 252 mV (b) 326 mV (c) 400 mV, and (d) 473 mV during contact with an Al_2O_3 thermal asperity.

state value of 92.8 Ω to a maximum value of 95.2 Ω as the asperity makes contact with the sensor, and decays slowly after the asperity has passed the sensor. This variation is typical for thermal processes, i.e., heating occurs at a very short time scale and cooling at a much longer time scale. If the bias voltage U is increased to 326 mV, we observe that the maximum resistance increase of the sensor due to contact with the asperity is only 1.6 Ω (Figure 6.3 (b)). If the bias voltage of the sensor is further increased, say, to 400 mV (Figure 6.3 (c)), we observe that the resistance of the sensor decreases initially by approximately 0.4 Ω, then increases by 0.4 Ω, and finally reaches a steady state value. Increasing the bias voltage of the sensor even further to 473 mV, we observe from Figure 6.3 (d) that the resistance of the sensor decreases by about 1 Ω, before it increases slowly to its steady state value. From the simulation results shown in Figure 6.3, we conclude that the bias voltage of the thermal sensor has a significant influence on the response of the sensor. An increase in the bias voltage of the sensor causes a reduction in the increase of the sensor resistance for the assumed contact conditions in Figure 6.3. Since the resistance change of the sensor is caused by the temperature change of the sensor, the observed behavior is clearly related to the change of heat transfer between the asperity and the sensor as a function of the bias voltage. We will address this point in the following section.

6.3.2 Heat Transfer Mechanism

Heat conduction between a thermal sensor and a thermal asperity can be modeled as time-dependent heat transfer between a moving heat source and a stationary thermal sensor. The heat source corresponds to the frictional heat generated at the

contact interface between the sensor and the asperity. Figure 6.4 shows a model for heat conduction during contact between a disk asperity and the sensor for three different times denoted by $t = t_1$, $t = t_2$, and $t = t_3$, respectively. At $t = t_1$ (Figure 6.4 (a)), the asperity has just started to contact the sensor. At $t = t_2$ (Figure 6.4 (b)), the asperity peak is positioned symmetrically beneath the sensor, and at $t = t_3$ (Figure 6.4 (c)), the asperity has almost passed the sensor. In Figure 6.4, v denotes the velocity between the asperity and the sensor; T_1 and T_2 are the temperatures of the sensor and the asperity, respectively; k_1 and k_2 are the thermal conductivities of the sensor and the asperity; q_{in} represents the heat flow into the sensor due to frictional heating and q_{out} is the heat flow out of the sensor caused by the temperature difference between the sensor and the thermal asperity. N is the contact force and A is the contact area. Both the contact force N and the contact area A change as a function of time, assuming the curvature of the asperity and the interference between asperity and disk are constant. Consequently, the temperature of the sensor and the asperity are functions of time, as well as the heat flow between sensor and asperity. The heat conduction model of Figure 6.4 for the different times during the contact event is summarized in Figure 6.5 using the same definitions as in Figure 6.4. The parameters l_1 and l_2 in Figure 6.5 are the linear diffusion distance of the sensor and the asperity, respectively [168]. The net heat change of the sensor Q_{net} is given by [169], [170]

$$Q_{net} = Q_{in}^{total} - Q_{out}^{total}$$

$$= \int_{t_{ini}}^{t_{end}} \alpha \mu N(t) v \, dt - \int_{t_{ini}}^{t_{end}} \frac{T_1(t) - T_2(t)}{\frac{l_1}{k_1 A(t)} + \frac{l_2}{k_2 A(t)} + \frac{1}{h_c A(t)}} \, dt \qquad (6.3)$$

(a) $t = t_1$

(b) $t = t_2$

(c) $t = t_3$
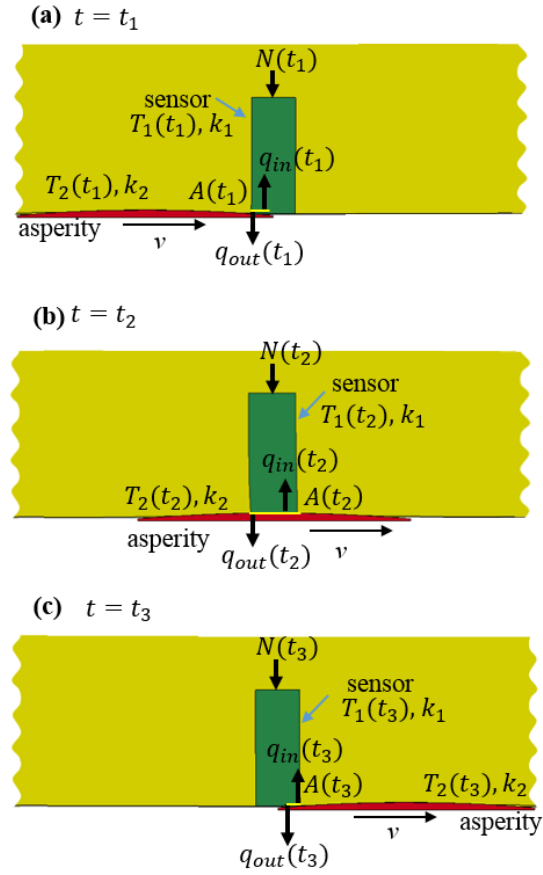
Figure 6.4 Heat conduction model for transient contact between sensor and asperity as a function of time
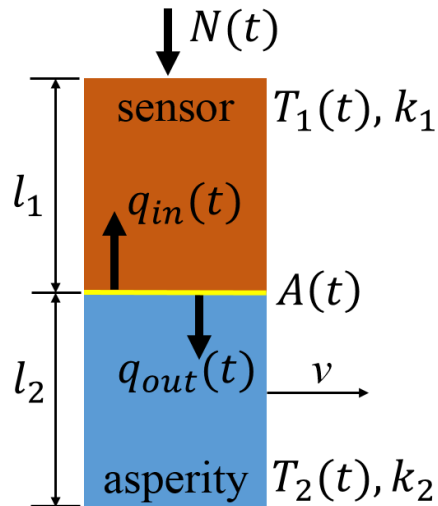
Figure 6.5 Generalized heat conduction model for contact between sensor and asperity

where Q_{in}^{total} represents the total amount of heat gained by the sensor during contact and Q_{out}^{total} is the total amount of heat lost by the sensor during contact. In the expression for Q_{in}^{total}, α is the heat partitioning factor, and μ is the friction coefficient. The heat partitioning factor α can be calculated using the following relationships [171]:

$$\frac{Q_1\sqrt{D_1}}{k_1} = \frac{Q_2\sqrt{D_2}}{k_2} \tag{6.4}$$

$$\alpha = \frac{Q_1}{Q_1 + Q_2} \tag{6.5}$$

where Q_1 and Q_2 are the heat flux to the sensor and the asperity, respectively, caused by frictional heating; k_1 and k_2 are the thermal conductivity of the sensor and the asperity, respectively; D_1 and D_2 are the thermal diffusivity of the sensor and the asperity, respectively. The thermal diffusivity is given by

$$D = \frac{k}{\rho c} \tag{6.6}$$

where k is the thermal conductivity, ρ is the material density, and c is the heat capacity. For contact between the thermal sensor and an Al$_2$O$_3$ asperity, Equations 6.4 and 6.5 give $\alpha = 0.85$. In the expression for Q_{out}^{total} in Equation 6.3, h_c is the interfacial conductance between the contact surfaces. The value of h_c depends on the surface roughness, contact pressure, and material properties of the contact bodies [172]. To satisfy Blok's postulate [173], the temperature at contacting nodes in the finite element model is assumed to be the same. This is accomplished by setting the interfacial conductance h_c infinite. In Equation 6.3, t_{ini} represents the time when the asperity starts to contact the sensor (Figure 6.4 (a)) and t_{end} represents the time when the

asperity leaves the sensor (Figure 6.4 (c)). The definition of all other parameters in Equation 6.3 is the same as in Figure 6.4 and Figure 6.5. According to Equation 6.3, if the operational temperature of the sensor T_1 is 400 K (U=252 mV), and Q_{out}^{total} is smaller than Q_{in}^{total}, the resistance of the sensor increases as shown in Figure 6.3 (a), i.e., the sensor temperature increases. If the operational temperature of the sensor is increased to 450 K (U=326 mV), Q_{in}^{total} due to frictional heating remains the same as before if the contact conditions have not changed. However, Q_{out}^{total} increases due to the increased temperature difference between the sensor and the asperity. Therefore, the net heat flux of the sensor Q_{net} decreases and the maximum temperature and resistance increase of the sensor is reduced. If the operational temperature of the sensor is increased to 500 K (U=400 mV), Q_{out}^{total} is further increased, reaching a value close to Q_{in}^{total}. In this case, the net heat flux of the sensor Q_{net} is approximately zero. Therefore, as shown in Figure 6.3 (c), the temperature and resistance of the sensor remain nearly constant. If the operational temperature of the sensor is increased to 550 K (U=473 mV), the heat flux from the sensor to the thermal asperity Q_{out}^{total} becomes larger than the frictional heat Q_{in}^{total}. In this case, the net heat flux of the sensor Q_{net} becomes negative, causing a decrease of the sensor temperature. Clearly, the sensor is cooled and the resistance of the sensor decreases as shown in Figure 6.3 (d).

6.3.3 Effect of Friction Coefficient

Figure 6.6 shows the resistance of the sensor during contact with an Al$_2$O$_3$ thermal asperity for three different values of the friction coefficient. We observe that the maximum sensor resistance increases if the friction coefficient μ increases from 0.1

to 0.3. According to Equation 6.3, the amount of frictional heating generated at the contact interface increases linearly with an increase of the friction coefficient, leading to an increase in the maximum sensor resistance.
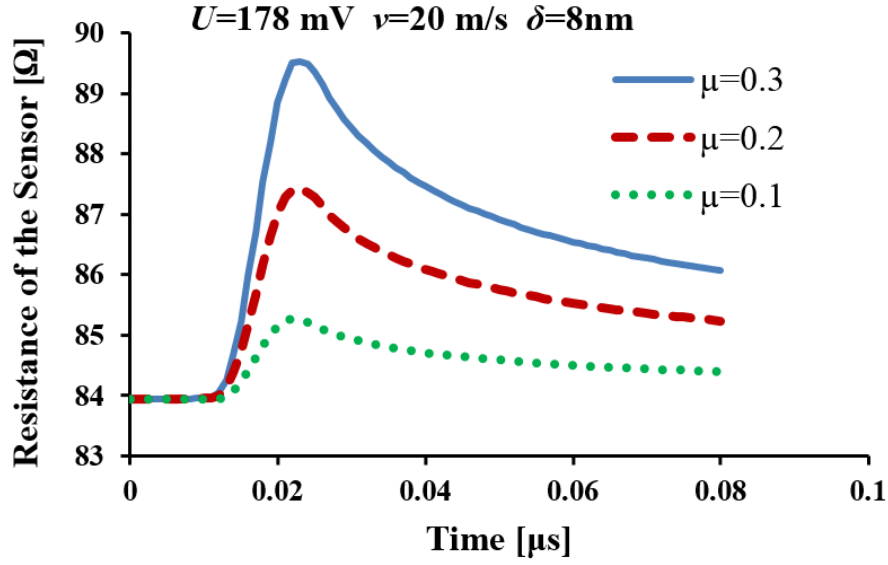
Figure 6.6 Resistance of a thermal asperity sensor during contact with an Al_2O_3 thermal asperity for different friction coefficients (μ=0.1, μ=0.2, and μ=0.3). The bias voltage U is 178 mV; the disk velocity v is 20 m/s; the contact interference δ is 8 nm.

Figure 6.7 shows the resistance change ΔR of the sensor as a function of the bias voltage of the sensor for three values of the friction coefficient (μ=0.1, μ=0.2, and μ=0.3). We observe that ΔR is positive if the bias voltage of the sensor is 178 mV. As shown in Figure 6.7, the resistance change ΔR of the sensor decreases linearly with an increase in the bias voltage and becomes zero for all three cases (μ=0.1, μ=0.2, and μ=0.3). If the bias voltage is further increased, ΔR becomes negative, which means the sensor temperature decreases, i.e. "thermal cooling" of the sensor occurs. Since the detection of thermal asperities depends on the resistance change of the sensor, it is apparent that
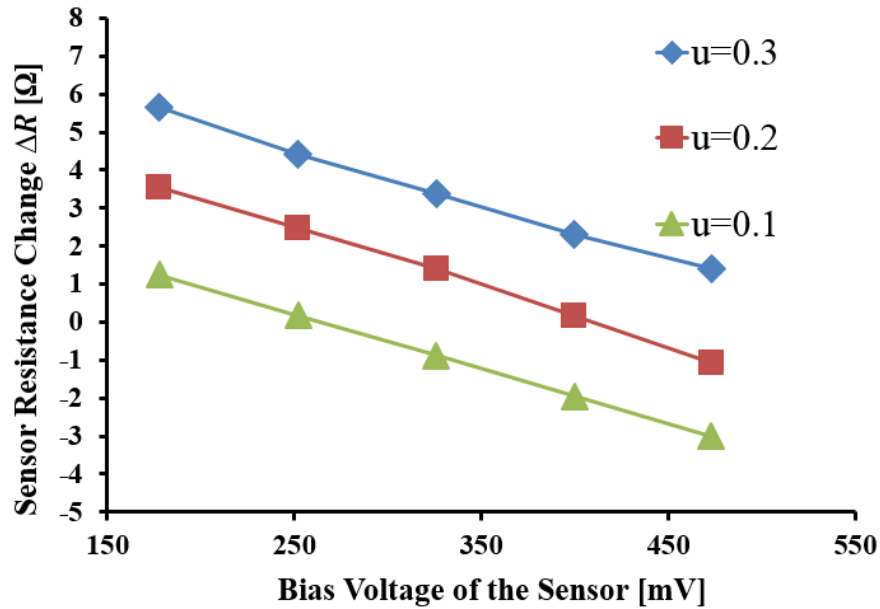
Figure 6.7 Sensor resistance change as a function of the bias voltage of the sensor for three values of the friction coefficient (μ=0.1, μ=0.2, μ=0.3). The disk velocity v is 20 m/s; the contact interference δ is 8 nm.

contact between a thermal asperity sensor and a thermal asperity cannot be detected if the resistance change of the sensor is zero. As shown in Figure 6.7, if the friction coefficient increases, the bias voltage, which causes the resistance change of the sensor to become zero, would increase keeping all other parameters constant. To detect asperities even in the case of zero resistance change of the sensor, a non-constant bias voltage with a range of, say, 100mV could be applied to the thermal sensor, and the same location on the disk could be scanned multiple times with different bias voltages.

6.3.4 Effect of Disk Velocity

Figure 6.8 shows the resistance of a thermal asperity sensor during contact with an asperity for disk velocities of 20 m/s and 30 m/s, respectively. We observe that the maximum resistance of the sensor for a velocity of 30 m/s is 0.8 Ω higher than for 20

m/s. According to Equation 6.3, the frictional heating increases linearly with increasing relative velocity between the asperity and the sensor. Therefore, higher relative velocity causes a larger amount of frictional heating and a larger resistance increase.
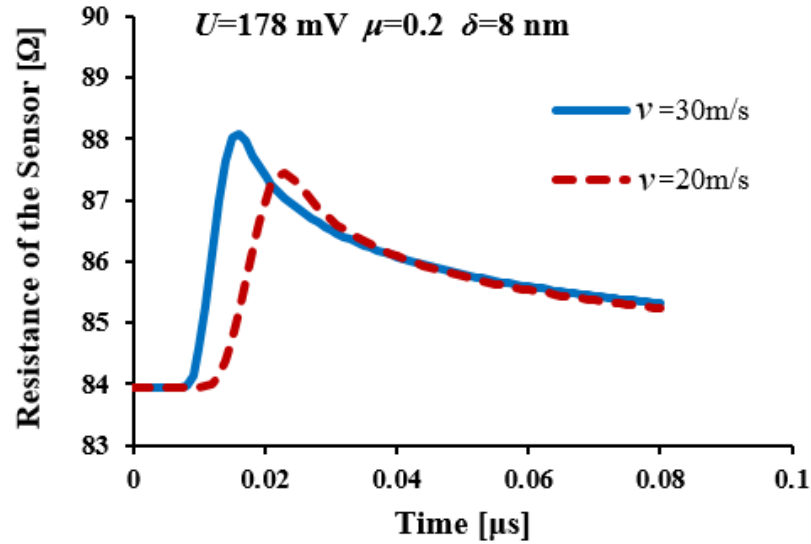
Figure 6.8 Resistance of a thermal asperity sensor during contact with an Al_2O_3 thermal asperity for different velocities (v=20 m/s and v=30 m/s). The bias voltage U is 178 mV; the friction coefficient μ is 0.2; the contact interference δ is 8 nm.

Figure 6.9 shows the resistance change ΔR of the sensor as a function of the bias voltage of the sensor for disk velocities of 20 m/s and 30 m/s, respectively. We observe from Figure 6.9 that the resistance change ΔR for a sensor operating at low bias voltage (U =178 mV) is almost independent of disk velocity. If the bias voltage increases, ΔR is different for v=20 m/s and v=30 m/s. Since a decrease in disk velocity leads to an increase in contact time between the sensor and the asperity, the integral for the heat conduction term in Equation 6.3 is larger for v=20 m/s than for 30 m/s. This causes more heat dissipation from the sensor to the asperity for v=20 m/s. Therefore, we observe from Figure 6.9 that the resistance decrease of the sensor is greater for v=20 m/s if the bias voltage increases. Figure 6.9 also shows that the resistance change ΔR of the sensor

is larger for high disk velocity than for low disk velocity. This implies that it is easier to detect thermal asperities at the outer diameter of a disk where the linear velocity is higher.
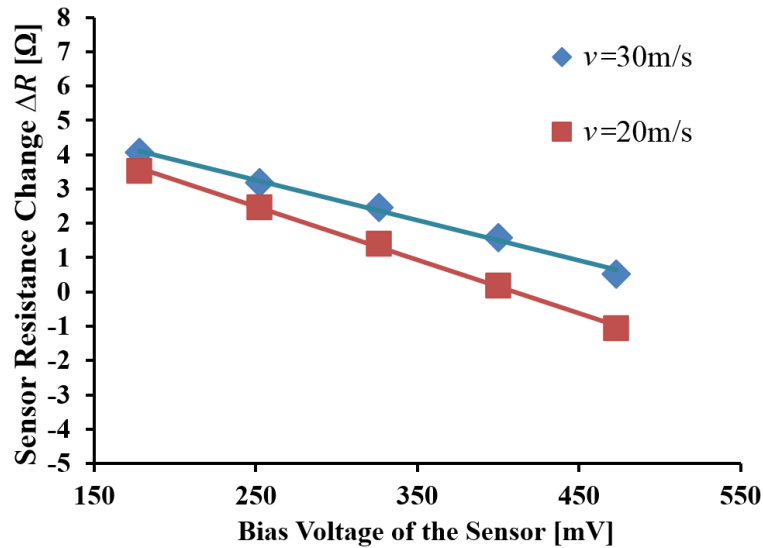
Figure 6.9 Sensor resistance change as a function of the bias voltage of the sensor for different disk velocities (v=20 m/s, v=30 m/s). The friction coefficient μ is 0.2; the contact interference δ is 8 nm.

6.3.5 Effect of Contact Interference

Figure 6.10 shows the resistance of a thermal asperity sensor during contact with a thermal asperity as a function of the contact interference between the asperity and the sensor. We observe from Figure 6.10 that an increase in contact interference causes an increase in resistance and temperature. This can be explained by the fact that an increase in contact interference between an asperity and a sensor causes an increase in the contact force. Figure 6.11 shows the contact force between the sensor and the asperity for different values of the contact interference. The contact force for 10 nm contact interference (94 μN) is about 2.5 times the contact force for 6 nm contact interference

(38 μN). Since frictional heating is larger for a contact interference of 10 nm than for an interference of 6 nm, a larger resistance increase is observed for δ =10 nm.
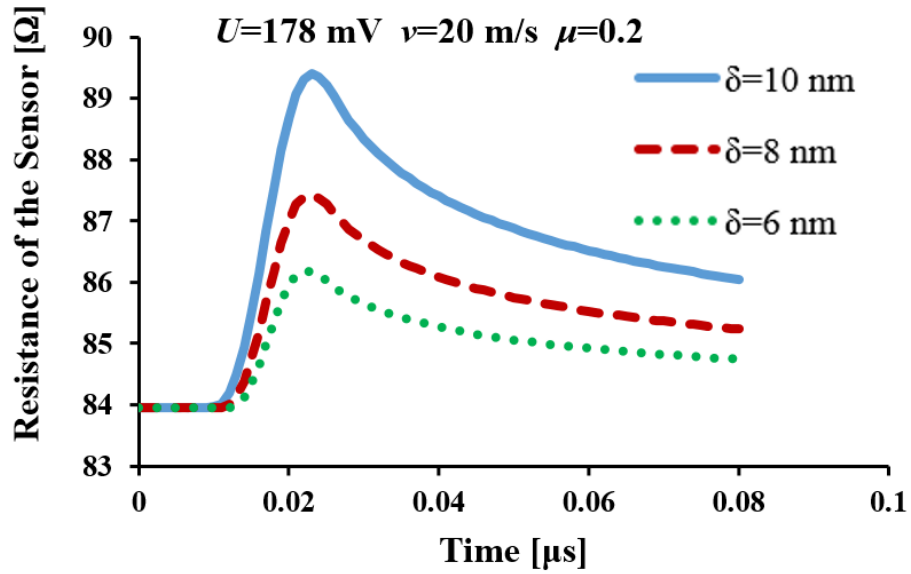
Figure 6.10 Resistance of a thermal asperity sensor during contact with an Al_2O_3 thermal asperity for different contact interferences (δ=6 nm, δ=8 nm, and δ=10 nm). The bias voltage U is 178 mV; the disk velocity v is 20 m/s; the friction coefficient μ is 0.2.
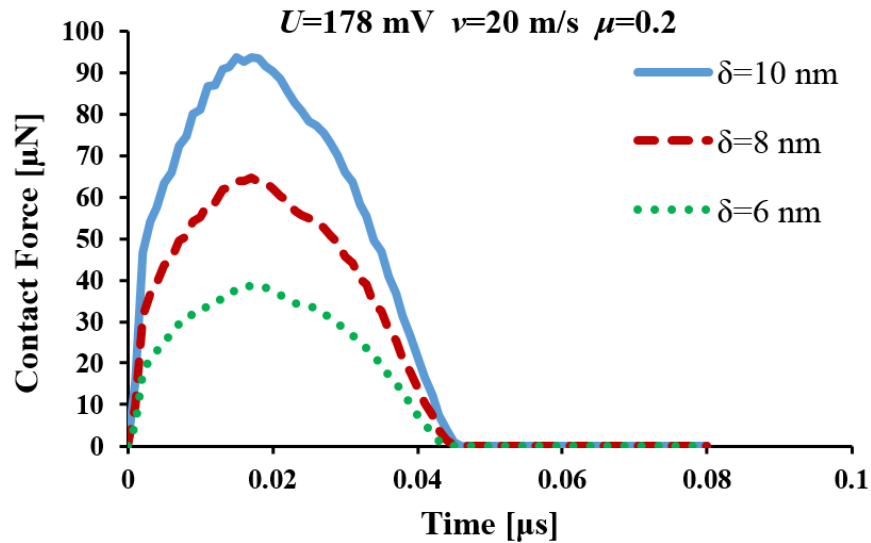
Figure 6.11 Contact force between a thermal asperity sensor and an Al_2O_3 thermal asperity for different contact interferences (δ=6 nm, δ=8 nm, and δ=10 nm).

Figure 6.12 shows the resistance change ΔR of the sensor as a function of the bias voltage of the sensor for different values of contact interference. We observe that ΔR decreases for all three contact interference values if the bias voltage of the sensor U increases from 178 mV to 473 mV. As the bias voltage of the sensor increases, the heat conduction term in Equation 6.3 increases by a larger magnitude if the sensor and the asperity have a larger contact area. Therefore, ΔR for δ=10 nm decreases by 6.0 Ω, while ΔR for δ=6 nm decreases by only 3.7 Ω due to the smaller contact area. If the sensor operates at 473 mV bias voltage, ΔR for δ=6 nm and δ=10 nm is nearly the same. This occurs because heat conduction from the sensor to the asperity for the case of 10 nm contact interference is larger than that for the case of 6 nm contact interference. On the other hand, the frictional heating for the case of 10 nm is larger than that for the case of 6 nm. Based on the simulation result shown in Figure 6.12, we conclude that the effect
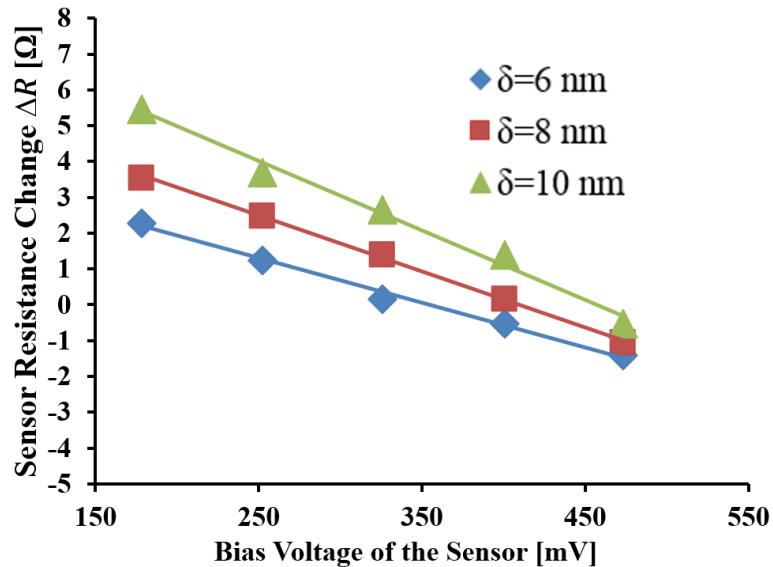
Figure 6.12 Sensor resistance change as a function of the bias voltage of the sensor for different contact interferences (δ=6 nm, δ=8 nm, and δ=10 nm). The disk velocity v is 20 m/s; the friction coefficient μ is 0.2.

of contact interference on the resistance change of the sensor decreases, if the bias voltage of the sensor increases. In addition, since an increase in the contact interference shows an increase in resistance change, we conclude that a thermal sensor is more sensitive to a thermal asperity if the slider flies at a lower flying height and contacts an asperity at a larger contact interference. However, contact at lower flying height may lead to a larger contact force and plastic deformation of the read and write elements.

6.3.6 Effect of Asperity Material Properties

Figure 6.13 shows the resistance of a thermal asperity sensor during contact with NiP and Al_2O_3 asperities for a bias voltage of 178 mV. We observe that the resistance increase of the sensor is similar for an Al_2O_3 asperity and a NiP asperity. The maximum resistance of the sensor contacting an Al_2O_3 asperity is only 0.5 Ω higher than during contact with a NiP asperity.
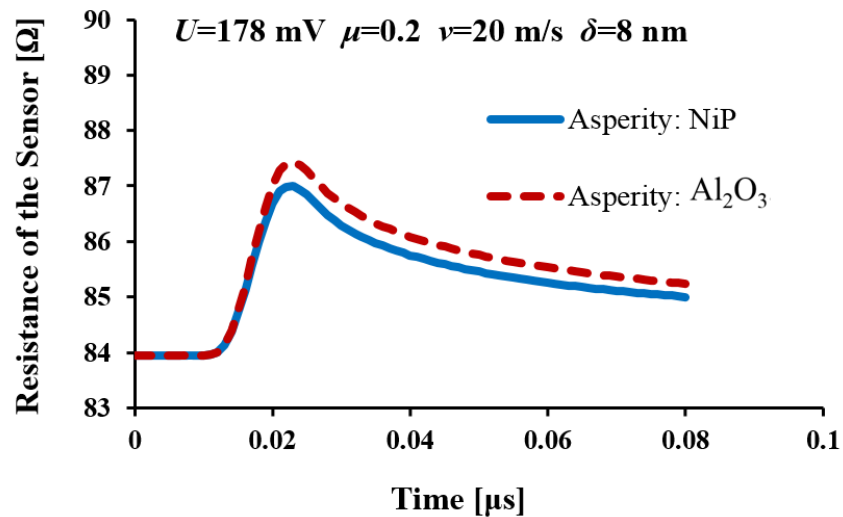
Figure 6.13 Resistance of a thermal asperity sensor during contact with different thermal asperities (NiP and Al_2O_3) at the bias voltage of 178 mV. The friction coefficient μ is 0.2; the disk velocity v is 20 m/s; the contact interference δ is 8 nm.

Figure 6.14 shows the resistance change of the sensor as a function of the bias voltage for contacting a NiP asperity and an Al_2O_3 asperity. We observe that the resistance change ΔR of the sensor is similar for contact with a NiP or Al_2O_3 asperity if a bias voltage of 178 mV is applied to the sensor. If the bias voltage increases, the resistance change ΔR of the sensor for a NiP asperity and an Al_2O_3 asperity becomes different. This suggests that the effect of asperity material properties on the resistance change of the sensor becomes significant if the bias voltage of the sensor increases. As shown in Table 1, the thermal conductivity of NiP is four times the thermal conductivity of Al_2O_3. Thus, a larger amount of heat transfers from the sensor to a NiP asperity than from the sensor to an Al_2O_3 asperity. If the sensor operates at low bias voltage (U=178 mV) or low operational temperature (T=350 K) close to the initial temperature of the asperity (300 K), the effect of the thermal conductivity of asperity material properties on the heat conduction term in Equation 6.3 is not significant. If the bias voltage or the operational temperature of the sensor increases, the temperature difference between the sensor and the asperity increases. Therefore, the influence of the asperity material on the resistance change of the sensor increases. As shown in Figure 6.14, ΔR for the sensor contacting a NiP asperity and an Al_2O_3 asperity is quite different if the sensor operates at a high bias voltage (U=473 mV, T=550 K). In other words, the sensor is more sensitive to discriminate between NiP and Al_2O_3 asperities if it operates at a high bias voltage or a high temperature.
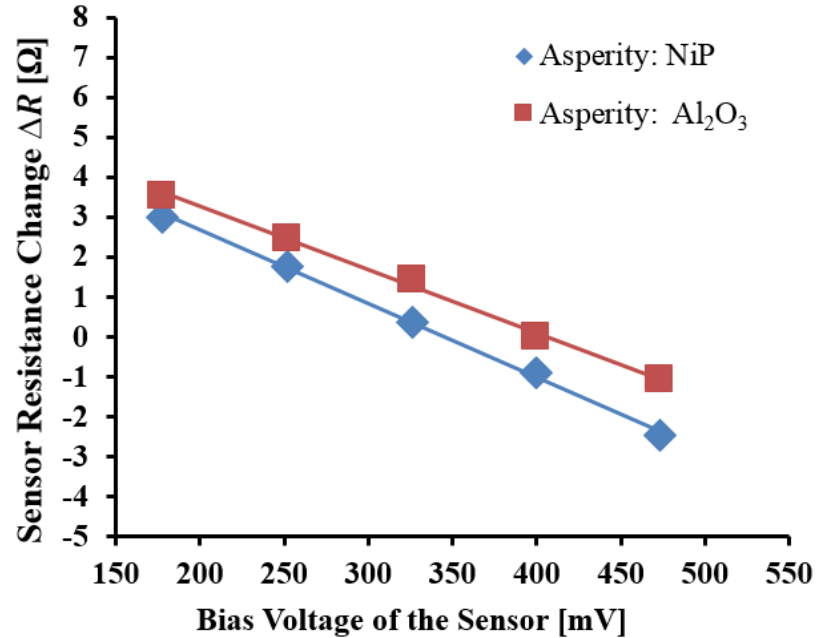
Figure 6.14 Sensor resistance change as a function of the bias voltage of the sensor contacting different thermal asperities (NiP and Al_2O_3). The friction coefficient μ is 0.2; the disk velocity v is 20 m/s; the contact interference δ is 8 nm.

6.4 Discussion

For the heat conduction problem of a heat source sliding over a semi-infinite body, analytical solutions are available to calculate the temperature rise at the contact interface. To validate our finite element simulation results, we compared the maximum average temperature change obtained from the simulation with the temperature change obtained from the analytical models developed by Ashby et al. [174] and Tian et al. [175]. In the analytical models, the temperature at the contacting surfaces was assumed to reach quasi-steady state during elastic contact. However, the temperature change of the sensor obtained from our numerical simulations is time dependent and includes plastic deformation. According to the model developed by Ashby et al. [174], the average temperature rise at the contact interface for a sliding contact is

$$\Delta T = \frac{\mu N v}{A} [\frac{k_1}{l_1} + \frac{k_2}{l_2}]^{-1} \tag{6.7}$$

The definition of the variables in Equation 6.7 is the same as in Equation 6.3. In Ashby's model, a uniform circular heat source was assumed. The contact area A can be obtained from the Hertzian contact theory [92]. Using Equation 6.7, we obtain that the average temperature rise at the contact interface between the thermal asperity sensor and an Al$_2$O$_3$ asperity is about 38 K for a friction coefficient μ of 0.2, a contact force N of 64 µN (δ=8 nm) , and a disk velocity v of 20 m/s.

Based on the model derived by Tian et al. for a parabolic heat source [175], the maximum temperature rise at the contact interface for an elastic Hertzian contact can be expressed as

$$\Delta T_{max} = \frac{1.31 \mu p_{avg} r v}{k_1 \sqrt{1.23 + Pe_1} + k_2 \sqrt{1.23 + Pe_2}} \tag{6.8}$$

where p_{avg} is the average contact pressure; r is the radius of the contact area; Pe_1 and Pe_2 are the Peclet number of the sensor and the asperity, respectively, defined as

$$Pe = \frac{r v \rho c_p}{2k} \tag{6.9}$$

where ρ is the material density; c_p is the heat capacity. The definition of all other variables in Equations 6.8 and 6.9 is the same as in Equation 6.3. Using Equation 6.8, we obtain that the increase in the maximum temperature at the contact interface between the sensor and the asperity is 37 K, assuming the same contact conditions used in Ashby's model.

In both Ashby's model [174] and Tian's model [175], analytical solutions were obtained by assuming the same initial temperature for the two contact bodies. For the same assumption, numerical simulations show that the increase of average temperature at the contact surface is about 42 K. This value is in good agreement with the values obtained using the analytical solutions. For cases that the operational temperature of the sensor is higher than the temperature of the thermal asperity, Equations 6.7 and 6.8 cannot be used because the contact condition is different from the assumption in the analytical models [174], [175], i.e., the two contact bodies are assumed to have the same initial temperature.

6.5 Conclusion

Numerical simulations were performed to calculate the temperature change of a thermal sensor during contact with a thermal asperity. The simulation results were converted to resistance changes of the sensor by correlating the resistance of the sensor to the temperature of the sensor. We observe from the simulation results that the resistance change ΔR of the sensor increases with a decrease in bias voltage or with an increase in the friction coefficient at the contact interface, disk velocity, and contact interference. The influence of disk velocity and contact interference on the resistance change of the sensor is affected by the bias voltage of the sensor. If the bias voltage of the sensor increases, the influence of disk velocity on the resistance change of the sensor increases, while the effect of contact interference on the resistance change of the sensor decreases. The resistance change of a sensor during contact with a thermal asperity is also affected by asperity material properties, i.e., the thermal conductivity. Simulation

results show that the influence of the asperity material on the resistance change of the sensor increases if the bias voltage of the sensor increases.

Based on the simulation results, high disk velocity and low flying height are recommended to improve the sensitivity of the sensor because the thermal sensor has a larger resistance change for those conditions. For the purpose of differentiating asperity types on a disk, high bias voltage of the sensor is beneficial because the difference of the thermal response of the sensor to different types of asperities increases with increasing bias voltage of the sensor.

6.6 Acknowledgement

Chapter 7

Tribology of the Lift Tab/Ramp Interface

7.1 Introduction

To improve the reliability of hard disk drives, ramp load/unload technology was introduced in hard disk drives approximately 20 years ago [176], [177]. When a disk drive is started from rest, an electric current is applied to the voice coil motor (VCM) to generate a torque which loads the slider from the ramp onto to the disk [178]. This process is called "loading". During shut-down of the drive, an electric current in the opposite direction is applied to the voice coil motor to retract the slider from the disk back to the rest position on the ramp. This process is called "unloading". Many experimental studies have been conducted in the past to investigate the load/unload process and the tribological interactions between the slider and the disk during load/unload [179]–[184]. In addition, numerical simulations have been performed to study the effect of air bearing design, load/unload velocity, shock, and voice coil motor design on the load/unload process [185]–[188].

During load/unload, the suspension lift tab slides along the ramp surface causing the generation of wear debris at the lift tab/ramp interface. Since surface damage and formation of wear debris are likely to affect the frictional characteristics of the lift

141

tab/ramp interface [189], understanding of the friction force between the lift tab and the ramp during load/unload is highly desirable. Hiller et al. [190] measured the friction force at the lift tab/ramp interface by attaching a load cell to the actuator arm and determining the torque applied by the voice coil motor. They found that the friction force between the lift tab and the ramp is a function of temperature, lateral velocity of the suspension lift tab, and the ramp material. Suk et al. [191] calculated the friction force between the lift tab and the ramp using voice coil motor current measurements and compared their results with the data of Hiller et al. [190]. They concluded that both methods allow the measurement of the friction force between the lift tab and the ramp.

Since wear debris is detrimental for the reliability of a hard disk drive, a better understanding of the lift tab/ramp interface is needed to minimize the generation of wear debris [192], [193]. In this study, we investigate the change of the friction force and the generation of wear debris at the lift tab/ramp interface during load/unload testing by examining the voice coil motor current as a function of load/unload cycles. In particular, we measure the voice coil motor current used to load and unload the slider and obtain the friction force between the lift tab and the ramp as a function of load/unload cycles and temperature. We analyze the amount of wear debris on the lift tab using scanning electron microscopy and determine the mechanism of wear at the lift tab/ramp interface using energy-dispersive X-ray (EDX). To explain the experimental results and further investigate the tribological performance of the lift tab/ramp interface, a three-dimensional finite element model is developed to calculate the contact stress on the lift tab and the ramp during load/unload.

7.2 Experimental Method and Procedure

Figure 7.1 shows a schematic of the load/unload mechanism in a typical hard disk drive, consisting of the load/unload ramp, the lift tab, the pivoted actuator arm, and the voice coil motor. The close-up on the right of Figure 7.1 shows the motion of the lift tab on the ramp as it travels from position A to position E* during loading. The material of the ramp is polyoxymethylene (POM) and the lift tab was made of stainless steel. The center line average surface roughness (Ra) of the lift tab and the ramp is 150 nm and 100 nm, respectively. Since the friction coefficient between stainless steel and POM is a function of temperature [194], drive-level load/unload testing was conducted in a temperature controlled chamber. Because the lift tab/ramp interface is isolated from the external environment by the drive enclosure, one can assume that the water vapor content in the drive is constant and the absolute humidity at the lift tab/ramp interface remains the same for all drives. In this study, hard disk drives with five 3.5 inch magnetic disks and ten sliders were used. A total of 300,000 load/unload cycles with a
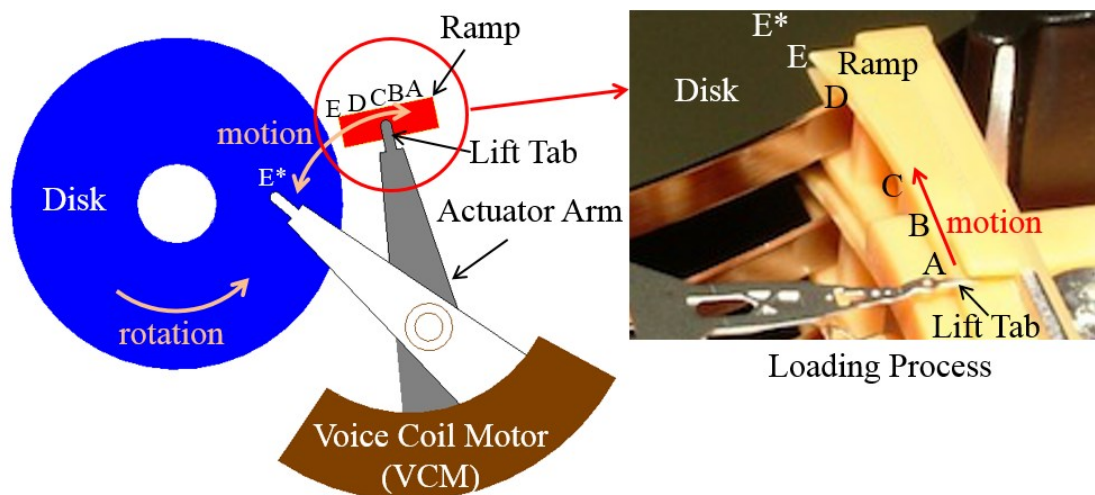
Figure 7.1 Schematic of the ramp load/unload mechanism in hard disk drives

frequency of 1.8 Hz was performed for each drive, and the voice coil motor current was recorded throughout the test. Figure 7.2 shows a typical voice coil motor current profile during loading. At time t=0, the lift tab is at its rest position A and the voice coil motor current is zero. As the loading process begins, current is applied to the voice coil motor to move the actuator arm, and the lift tab slides on the ramp surface from position A to E. The lift tab separates from the ramp at position E and the slider establishes flying over the disk as it travels from position E to E*. We note that the amplitude of the voice coil motor current is near zero after the lift tab has passed position E, although it is not zero, since a small torque is still needed to overcome pivot friction, air drag, and flexure bias [20]. Flexure bias is the drag force applied on the head stack assembly by the flexible printed circuit in hard disk drives.
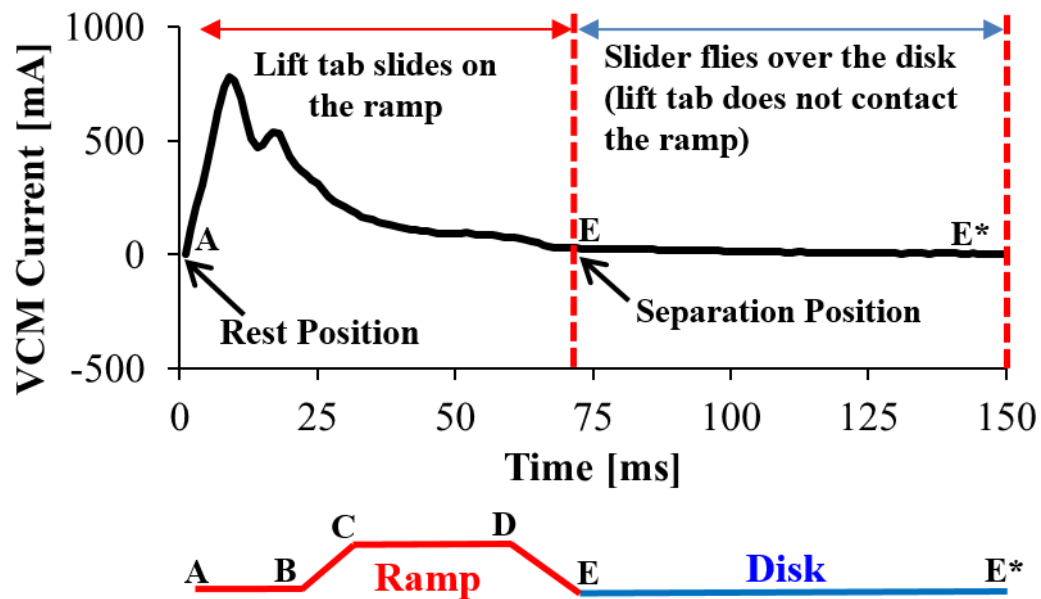
Figure 7.2 Typical profile of the voice coil motor current during loading process

Figure 7.3 shows the schematic of a voice coil motor with the head stack assembly (HSA) in a typical hard disk drive. The voice coil motor is energized by a

current I and exerts a torque M which accelerates the actuator arm to load or unload the slider. A magnetic field with a magnetic flux density H is generated by the neodymium magnets shown in Figure 7.3. The magnetic field applied on section 1-2 and section 3-4 of the coil is in the opposite direction. The length of section 1-2 and 3-4 of the coil is a. L is the distance between the friction force F and the pivot point of the head stack assembly (HSA). The moment arm between the magnetic force P_{mag} and the pivot point is d. The torque M generated by the voice coil motor is given by

$$M = 2 \cdot P_{mag} \cdot d = K_t \cdot I \qquad (7.1)$$

where K_t is the torque constant of the voice coil motor. The definitions of P_{mag}, d, and I in Equation 7.1 are shown in Figure 7.3. During loading, the lift tab slides on the
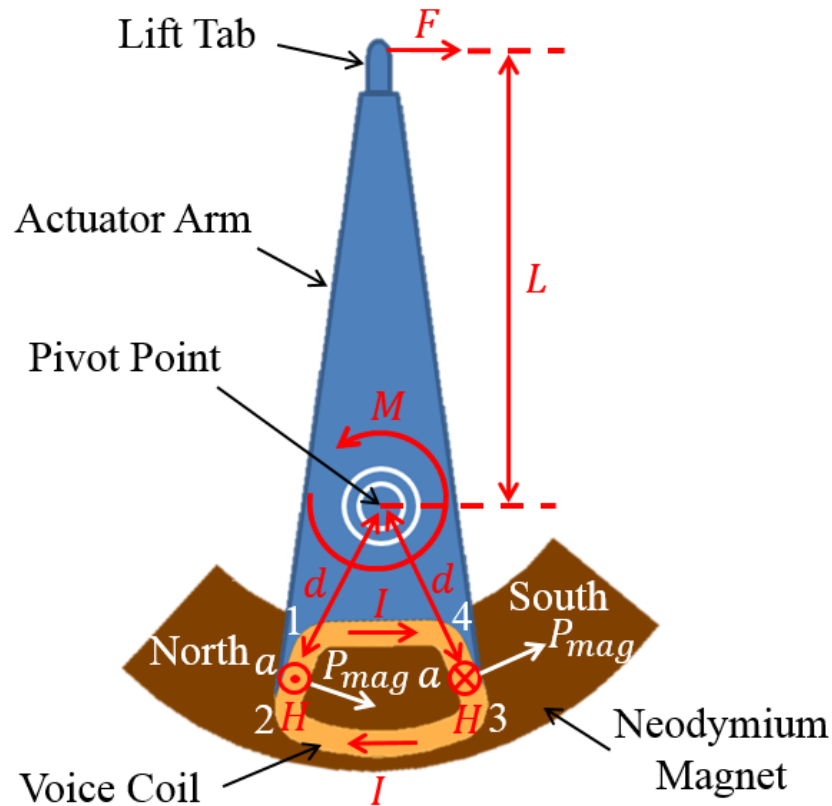
Figure 7.3 Schematic of the voice coil motor and the head stack assembly in a hard disk drive

ramp surface from its rest position A to position E where it separates from the ramp. In the unloading cycle, the process is repeated in the reverse order. During the motion of the lift tab on the ramp, a voltage (back electromotive force) is generated in the voice coil motor. This voltage is used to determine the velocity of the actuator arm [195]. If the lift tab or the ramp surface is damaged by wear during load/unload, it is likely that the friction force F between the lift tab and the ramp changes, leading to a change in the velocity. To keep the velocity constant during the life of a hard disk drive, a feedback loop is implemented in hard disk drives between the voice coil motor current I and the velocity [195], i.e., if the velocity decreases, the current is increased and vice versa. Thus, the voice coil motor current I is a function of the friction force F of the lift tab/ramp interface during load/unload testing. The relationship between a change of the friction force ΔF and a change of the voice coil motor current ΔI is given by

$$\Delta F = \frac{\Delta M}{L} = \frac{K_t \cdot \Delta I}{L} \tag{7.2}$$

where ΔM is the change of the torque applied to the actuator arm. The definitions of K_t and L in Equation 7.2 are the same as in Equation 7.1 and Figure 7.3.

In this study, each drive was tested for 300,000 load/unload cycles. The voice coil motor current was measured every 50,000 load/unload cycles and compared with the initial voice coil motor current, resulting in the change of the voice coil motor current ΔI as a function of the number of cycles.

7.3 Experimental Results and Discussion

7.3.1 Change of the Voice Coil Motor Current During Load/Unload Testing

Figure 7.4 shows the change of the voice coil motor current ΔI after 50,000, 150,000, and 300,000 load/unload cycles, respectively, at 14°C. We observe that the magnitude of the voice coil motor current increases in the section A-E as a function of the number of load/unload cycles. On the other hand, we observe that the voice coil motor current does not change in the section E - E*, i.e., after the lift tab has disengaged from the ramp. Thus, it is justifiable to conclude that the increase in the voice coil motor
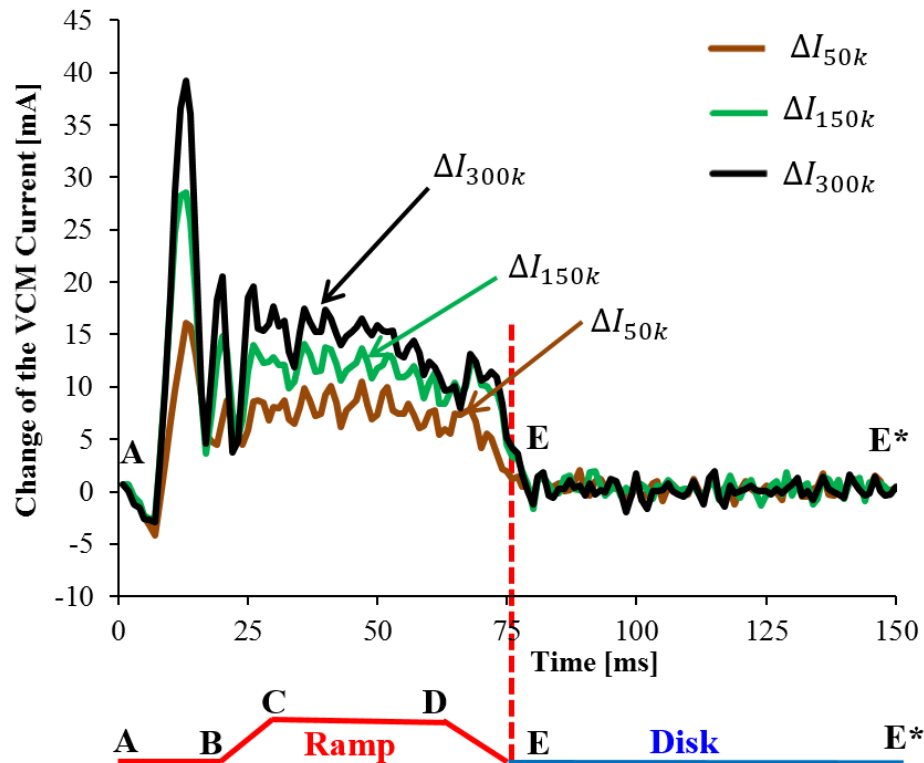
Figure 7.4 Change of the voice coil motor current after 50,000, 15,000, and 300,000 load/unload cycles at 14°C.

current is due to the increase in the friction force between the lift tab and the ramp as a function of load/unload cycles.

Figure 7.5 shows the average change of the voice coil motor current of five drives and the standard deviation as a function of the number of load/unload cycles at 14°C. For each drive, the voice coil motor current is calculated by averaging the current when the lift tab slides on the section C-D of the ramp. We observe from Figure 7.5 that the average change of the voice coil motor current increases during the wear test, reaching a value of 12 mA after 300,000 cycles. Using Equation 7.2, we obtain that the 12 mA increase in the voice coil motor current corresponds to an increase in the friction force of approximately 14 mN. Since each test was conducted on a drive with ten heads, the average increase of the friction force at each lift tab/ramp interface is
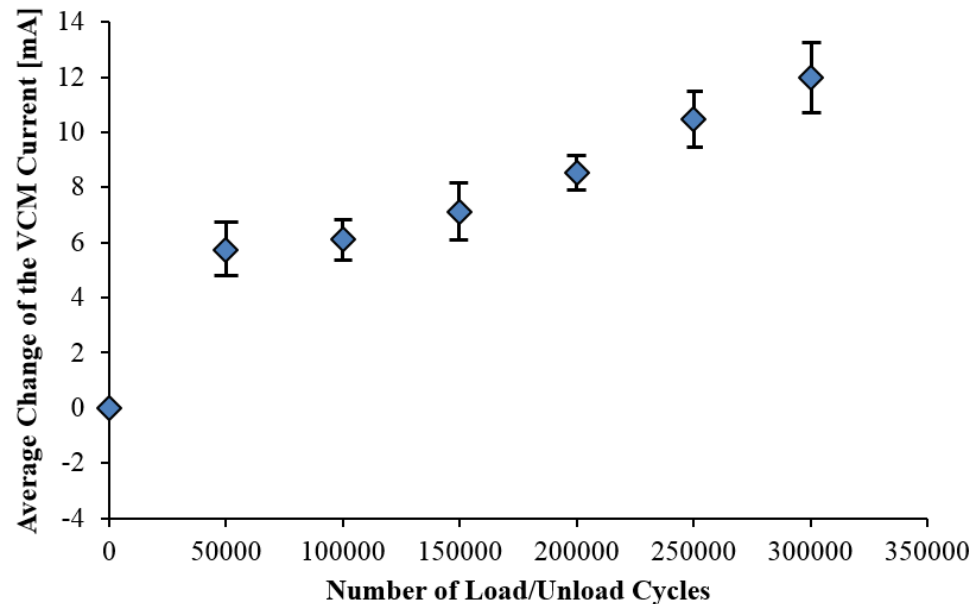
Figure 7.5 Average change of the voice coil motor current versus number of load/unload cycles at 14°C

about 1.4 mN. During the first 50,000 load/unload cycles, the voice coil motor current increased by 6 mA, corresponding to an increase in the friction force of 7 mN. In the following 250,000 load/unload cycles, the same amount of increase of the voice coil motor current was observed. Thus, we conclude that the increase of the friction force at the lift tab/ramp interface occurs predominantly at the beginning of the load/unload testing, i.e., during "wear-in" of the lift tab/ramp interface.

7.3.2 Mechanism of Wear Generation at the Lift Tab/Ramp Interface

In Figure 7.6, an SEM image of a lift tab is shown after 300,000 load/unload cycles at 40°C. We observe dark areas on the lift tab, indicating material transfer and build-up of a "transfer" layer. We also observe from Figure 7.6 that the dark areas appear at two distinct locations on the lift tab due to the change of contact location between the lift tab and the ramp during load/unload. When the lift tab slides on the section A-B of the ramp, location 1 of the lift tab contacts with the ramp. As the lift tab slides from the
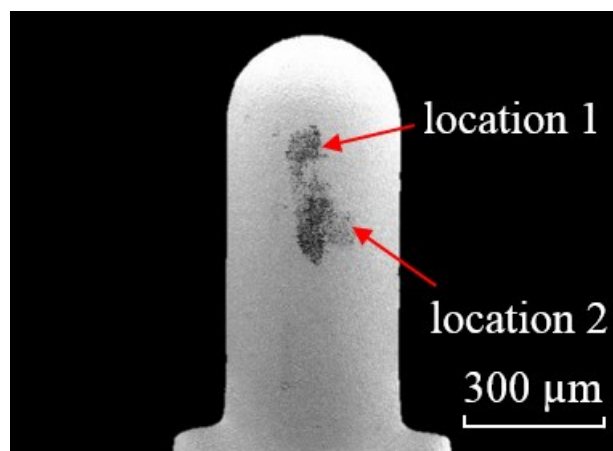
Figure 7.6 Typical wear scar on lift tab surface after 300,000 load/unload cycles at 40°C

section A-B to the section C-D during loading, the lift tab is displaced vertically due to the increase of the ramp height as shown in Figure 7.4. Therefore, the lift tab "rotates" up and the contact location of the lift tab changes from location 1 to location 2. When the lift tab slides in the reverse direction during unloading, the lift tab "rotates" down and the contact location changes back to location 1 due to the decrease of the ramp height. Therefore, two separate dark areas of material deposition were observed on the lift tab surface after load/unload testing.
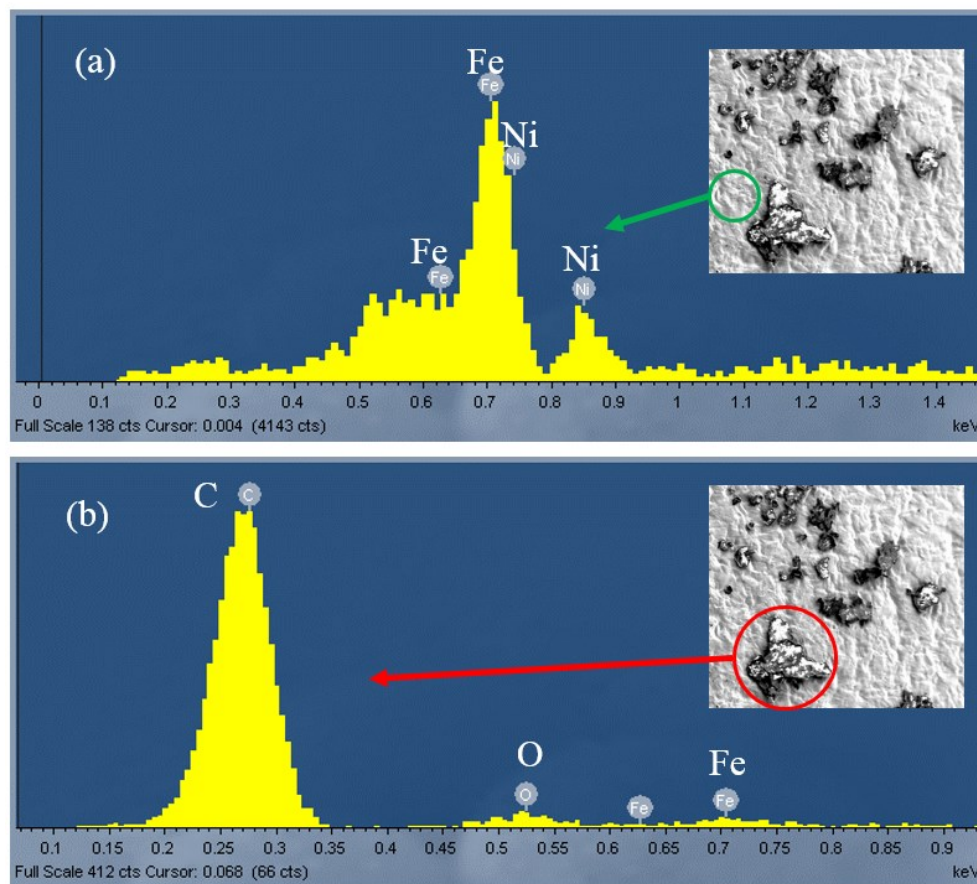
Figure 7.7 EDX analysis results for (a) clean area on the lift tab and (b) area with wear debris on the lift tab

To identify the chemical composition of the transferred material on the lift tab, energy-dispersive X-ray (EDX) analysis was performed. Figure 7.7 shows EDX results

for the transferred material on the lift tab together with high magnification SEM images of the lift tab surface. Figure 7.7 (a) shows the results for an area without deposits and Figure 7.7 (b) shows the results for an area with material deposits. In Figure 7.7 (a), we see predominantly iron and nickel, i.e., components of stainless steel. On the other hand, Figure 7.7 (b) shows large amounts of carbon and oxygen, which are the main chemical components of the ramp material (POM). A much smaller Fe peak is observed in Figure 7.7 (b) than in Figure 7.7 (a). Clearly, the EDX results indicate that the dark area on the lift tab is wear debris originating from the polyoxymethylene ramp. Since material transfer is typically observed in adhesive wear [77], we conclude that dark areas are adhering wear debris due to adhesive wear. As shown schematically in Figure 7.8, the generation of wear debris due to adhesion can be divided into three stages [196]. In the first stage, wear particles are formed and transferred from the ramp to the lift tab if the strength of the adhesive bonds between the lift tab and the ramp is greater than the cohesive strength of the polymer material [197]. In the second stage, a "transfer" layer is formed on the stainless steel lift tab. In the third stage, wear particles escape the contact zone as wear debris if the elastic strain energy in the transferred material is greater than the adhesive energy between the transferred material and the lift tab surface [194]. A similar phenomenon was also observed by Mergler et al.[196]. They reported that for sliding contact between stainless steel and polyoxymethylene, the latter will be worn away and transferred to the stainless steel surface at the beginning of wear testing. After a polyoxymethylene layer is formed on the lift tab, the wear situation at the lift tab/ramp interface has changed from stainless steel versus polyoxymethylene to polyoxymethylene versus polyoxymethylene. Since the friction coefficient of

polyoxymethylene versus polyoxymethylene is higher than that of stainless steel versus polyoxymethylene [196], we conclude that the increase in the voice coil motor current during load/unload testing shown in Figure 7.5 is a consequence of the increase in the friction force at the lift tab/ramp interface due to the build-up of a polyoxymethylene transfer layer during load/unload testing.
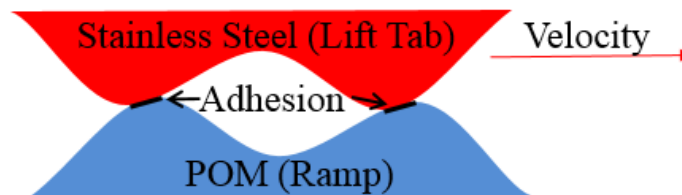
Figure 7.8 Formation of "transfer" layer and generation of wear debris due to adhesion

Figure 7.9 shows a high magnification image of a typical ramp surface near ramp position E after 300,000 load/unload cycles at 40°C. This image was captured using an

optical microscope. We observe a number of horizontal grooves and the deposition of polyoxymethylene wear debris on the ramp surface. The presence of horizontal grooves indicates that the ramp surface is "ploughed" by asperities on the lift tab surface. Since the formation of grooves is typical for abrasive wear [198], we conclude that both abrasion and adhesion are present at the lift tab/ramp interface. This results also agree with the commonly observed result that wear debris is predominantly generated from the surface of the softer material in the case of sliding of a hard material on a soft material [124]. Using nano-indentation measurements, we have found that the hardness of the polyoxymethylene ramp is about 0.4 GPa and that the hardness of the stainless steel of the lift tab is about 5 GPa. Clearly, wear debris should be generated predominantly from the soft ramp surface.
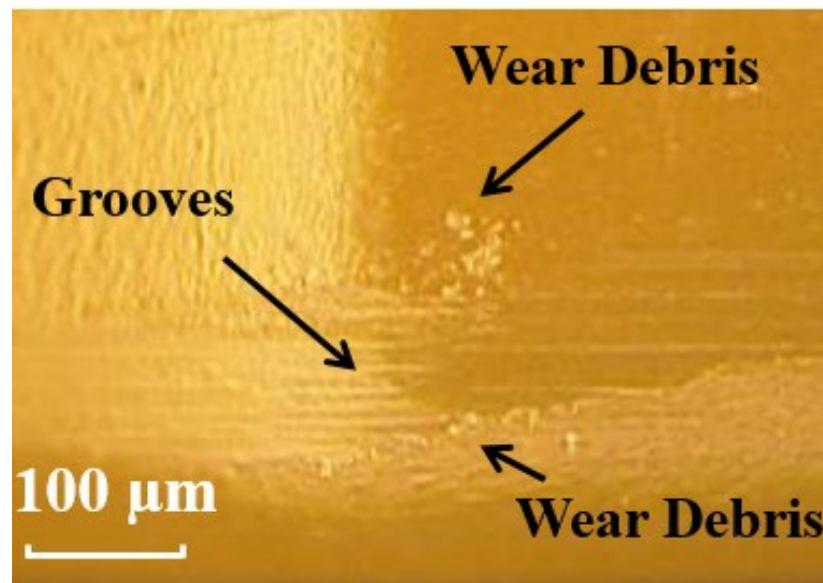
Figure 7.9 Typical wear scar on ramp surface after 300,000 load/unload cycles at 40°C

1ˢᵗ Stage: Penetration and Interlock of Asperities

2ⁿᵈ Stage: Generation of Wear Debris
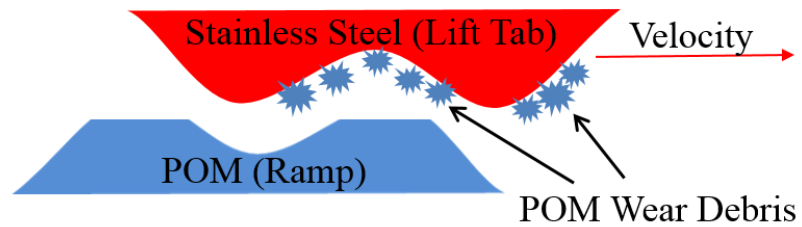
Figure 7.10 Generation of wear debris due to abrasion

Figure 7.10 shows a schematic of the generation of wear debris due to abrasion. First, asperities on the stainless steel lift tab penetrate into the polyoxymethylene ramp, or asperities on the lift tab and the ramp interlock with each other. Then, the soft polyoxymethylene is removed by hard stainless steel asperities and wear debris is generated, adhering to the lift tab surface due to adhesion between the wear debris and the lift tab surface. During this phase of load/unload testing, contact at the lift tab/ramp interface changes from stainless steel versus polyoxymethylene to that of polyoxymethylene versus polyoxymethylene.

7.3.3 Effect of Temperature on the Generation of Wear Debris at the Lift Tab/Ramp Interface

In Figure 7.11, SEM images of three lift tabs are shown after 300,000 load/unload cycles at 14°C, 40°C, and 60°C respectively. To quantify the adhering wear debris on the lift tab, we calculated the ratio of the area covered by wear debris versus the total area of the lift tab using image analysis. The total area of the lift tab is the area of the region outlined in Figure 7.11. From the SEM images in Figure 7.11, we observe that the lift tab tested at 14°C shows the largest amount of wear debris. The wear debris covers approximately 11.2% of the lift tab area. For the drives tested at 40°C and 60°C, the wear debris covers only 4.8% and 2.0% of the lift tab area, respectively. Therefore, we conclude that wear debris on the lift tab decreases with an increase in temperature. Figure 7.12 shows high magnification images of the ramp surface near ramp position E after 300,000 load/unload cycles for temperatures of 14°C, 40°C and 60°C respectively. This result is consistent with the results shown in Figure 7.11, i.e., the amount of wear debris on the ramp surface decreases with an increase in temperature.
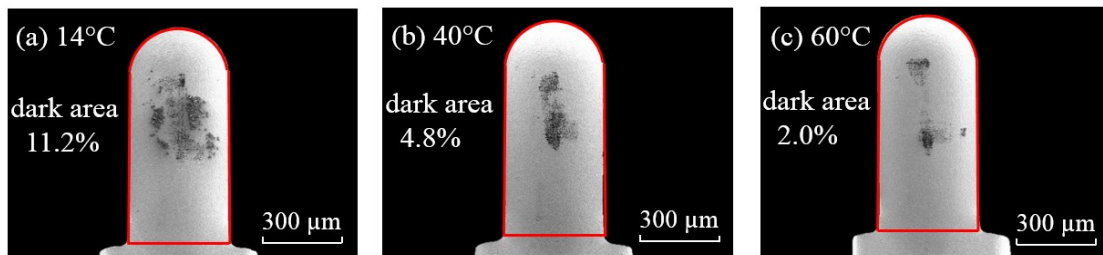
Figure 7.11 SEM images of lift tabs after 300,000 load/unload cycles at different temperatures
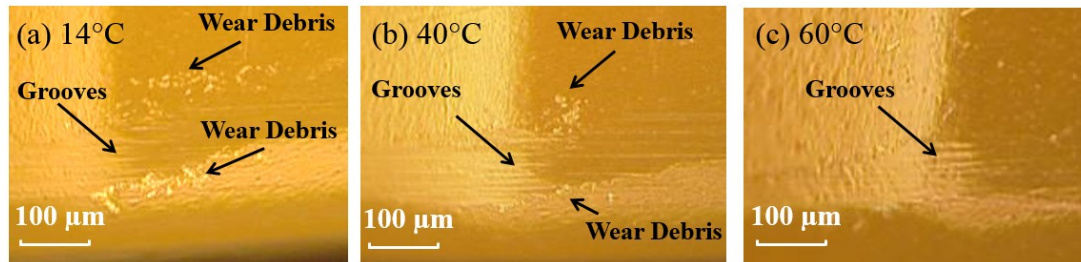
Figure 7.12 Wear scar on typical ramp surface after 300,000 load/unload cycles at different temperatures

In Figure 7.13, the area of the lift tab covered by wear debris is plotted against temprature. At each temperature, four drives were tested. The area of wear debris of each drive shown in Figure 7.13 corresponds to the average value of ten heads in that drive. The change in the wear debris area for drives tested at the same temperature is a typical result expected in any wear test. As shown in Figure 7.13, for a temperature increase from 14°C to 40°C, the average area of the lift tab with wear debris decreased from 7.7% to 4.0%. If the temperature is further increased to 60°C, the average area of
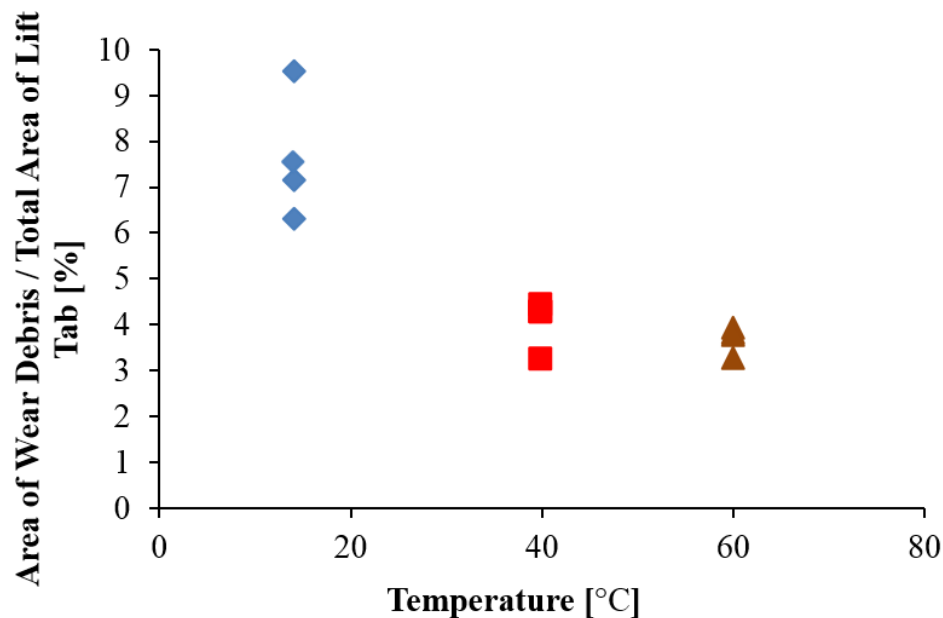
Figure 7.13 Area of the lift tab with wear debris after 300,000 load/unload cycles at 14°C, 40°C, and 60°C, respectively.

the lift tab with wear debris becomes 3.7%. Clearly, the amount of wear debris at the lift tab/ramp interface decreases with an increase in temperature. This result can be explained as follows. Due to the low melting point and the low thermal conductivity of polyoxymethylene, thermal softening of the polyoxymethylene occurs with an increase in temperature. This lowers the shear strength of the lift tab/ramp interface [199]. Consequently, the friction coefficient between polyoxymethylene and stainless steel decreases with an increase in temperature. The wear volume W (Unit: m^3), per unit sliding distance, can be calculated from [200], [201]:

$$W = \frac{K\mu P}{H\sigma\epsilon} \tag{7.3}$$

where K is a constant (Unit: N/m^2), μ is the friction coefficient, P is the contact force (Unit: N), H is the hardness of the polymer (Unit: Pa), σ is the tensile strength of the polymer (Unit: Pa), and ϵ is the strain of the polymer when the stress reaches its tensile strength. When the temperature increases from 14°C to 60°C, the hardness H of polyoxymethylene is constant [202], while $1/\sigma\epsilon$ of polyoxymethylene increases [203]. This indicates that the wear volume would increase if other parameters are kept constant. However, we observed from the experimental results that the amount of wear debris on both the lift tab and the ramp decreases with an increase in temperature. Since the wear volume is proportional to the friction coefficient according to Equation 7.3, one can conclude that the friction coefficient between the lift tab and the ramp decreases as the temperature increases.

7.3.4 Correlation between the Change of the Voice Coil Motor Current and the Amount of Wear Debris on the Lift Tab

Figure 7.14 shows the change of the voice coil motor current after 300,000 load/unload cycles as a function of temperature. Four drives were tested at each temperature. We observe from Figure 7.14 that the average change of the voice coil motor current for the four drives is 11.4 mA at 14°C, 2.2 mA at 40°C, and 0.5 mA at 60°C, corresponding to an increase of the friction force by 13.3 mN, 2.6 mN, and 0.6 mN, respectively. This result suggests that the friction force between the lift tab and the ramp increases by a larger amount if load/unload testing is conducted at lower temperature. This phenomenon can be explained with reference to Figure 7.13. The lift tab tested at low temperature has a large area covered by polyoxymethylene wear debris during load/unload testing. Therefore, the lift tab tested at low temperature has a larger POM/POM contact area than the lift tab tested at high temperature. Because the friction
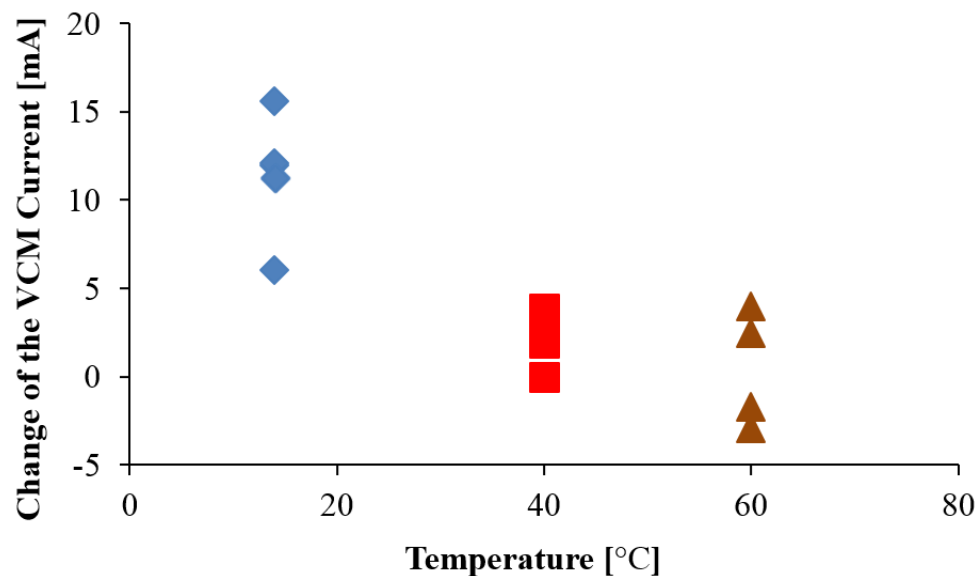
Figure 7.14 Change of the voice coil motor current after 300,000 load/unload cycles as a function of temperature

coefficient of POM/POM contact is higher than that of stainless steel/POM contact [177], the friction force between the lift tab and the ramp increases by a larger amount for drives tested at lower temperature.

Comparing Figure 7.13 and Figure 7.14, we observe that the area covered by wear debris exhibits a similar behavior as the change of the voice coil motor current versus temperature. This suggests that a correlation exists between the amount of wear debris on the lift tab and the change of the voice coil motor current. Figure 7.15 shows the change of the voice coil motor current as a function of the area of the lift tab covered by wear debris for twelve drives. We observe that the change of the voice coil motor current increases monotonically with the increase of the area of the lift tab covered by wear debris. Therefore, we conclude that the voice coil motor current is a good indicator for monitoring the generation of wear debris at the lift tab/ramp interface. Compared to
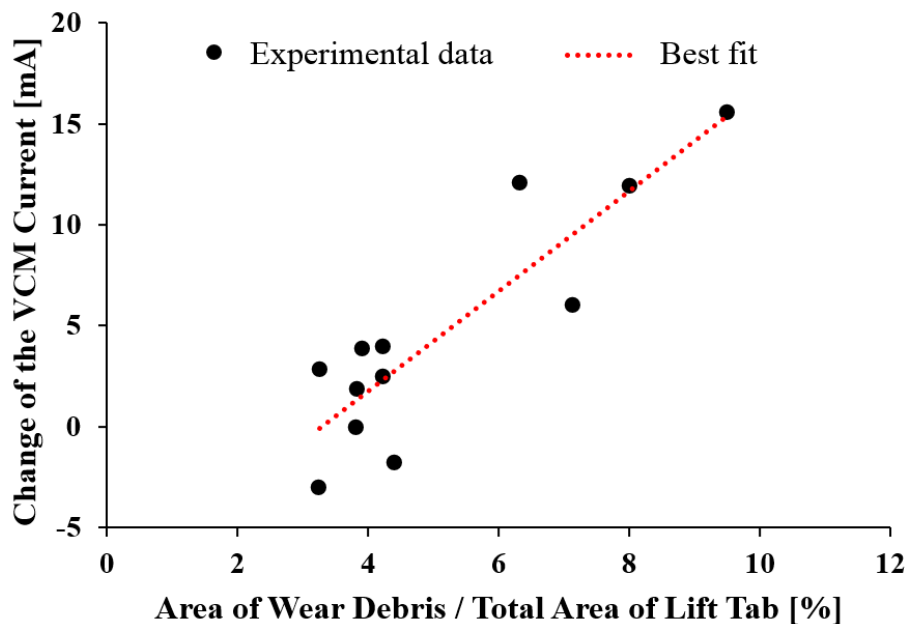
Figure 7.15 Change of the voice coil motor current versus area of wear debris/ total area of lift tab

the conventional method of disassembling a hard disk drive and inspecting the lift tab using an SEM, measurement of the voice coil motor current is a more efficient method that significantly reduces the time for evaluating wear at the lift tab/ramp interface.

7.4 Analytical Model of Contact between the Lift Tab and the Ramp

To explain the experimental results reported in the previous sections and further investigate the tribological performance of the lift tab/ramp interface, we need to calculate the contact stress on the lift tab and the ramp during load/unload. Lift tab/ramp contact is similar to contact between a semi-cylinder and a flat surface as shown in Figure 7.16. This contact problem was investigated by Smith and Liu [204] and Sackfield and Hills [205], [206] based on the analytical solution obtained from Hertzian contact theory [91]. Hertzian contact theory predicts that the contact area between a semi-cylinder and a flat surface is rectangular. The half width b of the contact area is given by [92]
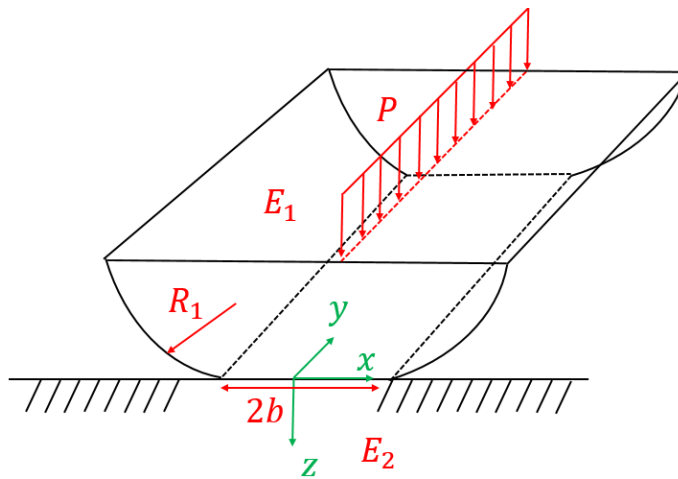
Figure 7.16 Contact between a semi-cylinder and a flat surface

$$b = \sqrt{\frac{4PR^*}{\pi E^*}} \qquad (7.4)$$

where P is the normal load per unit length of the cylinder, and R^* and E^* are the effective radius and the effective elastic modulus of the contact bodies, respectively, defined as

$$R^* = \frac{R_1 R_2}{R_1 + R_2} \qquad (7.5)$$

and

$$E^* = \frac{E_1 E_2}{E_1(1 - v_2{}^2) + E_2(1 - v_1{}^2)} \qquad (7.6)$$

In Equation 7.5, R_1 is the radius of the semi-cylinder and R_2 is the radius of the flat surface, considered to be infinite. In Equation 7.6, the elastic moduli and the Poisson's ratios of the semi-cylinder and the flat surface are E_1, E_2, v_1, and v_2, respectively. According to the Hertzian contact model, the contact pressure at the contact interface along the x-direction follows a semi-elliptic distribution

$$p(x) = p_{max}\sqrt{1 - \frac{x^2}{b^2}} \qquad (7.7)$$

where p_{max} is the maximum pressure at x=0, given by

$$p_{max} = \sqrt{\frac{PE^*}{\pi R^*}} \qquad (7.8)$$

If the semi-cylinder moves relative to the flat surface, the tangential load due to friction must be considered. To calculate the contact stress for this case, Sackfield and Hills [206] derived a set of explicit equations using Boussinesq-Cerruti potential functions [207] and Papkovich-Neuber potential functions [208], [209]. For a moving

sliding contact, Sackfield and Hills's equations are difficult to implement, and numerical analysis is a more expedient approach. In this study, we have studied the lift tab/ramp interface using finite element analysis rather than the analytical solution of [206].

7.5 Finite Element Model

Figure 7.17 shows the finite element model used for the suspension and the ramp. The model includes the base plate, the spring area, the load beam, the flexure, the slider, and the ramp. The suspension is divided into the base plate, the spring area, and the load beam. The tip of the load beam is the so-called "lift tab" which slides on the ramp. The slider is attached to the load beam through the flexure. The suspension and the flexure were constructed with triangular and quadrilateral shell elements. 8-node brick elements were used to model the ramp and the slider.
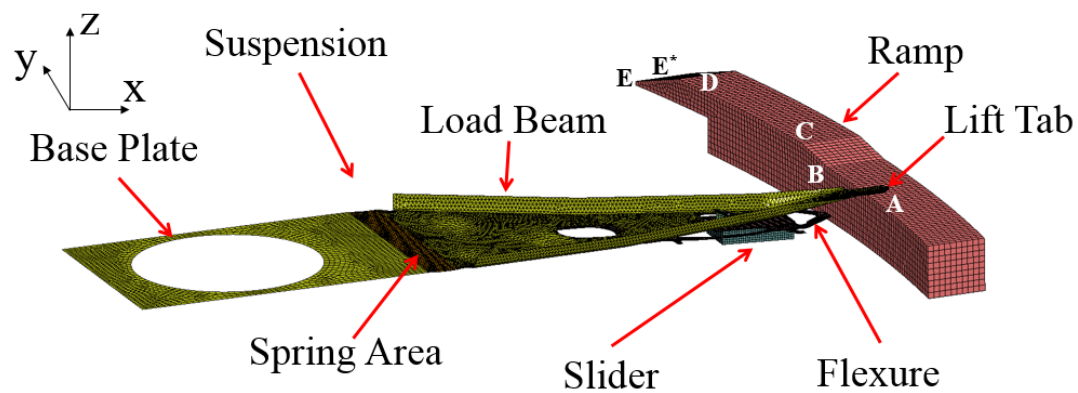
Figure 7.17 Finite element model for the suspension and the ramp
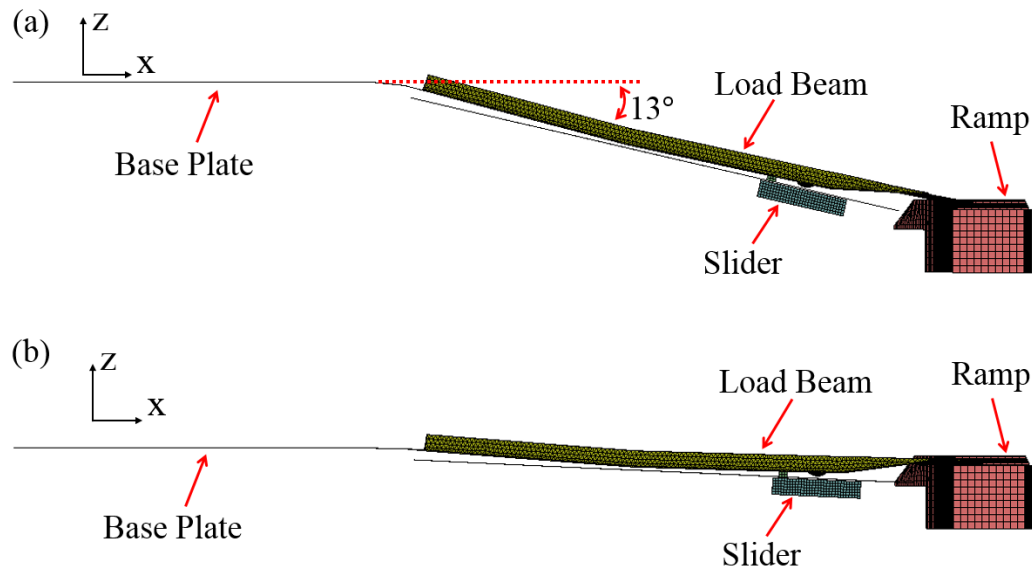
Figure 7.18 Suspension lift tab/ramp interface at (a) the beginning and (b) the end of the "contact" stage.

The simulation process consists of two stages, the "contact" stage and the "sliding" stage. During the "contact" stage, all base plate nodes were fixed. As shown in Figure 7.18 (a), at the beginning of the "contact" stage, the angle between the base plate and the load beam is approximately 13°. At the onset of the loading process, a displacement in the positive z-direction was applied to the ramp until the load beam became nearly horizontal as shown in Figure 7.18 (b). At this position, the "sliding" stage begins. During "sliding", all nodes at the bottom of the ramp were fixed. Nodes on the base plate were constrained in the z-direction but were free to move in the x-y plane. As shown in Figure 7.19 (a), the suspension rotates about the pivot point from position A to E. During this process, the vertical displacement of the lift tab follows the ramp profile as shown in Figure 7.19 (b). At position E^*, a 20 mN air bearing force in the positive z direction was applied to the bottom nodes of the slider. In our model, material properties were assumed to be elastic. Material properties of the suspension,

the ramp, and the slider are summarized in Table 7.1. A penalty-based contact method [130] was used in the model to calculate the contact force. The implicit solver of LS-DYNA [130], a commercially available finite element analysis software, was used to perform the numerical calculation.
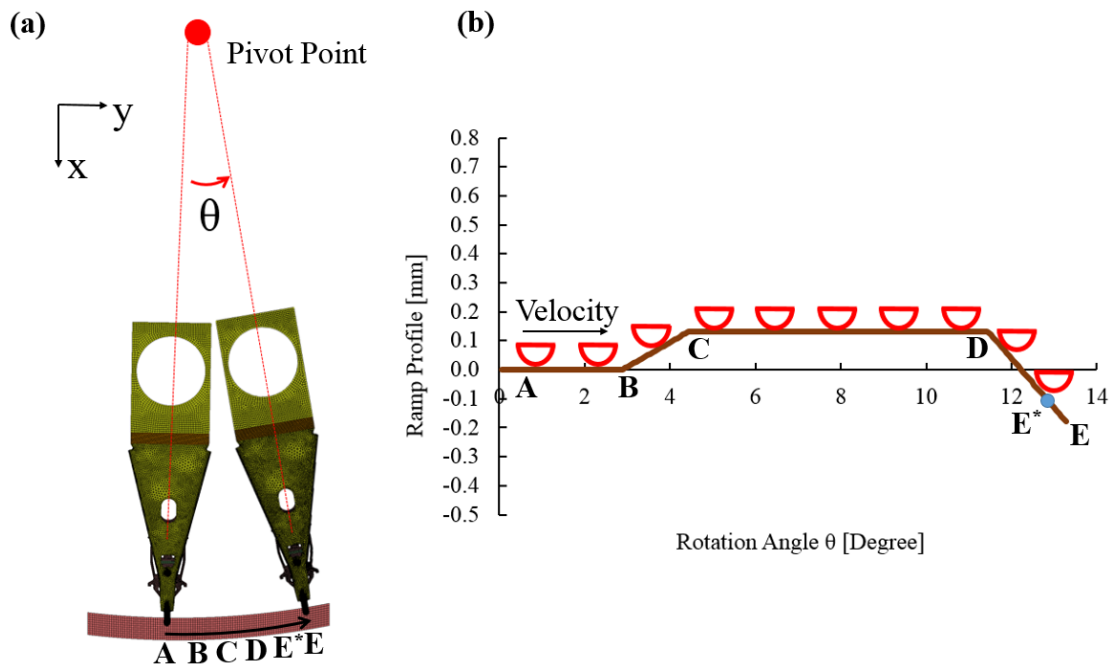
Figure 7.19 (a) Motion of suspension during loading process; (b) lift tab on the ramp during loading process.

Table 7.1 Material properties of different parts in the simulation

Title	Suspension/ Flexure (Stainless Steel)	Ramp (POM)	Slider (Al$_2$O$_3$)
Young's Modulus [GPa]	200	3	120
Density [kg/m^3]	8000	1422	4217
Poisson's Ratio	0.3	0.35	0.25

7.6 Simulation Results and Discussion

7.6.1 Comparison of Simulation Results with Experimental Results for the Ramp

As shown in section 7.3, wear debris is predominantly generated on the ramp surface and then transferred to the lift tab. To study this behavior, we focused our investigation on the analysis of the stress distribution on the ramp and used the maximum von Mises stress as an indicator for the likelihood of wear at the lift tab/ramp interface.

Figure 7.20 shows the maximum von Mises stress on the ramp for a lift tab velocity of 0.076 m/s (3 in/s) and a friction coefficient of 0.3. We observe from Figure 7.20 that the maximum von Mises stress on the ramp section A-B is about 0.37 MPa. During sliding of the lift tab from position B to position C, the maximum von Mises stress on the ramp increases from 0.37 MPa to 0.87 MPa. This increase is caused by the increase in friction and contact force. In the finite element model, the friction force F is determined from

$$F = \mu N \tag{7.9}$$

where μ is the friction coefficient and N is the contact force. During sliding of the lift tab along section B-C, the load beam bends and the moment applied to the load beam increases. In section C-D, the maximum von Mises stress on the ramp is almost constant. At position D, the maximum von Mises stress increases step function–like from 1.0 MPa

to 1.63 MPa. This increase is caused by the decrease of the lift tab/ramp contact area (Figure 7.21) as a function of the lift tab position on the ramp.
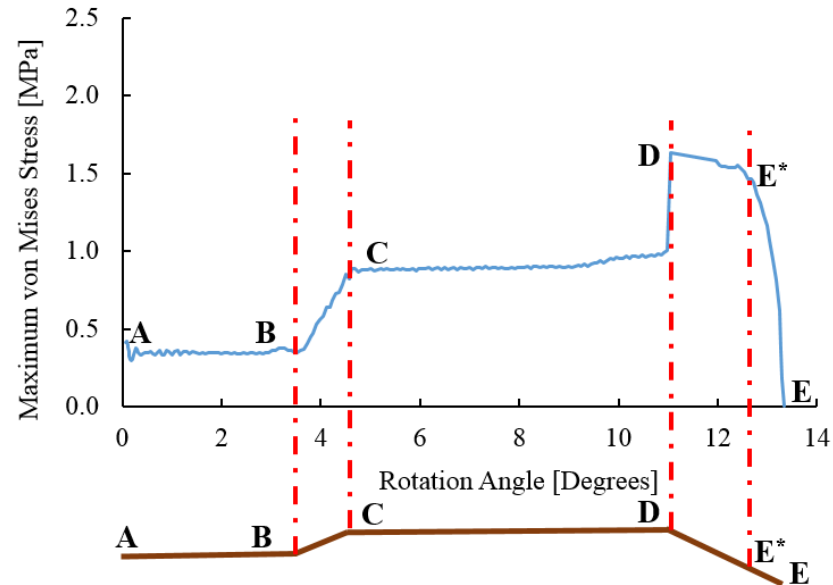
Figure 7.20 The maximum von Mises stress on the ramp when the lift tab slides over the ramp surface with a lateral velocity of 0.076 m/s and a friction coefficient of 0.3
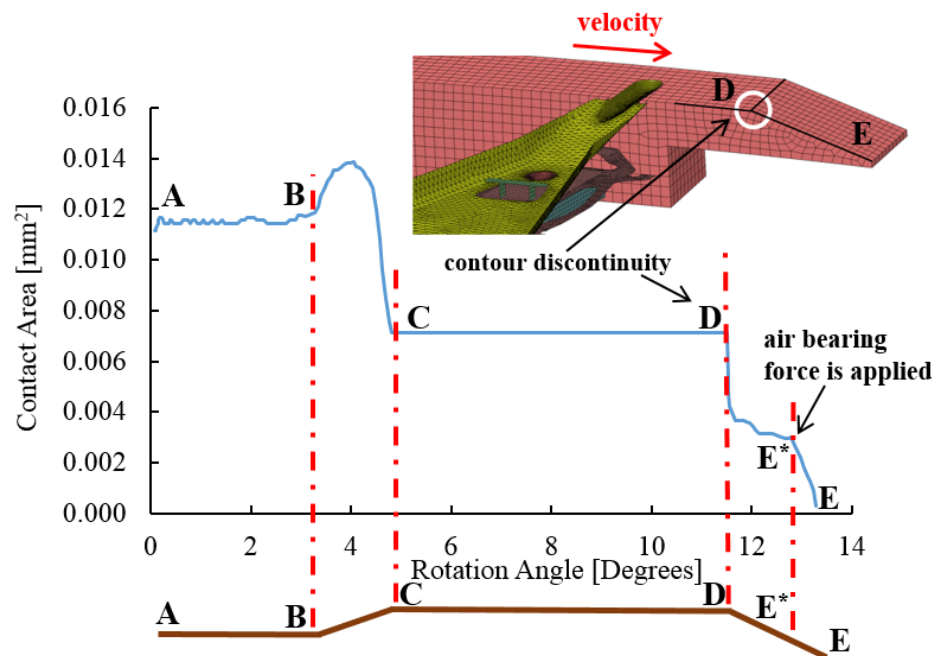
Figure 7.21 Contact area between the lift tab and the ramp

Figure 7.22 shows a magnified image of the ramp near position D after 300,000 load/unload cycles. We observe wear debris accumulation and the presence of grooves on the ramp surface. Comparing the simulation results in Figure 7.20 with the experimental results in Figure 7.22, we observe that the area where wear debris accumulates on the ramp coincides with the location where the largest maximum von Mises stress occurs.
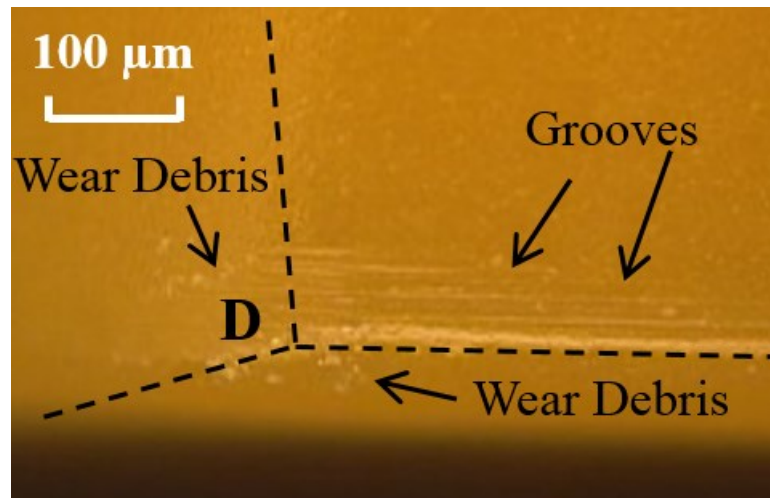
Figure 7.22 Optical microscope image of wear scar near position D of the ramp surface after 300,000 cycles of load/unload testing

7.6.2 Comparison of Simulation Results with Experimental Results for the Lift Tab

Figure 7.23 shows the accumulation of wear debris on the lift tab after 300,000 load/unload cycles. We observe that wear debris is present at two distinct locations, marked "location 1" and "location 2" and that wear debris accumulation is larger in "location 2" of the lift tab than in "location 1". Figure 7.24 shows the von Mises stress on the lift tab during sliding in sections A-B and C-D of the ramp, respectively. We see

that the stress distribution on the lift tab in section A-B shows two distinct stress peaks, similar in shape to the two regions of wear accumulation shown in Figure 7.23 for the lift tab. During sliding of the lift tab on section C-D, the lift tab bends up, causing the contact region to move towards the trailing edge of the lift tab. In this case, only "location 2" is in contact with the ramp.
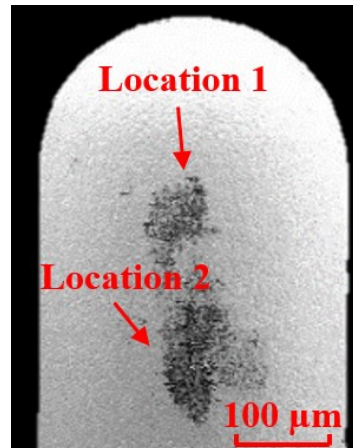
Figure 7.23 Accumulation of wear debris on the lift tab after 300,000 load/unload cycles
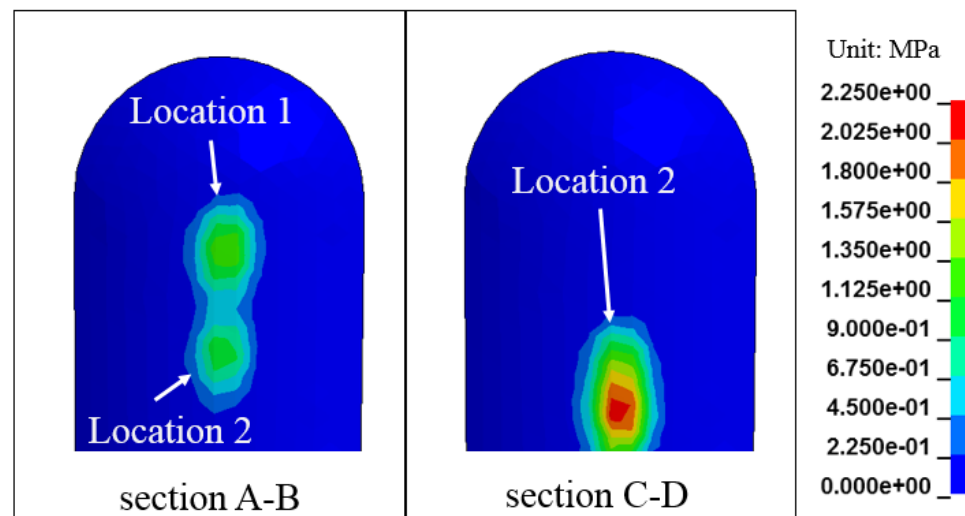
Figure 7.24 Von Mises stress on lift tab in ramp sections A-B and C-D

7.6.3 Effect of Ramp Profile

From investigating the ramp profile after wear, it is apparent that position D on the ramp profile is the location where wear debris and grooves are present (Figure 7.22). Clearly, this location corresponds to the position of largest von Mises stress and it is apparent that ramp design, wear debris generation, and stress levels are related to each other.

To investigate the effect of ramp design on contact stress and wear, we have modified the ramp design by eliminating the slope discontinuity of the ramp at position D. Figure 7.25 shows three different ramp profiles. The "ramp without fillets" has a sharp transition at positions B, C, and D, while the "ramp with 3 mm fillets" and the "ramp with 6 mm fillets" have a smooth transition at positions B, C, and D. Figure 7.26 shows the maximum von Mises stress for these three ramp profiles as the lift tab slides from position A to E. We observe that the largest maximum von Mises stress decreases with an increase in the radius of the fillet.
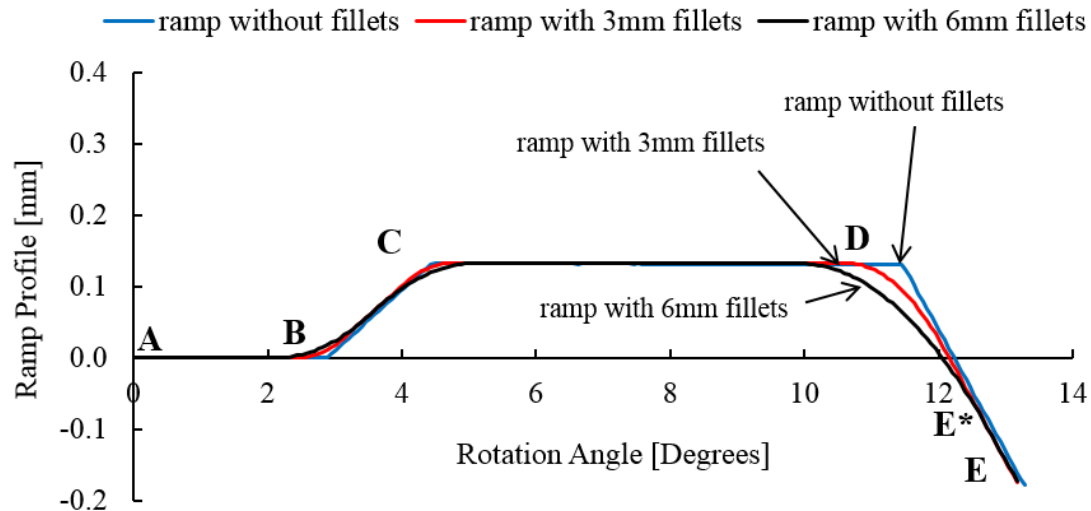
Figure 7.25 Ramp profiles investigated
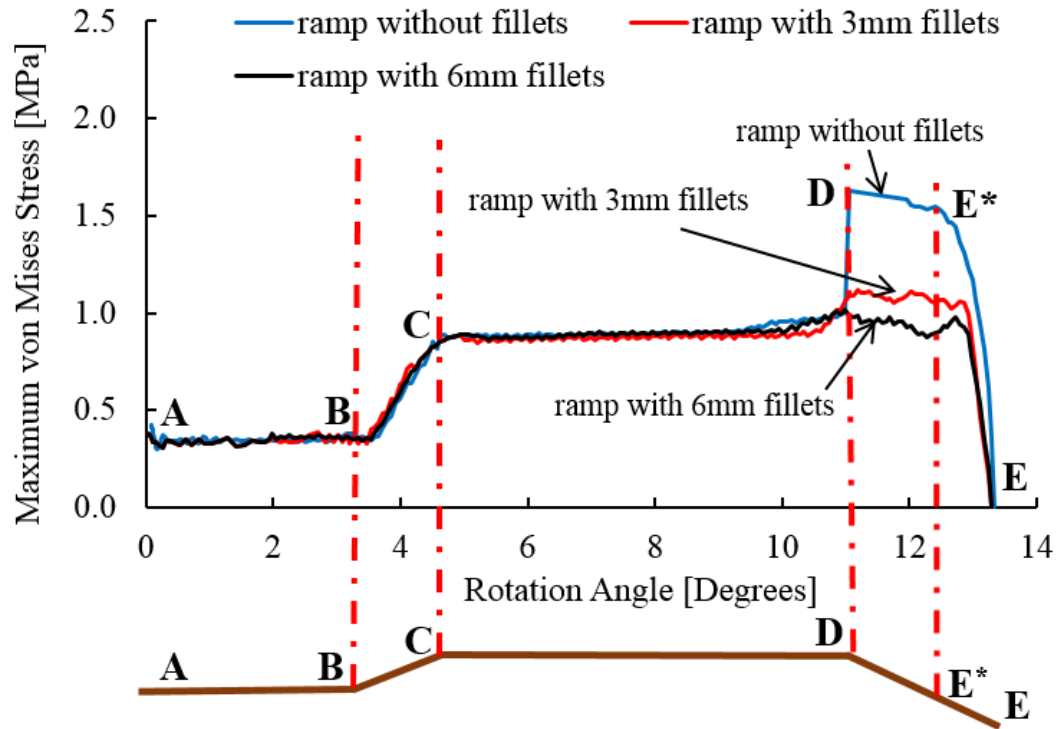
Figure 7.26 Maximum von Mises stress for different ramp contour designs.

In Figure 7.27, the von Mises stress is shown at position D for the "ramp without fillets" and the "ramp with 6 mm fillets". We observe that the presence of the fillet at position D reduces the stress peak of the ramp. Clearly, the design of the ramp contour is an important parameter in reducing contact stress and mitigating wear of the lift tab/ramp interface.
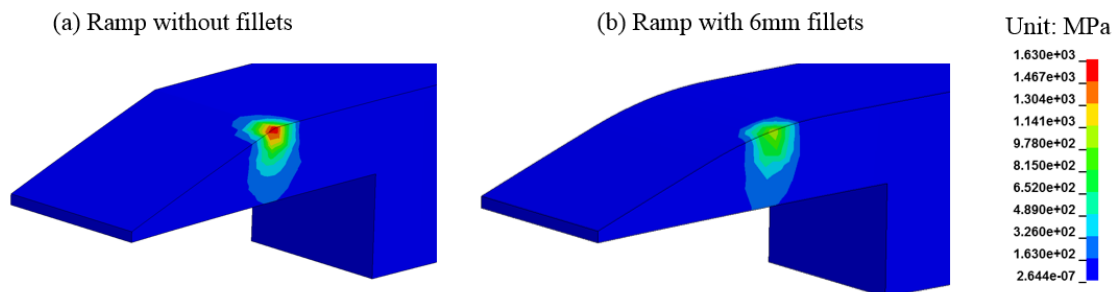
Figure 7.27 Von Mises stress at ramp position D for (a) ramp contour without fillets and (b) ramp contour with 6mm fillets.

7.6.4 Effect of Friction Coefficient and Lift Tab Velocity

Figure 7.28 shows the maximum von Mises stress on the ramp for friction coefficients of μ = 0.1, 0.2, 0.3, and 0.4, respectively. We observe that the von Mises stress is nearly independent of the friction coefficient between positions A and C. Between positions C and D, the maximum von Mises stress increases slightly with the friction coefficient, while in section D to E the von Mises stress is independent of the friction coefficient.
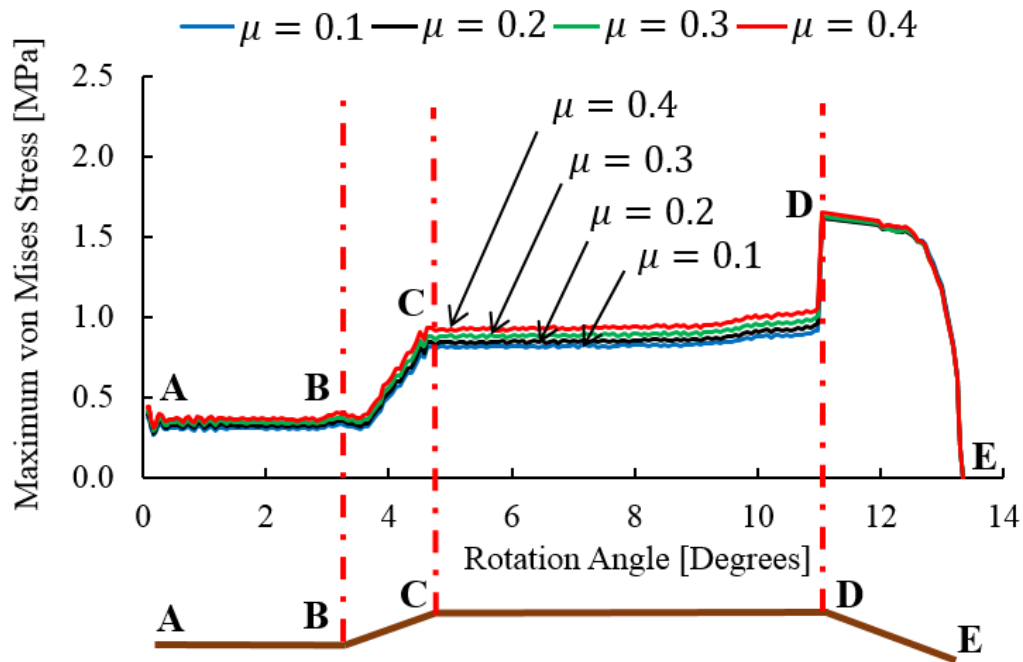
Figure 7.28 Maximum von Mises stress between the lift tab and the ramp (friction coefficient μ = 0.1, 0.2, 0.3, and 0.4, respectively; v=0.076 m/s).

In Figure 7.29, the maximum von Mises stress is shown for lift tab velocities of v=0.076 m/s, 0.102 m/s, and 0.127 m/s, respectively. It is apparent that the magnitude of the von Mises stress is nearly independent of the velocity.
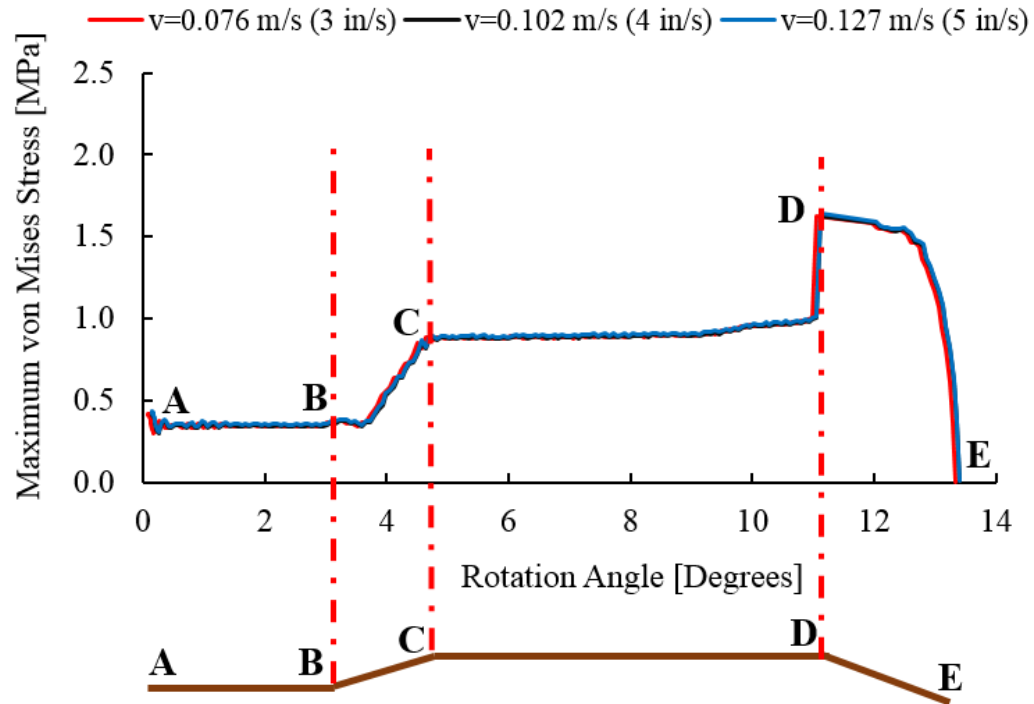
Figure 7.29 Maximum von Mises stress on the ramp during sliding of lift tab on the ramp (v=0.076 m/s, 0.102 m/s, and 0.127 m/s, friction coefficient μ is 0.3).

7.7 Summary

In this study, the tribological performance of the lift tab/ramp interface in a hard disk drive was investigated as a function of the number of load/unload cycles and temperature. It was found that temperature has a significant influence on the generation of wear debris at the lift tab/ramp interface. As the temperature increases, the amount of wear debris was found to decrease. Based on EDX and SEM image analyses, we concluded that wear debris at the lift tab/ramp interface is generated by both adhesion and abrasion. EDX analysis shows that wear debris at the lift tab/ramp interface originates at the ramp and is transferred subsequently to the lift tab during load/unload. During wear testing, the friction force between the lift tab and the ramp appears to

increase because contact changes from a stainless steel/POM situation to a POM/POM situation. The change of the voice coil motor current was found to increase with the amount of wear debris on the lift tab. This indicates that the voice coil motor current of a hard disk drive can be used to characterize the generation of wear debris at the lift tab/ramp interface during load/unload testing. Clearly, this would significantly reduce the time and expenses for failure analysis of the lift tab/ramp interface in hard disk drives.

The simulation results showed that a step function-like stress increase occurs where the slope of the ramp profile changes abruptly (Figure 7.20). Experimental observations showed that wear and wear debris accumulation occurs at the slope discontinuity of the ramp profile at position D (Figure 7.22), i.e., at the position where the largest maximum von Mises stress occurs. Clearly, wear debris generation and maximum von Mises stress are related to each other. To reduce contact stress and wear debris, a smooth ramp profile and a low friction coefficient are required at the lift tab/ramp interface. The numerical simulation results showed little influence of lift tab velocity on contact stress.

7.8 Acknowledgement

Chapter 7, in part, is a reprint of the material in "Simulation of lift tab ramp contact during load unload," Y. Fu, K. Morris, and F. E. Talke, currently under preparation for publication. The dissertation author was the primary investigator and author of this paper.

Chapter 8

Summary and Conclusions

Since the spacing between the slider and the disk in hard disk drives has been reduced to 1 to 2 nm, wear debris on the disk can cause catastrophic damage to the magnetic head and the magnetic disk during head/disk contacts. In this dissertation, the tribological performance of several contact interfaces in hard disk drives was studied.

First, the tribological performance of the dimple/gimbal interface in hard disk drives was investigated. A fretting wear tester was built to study how the DLC overcoat on the gimbal affects the tribological performance of the dimple/gimbal interface. From the experimental results, we found that a thick and soft DLC overcoat is beneficial for reducing the generation of wear debris at the dimple/gimbal interface and the formation of cracks on the dimple. In addition, a finite element analysis model was developed to calculate the contact stress. By comparing the simulation results with the experimental results, we found that a larger maximum principal stress on the dimple and the gimbal causes a larger amount of wear debris generated at the dimple/gimbal interface. The cracks observed on the dimple were found to be generated due to the cyclic stress applied at the edge of the contact area.

Then, a drive-level lubricant migration test was conducted to investigate the effect of parking time, temperature, and slider position on the lubricant migration of the slider. It was found that the head medium spacing decreases when lubricant on the air

bearing surface migrates to the trailing edge of the slider. If the parking time of the slider on the load/unload ramp increases, a larger amount of lubricant migration was observed. It was also found that lubricant migrates at a faster speed if the temperature inside the drive was increased. At 50℃, the largest amount of lubricant migration was observed. With respect to the effect of slider position, when the slider flies at different locations on the disk, the same amount of lubricant migration was observed. However, when the slider flies at the outer diameter position of the disk, lubricants migrate faster on the air bearing surface due to the larger shear stress applied on the lubricant.

Thereafter, a finite element analysis model was developed to study the thermal response of the thermal asperity sensor as it makes contact with thermal asperities on a disk. The simulation results showed that at a particular operational temperature, the resistance of an asperity sensor can remain constant even if the sensor has contact with the thermal asperities. This would lead to asperity detection failure. The simulation results also showed that high disk velocity and low flying height can improve the sensitivity of the sensor. The high bias voltage applied to the sensor can enhance the ability of the sensor to differentiate various types of asperities on the disk.

At the end of this dissertation, a new experimental method was developed to characterize the generation of wear debris at the lift tab/ramp interface. It was found that the voice coil motor current of hard disk drives can be used to characterize the generation of wear debris at the lift tab/ramp interface during load/unload processes. The voice coil motor current increases if a larger amount of wear debris is generated at the lift tab/ramp interface. It was also found that temperature inside the hard disk drive has a significant influence on the generation of wear debris at the lift tab/ramp interface.

If the temperature increases, the amount of wear debris decreases. In addition to the experiment, a numerical simulation was conducted to calculate the contact stress between the lift tab and the ramp. By comparing the simulation results with experimental results, we found that the largest amount of wear debris was generated at the position where the largest von Mises stress occurs. The largest von Mises stress occurs as a result of a stress concentration at the geometric discontinuity of the ramp. The amplitude of stress concentration can be reduced by implementing fillets at the transition section of the ramp.

In conclusion, as the spacing between the slider and the disk in hard disk drives decreases to 1 to 2 nm, wear debris and lubricant migration at the head/disk interface can lead to significant decrease in the read/write performance of hard disk drives. Thus, the tribological performance of contact interfaces in hard disk drives becomes more and more critical in regard to the reliability and lifetime of hard disk drives. The studies presented in this dissertation provide a thorough understanding of the tribological performance of the head/disk interface, the dimple/gimbal interface, and the lift tab/ramp interface of hard disk drives. The experimental and numerical simulation results presented in this dissertation can be used as a guide to improve the tribological performance of hard disk drive.

Appendix A

Contact in LS-DYNA

In this dissertation, finite element simulations were performed using the commercially available software LS-DYNA. LS-DYNA was developed by Livermore Software Technology Corporation (LSTC) based on the finite element software DYNA3D, which was written by Dr. John O. Hallquist in 1970s. In the past four decades, LS-DYNA has been developed to be a general-purpose finite element software, which is being widely used in automotive and aerospace industries. LS-DYNA can perform linear static, quasi-static, rigid body dynamic, non-linear transient dynamic, thermal, fluid, electromagnetic, acoustic, and multi-physics simulations. Compared to other commercially available finite element analysis software, LS-DYNA has higher accuracy for solving non-linear transient dynamic problems, such as automotive crash simulations, airbag inflation, sheet metal stamping, explosions, etc. Explicit time integration is the main method used in LS-DYNA. However, an implicit time solver is also available in LS-DYNA to perform structural and heat transfer analysis.

The command-line driven executable file of LS-DYNA is called "k file". All the "keywords" such as "boundary", "constrained", "contact", "element", "node", "material", "load" and their values are defined in "k file". LS-PrePost is the pre and post processer used to visualize the finite element model defined in the "k file" and show the simulation results.

In LS-DYNA, three different methods can be used to solve contact problems: the penalty method, the kinematic constraint method, and the distributed parameter method. Since all simulations performed in this dissertation use the penalty method, only this method is discussed here.

Figure A.1 shows contact between two surfaces in LS-DYNA. At the beginning of a simulation, penetration (D_p) between contact surfaces is first detected using the bucket-sort approach and the incremental search technique [130]. Then, a virtual spring generates a contact force between the two surfaces to eliminate the penetration. For "one-way contact" in LS-DYNA, a slave surface and a master surface need to be defined to check the penetration of slave nodes into the master surface. The penetration of master nodes into the slave surface is not checked. To detect penetration, the contact
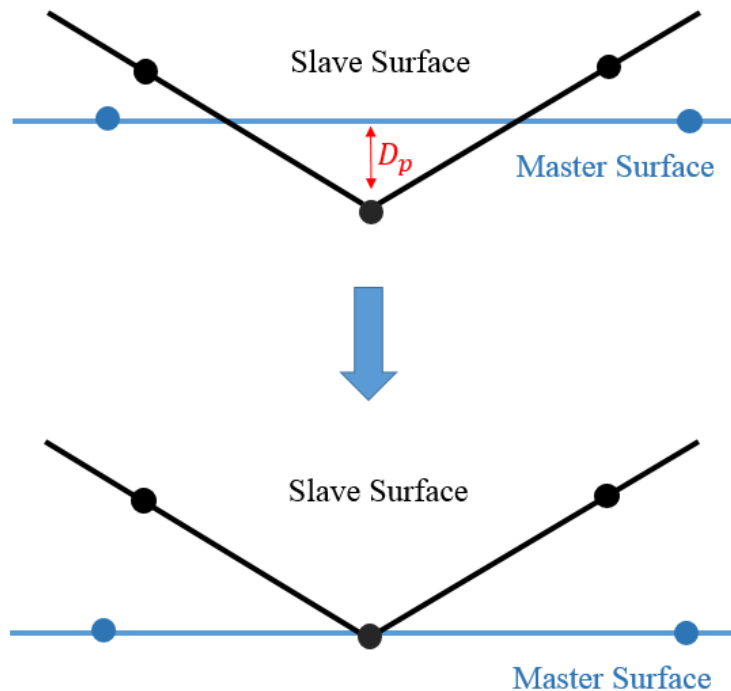
Figure A.1 Contact between a slave surface and a master surface in LS-DYNA

algorithm projects nodes on the slave surface to the master surface. If the projected distance is positive, the node on the slave surface is outside the master surface, i.e., no penetration occurs. Conversely, if the sign of the projected distance is negative, the node on the slave surface is inside the master surface, i.e., penetration occurs. Normally, surfaces with coarse mesh, low order element, large elastic modulus, and flat or concave shape should be defined as the master surface. For "two-surface contact" in LS-DYNA, penetration is checked for nodes on both slave and master surfaces. Therefore, slave surface and master surface can be defined arbitrarily. However, "two-way contact" will cause longer computational time than "one-way contact".

In penalty method, the contact force F_c is proportional to the penetration depth D_p between contact surfaces:

$$F_c = K_c D_p \tag{A.1}$$

where K_c is the contact stiffness, which is adjusted in every time step until the penetration between contact surfaces is minimized. The contact stiffness K_c is a function of the contact area A, the bulk modulus K of contacted element, the user-defined scale factor f_s, and the dimension of contacted element. For solid element, K_c is given by

$$K_c = \frac{A^2 K f_s}{V} \tag{A.2}$$

where V is the volume of the solid element. For shells element, K_c is given by

$$K_c = \frac{A K f_s}{d} \tag{A.3}$$

where d is the maximum diagonal of the shell element.

In LS-DYNA, the friction force between contact surfaces is calculated based on Amontons' law: the friction force is proportional to the contact force. The friction coefficient μ in LS-DYNA is expressed as

$$\mu = \mu_s + (\mu_d - \mu_s)e^{-cv} \tag{A.4}$$

where μ_s and μ_d are static and dynamic friction coefficients, respectively. The constant e is Euler's number. The constant c is called decay constant. The relative velocity between contact surfaces is denoted by v. In this dissertation, friction force between contact surfaces is assumed to be independent of velocity, i.e., the constant c is equal to zero.

Bibliography

[1] "Bringing big data to the enterprise." [Online]. Available: http://www-01.ibm.com/software/data/bigdata/what-is-big-data.html.

[2] "IBM 305 RAMAC." [Online]. Available: https://en.wikipedia.org/wiki/IBM_305_RAMAC.

[3] Dave Bennet, "IBM 305 RAMAC system," *International Business Machines Corporation (IBM)*, 1956. [Online]. Available: http://www.computerhistory.org/revolution/memory-storage/8/259/1044.

[4] MiniTool Solution Ltd, "Seagate launches world's thinnest 2TB mobile hard drive," 2016. [Online]. Available: http://www.partitionwizard.com/partitionmagic/world-thinnest-2tb-mobile-hard-drive.html.

[5] "Hard disk drive." [Online]. Available: https://en.wikipedia.org/wiki/Hard_disk_drive.

[6] H. Zheng, "Investigation of bit patterned media, thermal flying height control sliders and heat assisted magnetic recording in hard disk drives," University of California, San Diego, 2011.

[7] Tylzael, "Longitudinal recording," *wikipedia*, 2005. [Online]. Available: https://de.wikipedia.org/wiki/Longitudinal_Recording.

[8] D. A. Thompson and J. S. Best, "The future of magnetic data storage techology," *IBM J. Res. Dev.*, vol. 44, no. 3, pp. 311–322, 2000.

[9] R. Wood, "The feasibility of magnetic recording at 1 Terabit per square inch," *IEEE Trans. Magn.*, vol. 36, no. 1, pp. 917–923, 2000.

[10] Hitachi Global Storage Technologies, "Perpendicular magnetic recording technology," 2007. [Online]. Available: https://www.hgst.com/sites/default/files/resources/PMR_white_paper_final.pdf.

[11] D. Weller and M. F. Doerner, "Extremely high-density longitudinal magnetic recording media," *Annu. Rev. Mater. Sci.*, vol. 30, pp. 611–655, 2000.

[12] A. M. Taratorin, *Magnetic recording systems and measurements*. Mountain View: Guzik Technical Enterprises, 2004.

[13] John C. Mallinson, "On extremely high density digital recording," *IEEE Trans. Magn.*, vol. 10, no. 2, pp. 368–373, 1981.

[14] T. R. Albrecht, H. Arora, V. A.-V. Yang, J. M. Beaujour, D. Bedau, D. Berman, A. L. Bogdanov, Y. A. Chapuis, J. Cushen, E. E. Dobisz, G. Doerk, H. Gao, M. Grobis, B. Gurney, W. Hanson, O. Hellwig, T. Hirano, P. O. Jubert, D. Kercher, J. Lille, Z. Liu, C. M. Mate, Y. Obukhov, K. C. Patel, K. Rubin, R. Ruiz, M. Schabes, L. Wan, D. Weller, T. W. Wu, and E. Yang, "Bit patterned magnetic recording: theory, media fabrication, and recording performance," *IEEE Trans. Magn.*, vol. 51, no. 5, pp. 1–44, 2015.

[15] E. A. Dobisz, Z. Z. Bandić, T. W. Wu, and T. Albrecht, "Patterned media: Nanofabrication challenges of future disk drives," *Proc. IEEE*, vol. 96, no. 11, pp. 1836–1846, 2008.

[16] C. A. Ross, "Patterned magnetic recording media," *Annu. Rev. Mater. Res.*, vol. 31, pp. 203–235, 2001.

[17] Seagate, "Breaking capacity barriers with seagate shingled magnetic recording," 2014. [Online]. Available: http://www.seagate.com/tech-insights/breaking-areal-density-barriers-with-seagate-smr-master-ti/.

[18] R. Wood, "Shingled magnetic recording and two-dimensional magnetic recording," Santa Clara, CA, 2010.

[19] R. Wood, M. Williams, A. Kavcic, and J. Miles, "The feasibility of magnetic recording at 10 Terabit per square inch on conventional media," *IEEE Trans. Magn.*, vol. 36, no. 1, pp. 917–923, 2000.

[20] R. H. Victora, S. M. Morgan, K. Momsen, E. Cho, and M. F. Erden, "Two-dimensional magnetic recording at 10 Tbits/in2," *IEEE Trans. Magn.*, vol. 48, no. 5, pp. 1697–1703, 2012.

[21] C. M. Kozierok, "Ferrite heads," *The PC Guide*, 2001. [Online]. Available: http://www.pcguide.com/ref/hdd/op/heads/techFerrite-c.html.

[22] W. Thomson, "On the electro-dynamic qualities of metals: Effects of magnetization on the electric conductivity of nickel and of iron," *Proc. R. Soc. London*, vol. 8, pp. 546–550, 1856.

[23] M. N. Baibich, J. M. Broto, A. Fert, F. N. Van Dau, F. Petroff, P. Eitenne, G. Creuzet, A. Friederich, and J. Chazelas, "Giant magnetoresistance of (001)Fe/(001)Cr magnetic superlattices," *Phys. Rev. Lett.*, vol. 61, no. 21, pp. 2472–2475, 1988.

[24] G. Binasch, P. Grunberg, F. Saurenbach, and W. Zinn, "Enhanced magnetoresistance in layered magnetic structures with antiferromagnetic interlayer exchange," *Phys. Rev. B*, vol. 39, no. 7, pp. 4828–4830, 1989.

[25] Nobelprize.org, "The Nobel prize in physics 2007," 2016. [Online]. Available: http://www.nobelprize.org/nobel_prizes/physics/laureates/2007/.

[26] E. Y. Tsymbal and D. G. Pettifor, "Giant magnetoresistance in magnetic metallic multilayers," 1999. [Online]. Available: http://unlcms.unl.edu/cas/physics/tsymbal/tsymbal_files/Presentations/JMW-1999.pdf.

[27] K. Coyne and E. Smith, "Giant magnetoresistance," *Magnet Academy from National High Magnetic Field Laboratory*, 2015. [Online]. Available: https://nationalmaglab.org/education/magnet-academy/learn-the-basics/stories/giant-magnetoresistance.

[28] M. Julliere, "Tunneling between ferromagnetic films," *Phys. Lett. A*, vol. 54, no. 3, pp. 225–226, 1975.

[29] F. J. Himpsel, "GMR vs. TMR (tunnel magnetoresistance): replace metal spacer by insulating spacer," 2010. [Online]. Available: https://www.google.com/patents/US20100128510?dq=cowburn+US+20100128510&hl=en&sa=X&ei=XlVrVOKPENKvacy3gogM&ved=0CB8Q6AEwAA.

[30] K. Kobayashi and H. Akimoto, "TMR film and head technologies," *Fujitsu Sci. Tech. J.*, vol. 42, no. 1, pp. 139–148, 2006.

[31] Y. Shiroishi, K. Fukuda, I. Tagawa, H. Iwasaki, S. Takenoiri, H. Tanaka, H. Mutoh, and N. Yoshikawa, "Future options for HDD storage," *Magn. IEEE Trans.*, vol. 45, no. 10, pp. 3816–3822, 2009.

[32] R. E. Rottmayer, S. Batra, D. Buechel, W. A. Challener, J. Hohlfeld, Y. Kubota, L. Li, B. L. Bin Lu, C. Mihalcea, K. Mountfield, K. Pelhos, C. P. C. Peng, T. Rausch, M. A. Seigler, D. Weller, and X. Y. X. Yang, "Heat-assisted magnetic recording," *IEEE Trans. Magn.*, vol. 42, no. 10, pp. 2417–2421, 2006.

[33] W. A. Challener, C. Peng, A. V. Itagi, D. Karns, W. Peng, Y. Peng, X. Yang, X. Zhu, N. J. Gokemeijer, Y.-T. Hsia, G. Ju, R. E. Rottmayer, M. A. Seigler, and E. C. Gage, "Heat-assisted magnetic recording by a near-field transducer with efficient optical energy transfer," *Nat. Photonics*, vol. 3, no. 5, pp. 220–224, 2009.

[34] M. H. Kryder, E. C. Gage, T. W. McDaniel, W. A. Challener, R. E. Rottmayer, G. Ju, Y. T. Hsia, and M. F. Erden, "Heat assisted magnetic recording," *Proc. IEEE*, vol. 96, no. 11, pp. 1810–1835, 2008.

[35] S. N. Piramanayagam and T. C. Chong, *Developments in data storage: materials perspective*. Hoboken: John Wiley & Sons, 2011.

[36] M. H. Kryder and R. W. Gustafson, "High-density perpendicular recording—advances, issues, and extensibility," *J. Magn. Magn. Mater.*, vol. 287, pp. 449–458, 2005.

[37] I. M. Hutchings, *Tribology: friction and wear of engineering materials*. Oxford: Butterworth-Heinemann Ltd, 1992.

[38] E. M. Jayson, J. Murphy, P. W. Smith, and F. E. Talke, "Effects of air bearing stiffness on a hard disk drive subject to shock and vibration," *J. Tribol.*, vol. 125, no. 2, pp. 343–349, Mar. 2003.

[39] S. Fukui and R. Kaneko, "Analysis of ultra-thin gas film lubrication based on linearized Boltzmann equation: first report—derivation of a generalized lubrication equation including thermal creep flow," *J. Tribol.*, vol. 110, no. 2, pp. 253–261, Apr. 1988.

[40] M. H. Wahl, P. R. Lee, and F. E. Talke, "An efficient finite element-based air bearing simulator for pivoted slider bearings using bi-conjugate gradient algorithms," *Tribol. Trans.*, vol. 39, no. 1, pp. 130–138, Jan. 1996.

[41] Y. Morinishi, T. S. Lund, O. V Vasilyev, and P. Moin, "Fully conservative higher order finite difference schemes for incompressible flow," *J. Comput. Phys.*, vol. 143, no. 1, pp. 90–124, 1998.

[42] L. Wu and D. B. Bogy, "Unstructured adaptive triangular mesh generation techniques and finite volume schemes for the air bearing problem in hard disk drives," *J. Tribol.*, vol. 122, no. 4, pp. 761–770, 2000.

[43] M. Duwensee, S. Suzuki, J. Lin, D. Wachenschwanz, and F. E. Talke, "Air bearing simulation of discrete track recording media," *Magn. IEEE Trans.*, vol.

42, no. 10, pp. 2489–2491, 2006.

[44]   H. Li, H. Zheng, Y. Yoon, and F. E. Talke, "Air bearing simulation for bit patterned media," *Tribol. Lett.*, vol. 33, no. 3, pp. 199–204, 2009.

[45]   P. A. Salas and F. E. Talke, "Numerical simulation of thermal flying-height control sliders to dynamically minimize flying height variations," *Magn. IEEE Trans.*, vol. 49, no. 4, pp. 1337–1342, 2013.

[46]   C. E. Yeack-Scranton, V. D. Khanna, K. F. Etzold, and A. P. Praino, "An active slider for practical contact recording," *Magn. IEEE Trans.*, vol. 26, no. 5, pp. 2478–2483, 1990.

[47]   B. E. Schultz, "Thermal fly-height control (TFC) technology in HGST hard disk drives," *White Pap. Hitachi Glob. Storage Technol.*, 2007.

[48]   J. Zheng, D. B. Bogy, S. Zhang, and W. Yan, "Effects of altitude on thermal flying-height control actuation," *Tribol. Lett.*, vol. 40, no. 3, pp. 295–299, 2010.

[49]   H. Zheng, H. Li, and F. E. Talke, "Numerical simulation of a thermal flying height control slider with dual heater and insulator elements," *IEEE Transactions on Magnetics*, vol. 45, no. 10. pp. 3628–3631, 2009.

[50]   U. Boettcher, H. Li, R. A. de Callafon, and F. E. Talke, "Dynamic flying height adjustment in hard disk drives through feedforward control," *IEEE Transactions on Magnetics*, vol. 47, no. 7. pp. 1823–1829, 2011.

[51]   T. Y. Tsui, G. M. Pharr, W. C. Oliver, C. S. Bhatia, R. L. White, S. Anders, A. Anders, and I. G. Brown, "Nanoindentation and nanoscratching of hard carbon coatings for magnetic disks," in *MRS Proceedings*, 1995, vol. 383, p. 447.

[52]   J. C. Damasceno, S. S. Camargo, F. L. Freire, and R. Carius, "Deposition of Si-DLC films with high hardness, low stress and high deposition rates," *Surf. Coatings Technol.*, vol. 133, pp. 247–252, 2000.

[53]   X. Li and B. Bhushan, "A review of nanoindentation continuous stiffness measurement technique and its applications," *Mater. Charact.*, vol. 48, no. 1, pp. 11–36, 2002.

[54]   A. Khurshudov and R. J. Waltman, "Tribology challenges of modern magnetic hard disk drives," *Wear*, vol. 251, no. 1–12, pp. 1124–1132, Oct. 2001.

[55] M. S. Jhon, P. S. Chung, R. L. Smith, and L. T. Biegler, "A description of multiscale modeling for the head-disk interface focusing on bottom-level lubricant and carbon overcoat models," *Adv. Tribol.*, vol. 2013, 2013.

[56] T. Cheng, B. Zhao, J. Chao, S. W. Meeks, and V. Velidandea, "The lubricant migration rate on the hard disk surface," *Tribol. Lett.*, vol. 9, no. 3–4, pp. 181–185, 2001.

[57] R. Brunner, "Properties of carbon overcoats and perfluoro-polyether lubricants in hard disk drives," University of California, San Diego, 2009.

[58] J. Gui and B. Marchon, "Fly/stiction: mechanical instability of a head-disc interface," *Magn. IEEE Trans.*, vol. 34, no. 4, pp. 1804–1806, 1998.

[59] C. Gao, P. Dai, and V. Vu, "Flying stiction, lubricant pick-up and carbon-overcoat wear of magnetic heads," *J. Tribol.*, vol. 121, no. 1, pp. 97–101, 1999.

[60] Y. Ma and B. Liu, "Lubricant transfer from disk to slider in hard disk drives," *Appl. Phys. Lett.*, vol. 90, no. 14, p. 143516, 2007.

[61] S. V. Canchi and D. B. Bogy, "Experiments on slider lubricant interactions and lubricant transfer using TFC sliders," *Microsyst. Technol.*, vol. 18, no. 9, pp. 1517–1523, 2012.

[62] B. Marchon, T. Karis, Q. Dai, and R. Pit, "A model for lubricant flow from disk to slider," *IEEE Transactions on Magnetics*, vol. 39, no. 5. pp. 2447–2449, 2003.

[63] R. P. Ambekar, D. B. Bogy, and C. S. Bhatia, "Lubricant depletion and disk-to-head lubricant transfer at the head-disk interface in hard disk drives," *Journal of Tribology*, vol. 131, no. 3. p. 031901, 2009.

[64] Y. W. Seo, D. Pan, A. Ovcharenko, M. Yang, and F. E. Talke, "Molecular dynamics simulation of lubricant transfer at the head-disk interface," *IEEE Transactions on Magnetics*, vol. 50, no. 11. pp. 1–4, 2014.

[65] R. Pit, B. Marchon, S. Meeks, and V. Velidandla, "Formation of lubricant ' moguls ' at the head / disk interface," vol. 10, no. 3, pp. 133–142, 2001.

[66] M. Suk, P. Dennig, and D. Gillis, "Magnetic erasures due to impact induced interfacial heating and magnetostriction," *J. Tribol.*, vol. 122, no. 1, pp. 264–268, May 1999.

[67] M. Furukawa, J. Xu, Y. Shimizu, and Y. Kato, "Scratch-induced demagnetization of perpendicular magnetic disk," *IEEE Transactions on Magnetics*, vol. 44, no. 11. pp. 3633–3636, 2008.

[68] S.-C. Lee, S.-Y. Hong, N.-Y. Kim, J. Ferber, X. Che, and B. D. Strom, "Stress induced permanent magnetic signal degradation of perpendicular magnetic recording system," *J. Tribol.*, vol. 131, no. 1, p. 11904, Dec. 2008.

[69] J. Xu, M. Furukawa, A. Nakamura, and M. Honda, "Mechanical demagnetization at head disk interface of perpendicular recording," *IEEE Transactions on Magnetics*, vol. 45, no. 2. pp. 893–898, 2009.

[70] W. Song, A. Ovcharenko, M. Yang, H. Zheng, and F. E. Talke, "Contact between a thermal flying height control slider and a disk asperity," *Microsyst. Technol.*, vol. 18, no. 9–10, pp. 1549–1557, 2012.

[71] B. Bhushan, *Introduction to tribology*, 2nd ed. New York: John Wiley & Sons, 2013.

[72] F. P. Bowden and D. Tabor, *The friction and lubrication of solids*, vol. 1. Oxford: Oxford university press, 2001.

[73] B. Bhushan, *Principles and applications of tribology*. New York: John Wiley & Sons, 2013.

[74] E. Rabinowicz, *Friction and wear of materials*. New York: Wiley, 1965.

[75] J. Archard, "Contact and rubbing of flat surfaces," *J. Appl. Phys.*, vol. 24, no. 8, pp. 981–988, 1953.

[76] J. M. Thompson and M. K. Thompson, "A proposal for the calculation of wear," in *Proceedings Of The 2006 International Ansys Users Conference & Exhibition, Pittsburgh, Pa*, 2006.

[77] N. K. Myshkin, M. I. Petrokovets, and A. V. Kovalev, "Tribology of polymers: adhesion, friction, wear, and mass-transfer," *Tribol. Int.*, vol. 38, no. 11, pp. 910–921, 2005.

[78] J. A. Greenwood and D. Tabor, "Deformation properties of friction junctions," *Proc. Phys. Soc. Sect. B*, vol. 68, no. 9, p. 609, 1955.

[79] K.-H. Zum Gahr, "Wear by hard particles," *Tribol. Int.*, vol. 31, no. 10, pp. 587–

596, 1998.

[80] A. P. Harsha and U. S. Tewari, "Two-body and three-body abrasive wear behaviour of polyaryletherketone composites," *Polym. Test.*, vol. 22, no. 4, pp. 403–418, 2003.

[81] E. Rabinowicz, L. A. Dunn, and P. G. Russell, "A study of abrasive wear under three-body conditions," *Wear*, vol. 4, no. 5, pp. 345–355, 1961.

[82] L. Fang, X. L. Kong, J. Y. Su, and Q. D. Zhou, "Movement patterns of abrasive particles in three-body abrasion," *Wear*, vol. 162, pp. 782–789, 1993.

[83] Y. Xie and B. Bhushan, "Effects of particle size, polishing pad and contact pressure in free abrasive polishing," *Wear*, vol. 200, no. 1, pp. 281–295, 1996.

[84] R. I. Trezona, D. N. Allsopp, and I. M. Hutchings, "Transitions between two-body and three-body abrasive wear: influence of test conditions in the microscale abrasive wear test," *Wear*, vol. 225–229, pp. 205–214, 1999.

[85] M. A. Miner, "Cumulative damage in fatigue," *J. Appl. Mech.*, vol. 12, no. 3, pp. 159–164, 1945.

[86] Nicoguaro, "Fatigue (material)," 2016. [Online]. Available: https://en.wikipedia.org/wiki/Fatigue_(material).

[87] O. Vingsbo and S. Söderberg, "On fretting maps," *Wear*, vol. 126, no. 2, pp. 131–147, 1988.

[88] R. B. Waterhouse, "Fretting wear," *Wear*, vol. 100, no. 1–3, pp. 107–118, 1984.

[89] J. A. Williams, "Wear and wear particles—some fundamentals," *Tribol. Int.*, vol. 38, no. 10, pp. 863–870, 2005.

[90] B. J. Hamrock, S. R. Schmid, and B. O. Jacobson, *Fundamentals of fluid film lubrication*. New York: CRC press, 2004.

[91] H. Hertz, "On the contact of elastic solids," *J. reine angew. Math*, vol. 92, no. 110, pp. 156–171, 1881.

[92] K. L. Johnson, *Contact mechanics*. Cambridge: Cambridge University Press, 1987.

[93]   K. L. Johnson, K. Kendall, and A. D. Roberts, "Surface energy and the contact of elastic solids," in *Proceedings of the Royal Society of London A: Mathematical, Physical and Engineering Sciences*, 1971, vol. 324, no. 1558, pp. 301–313.

[94]   B. V. Derjaguin, V. M. Muller, and Y. P. Toporov, "Effect of contact deformations on the adhesion of particles," *J. Colloid Interface Sci.*, vol. 53, no. 2, pp. 314–326, 1975.

[95]   A. B. Mann, "Nanomechanical properties of solid surfaces and thin films," in *Nanotribology and Nanomechanics*, Springer, 2005, pp. 575–622.

[96]   D. Tabor, "Surface forces and surface interactions," *J. Colloid Interface Sci.*, vol. 58, no. 1, pp. 2–13, 1977.

[97]   K. L. Johnson and J. A. Greenwood, "An adhesion map for the contact of elastic spheres," *J. Colloid Interface Sci.*, vol. 192, no. 2, pp. 326–333, 1997.

[98]   J. A. Greenwood and J. B. P. Williamson, "Contact of nominally flat surfaces," *Proc. R. Soc. London A Math. Phys. Eng. Sci.*, vol. 295, no. 1442, pp. 300–319, Dec. 1966.

[99]   W. R. Chang, I. Etsion, and D. B. Bogy, "An elastic-plastic model for the contact of rough surfaces," *J. Tribol.*, vol. 109, no. 2, pp. 257–263, Apr. 1987.

[100]   W. R. Chang, I. Etsion, and D. B. Bogy, "Static friction coefficient model for metallic rough surfaces," *J. Tribol.*, vol. 110, no. 1, pp. 57–63, Jan. 1988.

[101]   J. Atteberry, "How scanning electron microscopes work," *HowStuffWorks*. [Online]. Available: http://science.howstuffworks.com/scanning-electron-microscope2.htm.

[102]   ISAAC: Imaging Spectroscopy and Analysis Centre, "Scanning electron microscopy (SEM)." [Online]. Available: http://www.gla.ac.uk/schools/ges/research/researchfacilities/isaac/services/scanningelectronmicroscopy/.

[103]   G. Binnig, C. F. Quate, and C. Gerber, "Atomic force microscope," *Phys. Rev. Lett.*, vol. 56, no. 9, p. 930, 1986.

[104]   H. G. Hansma, "How does the AFM work?" [Online]. Available: http://web.physics.ucsb.edu/~hhansma/biomolecules.htm.

[105] S. Laboratories, "How SEM Works," *EAG Inc.* [Online]. Available: http://www.seallabs.com/how-sem-works.html.

[106] R. Egerton, *Electron energy-loss spectroscopy in the electron microscope*, 3rd ed. New York: Springer Science & Business Media, 2011.

[107] A. Tegeder, "High resolution electron energy loss spectroscopy (HREELS)," *Universität Heidelberg*. [Online]. Available: http://www.uni-heidelberg.de/fakultaeten/chemgeo/pci/tegeder/research/methods.html.

[108] ION-TOF, "No Title." [Online]. Available: https://www.iontof.com/pics/customised-tof-sims-5-100p-with-xps-components.jpg.

[109] B. Raeymaekers, S. Helm, R. Brunner, E. B. Fanslau, and F. E. Talke, "Fretting wear between a hollow sphere and flat surface," in *ASME/STLE 2009 International Joint Tribology Conference*, 2009, pp. 435–437.

[110] B. Raeymaekers, S. Helm, R. Brunner, E. B. Fanslau, and F. E. Talke, "Investigation of fretting wear at the dimple/gimbal interface in a hard disk drive suspension," *Wear*, vol. 268, no. 11–12, pp. 1347–1353, 2010.

[111] Y. Yoon, I. Etsion, and F. E. Talke, "The evolution of fretting wear in a micro-spherical contact," *Wear*, vol. 270, no. 9–10, pp. 567–575, 2011.

[112] L. Li, E. B. Fanslau, and F. E. Talke, "An experimental study of the dimple/gimbal interface in a hard disk drive," *Microsyst. Technol.*, vol. 17, no. 5–7, pp. 863–868, 2011.

[113] L. Li, H. Zheng, E. B. Fanslau, and F. E. Talke, "A numerical study of the dimple gimbal interface in a hard disk drive," *Microsyst. Technol.*, vol. 17, no. 5–7, pp. 869–873, 2011.

[114] P. A. Dearnley, "A review of metallic, ceramic and surface-treated metals used for bearing surfaces in human joint replacements.," *Proc. Inst. Mech. Eng. H.*, vol. 213, no. 2, pp. 107–135, 1999.

[115] A. Vanhulsel, F. Velasco, R. Jacobs, L. Eersels, D. Havermans, E. W. Roberts, I. Sherrington, M. J. Anderson, and L. Gaillard, "DLC solid lubricant coatings on ball bearings for space applications," *Tribol. Int.*, vol. 40, no. 7, pp. 1186–1194, 2007.

[116] B. Shi, O. O. Ajayi, G. Fenske, A. Erdemir, and H. Liang, "Tribological performance of some alternative bearing materials for artificial joints," *Wear*, vol. 255, no. 7–12, pp. 1015–1021, 2003.

[117] S. Fouvry, P. Kapsa, H. Zahouani, and L. Vincent, "Wear analysis in fretting of hard coatings through a dissipated energy concept," *Wear*, vol. 203–204, no. 96, pp. 393–403, 1997.

[118] Y. Liu, A. Erdemir, and E. I. Meletis, "A study of the wear mechanism of diamond-like carbon films," *Surf. Coatings Technol.*, vol. 82, no. 1–2, pp. 48–56, 1996.

[119] K. Kato, "Wear in relation to friction — a review," *Wear*, vol. 241, pp. 151–157, 2000.

[120] G. M. Pharr and W. C. Oliver, "Measurement of thin film mechanical properties using nanoindentation," *Mrs Bull.*, vol. 17, no. 7, pp. 28–33, 1992.

[121] R. Saha and W. D. Nix, "Effects of the substrate on the determination of thin film mechanical properties by nanoindentation," *Acta Mater.*, vol. 50, pp. 23–38, 2002.

[122] J. Robertson, "Gap states in amorphous carbon," *Philos. Mag. Lett.*, vol. 57, no. 2, pp. 143–148, 1988.

[123] S. Xu, D. Flynn, B. K. Tay, S. Prawer, K. W. Nugent, S. R. P. Silva, Y. Lifshitz, and W. I. Milne, "Mechanical properties and Raman spectra of tetrahedral amorphous carbon films with high sp 3 fraction deposited using a filtered cathodic arc," *Philos. Mag. Part B*, vol. 76, no. 3, pp. 351–361, 1997.

[124] Y. Xie and J. A. Williams, "The prediction of friction and wear when a soft surface slides against a harder rough surface," *Wear*, vol. 196, no. 1–2, pp. 21–34, 1996.

[125] N. Savvides and T. J. Bell, "Hardness and elastic modulus of diamond and diamond-like carbon films," *Thin Solid Films*, vol. 228, no. 1–2, pp. 289–292, 1993.

[126] A. M. Korsunsky, M. R. McGurk, S. J. Bull, and T. F. Page, "On the hardness of coated systems," *Surf. Coatings Technol.*, vol. 99, no. 1–2, pp. 171–183, 1998.

[127] M. P. Szolwinski and T. N. Farris, "Mechanics of fretting fatigue crack formation," *Wear*, vol. 198, no. 1–2, pp. 93–107, 1996.

[128] G. M. Hamilton, "Explicit equations for the stresses beneath a sliding spherical contact," *Arch. Proc. Inst. Mech. Eng. Part C Mech. Eng. Sci.*, vol. 197, pp. 53–59, 1983.

[129] F. F. Ling, M. Lai, and D. A. Lucca, *Fundamentals of surface mechanics with applications*. New York: Springer, 2002.

[130] J. O. Hallquist, "LS-DYNA theoretical manual," *Livermore Softw. Technol. Corp. Livermore*, 2006.

[131] W. Han and S. Mircea, *Quasistatic contact problems in viscoelasticity and viscoplasticity*. Providence: American Mathematical Society/International Press, 2002.

[132] R. B. Waterhouse, "Fretting fatigue," *Int. Mater. Rev.*, vol. 37, no. 2, pp. 77–97, 1992.

[133] V. Lamacq and M. C. Dubourg, "Modelling of initial fatigue crack growth and crack branching under fretting conditions," *Fatigue Fract. Eng. Mater. Struct.*, vol. 22, no. 6, pp. 535–542, 1999.

[134] U. Krupp, *Fatigue crack propagation in metals and alloys: microstructural aspects and modelling concepts*. Weinheim: John Wiley & Sons, 2007.

[135] Y. Sumi, *Mathematical and computational analyses of cracking formation*. Tokyo: Springer, 2014.

[136] M. Okazaki, H. Yamada, and S. Nohmi, "Temperature dependence of the intrinsic small fatigue crack growth behavior in Ni-base superalloys based on measurement of crack closure," *Metall. Mater. Transcations A*, vol. 27A, no. 4, pp. 1021–1031, 1996.

[137] P. C. Paris and F. Erdogan, "A critical analysis of crack propagation laws," *J. Basic Eng.*, vol. 85, no. 4, pp. 528–533, 1960.

[138] M. H. E. Haddad, K. N. Smith, and T. H. Topper, "Fatigue crack propagation of short cracks," *J. Eng. Mater. Technol.*, vol. 101, no. 1, pp. 42–46, 1979.

[139] D. A. Hills, D. Nowell, and J. J. O'connor, "On the mechanics of fretting fatigue," *Wear*, vol. 125, pp. 129–146, 1988.

[140] T. Nishida, K. Kondoh, X. J, and Y. Mutoh, "Observations and analysis of

relative slip in fretting fatigue," *ASTM Spec. Tech. Publ.*, vol. 1425, pp. 33–43, 2003.

[141] M. C. Dubourg, "Local fretting regime influences on crack initiation and early growth," *ASTM Spec. Tech. Publ.*, vol. 1425, pp. 206–219, 2003.

[142] M. F. Ashby and S. C. Lim, "Wear-mechanism maps," *Scr. Metall. Mater.*, vol. 24, no. 5, pp. 805–810, 1990.

[143] Asaro, R. J. and V. A. Lubarda, *Mechanics of solids and materails*. New York: Cambridge University Press, 2006.

[144] X. Li and B. Bhushan, "Micro/nanomechanical and tribological characterization of ultrathin amorphous carbon coatings," *J. Mater. Res.*, vol. 14, no. 06, pp. 2328–2337, 1996.

[145] K. Holmberg, A. Laukkanen, H. Ronkainen, K. Wallin, S. Varjus, and J. Koskinen, "Tribological contact analysis of a rigid ball sliding on a hard coated surface. Part II: Material deformations influence of coating thickness and young's modulus," *Surf. Coatings Technol.*, vol. 200, no. 12–13, pp. 3810–3823, 2006.

[146] C. M. Mate, "Molecular tribology of disk drives," *Tribol. Lett.*, vol. 4, no. 2, pp. 119–123, 1998.

[147] D. Pan, A. Ovcharenko, R. Tangaraj, M. Yang, and F. E. Talke, "Investigation of lubricant transfer between slider and disk using molecular dynamics simulation," *Tribol. Lett.*, vol. 53, no. 1, pp. 373–381, 2014.

[148] B. Marchon, X. C. Guo, A. Moser, A. Spool, R. Kroeker, and F. Crimi, "Lubricant dynamics on a slider:'The waterfall effect,'" *J. Appl. Phys.*, vol. 105, no. 7, p. 74313, 2009.

[149] C. M. Mate, B. Marchon, A. N. Murthy, and S.-H. Kim, "Lubricant-induced spacing increases at slider–disk interfaces in disk drives," *Tribol. Lett.*, vol. 37, no. 3, pp. 581–590, 2010.

[150] R. L. Wallace, "The reproduction of magnetically recorded signals," *Bell Syst. Tech. J.*, vol. 30, no. 4, pp. 1145–1173, 1951.

[151] M. J. R. Cantow, E. M. Barrall, B. A. Wolf, and H. Geerissen, "Temperature and pressure dependence of the viscosities of perfluoropolyether fluids," *J. Polym. Sci. Part B Polym. Phys.*, vol. 25, no. 3, pp. 603–609, 1987.

[152] Z. Zhao and B. Bhushan, "Effect of bonded lubricant films on the tribological performance of magnetic thin-film rigid disks," *Wear*, vol. 202, no. 1, pp. 50–59, 1996.

[153] M. Kawaguchi, S. Aoki, A. Mitsuo, J. Choi, and T. Kato, "Effect of heat treatment temperature on PFPE molecules bonded on DLC surface," *Tribol. Online*, vol. 3, no. 5, pp. 259–263, 2008.

[154] S. E. Stupp, M. A. Baldwinson, P. McEwen, T. M. Crawford, and C. T. Rogers, "Thermal asperity trends," *IEEE Trans. Magn.*, vol. 35, no. 2, pp. 752–757, 1999.

[155] V. Sharma, S. H. Kim, and S. H. Choa, "Head and media design considerations for reducing thermal asperity," *Tribol. Int.*, vol. 34, no. 5, pp. 307–314, 2001.

[156] M. F. Erden and E. M. Kurtas, "Thermal asperity detection and cancellation in perpendicular magnetic recording systems," *IEEE Trans. Magn.*, vol. 40, no. 3, pp. 1732–1737, 2004.

[157] G. Mathew and I. Tjhia, "Thermal asperity suppression in perpendicular recording channels," *IEEE Trans. Magn.*, vol. 41, no. 10, pp. 2878–2880, 2005.

[158] A. Ovcharenko, M. Yang, K. Chun, and F. E. Talke, "Simulation of magnetic erasure due to transient slider-disk contacts," *IEEE Trans. Magn.*, vol. 46, no. 3 PART 1, pp. 770–777, 2010.

[159] A. Ovcharenko, M. Yang, K. Chun, and F. E. Talke, "Transient thermomechanical contact of an impacting sphere on a moving flat," *J. Tribol.*, vol. 133, no. 3, pp. 031404–1–031404–9, 2011.

[160] W. Song, A. Ovcharenko, B. Knigge, M. Yang, and F. E. Talke, "Effect of contact conditions during thermo-mechanical contact between a thermal flying height control slider and a disk asperity," *Tribol. Int.*, vol. 55, no. 9–10, pp. 100–107, 2012.

[161] M. Roy, K. Gao, I. Jin, W. B. Fitzpatrick, H. S. Dakroub, S. Mao, S. S. Xue, J. H. Lake, and D. Setiadi, "Magnetic recording device including a thermal proximity sensor," US007589928B2, 2009.

[162] Y. Shimizu, J. Xu, H. Kohira, M. Kurita, T. Shiramatsu, and M. Furukawa, "Nano-scale defect mapping on a magnetic disk surface using a contact sensor," *IEEE Trans. Magn.*, vol. 47, no. 10, pp. 3426–3432, 2011.

[163] J. Li, J. Xu, J. Liu, and H. Kohira, "Thermal mechanics of a contact sensor used in hard disk drives," *Microsyst. Technol.*, vol. 19, no. 9–10, pp. 1607–1614, 2013.

[164] S. Lee and C. D. Yeo, "Microwear mechanism of head carbon film during head disk interface sliding contact," *Tribol. Int.*, vol. 45, no. 1, pp. 30–37, 2012.

[165] C. M. Mate, H. Deng, G.-J. Lo, I. Boszormenyi, E. Schreck, and B. Marchon, "Measuring and modeling flash temperatures at magnetic recording head–disk interfaces for well-defined asperity contacts," *Tribol. Lett.*, vol. 58, no. 2, pp. 1–10, 2015.

[166] C. Zhang, A. Ovcharenko, M. Yang, N. Knudson, and F. E. Talke, "An investigation of thermal asperity sensors during contact with disk asperities," *Microsyst. Technol.*, vol. 20, no. 8–9, pp. 1529–1534, 2014.

[167] C. Zhang, A. Ovcharenko, M. Yang, N. Knutson, and F. E. Talke, "Investigations of thermal asperity sensors in thermal flying-height control sliders," *IEEE Trans. Magn.*, vol. 50, no. 11, pp. 18–21, 2014.

[168] R. G. Bayer, *Mechanical wear fundamentals and testing*, 2nd ed. New York: Marcel Dekker Inc, 2004.

[169] B. Bhushan, *Modern tribology handbook*. Boca Raton: CRC Press, 2000.

[170] J. H. Lienhard, *A heat transfer textbook*, 3rd ed. Cambridge: Courier Corporation, 2008.

[171] H. S. Carslaw and J. C. Jaeger, *Conduction of heat in solids*, 2nd ed. Oxford: Clarendon Press, 1959.

[172] M. G. Cooper, B. B. Mikic, and M. M. Yovanovich, "Thermal contact conductance," *Int J. Heat Mass Transf.*, vol. 12, no. 3, pp. 279–300, 1969.

[173] H. Blok, "Theoretical study of temperature rise at surfaces of actual contact under oiliness lubricating conditions," in *Proceedings of the general discussion on lubrication and lubricants*, 1937, pp. 222–235.

[174] M. F. Ashby, J. Abulawi, and H. S. Kong, "Temperature maps for frictional heating in dry sliding," *Tribol. Trans.*, vol. 34, no. 4, pp. 577–587, 1991.

[175] X. Tian and F. E. Kennedy, "Maximum and average flash temperatures in sliding contacts," *J. Tribol.*, vol. 116, no. 1, pp. 167–174, 1994.

[176] T. R. Albrecht, "Load / unload technology for disk drives," *IEEE Trans. Magn.*, vol. 35, no. 2, pp. 2–7, 1999.

[177] M. Suk and T. R. Albrecht, "The evolution of load/unload technology," *Microsyst. Technol.*, vol. 8, no. 1, pp. 10–16, 2002.

[178] H. Ao, H. Wei, and H. Jiang, "Simulation of head-disk interface and ramp/lift-tab interfaces during load/unload process of hard disk drive," *J. Adv. Mech. Des. Syst. Manuf.*, vol. 4, no. 1, pp. 23–31, 2010.

[179] S. Yonemura, S. Weissner, L. Zhou, and F. E. Talke, "Investigation of disk damage caused during load/unload using a surface reflectance analyzer," *Tribol. Int.*, vol. 38, no. 2, pp. 81–87, 2005.

[180] M. Suk and D. Jen, "Potential data loss due to head/disk contacts during dynamic load/unload," *IEEE Trans. Magn.*, vol. 34, no. 4, pp. 1711–1713, 1998.

[181] M. Shoda and H. Tani, "Catastrophic damage of magnetic recording disk caused by slider-disk impact during loading/unloading," *IEEE Trans. Magn.*, vol. 39, no. 2, pp. 893–897, 2003.

[182] P. G. Levi and F. E. Talke, "Load/unload investigations on a rotary actuator disk drive," *IEEE Trans. Magn.*, vol. 28, no. 5, pp. 2877–2879, 1992.

[183] S. Weissner and F. E. Talke, "Load/unload measurements using laser doppler vibrometry and acoustic emission," *Tribol. Int.*, vol. 33, no. 5, pp. 367–372, 2000.

[184] B. Liu and Y. Ma, "Visualization and characterization of slider – disk interactions in dynamic load / unload processes," *IEEE Trans. Magn.*, vol. 39, no. 2, pp. 743–748, 2003.

[185] J. P. Peng, "Theoretical prediction of ramp loading/unloading process in hard disk drives," *J. Tribol.*, vol. 121, no. 3, pp. 568–574, 1999.

[186] K. Peng, B. M. Chen, G. Cheng, and T. H. Lee, "Modeling and compensation of nonlinearities and friction in a micro hard disk drive servo system with nonlinear feedback control," *IEEE Trans. Control Syst. Technol.*, vol. 13, no. 5, pp. 708–721, 2005.

[187] S. Weissner, U. Zander, and F. E. Talke, "A new finite-element based suspension model including displacement limiters for load/unload simulations," *J. Tribol.*, vol. 125, no. 1, pp. 162–167, 2003.

[188] H. Zheng, A. N. Murthy, E. B. Fanslau, and F. E. Talke, "Effect of suspension design on the non-operational shock response in a load/unload hard disk drive," *Microsyst. Technol.*, vol. 16, no. 1–2, pp. 267–271, 2010.

[189] P. J. Blau, "Mechanisms for transitional friction and wear behavior of sliding metals," *Wear*, vol. 72, no. 1, pp. 55–66, 1981.

[190] B. Hiller, J. R. Yaeger, and R. G. Sonnenfeld, "Ramp load/unload friction dependence on temperature, velocity and ramp material," *IEEE Trans. Magn.*, vol. 37, no. 4, pp. 1852–1854, 2001.

[191] M. Suk and D. R. Gillis, "Comparison of friction measurement between load/unload ramps and suspension lift tabs using strain gage and actuator current," *IEEE Trans. Magn.*, vol. 36, no. 5, pp. 2721–2723, 2000.

[192] J. R. Yaeger, "Ramp wear and debris from load/unload lift-tab roughness," *IEEE Trans. Magn.*, vol. 38, no. 5, pp. 2126–2128, 2002.

[193] H. Kuwajima, Y. Ueno, M. Umeda, T. Inaji, A. Ochi, and K. Matsuoka, "New type latch for hard disk drive," *Microsyst. Technol.*, vol. 13, no. 8, pp. 1417–1424, 2007.

[194] Rymuza Zygmunt, *Tribology of Miniature Systems*. Amsterdam: Elsevier, 1989.

[195] C. Ji and J. Ding, "Disk drive employing a velocity profile and back EMF feedback to control a voice coil motor," US 7068463 B1, 2006.

[196] Y. J. Mergler, R. P. Schaake, and A. J. Huis in't Veld, "Material transfer of POM in sliding contact," *Wear*, vol. 256, no. 3, pp. 294–301, 2004.

[197] V. A. Bely, A. I. Sviridenok, M. I. Petrokovets, and V. G. Savkin, *Friction and wear in polymer-based materials*. Oxford: Pergamon Press, 1982.

[198] K. Hokkirigawa and K. Kato, "An experimental and theoretical investigation of ploughing, cutting and wedge formation during abrasive wear," *Tribol. Int.*, vol. 21, no. 1, pp. 51–57, 1988.

[199] S. Bahadur, "Friction of polymers," in *Encyclopedia of tribology*, Springer US, 2013, pp. 1365–1372.

[200] J. K. Lancaster, "Relationships between the wear of polymers and their mechanical properties," in *Proceedings of the Institution of Mechanical*

Engineers, 1968, vol. 183, pp. 98–106.

[201] M. Vaziri, R. T. Spurr, and F. H. Stott, "An investigation of the wear of polymeric materials," *Wear*, vol. 122, no. 3, pp. 329 – 342, 1988.

[202] S. B. Ratner, I. I. Farberova, O. V Radyukevich, and E. G. Lure, "Connection between wear resistance of plastics and other mechanical properties," *Sov. Plast.*, vol. 7, pp. 37–45, 1964.

[203] J. K. Lancaster, "Abrasive wear of polymers," *Wear*, vol. 14, no. 4, pp. 223–239, 1969.

[204] J. O. Smith and C. K. Liu, "Stresses due to tangential and normal loads on an elastic solid with application to some contact stress problems," *J. Appl. Mech. ASME*, vol. 20, no. 2, pp. 157–166, 1953.

[205] A. Sackfield and D. A. Hills, "Some useful results in the classical Hertz contact problem," *J. Strain Anal. Eng. Des.*, vol. 18, no. 2, pp. 101–105, 1983.

[206] A. Sackfield and D. Hills, "A note on the Hertz contact problem: a correlation of standard formulae," *J. Strain Anal. Eng. Des.*, vol. 18, no. 3, pp. 195–197, 1983.

[207] A. E. H. Love, *A treatise on the mathematical theory of elasticity*, vol. 1. Cambridge University Press, 2013.

[208] P. F. Papkovich, "Solution générale des équations différentielles fondamentales d'élasticité, exprimée par trois fonctions harmoniques," *CR Acad. Sci. Paris*, vol. 195, no. 3, pp. 513–515, 1932.

[209] H. V. Neuber, "Ein neuer ansatz zur lösung räumlicher probleme der elastizitätstheorie. der hohlkegel unter einzellast als beispiel," *ZAMM‑Journal Appl. Math. Mech. für Angew. Math. und Mech.*, vol. 14, no. 4, pp. 203–212, 1934.